

THE ENERGY ANALYSIS OF ELECTRONS
EMITTED FROM LOCALISED SITES ON
EXTENDED-AREA HIGH VOLTAGE ELECTRODES

Nicholas Kenneth Allen B.Sc., M.Sc.

A THESIS SUBMITTED FOR THE DEGREE OF
DOCTOR OF PHILOSOPHY

THE UNIVERSITY OF ASTON IN BIRMINGHAM

February 1979

THE ENERGY ANALYSIS OF ELECTRONS
EMITTED FROM LOCALISED SITES ON
EXTENDED-AREA HIGH VOLTAGE ELECTRODES

Nicholas Kenneth Allen B.Sc., M.Sc.

A THESIS SUBMITTED FOR THE DEGREE OF
DOCTOR OF PHILOSOPHY 1979

ABSTRACT

An advanced high resolution hemispherical electron spectrometer has been used to measure the energy spectra of the pre-breakdown electron currents emitted from localised sites on broad-area high voltage electrodes under U.H.V. ($\sim 10^{-10}$ torr) conditions. Four electrode materials have been examined which are of interest in the industrial application of high voltage vacuum insulation. The energy spectra of these electron currents are shifted to low energies by $\sim 100-500$ meV compared to that normally obtained from a metallic field emission source. This displacement is characteristic of the electron energy spectra of semiconducting microtip emitters. A qualitative model for the emission mechanism at these sites has therefore been proposed which involves electron tunnelling through a semiconducting/insulating oxide or impurity microstructure overlaying the metallic electrode surface. This model also accounts for other important properties of the emission sites such as their apparently high field enhancement (β) factor as predicted from the Fowler-Nordheim graphs and their very localised existence. Complementary electron optical and X-Ray analysis studies have also been carried out which provide supporting evidence for this interpretation.

Key words: Field emission,
High Voltage Breakdown

INDEX

	<u>Page</u>
1.0.0 INTRODUCTION	6 - 24
1.1.0 Vacuum breakdown phenomenon.	6 - 8
1.2.0 A review of the work carried out on high voltage breakdown prior to the introduction of ultra high vacuum techniques.	8 - 12
1.3.0 Pre-breakdown studies subsequent to the introduction of ultra high vacuum techniques.	12 - 14
1.4.0 Microparticle breakdown mechanisms.	14 - 16
1.5.0 Microdischarges.	17
1.6.0 The origin of pre-breakdown currents.	17 - 24
1.7.0 The industrial interest.	24
2.0.0 FIELD ELECTRON EMISSION FROM METALS	25 - 58
2.1.0 Introduction.	25
2.2.0 Field emission from metals using free electron theory.	25 - 40
2.3.0 Determination of work function (ϕ) and field enhancement (β) using free electron theory.	40 - 47
2.4.0 Field emission from metals using non-free electron theory.	48 - 52
2.5.0 Determination of work function (ϕ) and field enhancement (β) using non-free electron theory.	52 - 57
2.6.0 Summary.	57 - 58
3.0.0 EXPERIMENTAL	59 - 128
3.1.0 Introduction.	59
3.2.0 Choice of spectrometer.	59 - 62
3.3.0 Hemispherical deflection spectrometer (analyser).	62 - 76
3.4.0 The input and output lenses.	76 - 82
3.5.0 Energy scanning.	82 - 85
3.6.0 Calibration.	85 - 86

	<u>Page</u>
3.7.0	Modifications to spectrometer. 87
3.8.0	The interfacing input lens. 87 - 98
3.9.0	The manipulator assembly. 98 - 119
3.10.0	Obtaining the energy distribution of an emission site. 119 - 128
4.0.0	EXPERIMENTAL RESULTS 129 - 162
4.1.0	Introduction. 129
4.2.0	The performance of the modified spectrometer. 129 - 139
4.3.0	Description of measurements taken on each sample. 140 - 141
4.4.0	The distributions obtained from the test specimens. 141 - 162
5.0.0	STUDIES ON HIGH VOLTAGE VACUUM SWITCH CONTACTS 163 - 197
5.1.0	Introduction. 163
5.2.0	High voltage vacuum switches. 163 - 168
5.3.0	Description of the microscope facility. 168 - 177
5.4.0	Experimental procedure. 177 - 180
5.5.0	Results. 181 - 197
6.0.0	DISCUSSION OF RESULTS 198 - 232
6.1.0	The energy spectra. 198 - 207
6.2.0	The Fowler-Nordheim graphs. 207 - 209
6.3.0	Proposed model of the surface structure at an emission site on a broad area electrode. 210 - 211
6.4.0	Electronic structure of semi-conductors. 211 - 219
6.5.0	Model of field emission from broad area electrodes. 219 - 227
6.6.0	Measurement of work function. 227 - 231
6.7.0	Results of the X-Ray analysis. 231 - 232

	<u>Page</u>
7.0.0 CONCLUSION	233 - 236
REFERENCES	237 - 240
ACKNOWLEDGEMENTS	241

1.0.0 Introduction

1.1.0 Vacuum Breakdown Phenomenon

1.1.1 The phenomenon of vacuum breakdown may be readily demonstrated using an experimental test gap (fig 1). This consists of two plane parallel electrodes which have been polished prior to assembly into an experimental chamber, which is then evacuated to a high vacuum ($<10^{-6}$ torr). If a steadily increasing voltage is applied between the electrodes it will be found that a small but definite current flows between them despite the fact that the vacuum space should provide no electrical conduction. As the voltage is increased the current is found to consist of two components, a steady one which increases uniformly with the voltage and a random one superimposed on this which takes the form of spikes (fig 2) with a peak value which may be orders of magnitude greater than the steady component. If, however, the applied voltage is maintained at a constant value for an extended period of time, with a current limiting resistor included in the high voltage line, the frequency of the microdischarges gradually decreases, eventually disappearing to leave only the steady component. The electrodes are then said to be "conditioned" to this voltage and will behave as a stable insulating gap. The conditioned voltage may be increased by increasing the voltage in small steps and allowing the spike currents to be eliminated at each step before going on to the next one. Eventually, however, a voltage, V_b , is reached, at which the gap resistance falls to zero with the current suddenly increasing to a value determined solely by the external circuit resistance. This is the phenomenon of electrical breakdown and is accompanied by a glowing arc between the electrodes. The value of V_b will be higher if the voltage has been reached in small increments, as in electrode conditioning, rather than if the voltage is suddenly applied.

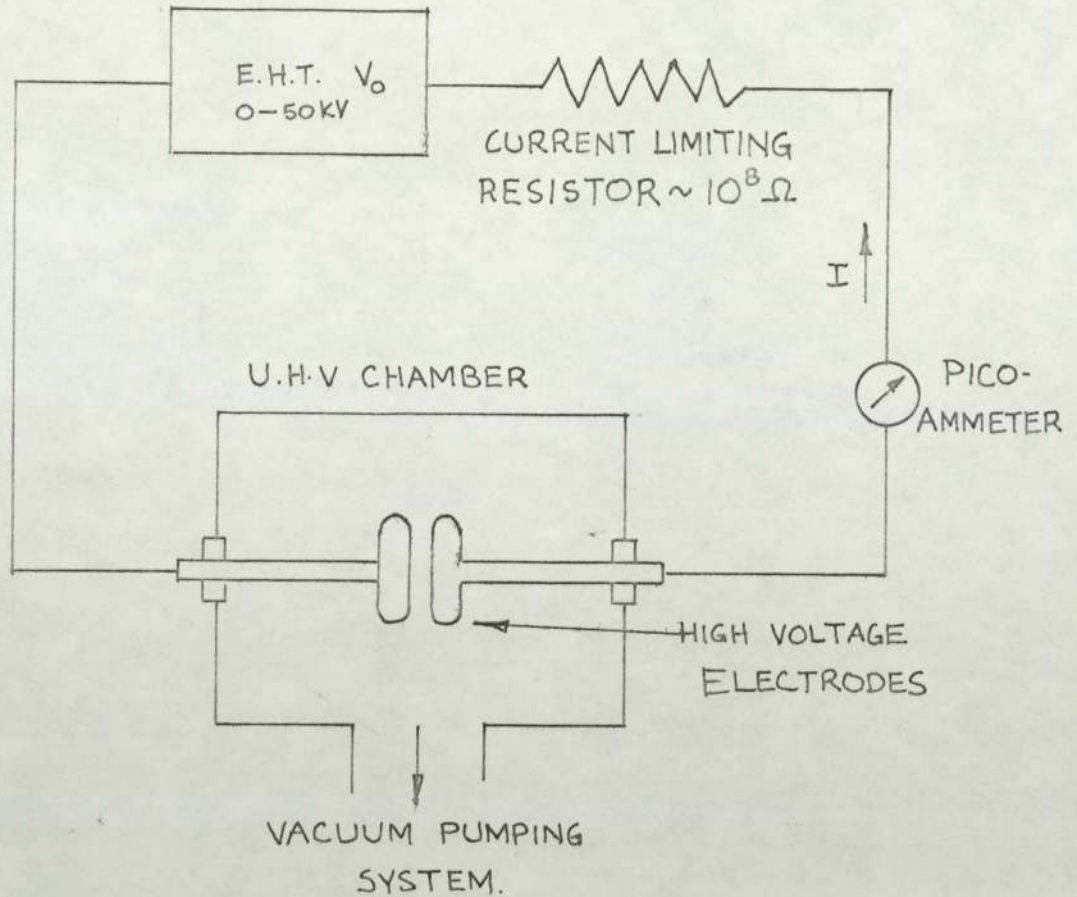


FIG 1. A PLANE-PARALLEL HIGH VOLTAGE VACUUM GAP WITH ITS ASSOCIATED TEST CIRCUITRY.

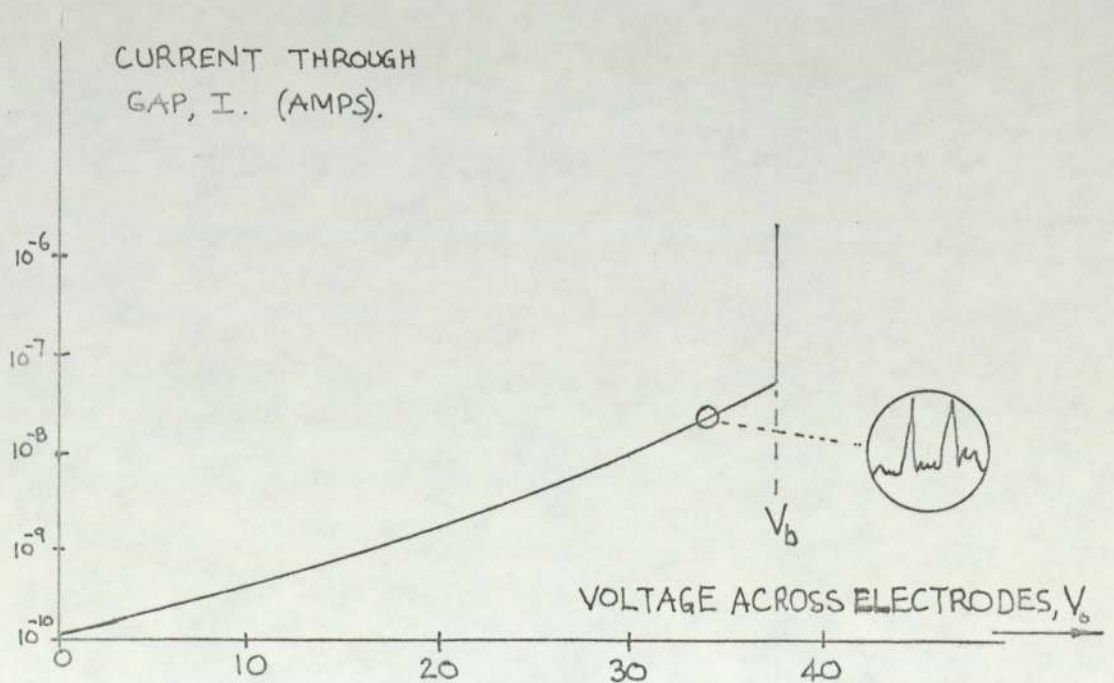


FIG 2. THE NON-LINEAR I - V CHARACTERISTIC OF A TYPICAL VACUUM GAP: IT IS REVERSIBLE FOR $V_0 < V_b$. THE INSET SHOWS THE "NOISY" NATURE OF THE PRE-BREAKDOWN CURRENT.

1.1.2 If the electrodes are removed and examined after electrical breakdown has occurred the surface is found to be in a ruptured state containing many peaks and troughs and generally covered in a vast amount of microscopic debris (fig 3). If the voltage gap between the electrode pair is again tested, it is found to have a much reduced breakdown voltage, V_b^1 , even after conditioning. This non-reversible characteristic makes the prevention of electrical breakdown very important in high voltage technology where a failure would be disastrous.

1.1.3 It is generally accepted that the development of the vacuum discharge occurs in a vapour medium, the vapour being composed of either atoms of one or both of the electrodes or desorbed gas. Moreover, in the final stage of the growth of the discharge, i.e. the arc phase, it is known that the current is sustained by cathode vapour. However, much controversy still exists concerning the detailed processes responsible for the initiation of breakdown in vacuum. Consequently, a great deal of research has been carried out on this phenomenon over many years with a view to explaining and suppressing it.

1.2.0 A review of the work carried out on high voltage breakdown prior to the introduction of ultra high vacuum techniques.

1.2.1 The first reported work on high voltage breakdown in vacuum was by Wood [1] in 1897. The phenomenon was investigated in more detail by Earhart [2] in 1901, who determined the voltage required to cause electrical breakdown between two electrodes at various pressures down to ~ 15 torr. Further work was carried out by Hobbs [3] who noted that breakdown was dependent on the electrode material and occurred at $\sim 10^6$ V/m. Although the work by Earhart and Hobbs was carried out at relatively high pressures, the electrode gaps were small so that the mean free path for electrons and



100 μm .

FIG 3. ELECTRON MICROGRAPH OF A HIGH VOLTAGE SWITCH CONTACT SURFACE THAT HAS SUFFERED ELECTRICAL BREAKDOWN.

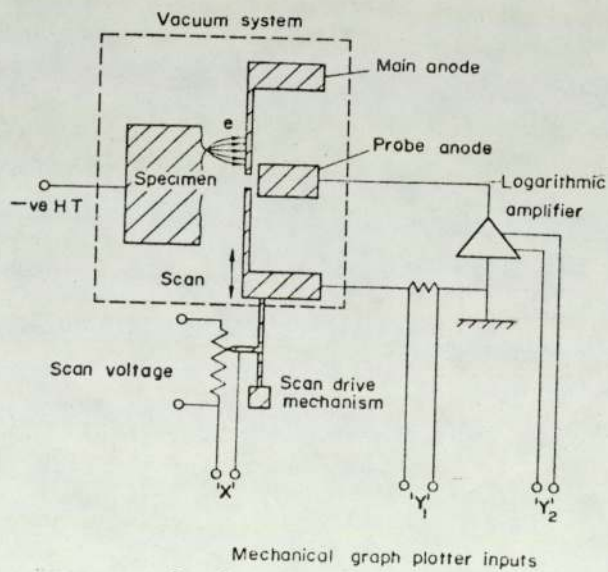


FIG 4. LAYOUT OF ELECTRON PROBE METHOD FOR MAPPING FIELD EMISSION SITES. [COX & WORT (30)].

gas molecules were comparable to, or greater than, the dimensions of the gap; thus the conditions were essentially comparable to those of later experiments which used larger gaps in high vacuum. Millikan and Sawyer [4] confirmed that the voltage required for breakdown was independent of gas pressure in the range $10^{-5} \sim 10^{-8}$ torr. They also made the observation of the effect now known as "electrode conditioning" in which the breakdown voltage performance can be improved by increasing the voltage across the gap in small steps, with a stabilising time following each increment during which sparking or microdischarges occur. By this process, Millikan and Sawyer found they could increase the breakdown field from $\sim 3 \times 10^7$ V/m to $\sim 1.2 \times 10^8$ V/m.

1.2.2 In 1920 Millikan and Shackelford [5] described the results of a long series of experiments on extracting electrons from metals under the influence of a high electric field, the process now known as "field emission". They detected minute currents at fields between $1-5 \times 10^7$ V/m at a pressure of $\sim 10^{-6}$ torr, and although various heat treatments could increase the voltage at which a current could first be detected, they concluded that this did not occur at a specific field.

1.2.3 More precise measurements were reported by Millikan and Eyring in 1926 [6] in which the current versus field relationship was measured for a tungsten wire under various conditioning procedures. They found that the relationship was reversible after an initial conditioning field had been applied. Moreover, they observed fluorescent spots appearing on the anode and concluded that these were caused by electrons emitted from specific spots on the surface of the wire and that these spots must either be isolated points where the work function had been enormously reduced by surface roughness, or caused by chemical impurities. They also pointed

out that the ions produced in the electron beam would be attracted back towards the wire surface and bombard the point of emission.

1.2.4 In 1928 Millikan and Lauritsen [7] drawing on previous results showed that a graph of $\log i$ v. i/F (i - emission current, F - applied field) resulted in a straight line and they also noted the importance that the condition of the surface would have on the results.

1.2.5 Far more comprehensive experiments were carried out by Anderson [8] in 1935 who measured breakdown voltages at various gap spacings and with six different materials at a pressure of $\sim 10^{-5}$ torr. Anderson found that among the materials tested the highest voltage breakdown was achieved with steel and the lowest with copper, using a gap of 1.0mm. The electrode surfaces gave best performance when smoothed with emery paper rather than when polished and the electrode conditioning procedure was to run a discharge between the electrodes of $\sim 0.25 \text{ Acm}^{-2}$ for 3 minutes at a hydrogen pressure of ~ 1 torr, followed by sparking under vacuum. A further observation was that the breakdown voltage for a given electrode material did not increase proportionately with the gap and therefore the electric field at breakdown was reduced with increasing gap. Anderson proposed that this result indicated that the breakdown process could not be one of just cathode field emission. Since the cathode field at breakdown decreased with increasing gap it supported the idea that an anodic process must also be involved. To confirm this, he carried out further experiments using a copper anode and steel cathode. He found that the breakdown voltage corresponded to that of copper electrodes rather than steel, and in each case subsequent spectroscopic examination of the steel cathode showed the presence of copper. In a further experiment to find the variation in current with voltage at a number of fixed values of field, Anderson found

that the current was voltage-sensitive as well as field-sensitive and concluded that this implied that ion transfer as well as electron emission contributed to the current and that therefore positive ions play a role in vacuum breakdown.

1.3.0 Pre-breakdown studies subsequent to the introduction of ultra high vacuum techniques.

1.3.1 A landmark in vacuum breakdown studies was reached with the advent of the field emission microscope [9] and the introduction of ultra high vacuum techniques [10], when it became possible to carry out experiments in which contamination from the vacuum system and the effects of residual gases could be eliminated or controlled and the nature of the cathode surface specified in detail. The first of such experiments was carried out by Dyke and others [11, 12, 13] and were based upon a point-to-plane geometry similar to that of a field emission microscope, with a typical gap of 5mm. The cathode surface could be atomically cleaned and maintained in this condition throughout the course of the experiment. Values for the electric field at breakdown of $\sim 7 \times 10^9$ V/m were obtained, which was one or two orders higher than that found on more usual electrode geometries. The authors also concluded that the breakdown mechanism in this point-to-plane geometry was resistive heating of the cathode tip by field emission currents. Whilst these results were far more controlled and definitive than anything previously published, they were quantitatively so different that it led to the conclusion that the point-to-plane geometry was not directly comparable to the plane-to-plane electrode geometry.

1.3.2 With a view to answering this problem, a series of experiments were carried out by Alpert et al [14] to determine whether the results of the Dyke group were reproducible in the case of broad area electrodes under

similar clean U.H.V. conditions. For their experiments they used electrodes consisting of 35mm dia discs cut from single crystal tungsten. The pressure throughout the measurements was $<2 \times 10^{-9}$ torr, and both the pre-breakdown voltage/current characteristics of the gap and the breakdown voltage were recorded for a range of gaps from 0.005mm to 4mm which covered a range of six orders of magnitude in i/V^2 . Essentially, they found that the pre-breakdown voltage/current characteristics closely followed the equation which Fowler and Nordheim [15] had put forward in 1928 in their theory of field electron emission. They also predicted from these results local field enhancement at the point of emission of 50 - 200 times. Also, after a number of successive breakdowns on a pair of electrodes at a given gap, the breakdown voltage and slope of the graph of $\log i/V^2$ v. $1/V$ (the Fowler Nordheim equation) became constant. They found that for the stated gap range the breakdown field as determined by the plot of $\log i/V^2$ v. $1/V$ was 6×10^9 V/m, virtually identical to the result obtained by both Dyke and Boyle et al [16]. A further point of interest arose from their investigations into the effect of gap spacing on the breakdown voltage. They found that the non-linearity between these two factors could be accounted for by the variation in local field enhancement, β , with gap spacing. They attributed this variation as being due to two contributions to β , a microscopic one caused by microscopic projections on the cathode and a macroscopic one from the changes in electric field distribution at larger gaps. They also noted the multiple anode spots previously obtained by other workers and concluded from this and the repeatability of the voltage/current characteristics that the emission must come from multiple sites on the cathode surface. They argued that it would be most unlikely that following breakdown a single emitting site could be replaced by another projection having identical characteristics. In a subsequent paper, Alpert et al [17]

showed that such emission sites were indeed attributable to protrusions on the cathode surface.

1.4.0 Microparticle Breakdown Mechanism

1.4.1 The studies described in the previous section show that the field emission pre-breakdown current still plays an important role in the breakdown initiation process for electrode separation of 5mm and applied voltages up to $\sim 250\text{kV}$. However, experiments carried out by Rohrbach [18][19] with broad area electrodes of stainless steel and titanium showed that for gap separations $> 10\text{mm}$ (corresponding to applied voltage $> 300\text{kV}$) breakdown occurs for field emission currents $\sim 10^{-9}\text{A}$. Such a low level of current is incompatible with the cathodic resistive heating model of vacuum breakdown proposed by Dolan [13], or a model based on local heating of the anode by the pre-breakdown current. Consequently, a different theory has been evolved to explain the breakdown phenomenon at larger gaps.

1.4.2 The first such theory was put forward by Cranberg in his "clump hypothesis" in 1952 [20]. In this model the initiation of breakdown was attributed to the transfer of charged clumps of material which had been ripped from the surface of one electrode under the influence of the high electric field, and accelerated to high velocities before impacting on the opposite electrode. Clearly, if the clump had sufficient energy it would impact the anode and cause material vaporisation. A connection between this effect and field emission currents was first noted by Little and Smith (1964) [21] who showed, using broad area electrodes, that pre-breakdown currents are associated with thin whisker-like protrusions on the cathode surface. This was further established in 1968 by Latham and Braun [22][23] who showed, using a hairpin cathode and plane anode, that protrusions are formed as a result of pre-breakdown currents. Microscopic

examination of these protrusions revealed them to be the lips of microcraters on the cathode surface apparently formed by the bombardment of the cathode by particles. A further observation was that the anode material would influence the degree of microcratering of the cathode despite the fact that no evidence was found of anode material embedded in the cathode and only slight erosion of the anode material had occurred.

1.4.3 A further relevant factor is that in order for particles ripped from the cathode surface to have sufficient energy to cause vaporisation of the anode material it has been calculated that the impact velocity must exceed $\sim 1500\text{ms}^{-1}$, which, based on estimates of the probable size and charge of a typical microparticle, corresponds to a gap voltage of $> 50\text{kV}$; in practice, however, the cathode microcratering described by Latham and Braun occurred at far lower gap voltages. This fact, together with the observations on the absence of anode damage led to the hypothesis that clumps of material removed from the cathode, having a sub-critical impact velocity, would be reflected back towards the cathode under predominantly elastic conditions. By further assuming that the charge on such a clump could be reversed during the elastic reflection, the possibility would exist of a further acceleration in the gap giving the clump sufficient energy to impact the cathode. Such a mechanism would explain why no anode material was detected on the cathode and the absence of significant anode microcratering. Also, since the charge reversal mechanism would be likely to depend on the electrical properties of the anode surface this would account for the dependence of cathode microcratering on anode material. It was later shown by Brah and Latham [24] that such a mechanism could indeed operate. This was demonstrated experimentally using a specially designed source of artificially generated microparticles in a controlled study of the momentum and charge reversal of such microparticles in a high

voltage vacuum gap for impact velocities in the range $5 - 200\text{ms}^{-1}$.

1.4.4 Another possible mechanism whereby microparticles could give rise to high voltage breakdown was put forward by Olendzkaya [25]. In this model, it is suggested that when a charged microparticle closely approaches the cathode surface the very high electric field set up is sufficient to cause a trigger spark.

1.4.5 Support for such microparticle mechanisms being responsible for vacuum breakdown was put forward by Martynov [26] in 1972, when he showed that particles artificially injected into a stressed vacuum gap could cause breakdown. However, in an experiment carried out by Smalley [27] using previously arced electrodes covered with loosely bound debris no particles were detected. More recently, Texier [28] has detected microparticles using polished stainless steel electrodes at a pressure of $\sim 10^{-5}$ torr. However, these were observed at a non-reproducible voltage which was far below breakdown conditions.

1.4.6 Summarising the present understanding of the relative importance of the two breakdown mechanisms, it can be said that whilst it is known that pre-breakdown currents occur for inter-electrode gap spacings of up to $\sim 5\text{mm}$ and applied voltages up to $\sim 250\text{kV}$, and that in certain situations resistive heating of the anode or cathode is sufficient to cause breakdown, it has yet to be established whether microparticles also have a role to play in this field range. For larger gap spacings it is thought that the microparticle mechanism is predominant although the precise way in which this occurs is still not fully established. In addition, a breakdown event caused solely by microparticles pulled from the electrode surface (rather than artificially induced) has yet to be observed.

1.5.0 Microdischarges

1.5.1 The microdischarges that are observed superimposed on the steady pre-breakdown field emission current (fig 2) represents an example of a phenomenon associated with breakdown which can also be explained in terms of either of the mechanisms discussed in the previous sections. Field emission explanations could be the vaporisation of cathode material in the emission region, or the desorption of occluded gas in the anode. An alternative explanation in terms of the microparticle model would be the transfer of high velocity charged particles between the electrodes; these could be in the form of either surface contamination or loosely bound microfeatures stripped by the electro-mechanical forces of the applied field. In view of the observed cathode microcratering that takes place during the flow of pre-breakdown currents [22] [23], it seems highly likely that microparticles are responsible for at least some of the microdischarges which occur.

1.6.0 The origin of pre-breakdown currents

1.6.1 The mechanism for field emission current initiated vacuum breakdown is well established. If the electrons acquire sufficient energy on crossing the inter-electrode gap they can give rise to an anode "hot spot" and the release of anode material; this can subsequently be ionised by other electrons traversing the gap; this is termed anode initiated breakdown. Alternatively, the heating effects of such currents at the cathode can cause rupture and release of cathode material into the gap with subsequent ionisation; this is known as cathode initiated breakdown.

1.6.2 As a result of the work of Dyke, Alpert and others [11] [12] [13] [14] [16] already discussed in 1.3.0, the explanation for the steady pre-breakdown inter-electrode current shown in fig 2 has generally been

accepted as being due to field emission which occurs at localised sites on the cathode surface where the gap field is locally enhanced. Support for this model comes in particular from the nature of the current-voltage characteristic of such sites which follow the Fowler-Nordheim equation [15]; this was originally put forward in 1928 to explain the emission of electrons from the surface of a metal under the influence of a high electric field at the surface by the process of electron tunnelling. Despite the apparent success of this explanation, there are certain features of the steady pre-breakdown currents which remain unexplained on this conventional metallic field emission model. These anomalies have become apparent in a number of fairly recent investigations into the nature of the pre-breakdown emission currents. These are reviewed in the following sections.

1.6.3 As will be shown more fully in (2.1.0), applying the Fowler-Nordheim analysis to the pre-breakdown emission sites predicts that they are either localised enhanced field regions or areas of much lower work function than normally attributed to the electrode material in question. In 1963, Little and Whitney [29] carried out some experiments in an attempt to resolve which of these two possibilities was responsible. They reasoned that if the pre-breakdown currents came from regions of low work function then from the Richardson-Schottky theory of thermionic emission there would be an easily observable temperature dependence of emission. In the experiments the cathode was made of stainless steel, 0.5 inch in diameter and the anode was of glass, suitably coated to be both conducting and fluorescent. With this arrangement the pre-breakdown currents gave rise to anode spots, the intensity of which could be individually monitored. It was found that the intensity of light was proportional to the anode current which permitted accurate voltage/current measurements for each emitting site. These showed that the pre-breakdown current remained

fairly constant from 77K to 1000K at which point the current began to rise exponentially. It was concluded from this that the emission sites did not originate from very low work function areas and must therefore be due to localised field enhancement. As additional evidence for this it was found that illuminating the cathode with visible light had no effect on the pre-breakdown current. Some further experiments were then carried out to see if the protrusions giving rise to the field enhancement were visible on the cathode surface. With the glass anode used in the experiments it was possible to directly observe the cathode surface in the region of the emission site using an optical microscope. Some irregularities were noted but there was insufficient resolution to make any definite conclusions.

1.6.4 By installing the cathode in a shadow electron microscope, it was possible to observe the region of the emission site after noting its position from the field emission experiment to an accuracy of about 0.25mm^2 . In each case a projection about 2μ in height was found. A further refinement was to carry out the field emission in the microscope and observe the surface in situ directly afterwards, thus eliminating the necessity of transferring the specimen from one system to the other. Again, surface protrusions were always found and their estimated size gave an enhancement factor which corresponded with that predicted from the Fowler-Nordheim plot of the emission characteristics. In the light of the more recent work to be discussed, the accuracy of emission site location must be regarded as rather poor and casts doubts as to whether the observed protrusions were indeed the origin of the field emitting sites.

1.6.5 In 1972, Cox and Wort [30] reported on an improved method of locating and mapping field emission sites on broad area electrodes. This method incorporated a probe hole technique which consisted essentially of a planar

main anode having a 0.5mm dia. central hole behind which was mounted a secondary probe anode (fig 4). On applying a high voltage between the specimen and the main anode a pre-breakdown field emission current could be established; the position of an emission site was determined by moving the anode assembly relative to the specimen. When the probe hole was over the site the main anode current would fall whilst the probe anode current would simultaneously rise. In addition, this technique allowed the measurement of the voltage/current characteristics of an individual site, and the mapping of constant current contours. The technique had an estimated accuracy of $\sim 0.1\text{mm}$. An interesting experiment was carried out with this apparatus by artificially inserting a tungsten tip into a planar copper surface and then measuring any emission from this "site". When this was done emission was obtained at a position close to, but quite separate from, this artificial protrusion. This result shows that the feature on the cathode surface which appears on microscopic examination to be the most likely source of emission is not necessarily the one which actually emits.

1.6.6 Following earlier doubts on the precise nature of the pre-breakdown emission mechanism [22] [23], Walters, Fox and Latham 1973 [31] attempted to identify the surface features at which emission occurred. They carried out experiments on a point cathode (in the form of an undamaged electron microscope filament) with a view to establishing the microfeatures responsible for the electron emission sites. The procedure adopted by WFL was to image the emission from the cathode using the electron lens system of a conventional electron microscope and then to subsequently examine the microtopography of the surface of the cathode using a scanning electron microscope. A necessary procedure for obtaining the emission image with the available field range was to raise the temperature of the emitter to 800°C . Using an undamaged cathode, an emission image was obtained which was then identified

with a particular ridged area on the magnified emitter surface. The geometry of these ridges were such that it was impossible to attribute local field enhancement as the cause of the level of emission current obtained if a metallic field emission model was assumed.

1.6.7 Further tests were therefore carried out to ascertain whether the elevated temperature of the emitter had altered the emission mechanism to that of field assisted thermionic emission. Accordingly, voltage/current measurements were made over a range of cathode temperatures and these plotted according to both the field emission (Fowler-Nordheim) equation and the thermionic emission (Richardson-Schottky) equation. The results showed linearity with the thermionic emission equation over the complete range of temperatures but linear agreement with the field emission equation only up to about 650°C. It was suggested by the authors that possibly field emission was operating at room temperature but became masked at higher temperatures by the thermionic effect. However, calculations based on the observations showed that a field emission mechanism would require local field enhancement of about 200 times which was incompatible with the geometry of the emitting microfeatures observed in the scanning electron microscope experiments. Assuming a thermionic emission model throughout, however, gave the realistic field enhancement value of $\sim 6x$.

1.6.8 Another explanation discussed was based on the presence of the thin oxide contaminating layer which would inevitably be covering the cathode at the experimental pressures used ($\sim 10^{-5}$ torr). With the dielectric nature of such a surface it is possible to consider an alternative mechanism known as Malter emission [32] in which the high field developed across the layer results in field emission from the cathode substrate followed by almost unimpeded acceleration of the electrons through the dielectric. Such a

model would not necessarily require a geometrical protrusion to account for the enhanced emission current.

1.6.9 Another technique for observing pre-breakdown emission from broad area electrodes was reported by Young in 1973 [33]. He used the principle first reported by Millikan and Eyring [6] that electron emission from the cathode surface produces light spots where the beam strikes the anode surface. In his technique, Young used an image intensifier to observe and measure the radiation from individual spots. He showed that the intensity of each spot was proportional to the beam current so that it was possible to measure the voltage current characteristic for each individual spot. Further, by using a simple graphical model to simulate the electron trajectory path for each spot, Young was able to estimate the position of each emission site on the cathode to within $40\mu\text{m}$. He found the voltage-current plots corresponded to the field emission theory, giving local field enhancement values between 150 and 250.

1.6.10 In 1975, Cox [34] reported on an improved probe hole technique for investigating emission from broad area electrodes which had been reported earlier [30]. The main improvement was in incorporating the probe hole facility into a scanning electron microscope. In this way it was possible to first locate and measure an individual emission site as before and then with the specimen in situ observe the surface microtopography in the region of the site using the microscope. By employing an improved electron trajectory technique it was possible to predict the position of an emission site to within a $20\mu\text{m}$ square and then take an electron micrograph of this exact area. The results again showed that whilst the electrical characteristics of many individual emission sites predicted a field enhancement factor of $\sim 100x$, no complementary surface features were found which would give enhancement of this order. Similar results were found on stainless

steel broad area electrodes by Cox and Williams [35] [36] using the same equipment. This technique was also employed for some of the experimental work carried out for this thesis and is described in greater detail in chapter (5).

1.6.11 Other work on the imaging of pre-breakdown field emission was carried out by Jüttner et al in 1975 [37] using tip cathodes of copper and molybdenum. The tip radii were $\sim 10\mu\text{m}$ and gap distance $\geq 1\text{mm}$ thus were not strictly broad area in nature. The measurements were carried out using nano-second pulses to reduce any undesirable effects on the tip caused by prolonged field emission such as blunting by ion bombardment. Imaging of the emission current and the effect of residual gas was further examined by Jüttner, Wolff and Altrichter [38] but revealed no symmetrical crystallographic pattern.

1.6.12 In 1977, Hurley and Dooley [39] reported on an investigation into spots of light which appear on the surface of the cathode during pre-breakdown current emission, a phenomenon earlier noted by Klyarfeld and Pokrovskayo-Soboleva in 1970 [40]. The technique used broad area copper electrodes and it was observed that these cathode spots were sometimes unambiguously associated with subsequent discharge flares and tracks. The procedure was to observe the cathode spots using an image intensifier and then to measure their spectral content using optical filters and a photomultiplier. The authors concluded from the spectrum obtained and the applied voltage/light intensity relationships of the spots that they were caused by field induced electroluminescence on semi-conducting inclusions on the surface.

1.6.13 It is clear from the work discussed in the previous paragraphs that the nature of the emission sites which give rise to the pre-breakdown

currents is still not fully understood. The work described in this thesis is concerned specifically with the study of such pre-breakdown currents and in particular with employing an original sophisticated technique in an attempt to explain their true origin.

1.7.0 The Industrial Interest

1.7.1 From the industrial point of view a distinction has to be made between two different types of application in high vacuum technology. In the first, which may be termed the "passive" situation, clean, polished electrodes are rigidly held in close proximity under vacuum and it is essential that - for the range of voltages to be applied - electrical breakdown should be prevented at all times. Typical examples are in particle accelerators, electron microscopes and transmission valves. The other situation, which may be termed the "active" model, is in the specialist application of the high voltage vacuum switch. This is used extensively in the electricity supply and distribution industry and is discussed more fully in Chapter 5. The work described in this thesis contains studies carried out on the nature of pre-breakdown currents on materials used in both the active and passive situations. If this phenomenon could be properly understood, it might reveal the complete mechanism of the breakdown event with the possibility of then being able to suppress it.

2.0.0 Field Electron Emission From Metals

2.1.0 Introduction

2.1.1 As has been indicated in the previous chapter, the traditionally accepted explanation for pre-breakdown emission sites has been the presence of whisker-like protrusions on the cathode surface which locally enhance the applied field. On such a model, the emission characteristics are assumed to be those corresponding to a metal. In order to put the present studies on pre-breakdown currents into perspective, therefore, it is necessary to review the present understanding of field electron emission from metals and the nature of the results to be expected. In addition, this chapter contains details of the ways in which the work function (ϕ) and local field enhancement (β) may be determined at the point of emission together with certain features of the energy distributions (spectra) of such field emitted electrons which can give further information on the nature of the emission mechanism operating at a given site. This latter aspect forms the basis of the experimental work presented in this thesis.

2.2.0 Field emission from metals using free electron theory.

2.2.1 It was established at an early stage that the current flowing between two electrodes prior to vacuum breakdown is caused by field emission from the cathode (5) (6), and later experiments have confirmed that the emission comes from localised sites on the surface, e.g. (6)(10)(29)(33)(30) (34). Field emission is the emission of electrons from a surface of a material into a vacuum under the influence of a high electric field. The first satisfactory theory of this phenomenon for electrical conductors was put forward by Fowler and Nordheim in 1928 [15] using the then-new quantum theory in which they proposed electron tunnelling through a reduced surface potential barrier as the explanation of the experimentally measured current. The important features of this model will now be discussed.

2.2.2 The Fowler Nordheim theory makes four basic assumptions:

- 2.2.2(1) The temperature of the metal is at OK
- 2.2.2(2) Inside the metal the free-electron approximation applies
- 2.2.2(3) The surface is taken to be smooth and plane
- 2.2.2(4) The potential barrier close to the surface in the vacuum region consists of an image-force potential and a potential due to the applied electric field.

A surface is defined as smooth when any irregularities are slight compared to the width of the potential barrier. Fig(5) shows the one-dimensional potential energy $V(x)$ of an electron as a function of its distance x from the surface. At OK the Fermi energy, ζ , corresponds to the highest filled energy level in the metal while ϕ , the work function of an infinitely large extended plane, gives the energy needed to remove an electron from the Fermi level to a point infinitely distant in the vacuum. The electrons in the metal have a potential V_p which, following the free electron model, is assumed constant. The image force is the Coulomb attraction towards the surface of an electron outside, due to its induced positive charge inside the metal [41].

2.2.3 The general method adopted by Fowler and Nordheim to solve this problem was to treat the conduction electrons in a metal as a gas of free particles which obey Fermi-Dirac statistics and then to consider a supply function, $N(W)dW$, which represents the number of these electrons with the x part of their energy within the range W to $W + dW$ incident on the metal surface per second per unit area. This is then multiplied by the penetration probability $D(W)$ to obtain the number of electrons within the range W to $W + dW$ that emerge from the metal surface per second per unit area, denoted $P(W)dW$. The total current density, which is the solution of the Fowler-Nordheim equation, is obtained by integrating $P(W)dW$ over all W .

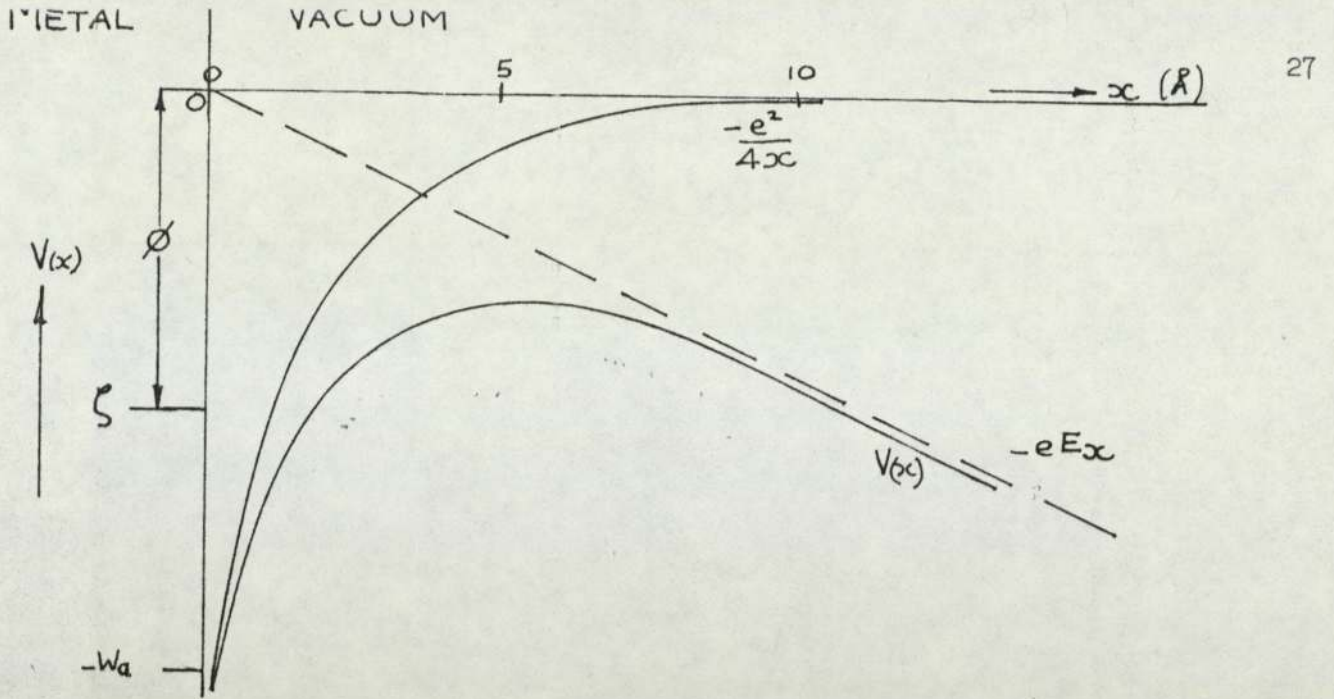


FIG 5. THE EFFECTIVE POTENTIAL ENERGY, $V(x)$, OF AN ELECTRON NEAR A TUNGSTEN SURFACE AS GIVEN BY EQNS. (1) & (2). FOR TUNGSTEN $W_a = 10.3 \text{ eV}$, $\zeta = -4.5 \text{ eV}$.

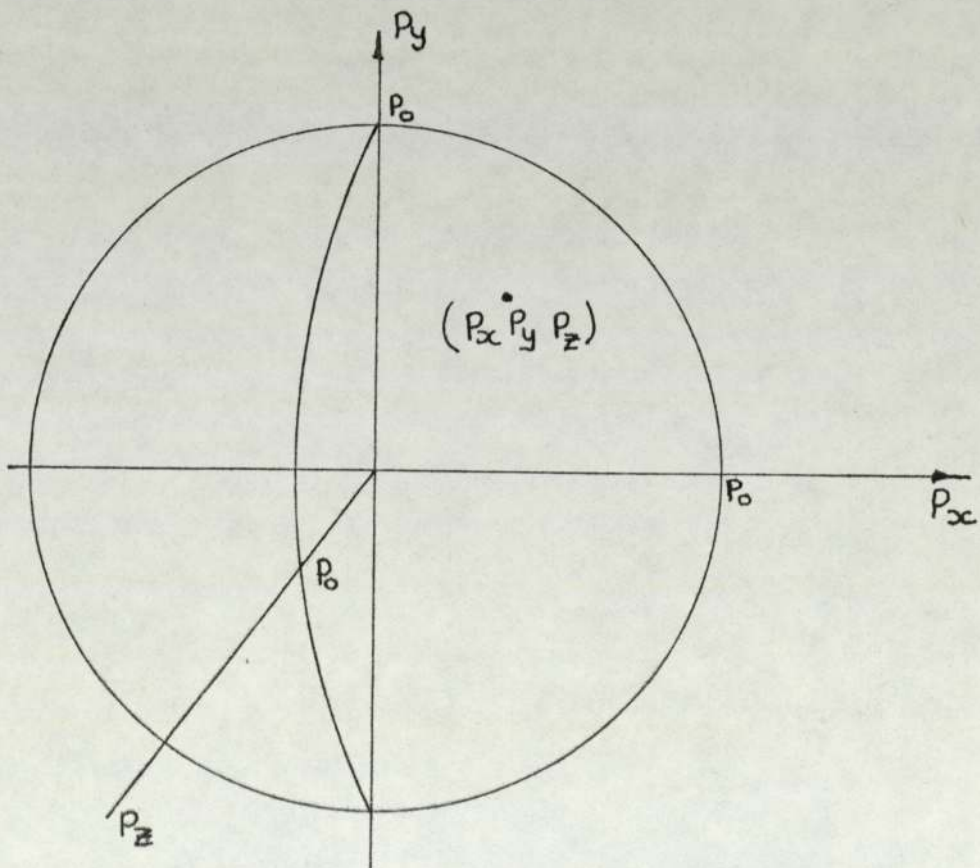


FIG 6. THE MOMENTUM, P , OF A PARTICLE IS SPECIFIED BY ITS COMPONENTS (P_x, P_y, P_z) , CORRESPONDING TO A POINT IN MOMENTUM SPACE. AT OK ALL ELECTRONS ARE SPECIFIED WITHIN THE SPHERE OF RADIUS (P_0) (MINIMUM ENERGY CONDITION)

Referring to fig(5)

$$V(x) = -Wa. \quad \text{Where } x < 0 \quad (1)$$

$$= -\frac{e^2}{4x} - eF_x \quad \text{Where } x > 0 \quad (2)$$

where $-e$ is the charge on the electron and F is the electric field.

The x part of the total energy of the electron is given by

$$W = \frac{P_x^2}{2m} + V(x) \quad (3)$$

where P_x is the electron momentum in the x direction and m is the electron rest mass.

The current density, J , is given by

$$J = e \int_{-Wa}^{\infty} P(W) dW$$

$$\text{or } J = e \int_{-Wa}^{\infty} N(W) D(W) dW \quad (4)$$

2.2.4 Considering now an electron in momentum space with co-ordinates $P_x P_y P_z$ (instead of position co-ordinates x, y, z), then the magnitude and direction of momentum are given by the length, P , and direction of a radius vector drawn from the origin to the point (fig 6). By the uncertainty relation, the momentum component P_x , cannot be determined more precisely than to an amount ΔP_x where

$$\Delta P_x \Delta x = h$$

and Δx is the uncertainty in the position co-ordinate

Similar relations hold for the other two axes; thus:

$$\Delta P_x \Delta P_y \Delta P_z = \frac{h^3}{\Delta x \Delta y \Delta z} = \frac{h^3}{V}$$

where the electron is constrained to be within a volume V . The Pauli exclusion principle applied to this situation states that there is only one allowed energy in each elemental volume of momentum space. Since, however, the electron can have two values of angular momentum due to its intrinsic spin, each point in an element of momentum space can accept a maximum of two electrons. Thus for momenta in the range $dP_x dP_y dP_z$, the number of states is

$$2 \times \frac{dP_x dP_y dP_z}{\Delta P_x \Delta P_y \Delta P_z} = \frac{2V}{h^3} dP_x dP_y dP_z$$

2.2.5 The number of electrons, dn , within volume V and having momenta in the range $dP_x dP_y dP_z$ is given by the number of states in that momenta range multiplied by the probability that such states will be occupied. The probability that these states will be occupied is given by the Fermi Dirac distribution function

$$f(E) = \frac{1}{\exp\left(\frac{E-\zeta}{kT}\right) + 1}$$

where E = Electron energy

ζ = Fermi energy

k = Boltzmann's constant

T = Temperature (Kelvins)

Thus:

$$dn = \frac{2V}{h^3} \frac{dP_x dP_y dP_z}{\exp\left(\frac{E-\zeta}{kT}\right) + 1}$$

(5)

2.2.6 The flux of electrons moving in the x direction and with x -momentum within dP_x is found by multiplying the number per unit volume with momenta within $dP_x dP_y dP_z$ by the x -velocity and integrating over all P_y and P_z

$$\int_{P_y=-\infty}^{\infty} \int_{P_z=-\infty}^{\infty} \frac{P_x}{m} \frac{2}{h^3} \frac{dP_x dP_y dP_z}{\exp\left(\frac{E-\zeta}{kT}\right) + 1} \quad (6)$$

But from equation (3)

$$P_x dx = m dW$$

by substituting this in equation (6) the integrand becomes the flux of electrons with x energy within dW incident on the surface, that is $N(W)dW$.

$$\text{Thus } N(W)dW = \frac{2}{h^3} dW \int_{-\infty}^{\infty} \int_{-\infty}^{\infty} \frac{dP_y dP_z}{\exp\left(\frac{E-\zeta}{kT}\right) + 1}$$

$$\text{But } E = W + \frac{P_y^2 + P_z^2}{2m}$$

$$\therefore N(W)dW = \frac{2}{h^3} dW \int_{-\infty}^{\infty} \int_{-\infty}^{\infty} \frac{dP_y dP_z}{\exp\left(\frac{W-\zeta}{kT} + \frac{P_y^2 + P_z^2}{2mkT}\right) + 1}$$

This can be evaluated by converting to polar co-ordinates.

$$P_y = \ell \cos \theta$$

$$P_z = \ell \sin \theta$$

$$\begin{aligned} N(W) &= \frac{2}{h^3} \int_{\ell=0}^{\infty} \int_{\theta=0}^{2\pi} \frac{\ell d\ell d\theta}{\exp\left(\frac{W-\zeta}{kT} + \frac{\ell^2}{2mkT}\right) + 1} \\ &= -\frac{4\pi kT}{h^3} \left[\log\left(\exp\frac{W-\zeta}{kT} + \exp - \left(\frac{\ell^2}{2mkT}\right)\right) \right]_0^{\infty} \end{aligned}$$

$$N(W) = \frac{4\pi mkT}{h^3} \log\left(1 + \exp\left(\frac{W-\zeta}{kT}\right)\right) \quad (7)$$

2.2.7 The transmission coefficient is found by solving the time-independent Schrödinger equation for the motion of one of the electrons in the x direction.

This equation is:

$$\frac{d^2 U}{dx^2} + \frac{2m}{h^2} [W - u(x)]u = 0$$

where $u(x)$ is the wave function.

Solutions to this equation may be found by using the Wentzel-Kramer-

Brillouin (WKB) approximation [42] which is applicable when $W \leq V_{\max}$ (i.e. when the electron energies are much smaller than the energy corresponding to the maximum height of the barrier) - a valid approximation in this case. The transmission coefficient may then be expressed as:

$$D(W) = \exp - \int_{x_1}^{x_2} \sqrt{\frac{8m}{\hbar^2} [V(x) - W]} dx$$

The evaluation of this expression has been very fully covered by Good and Müller [43] and leads to:

$$D(W) = \exp - \frac{4\sqrt{2m}|W|^2}{3\hbar e F} v(y) \quad (8)$$

and $y = \frac{\sqrt{3} e F}{|W|}$

Values for the function $v(y)$ with varying y have also been given by Good and Müller [43] ($y = 0.956 - 1.062y^2$). The value for $P(W)dW$ is given by substituting (8) and (7) in (4).

$$\text{Thus } P(W)dW = \frac{4\pi mkT}{h^3} \exp \frac{-4\sqrt{2m}|W|^2}{3\hbar e F} v(y) \log \left(1 + \exp - \left(\frac{W - \zeta}{kT} \right) \right) dW \quad (9)$$

Since the field emitted electrons have energies in the region $W = \zeta$, it is permissible to approximate the exponent in the transmission coefficient by the first two terms in a power series expansion at $W = \zeta$. This gives:

$$- \frac{4\sqrt{2m}|W|^3}{3\hbar e F} v(y) \simeq -c + \frac{W - \zeta}{d} \quad (10)$$

$$\text{where } c = \frac{4\sqrt{2m}\phi^3}{3\hbar e F} v(y) \quad (11)$$

$$d = \frac{\hbar e F}{2\sqrt{2m\phi} t(y)} \quad (12)$$

$$\text{and } t(y) = v(y) - \frac{2}{3} y \frac{dv(y)}{dy} \quad (13)$$

$\phi = -\zeta$ the work function.

Again, values of $t(y)$ for various y has been given by Good and Müller [43].

Substituting numerical values gives

$$c = \frac{6.83 \times 10^9 \phi^{3/2}}{F} v(y)$$

$$d = \frac{9.76 \times 10^{-7} F}{\phi^{1/2} t(y)} \text{ electron volts}$$

where F is in volts metre⁻¹
 ϕ is in electron volts

For low temperatures

$$kT \log \left(1 + \exp - \frac{W-\zeta}{kT} \right) = 0 \quad \text{when } W > \zeta \quad (14)$$

$$= \zeta - W \quad \text{when } W < \zeta \quad (15)$$

Substituting (10)(14) and (15) into (9) gives

$$P(W) = 0 \quad \text{when } W > \zeta$$

$$= \frac{4\pi m}{h^3} \exp \left(-c + \frac{W-\zeta}{d} \right) (\zeta - W) \quad (16)$$

when $W < \zeta$

By differentiation of (16) the maximum in $P(W)$ occurs when $W = \zeta - d$ and has the value

$$P_{\max} = \frac{4\pi m d}{h^3} \exp - (c + 1)$$

Good and Müller [43], referring to work carried out by Richter, state that the width of the distribution of electrons at half maximum is $2.44d$.

2.2.8 The total electric current is found by integrating equation (16) over all relevant values of W , i.e. $-W_a$ to ∞ . In practice, since $-W_a$ is far below the Fermi energy ζ , the lower limit is taken as $-\infty$. Also, since a metal at OK is being considered, the upper limit is ζ .

Thus

$$\begin{aligned}
 J &= e \int_{-\infty}^{\zeta} \frac{4\pi m}{h^3} \exp \left[-c + \left(\frac{W-\zeta}{d} \right) \right] (\zeta-W) dW = \frac{4\pi m e d^2}{h^3} \exp(-c) \\
 &= \frac{e^3 F^2}{8\pi h \phi t^2(y)} \exp \left(\frac{-4\sqrt{2m}}{3neF} \phi^{3/2} v(y) \right) \quad (17)
 \end{aligned}$$

Inserting numerical values for the constants

$$J = \frac{1.54 \times 10^{-6} F^2}{\phi t^2(y)} \exp \left[\frac{-6.83 \times 10^9 \phi^{3/2}}{F} v(y) \right] \quad (18)$$

amps/m²

This is the Fowler-Nordheim equation for the total emitted current density of field emitted electrons from a metal at OK. At finite temperatures there are electrons above the Fermi level incident on the barrier and these are more likely to penetrate because of the reduced width of the potential barrier. The effect of temperature can be considered by approximating the logarithm term in eqn (9) for the case when $W > \zeta$. This then gives

$$P(W) = \frac{4\pi m k T}{h^3} \exp \left[-c + (W-\zeta) \left(\frac{1}{d} - \frac{1}{kT} \right) \right] \quad (19)$$

This shows the effect of the experimental tail above the Fermi energy.

The temperature effect splits the emission into three regimes

- I) high temperature and low field (Schottky emission)
- II) low temperatures and high fields (Fowler Nordheim emission)
- III) temperature and field (T-F) emission at temperatures and fields between the two extremes.

2.2.9 Good and Müller [43] have further shown from a consideration of eqn (19) that the boundary of the field emission phenomenon is given by

$$F > 8.83 \times 10^5 \phi^{1/2} T \quad \text{volts/m}$$

Thus at room temperature with ϕ typically 4.5eV

$$F > 6 \times 10^8 \quad \text{volts/metre}$$

2.2.10 Curves showing the energy distribution of field emitted electrons under various conditions of field strength and temperature have been given by Dyke and Dolan [44] and are shown in fig (7). The temperature changes which take place at the point of emission are determined by two factors, Joule heating and the Nottingham effect. Resistive heating is a well known effect which for metals increases with temperature; with the high emission densities encountered in field or T-F emission this would quickly lead to an inherently unstable situation if there was no other stabilising factor. This factor is supplied by the energy exchange resulting from the difference between the average energy of the emitted electrons \bar{E} , and that of the replacement electrons supplied by the circuit \bar{E}' . This mechanism was first suggested for thermionic emission by Richardson [45] and later by Nottingham [46] and is now known as the Nottingham effect. Cathode cooling occurs when $\bar{E} > \bar{E}'$ and heating when $\bar{E} < \bar{E}'$. There is experimental evidence to suggest [47] that at low temperatures $\bar{E} < \bar{E}'$ but that as the temperature increases a point is reached (called the inversion temperature) at which the $\bar{E} > \bar{E}'$ and cooling of the cathode begins to occur. However, experiments that have been carried out to investigate the effect do not give results that are completely consistent with the theory when using a free-electron approach [48]. However, further theoretical studies which have incorporated non-free electron theory [49] are still not entirely satisfactory.

2.2.11 In a classic paper, R D Young in 1959 [50] pointed out that the analysis discussed in the previous section applies specifically to electron energies associated with the component of velocity normal to the emitting surface, whereas in experiments carried out to measure the distribution in

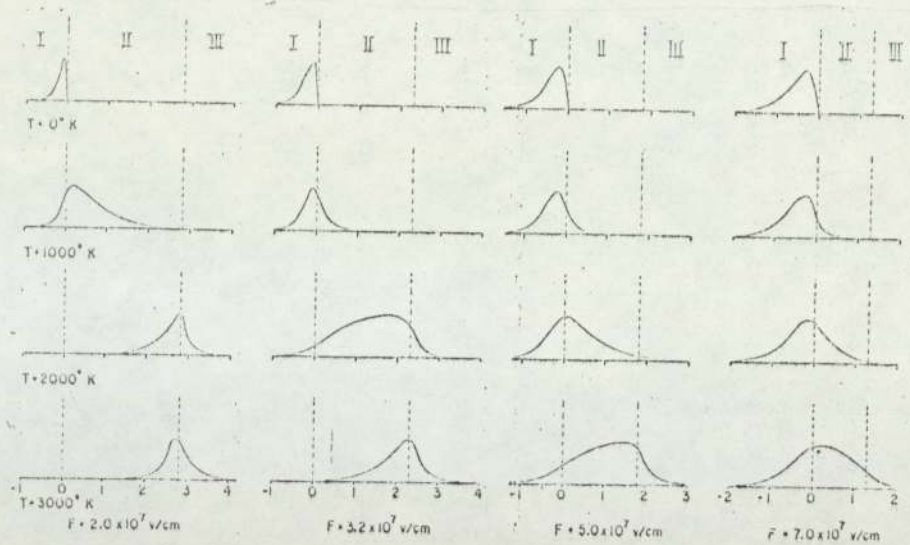


FIG 7. FIELD EMISSION ENERGY DISTRIBUTIONS AT VARIOUS TEMPERATURES AND FIELDS AS GIVEN BY DOLAN AND DYKE (44) REGION I CORRESPONDS TO FIELD EMISSION, REGION II TO T-F EMISSION AND REGION III TO THERMIONIC EMISSION. (INCREASING ENERGY LEFT TO RIGHT.)

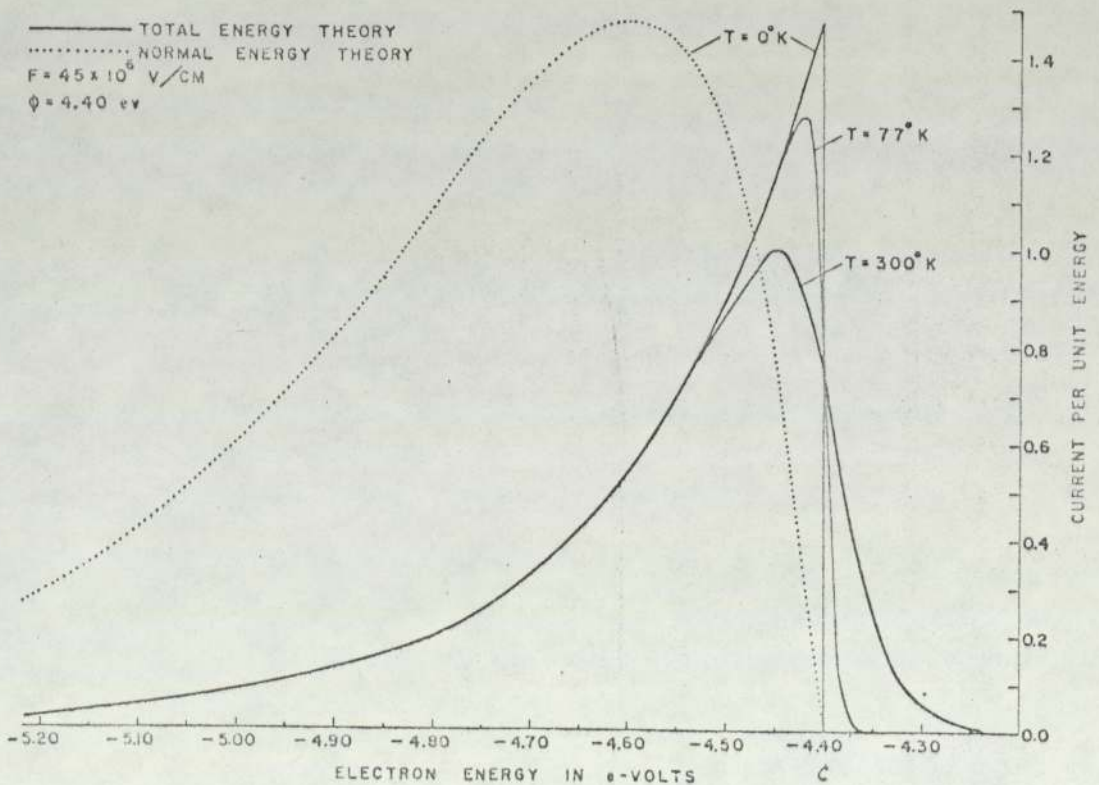


FIG 8. THE THEORETICAL TOTAL ENERGY DISTRIBUTION ACCORDING TO YOUNG (50) AT VARIOUS TEMPERATURES. THE NORMAL ENERGY DISTRIBUTION IS PLOTTED FOR COMPARISON. (INCREASING ENERGY LEFT TO RIGHT).

energy of field emitted electrons it is the distribution in total electron energy that is measured. The new parameters defined by Young to obtain an expression for the total energy distribution were:

$N(W,E)dWdE$ = number of electrons with energy within the range E to $E + dE$ whose x part of the energy lies in the range W to $W + dW$ incident upon the surface $x = 0$ per area per time.

$$P(W,E)dWdE = N(W,E)D(W)dWdE$$

= number of electrons in the given energy ranges penetrating the barrier.

$$P(E)dE = \int_W P(W,E)dWdE$$

= total energy distribution

$$J = e \int P(E)dE$$

= electric current per unit area

= Fowler Nordheim equation

Thus although the number of electrons involved is still the same, that is, the electrons having an x component of their energy normal to the surface, the distribution in the energy component normal to the surface is quite different from the distribution in total energy of these electrons. Thus, although the Fowler-Nordheim equation remains the same, the energy distribution expression alters.

2.2.12 Using the new parameters, Young showed that

$$P(E)dE = \frac{4\pi m d}{3h} \exp\left(-c \frac{\zeta}{d}\right) \times \frac{\exp(E/d)}{\exp[(E-\zeta)/kT] + 1} dE \quad 20(a)$$

This is the total energy distribution and should be compared to the normal energy distribution of eqn (9). Also the current density is given by

$$J = \frac{e^3 F^2}{8\pi h \phi^2(y)} \exp\left(\frac{-4(2m)^{1/2} \phi^{3/2}}{3\hbar e F} v(y)\right) \frac{\pi kT/d}{\sin(\pi kT/d)} \quad 20(b)$$

This is the higher temperature approximation of the Fowler-Nordheim curve and is identical to eqn (17) except for the addition of the $\frac{\pi kT/d}{\sin(\pi kT/d)}$ temperature approximation.

2.2.13 The value of E when $P(E)$ is a maximum can be found from differentiation of the exponential part of eqn (20) with respect to E . The maximum in $P(E)$ occurs when

$$E = \zeta - kT \ln(d/kT - 1)$$

When $T = 0K$ E is a maximum and $E_{\max} = \zeta$

The half-width of the total energy distribution at zero temperature is

$$\sigma(0) = 0.693d \quad (21)$$

Fig 8 shows the normal and total energy distribution curves obtained by Young according to equations (9) and (20) at three different temperatures.

2.2.14 Young has also given an expression for the total energy distribution for thermionic electrons:

$$P(E)dE = \frac{4\pi m}{3h} \exp \frac{-E + \zeta}{kT} dE$$

The F.W.H.M of this distribution is found to be $2.45kT$ and the maximum in the distribution occurs at $E_{\max} = kT$. It has been shown by Young [50] and also by Dyke and Dolan [44] that field emission can be clearly distinguished from T-F or thermionic emission by examination of the electron energy distribution.

2.2.15 At the same time as the Young paper was published, Young and Müller [51] gave details of field electron energy distribution (FEED) studies using an improved type of retarding potential analyser which gave

convincing experimental proof of the Young theory.

2.2.16 Christov [52] has put forward a unified theory of field emission which attempts to encompass electron emission from metals in vacuum, insulators and semi-conductors in the whole range between the extreme conditions of field and thermionic emission. The theory uses a free electron approximation for metallic emission using the equation for momentum

$$\frac{P^2}{2m_0} = \frac{(P_x^2 + P_y^2 + P_z^2)}{2m_0} = E - V(x)$$

For electron emission in dielectrics and semi-conductors on the basis of band theory, there is a non-parabolic relation between momentum and total energy:

$$\frac{P^2}{2m_c} = \epsilon \left[1 + \frac{(M_v/M_c) + 2}{E_g} \epsilon + \frac{(M_v/M_c)}{E_g^2} \epsilon^2 \right]$$

where $\epsilon = E - V(x)$

M_c = effective electron mass at lower edge of conduction band

M_v = effective electron mass at upper edge of valence band

E_g = forbidden energy gap.

Two further quantities defined are the "characteristic temperature", T_k , defined by the condition that the maximum of the normal energy distribution $F_n(E_x)$ is just at the top of the barrier $V(x_m) = V_{\max}$. It is shown that

$$T_k = \frac{h (\epsilon_0 D)^{1/4}}{\pi^2 k M_c^{1/2}} F^{3/4}$$

where F is the field strength

D is the dielectric constant

The second characteristic temperature is T_c at which the normal energy distribution has a maximum at $E_x \cong \mu^1 = \mu + 2kT$ where μ is the Fermi

energy of the metal. Adopting a quasi free electron approach for a semi-conductor

$$T_c = \frac{he^F}{4\pi k (2m_c X)^{1/2}} t(y)$$

X is the metal - semi-conductor or metal-vacuum work function.

The energy range of E is divided into three appropriate regions

- 1) $0 \leq E \leq \mu^1$
- 11) $\mu^1 \leq E \leq E^1$
- 111) $E \geq E^1$

Consequently, the emission current may be represented as the sum of three contributions

$$J = J_1^1 + J_2^1 + J_3^{11}$$

The extended thermionic emission region is defined by $T > T_k/2$ and

$$J = \frac{\pi/2 (T_k/T)}{\text{Sin}[(\pi/2)(T_k/T)]} J_{RS}$$

where J_{RS} is the current density expressed by a Richardson-Schottky type equation.

The extended field emission region is $T < T_c$ and

$$J = \frac{\pi(T/T_c)}{\text{Sin}[\pi(T/T_c)]} J_{FN}$$

J_{FN} is the current density represented by the Fowler-Nordheim expression.

The intermediate emission region is $T_c < T < T_k/2$ and

$$J = Q_1^1 (T/T_c) J_{FN} + Q_2^1 J_{MG} + Q_3^1 (T_k/T) J_{RS}$$

where J_{MG} is the generalised Murphy-Good formula for current density [53].

Q_1^1 , Q_2^1 and Q_3^1 are known functions of field and temperature.

Christov claims experimental agreement with this theory in measurements of current from particular crystal planes and plotting $\log(J/J_{FN})$ v. T/T_c or $\log(J/J_{RS})$ v. Tk/T . However, a crucial test of the theory (as shown in section 2.6.2) is in obtaining agreement with the experimental electron energy distributions, and this has not been done so far.

2.3.0 Determination of work function (ϕ) and field enhancement (β) using free electron theory.

2.3.1 In theory, it is possible to calculate the work function, ϕ , of an emitter from the Fowler-Nordheim equation. It can be seen from equation (18) that by measuring the current (i) versus field (F) characteristics of an emitter and then plotting $\ln i/F^2$ v. $1/F$, that the slope, m , of this graph will be given by

$$m = \frac{d \ln(i/F^2)}{d(1/F)} = -6.83 \times 10^9 \phi^{3/2} S(y)$$

$$\text{where } S(y) = v(y) - \frac{y}{2} \frac{dv(y)}{dy} \quad \text{values for } S(y) \text{ are given in [43]}$$

In practice, however, the field at the emitter surface, F , may be very difficult to measure. A simple approach in a plane parallel electrode geometry is to assume that

$$F = \beta \frac{V}{\ell} \quad \text{where } \ell \text{ is the electrode separation}$$

β is called the field enhancement factor which is a dimensionless quantity related to the geometrical shape of the emitting tip. It is an estimation of the local field enhancement at the emitter surface compared to the V/ℓ field which would be obtained between two idealised plane electrodes.

[Note: In the case of a point-to-plane geometry, the field enhancement is given by the equation $F = \beta V$ in which case β has the dimensions of $[L]^{-1}$ and will, of course, be quite different in magnitude. Since, however, most

authors concerned specifically with pre-breakdown field emission currents define β by $F = \beta \frac{V}{r}$, this will be used throughout this text]. A number of estimates have been made for β corresponding to various geometries by Good and Müller [43], Dyke and Dolan [44], Vibrans [54], Chatterton [55] and others. Typical results are given in Table 1. In practice, however, difficulties arise when attempting to determine the tip shape with the electron microscope since there is always uncertainty in magnification and the micrographs give profiles which depend on the direction of viewing and so are often difficult to interpret.

2.3.2 In the case of broad area electrodes, these formulae have been most commonly used in order to try and establish the surface protrusion giving rise to the field emission currents. As an example, the field enhancement due to a hemispherically capped cone of half angle 10° , height h and tip radius r is given by [55]

$$\beta_{co} = \frac{0.5h}{r} + 5 \quad (22)$$

The emitting area, S , can be defined as

$$S = \pi \delta^2 \quad (23)$$

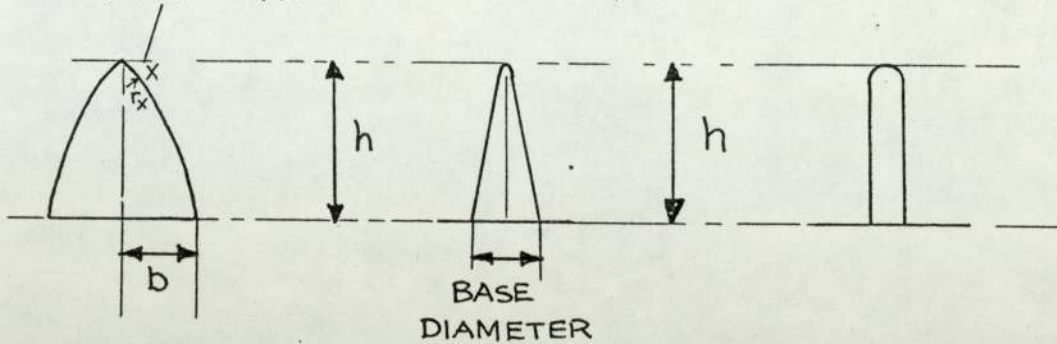
where

$\delta = r \sin \alpha$ and α is the angle at the centre of the hemisphere between the normal to the surface where the electric field has fallen by 5% from the peak value (this corresponds to the position where the emission current has fallen to $\sim 1\%$ of its maximum value). For the above model this angle is 40° [44].

2.3.3 The emitting area S can be obtained from the intercept of the pre-exponential term in the Fowler-Nordheim equation. Referring to fig (9) it can be seen that

TABLE I. FIELD ENHANCEMENT (β) FACTORS OF VARIOUS SURFACE PROTRUSION GEOMETRIES.

RADIUS OF CURVATURE
AT POINT $x = b^2/h$

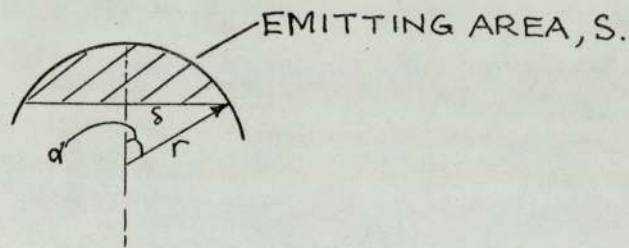


ELLIPSOID
SEMI AXES: b, b, h
ECCENTRICITY, e
 $= (1 - b^2/h^2)^{1/2}$

TRUNCATED
CONE

HEMISPHERICALLY
CAPPED CYLINDER

DETAIL OF END CAP OF PROTRUSIONS.



PROTRUSION GEOMETRY.	ENHANCEMENT FACTOR, β .	MAXIMUM EMISSION ANGLE, α^* .
ELLIPSOID	$\left[\frac{e^2}{1-e^2} \right] \left[\frac{1}{\frac{1}{2}e \ln \left(\frac{1+e}{1-e} \right)} - 1 \right]$ [99]	19° [54]
CONE	$0.5 \frac{h}{r} + 5$ [55]	40° [44]
CYLINDER	$\frac{h}{r} + 2$ [54]	60° [54]

* α CORRESPONDS TO THE POINT AT WHICH THE FIELD HAS DROPPED BY 5% OF ITS PEAK VALUE.

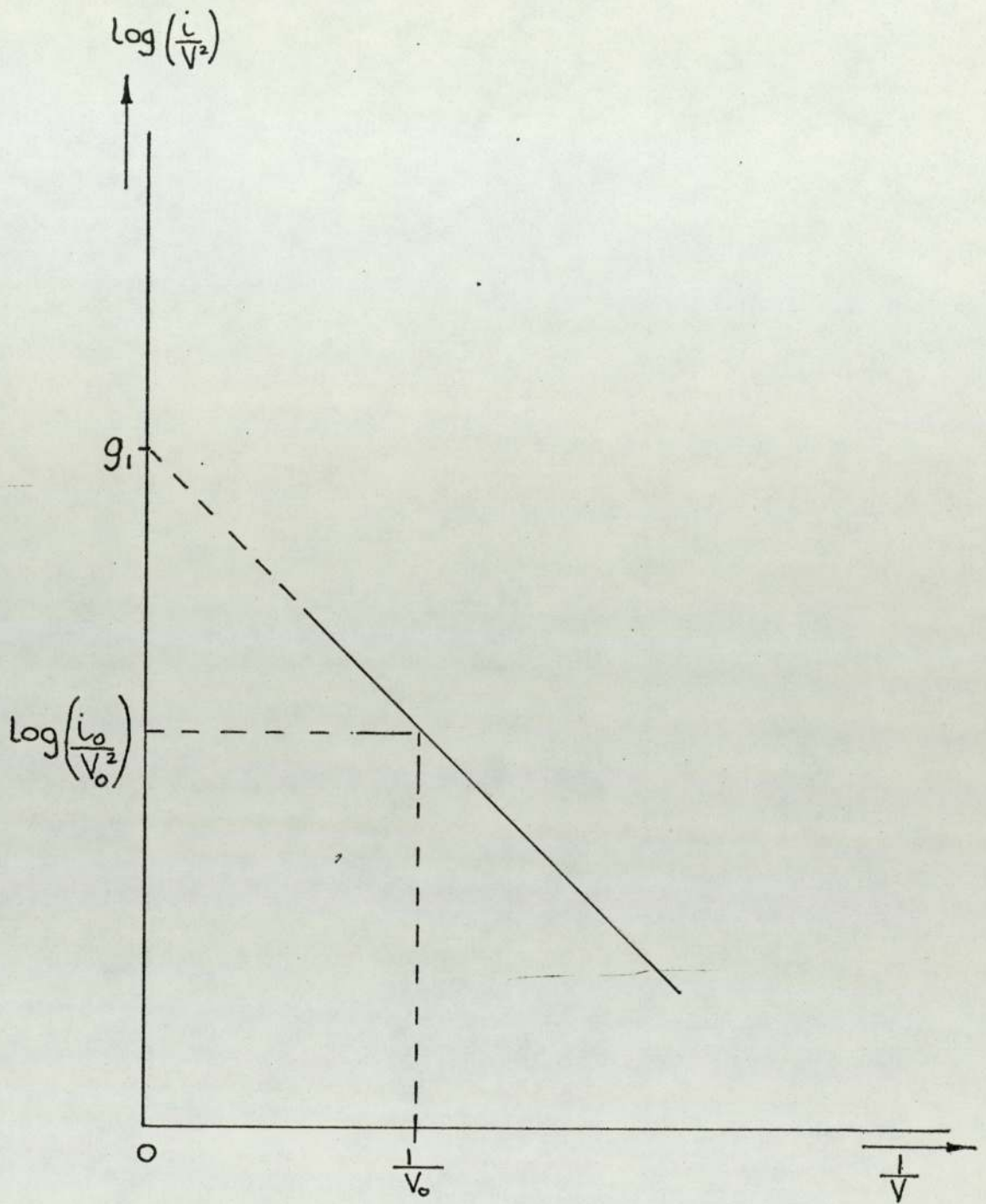


FIG 9. FINDING THE INTERCEPT ON A FOWLER-NORDHEIM GRAPH.

$$\text{Intercept} = \log_{10} \frac{i_0}{V_0^2} + m \frac{1}{V_0} \quad (24)$$

where m is the slope of the graph

It has been shown by Beukema [56] that, approximately in the field range $(3.0 - 5.5) \times 10^9 \text{ v/m}$, the function $v(y)$ can be expressed by the equation

$$v(y) = 0.956 - 1.062y^2$$

Also, $t(y) \cong 1$

Hence the Fowler-Nordheim equation becomes

$$\log_{10} \frac{i}{V^2} = \log_{10} \frac{1.54 \times 10^{-6} \beta^2 S}{\phi d^2} 10^{4.56/\phi^{1/2}} - \frac{2.81 \times 10^9 \phi^{3/2} \ell}{\beta V}$$

At the intercept, $1/V = 0$,

$$\log_{10} \frac{i}{V^2} = \frac{\log_{10} 1.54 \times 10^{-6} \beta^2 S}{\phi \ell^2} + \frac{4.56}{\phi^{1/2}} \quad (25)$$

Using the value for $\log_{10} \frac{i}{V^2}$ obtained from (24), the emitting area, S , can be calculated from (25). Thus, knowing β and ϕ , S can be determined.

Using equations (22) and (23) r and h can also be found. In experiments which measure the pre-breakdown currents from broad area electrodes, a value for ϕ is usually assumed and the above method is used to determine β , S , h and r ; the cathode surface is then examined to see if a protrusion of the calculated dimensions exists on the surface microtopography (e.g. (29)). In particular, the work of Cox [34] and more recently Cox and Williams [36] using the above analysis has failed to reveal surface protrusions of the expected geometry. This has, therefore, given rise to speculation as to whether this method of estimating surface fields is sufficiently accurate,

or whether other factors, such as incorrect assumption of work functions are responsible to the anomalous results.

2.3.4 An alternative method of estimating local field strength was suggested by Charbonnier and Martin [58]. They proposed that since

$$J = \frac{AF^2}{\phi t^2(y)} \exp\left(-\frac{B\phi^{3/2}}{F} v(y)\right) \quad (26)$$

and the slope, m , of the graph of $\log_{10} i/V^2$ v. $1/V$ is given by

$$m = \frac{B\phi^{3/2} \ell \cdot S(y)}{\beta} \quad (27)$$

then by substituting (27) into (26) then the equation becomes

$$J = \frac{C \phi^2}{(m/v)^2} \exp\left(\frac{D}{\phi^{1/2}}\right) \exp\left(-\frac{2.3m}{V}\right) \quad (28)$$

where C and D are constants

$$y = 3.79 \times 10^{-4} \frac{F^{1/2}}{\phi}$$

$$v(y) = 0.956 - 1.062y^2$$

$$t(y) = 1.044$$

$$S(y) = 0.956$$

or
$$J = \frac{C G(\phi)}{m/v^2} \exp\left(-\frac{2.3m}{V}\right) \quad \text{where } G(\phi) = \phi^2 \exp\left(\frac{D}{\phi^{1/2}}\right)$$

2.3.5 Calculations show that for $\phi \geq 4\text{eV}$ the function $G(\phi)$ goes through a flat minimum and departs by less than $\pm 7\%$ from a fixed value. Thus the current density J and therefore the effective emitting area, S , of the field emission source can be derived simply from the measured parameter m/V . While this may be useful in analysing field emission from specially fabricated tips where the work function may be known to be $> 4\text{eV}$, it is unsatisfactory in analysing the problem of pre-breakdown currents from broad

area electrodes where the exact nature of the material at the point of emission and, correspondingly, the value of ϕ , may be of considerable doubt.

2.3.6 Bormond [57] has suggested a method for determining local field strength by using T-F emission and the unified theory of Christov [52]. The method relies on the fact that in the T-F region a good approximation using Christov's theory is

$$\log J/E = A + BF^2 \quad \text{where A and B are constants.}$$

F is the true field at the surface and

$$F = \gamma F_{\text{app}}$$

F_{app} is an approximate measurement of the field which can be computed using one of the usual electrostatic methods and γ is determined experimentally. This is done by measuring the current, i , for various values of applied field and then plotting $\log i/F_{\text{app}}$ v. F_{app}^2 , from which a value for B_{exp} - the experimental slope of the graph - can be obtained. The true theoretical value of B can be calculated for a given value of T and

$$\gamma = (B_{\text{exp}}/B)^{\frac{1}{2}}$$

Hence the true value of F can be found.

2.3.7 In practice, γ is insensitive to the value of work function and because of the dependence on $(B)^{\frac{1}{2}}$ it is possible to estimate γ to about 5% when the error in B_{exp}/B is $\sim 10\%$. The difficulty with the method when applied to broad area electrodes is the estimate of the temperature T which is necessary to find the theoretical value of B.

2.3.8 A different approach was suggested by Young and Müller in 1962 [59]. They reasoned that since the slope of the Fowler-Nordheim curve is given by

$$\eta = \frac{d \ln(i/V^2)}{d(1/V)} = \frac{-6.83 \times 10^9 \phi^{3/2} \ell}{\beta} S(y) \quad (29)$$

and that the half width of the energy distribution of the electrons is given by (eqn (21))

$$\sigma_0 = 6.76 \times 10^{-7} (F/\phi^{1/2}) = 6.76 \times 10^{-7} \frac{\beta V}{\ell \phi^{1/2}} \quad (30)$$

(F in volts/m⁻¹)
(φ in eV)

the simultaneous solution of (29) and (30) will give independently values for β and φ. The main drawback with this procedure is that whilst both equations are defined for T = 0K, eqn (30) in particular is very sensitive to an increase in T. (see, for example, Table 2 - III in (60)).

2.3.9 Unfortunately, there is no useful solution to the value of σ at room temperature. Young and Müller [59] and van Oostrum [60], for example, have overcome this difficulty by measuring the half width of the distribution from an emitting tip at various temperatures and extrapolated to zero to obtain σ₀ and hence solve (29) and (30). Whilst such a procedure is feasible in the case of the fairly well controlled situation of an emitting tip, it is quite unrealistic for the broad area electrode situation where measurement of the temperature of the emitting site would present enormous difficulties. However, this method does give a way of estimating a maximum value for the field, assuming a value for φ, and is quite independent of the field estimation from the Fowler-Nordheim plot. It is, therefore, of interest to compare the value for field obtained by these two methods, at least to see if they are consistent.

2.4.0 Field emission from metals using non-free electron theory

2.4.1 It was first established by Swanson and Crouser [61] that equation (30) is not always valid. In particular, they found in experiments on tungsten tip emitters that the energy distribution from the $\langle 100 \rangle$ direction contained a low energy hump 0.35eV below the Fermi energy (now often known as the "Swanson hump"). This was attributed to the non-free electron behaviour for this direction caused by band structure effects. Similar effects were studied by Plummer and Bell [62] and they defined a quantity called the enhancement factor $R(E)$:

$$J^1(\epsilon) = R(\epsilon) J_0^1(\epsilon) \quad (31)$$

Here, $J_0^1(\epsilon)$ is the calculated free electron energy distribution, i.e.

$$J_0^1(\epsilon) = \frac{4\pi m d}{h^3} \exp(-C) \exp(\epsilon/d) f(\epsilon) \quad (32)$$

$\epsilon \equiv$ energy of the electron relative to the Fermi energy, ζ .

$J^1(\epsilon)$ is the measured total energy distribution. In practice, $R(\epsilon)$ can be found by dividing the measured distribution by the calculated free-electron energy distribution and this can be plotted against ϵ . Such plots show up structure in the energy distribution in far greater detail than is possible with the measured spectrum. Typical curves from four low index planes of tungsten are shown in fig (10).

2.4.2 The fact that in certain cases the $R(\epsilon)$ v. ϵ curves reveal structure in the electron distribution of clean contaminant-free metal surfaces has demonstrated the fact that a free-electron theory of field emission for metals is an over simplification in many cases. Indeed, it appears that

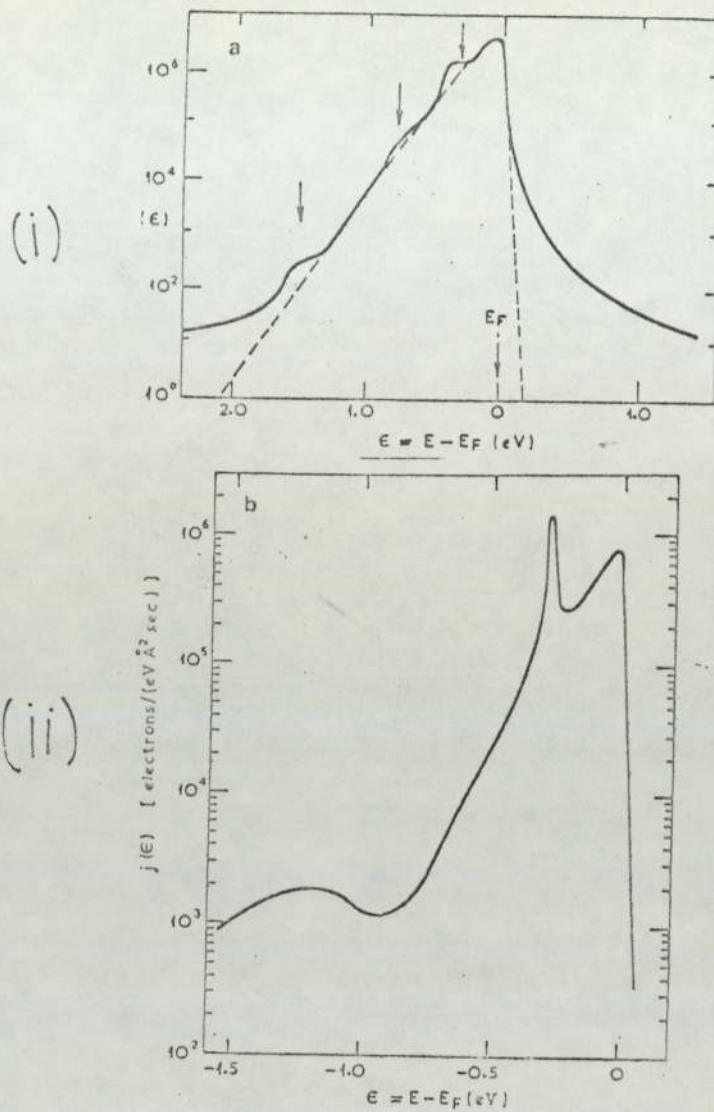


Fig 10(a) (i) EXPERIMENTAL ELECTRON ENERGY DISTRIBUTION FROM THE (100) PLANE OF TUNGSTEN AT $T=78\text{ K}$ (75). THE BROKEN CURVE INDICATES THE FREE ELECTRON ENERGY DISTRIBUTION.

(ii) CALCULATED THEORETICAL ENERGY DISTRIBUTION USING NON-FREE ELECTRON THEORY ACCORDING TO MODINOS & NICOLAOU (64). $T=78\text{ K}$
 $E=5 \times 10^7\text{ V/cm}$.

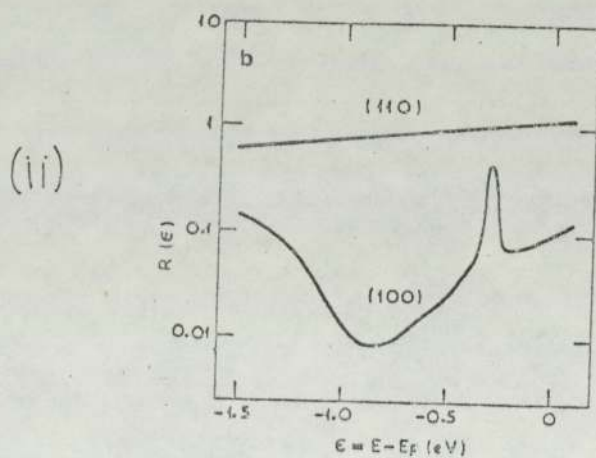
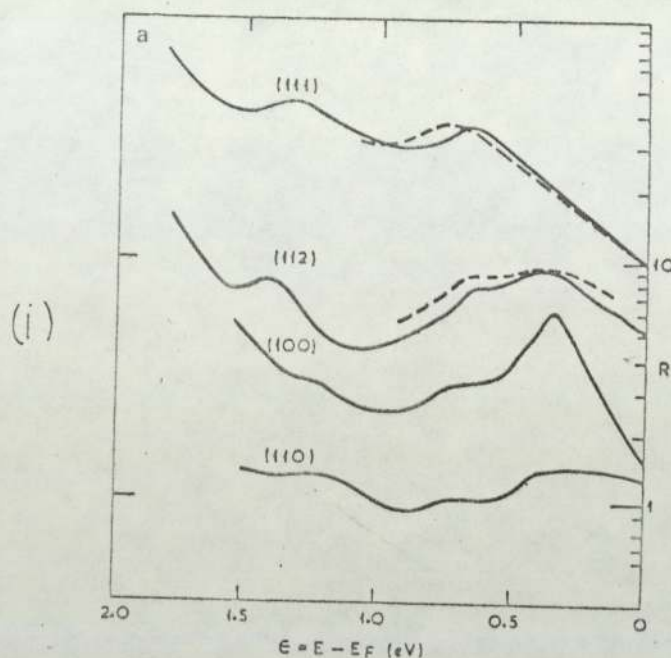


Fig 10(b) (i) EXPERIMENTAL ENHANCEMENT FACTOR $R(\epsilon)$ CURVES FOR THE FOUR LOW INDEX PLANES OF TUNGSTEN (72). THE BROKEN CURVES INDICATE THE CHANGE IN $R(\epsilon)$ FOR THE (111) AND (112) FOR REDUCED ELECTRIC FIELD.

(ii) THE CALCULATED ENHANCEMENT FACTORS USING NON-FREE ELECTRON THEORY ACCORDING TO MODINOS & NICOLAOU (64) $E = 5 \times 10^7$ V/cm.

deviation from free electron behaviour is the rule rather than the exception. Accordingly, a systematic theory of field emission has been put forward by Nicolaou and Modinos [63][64] on the basis of which realistic and accurate calculations of FEED distributions from transition metals has become possible.

2.4.3 The basis of this theory is that the potential as seen by an electron inside the metal can be represented by a superposition of non-overlapping spherical potentials centred on each of the ions of the crystal. Outside these spheres (muffin tin spheres) the potential is approximated by a constant. This approximation to the potential, known as the "Muffin tin approximation", has been extensively used in calculations of the energy band structure of transition metals. A simple model for a semi-infinite metal is used in which it is assumed that the bulk potential is terminated abruptly at the surface and outside the metal the potential depends only on the distance from the metal-vacuum interface. Low energy electron diffraction (LEED) data have shown that this is a reasonable approximation for transition metals, but for other metals it may not be valid and for semi-conductors it is certainly incorrect since re-arrangement occurs at the surface. Such a treatment leads to a rather complex expression for the total emitted current $J(\epsilon)$ (see, for example, equations (34)(37) and (38) in ref [65]) but numerical results have been calculated and have been shown to be in excellent agreement with the experimental results (fig 10).

2.4.4 A similar analysis has been applied to the (111) plane of copper by Kar and Soven [66] and in this case a discontinuity occurs in the $R(\epsilon)$ peak. This is explained as due to the fact that the density of states of a two-dimensional band does not go smoothly to zero at the edge of the band.

Results for copper published by Whittcut and Blott [67] give only the total emission distribution and not the enhancement curve, but even so, these results and some preliminary ones by Plummer and Weng [66] indicate that this peak is observed. Finally, results by Weng [68] on Molybdenum indicate that similar theoretical and experimental agreement exists when applying a non-free electron theory and measuring the $R(\epsilon)$ curve.

2.4.5 Non-free electron behaviour in emission from metals has also been studied by Czyzewski [69] who considered the effects of electron-phonon interactions and effects due to s-d transitions and overlapping of s and d bands and concluded that these effects were observable in the FEED data.

2.5.0 Determination of work function (ϕ) and field enhancement (β) using non-free electron theory.

2.5.1 An alternative approach to the determination of β and ϕ was put forward by Young and Clark in 1966 [70][71]. They pointed out the possibility of patch field effects, a factor which had not been taken into account in previous studies. They reasoned that differences in work function on adjacent regions of a single crystal emitter would give rise to substantial electrostatic fields at the surface. These were called surface patch fields and thus the field at the surface of an emitter becomes:

$$F = F_0 + \beta \frac{V}{\ell} \quad (33)$$

where F_0 is the patch field strength.

Thus the Fowler-Nordheim equation becomes:

$$J = \frac{1.54 \times 10^{-6} F^2}{\phi t^2(y)} \exp \left(\frac{-6.83 \times 10^9 \phi^{3/2} v(y)}{F_0 + \beta V/\ell} \right)$$

and the slope of this curve is:

$$S_{FN} = \frac{5 \log(i/V^2)}{5(1/V)} = \left(\frac{0.37V}{1 + \frac{5V}{\ell F_0}} \right) - \frac{2.96 \times 10^9 \phi^{3/2} s(y)}{\beta(F_0 \ell / \beta V + 1)^2} \quad (34)$$

If the field distribution of the emitter in the absence of the patch field is assumed to be constant ($\beta = \text{constant}$) then the ratio of the work function of a plane (a) (with patch field E_0) to plane (b) (no patch field) predicted from the slopes of the FN plots, neglecting the first term, is

$$\frac{\phi_a}{\phi_b} = \left[\frac{S_{FN(a)}}{S_{FN(b)}} \left(\frac{F_0 \ell}{\beta V} + 1 \right)^2 \right]^{2/3} \quad (35)$$

In a retarding potential energy analyser, as used, for example, by Young and Müller [51], the integral of the electron current is measured up to an energy E . Expressed as a fraction of the total current the current of an energy E is

$$\frac{i(E)}{i_0} = \frac{\int_{-\infty}^{\zeta} \exp(E/d) dE}{\int_{-\infty}^{\zeta} \exp(E/d) dE}$$

where i_0 is the total current.

Hence

$$\frac{i_0 - i(E)}{i_0} = \exp \frac{E - \zeta}{d}$$

The slope of the energy distribution curve is defined as:

$$S_E = \frac{d \log(i_0 - i(E))}{d(E)}$$

$$\therefore S_E = \frac{0.434 \times 2(2m\phi) t(y)}{\hbar e E} \quad (36)$$

Substituting (33) into (36) and dividing by (34) gives:

$$\phi = -\frac{3}{2} \frac{S_{FN}}{S_E} \frac{t(y)}{s(y)} \frac{1}{V} \left(\frac{F_0 \ell}{\beta V} + 1 \right) \quad (37)$$

When a value has been obtained for ϕ from (37) it can be substituted into (36) to obtain the field strength at the surface. In the final analysis, an iterative process must be used in assigning values to F_0 , $t(y)$, $s(y)$ and β .

2.5.2 If, however, equation (36) for the "slope" of the energy distribution curve is solved for F , the true field at the surface, and substituted into the F-N equation the current density is given by

$$J = \left(\frac{3.04 \times 10^9}{S_E^2} \right) \exp \left(\frac{-1.54 \phi S_E v(y)}{t(y)} \right)$$

Since $t(y)$ is extremely slowly varying, it can be considered independent of S_E and it follows that

$$\frac{d(\log i_0 S_E^2)}{d(S_E)} = -0.668 \phi \frac{S(y)}{t(y)} \quad (38)$$

By measuring the dependence of the slope of the energy distribution curve, S_E , on total current (by varying the applied field), it is possible to obtain accurate values of ϕ regardless of patch fields.

2.5.3 In another paper [71] Young and Clark described some experiments carried out to check the above theories. Unfortunately, due to failure of their emitter, it was not possible to verify equation (38) and they made no corrections for patch fields. However, some high values for the work function of the (110) plane of tungsten were found using equation (37) and by varying the size of the emitting area using field evaporation techniques the importance of patch field corrections was confirmed.

2.5.4 In 1975, Vorburger, Penn and Plummer [72] took this one stage further by pointing out that the Young and Clark approach needed modifying to take account of the non-free electron behaviour which is applicable in

many cases. As shown by Swanson and Crouser [61] an expression for the current density per unit total energy, $J_o^1(\epsilon)$, is given by

$$J_o^1(\epsilon) = J_o \frac{f(\epsilon) \exp(\epsilon/d)}{d} \quad \text{Where } J_o \text{ is the total current density.} \quad (39)$$

For the free electron model assumed by Young, $f(\epsilon)$ is the Fermi-Dirac distribution and so

$$J_o^1(\epsilon) = \frac{J_o \exp(\epsilon/d)}{(\exp[\epsilon/d] + 1)d} \quad (40)$$

Here, $P = kT/d$ is a dimensionless parameter; equation (40) breaks down for $P \geq 1$ and becomes unreliable when $P \gtrsim 0.7$. Young and Clark used equation (40) to show that the slope of the logarithm of $J_o^1(\epsilon)$ is

$$S_{ED} = \delta \frac{\ln J_o^1(\epsilon)}{\delta \epsilon} = \frac{1}{d} \quad (41)$$

Equation (41) is equivalent to equation (36). Vorburger et al introduced the enhancement factor to equation (40) by putting

$$J^1(\epsilon) = R(\epsilon) J_o^1(\epsilon)$$

where $R(\epsilon) =$ enhancement factor

$J^1(\epsilon) =$ measured total energy distribution

$J_o^1(\epsilon) =$ calculated ^{NON} free-electron total energy distribution ALLOWING FOR BAND STRUCTURE EFFECTS (SEE REF. (62)).

Thus, using equation (42),

$$\begin{aligned} S_{ED} &= \frac{\delta \ln J^1(\epsilon)}{\delta \epsilon} = \frac{\delta \ln R(\epsilon)}{\delta \epsilon} + \frac{\delta \ln J_o^1(\epsilon)}{\delta \epsilon} \\ &= \frac{\delta \ln R(\epsilon)}{\delta \epsilon} + \frac{3}{2} c' (\phi - \epsilon)^{\frac{1}{2}} \frac{t(y^1)}{F} \end{aligned} \quad (43)$$

$$c' = \frac{4}{3} (2m)^{\frac{1}{2}} \frac{e}{\hbar} v(y)$$

Since

$$S_{FN} = \frac{-c\phi^{3/2} s(y)l}{\beta} \quad (\text{equation (34) neglecting patch field effects}) \quad (44)$$

Then combining equations (44) and (43)

$$(\phi - \epsilon)^{\frac{1}{2}} \phi^{-3/2} = \frac{2}{3} \frac{S(y)V}{S_{FN}t(y^1)} \left[\frac{\delta \ln R(\epsilon)}{\delta \epsilon} - S_{ED} \right] \quad (45)$$

Equation (45) is derived for electron energies greater than 0.1 eV below the Fermi energy so that $f(\epsilon) = 1$ to a very good approximation. The presence of the $\frac{\delta \ln R(\epsilon)}{\delta \epsilon}$ term is the essential difference between equation (45) and equation (37) (neglecting patch fields). Thus, if non-free electron behaviour applies, equation (45) must be used and incorrect results for ϕ will be obtained if equation (37) applied. If the term $\frac{\delta \ln R(\epsilon)}{\delta \epsilon}$ is nearly field independent then the error introduced by the free electron equation (37) will be less important as the field is reduced since the $\frac{\delta \ln J_0^1(\epsilon)}{\delta \epsilon}$ term becomes dominant. Vorburger et al also showed that, in the same way that Young and Clark had obtained an expression for ϕ regardless of patch fields (eqn (38)), a similar result could be obtained for the non-free electron case:

$$\frac{d(\ln JS_{ED}^2)}{d(S_{LD})} = \frac{2 \phi^{3/2}}{3 (\phi - \epsilon)^{3/2}} \frac{S(y)}{t(y^1)} + \frac{2 \delta \ln R(\epsilon)/\delta \epsilon}{S_{ED}(S_{ED} - \delta \ln R(\epsilon)/\delta \epsilon)}$$

2.5.5 Experimental results were then reported by Vorburger et al using the (100), (112), (013) and (111) faces of tungsten. For the (112) face data were taken at 295K and 78K. Of particular interest was the (100) face which from the work of Swanson and Crouser was known to show a large $R(\epsilon)$ factor at $\epsilon = -0.35$ eV. The energy analyser used was a hemispherical deflecting instrument designed by Kuyatt and Plummer [73] operating at $\sim 3 \times 10^{-11}$ torr. Measurements were carried out to find the variation of ϕ^{-1} (equation (45)) with electric field at three different values of energy (ϵ). From the zero field intercept the value of ϕ could be calculated in each case, and the slope of each graph gave $\delta \ln R(\epsilon)/\delta \epsilon$. The

results showed that ϕ was approximately constant with varying ϵ for the (100) and (013) data but systematic deviations were found with the (111) and (112) data. The authors concluded and attributed this variation to the field dependence of $R(\epsilon)$. Consequently, a value for ϕ was obtained in these cases by extrapolating the $\delta \ln R(\epsilon)/d\epsilon$ v. ϕ^{-1} graph to zero $\delta \ln R(\epsilon)/d\epsilon$. Using this method the value for ϕ obtained for the (112) plane showed only a very small difference at 78K and 295K (the difference being less than the estimated error of the measurement). Also, a virtually constant value for ϕ was obtained for the (100) plane at varying values of ϵ showing that this method is capable of evaluating ϕ even when the energy distribution exhibits pronounced structure. In general, the results for ϕ showed good agreement with the most reliable values obtained by other workers.

2.6.0 Summary

2.6.1 The work described in Chapter 1 has shown that recently there has been difficulty in accounting for the pre-breakdown currents obtained from broad area electrodes on the basis of a theory of metallic field emission from enhancing micro-protrusions on the electrode surface. Walters et al [31] have suggested emission through a thin dielectric layer as a possible explanation whilst Cox [34] and Hurley and Dooley [39] have also suggested that some kind of semi-conducting inclusion in the surface may be responsible. As shown in section 2.4.0, an energy analysis of the emitted electrons is capable of distinguishing between field, T-F and thermionic emission; similarly, emission from a semi-conductor will have certain unique features. Also, measurement of $R(\epsilon)$ curves would show whether emission from sites on broad area electrodes could be satisfactorily explained on a free electron model. Cox [34] has suggested that difficulty in interpretation of the data may be due to incorrect assumptions about

the work function of the material at the point of emission. As shown in sections 2.5.0 and 2.7.0, electron energy analysis is capable of determining work function and local field strength actually at the point of emission. It can be seen, therefore, that energy analysis of the pre-breakdown electron currents emitted from broad area electrodes could prove a very powerful tool in explaining their origin.

2.6.2 Consequently, the work described in this thesis was carried out to obtain the energy spectrum of such currents using a high resolution field emission energy spectrometer. The work involved adapting an existing spectrometer [74] to the specialised requirements of broad area electrodes and carrying out measurements on a number of different materials.

3.0.0 Experimental.

3.1.0 Introduction

3.1.1 The development of the experimental facility described in this chapter formed part of a research programme primarily concerned with field emission energy distribution (FEED) measurements using both retarding potential, and hemispherical deflection, energy spectrometers. For the experimental work described in this thesis, one of these spectrometers had to be adapted to the special requirements of FEED measurements on broad area electrodes and a decision had to be made on the type of spectrometer to use.

3.2.0 Choice of spectrometer.

3.2.1 To date, much of the work carried out on field emission spectrometry both in this laboratory and elsewhere has used the retarding potential type of spectrometer, but this suffers from several disadvantages compared with the more recently developed deflection instrument.

3.2.2 The layout of a retarding potential analyser is shown schematically in fig (11). To generate the necessary high electric field required to produce field emission at the surface of the material ($\sim 10^9$ V/m) whilst using a reasonable accelerating potential, it is usual for the emitter to be in the form of a fine wire, the end of which has been etched to a sharp tip typically having an end form of ~ 100 nm radius. This shape provides sufficient local field enhancement to produce field emission with an anode-cathode voltage of 0.5 - 4.0kV. A retarding voltage (\cong the accelerating voltage) is then applied at the lens (L) to reduce the kinetic energy of the electrons to a few eV (Fig 11). If a slowly increasing voltage is now applied at the collector, C, the electrons will gradually

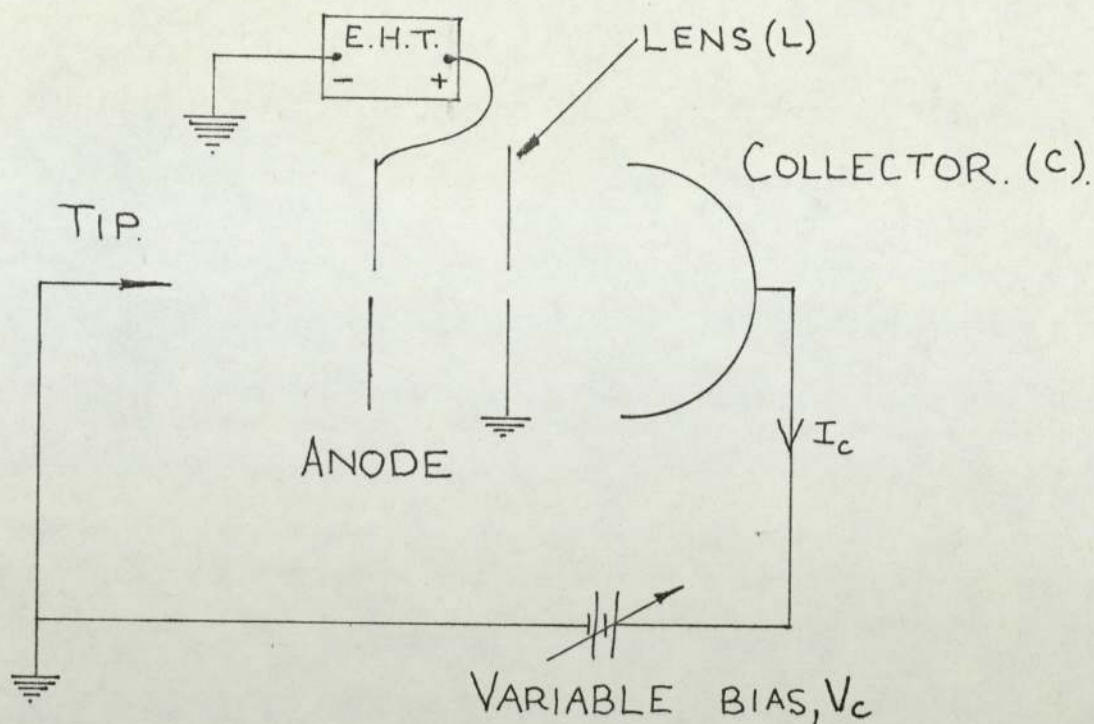


FIG 11. SCHEMATIC DIAGRAM OF THE ESSENTIAL FEATURES OF A RETARDING POTENTIAL ANALYSER.

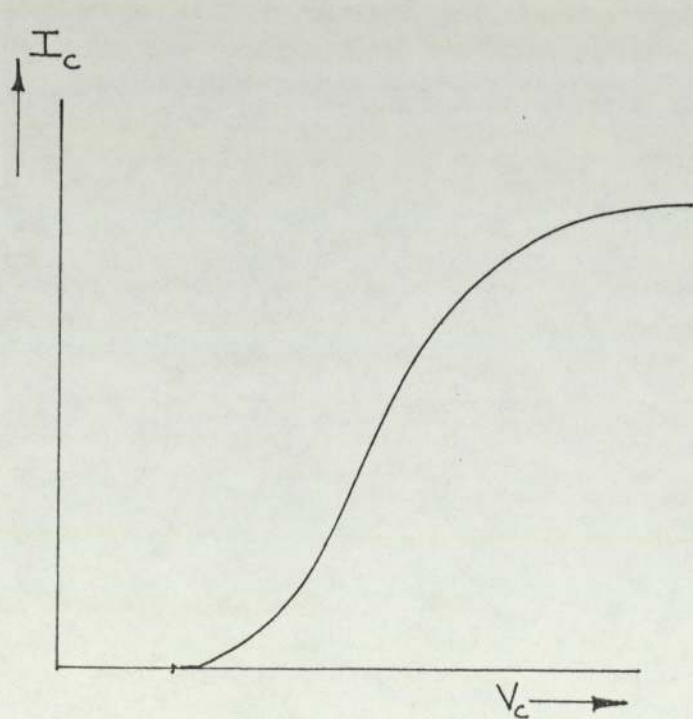


FIG 12(a) THE "INTEGRAL PLOT" OUTPUT FROM THE RETARDING POTENTIAL ANALYSER

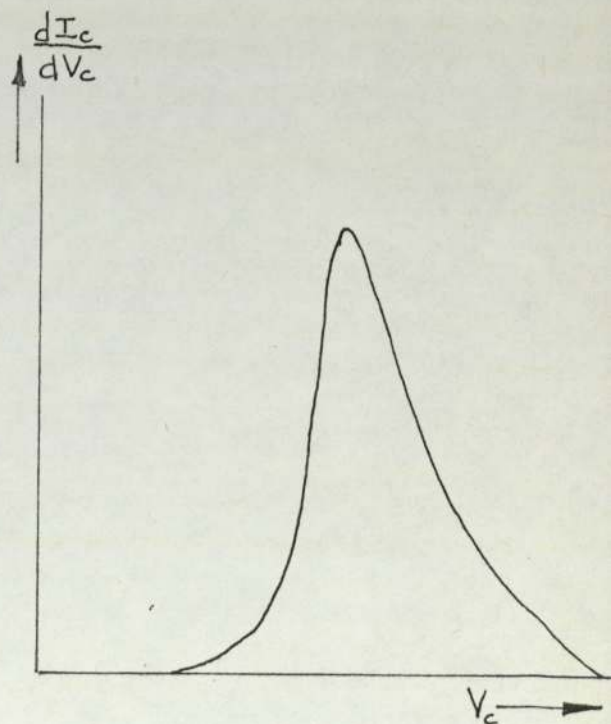


FIG 12(b) THE DIFFERENTIAL OF FIG 12(a) GIVING THE ELECTRON ENERGY DISTRIBUTION.

be collected, the most energetic at the lower voltage. Fig (12a) shows a typical graph of the collector current as the collector voltage is increased, and Fig (12b) shows the differential of this curve which represents the distribution of energies in the electron current. Typically, for an atomically clean surface, the F.W.H.M. of such a distribution, which depends on the crystal plane, the temperature and the surface field, may be $\sim 200\text{meV}$. An instrument resolution of $\sim 20\text{meV}$ is therefore desirable, which means that for an electron beam arriving at the anode with an average energy of 2keV , the overall resolving power requirement is $\sim 10^5$.

3.2.3 The detection system of a retarding potential spectrometer suffers from two drawbacks. Firstly, reference to Figure (12) shows that at the low energy end of the integral curve (higher values of V_c) there is only a relatively small increase in I_c which results in a poor signal to noise ratio. In addition, this shallow slope makes differentiation of the curve (often carried out manually) subject to greater error. Secondly, current detection at the collector in a retarding potential spectrometer is usually by an electrometer which gives rather limited sensitivity. Thus while this type of spectrometer can give a resolution $\sim 10^5$ near the peak of a FEED it cannot give comparable resolution at the low energy tail of the distribution. Since this part of the curve is very important in the study of surface electronic states where the presence or absence of relatively small peaks is crucial to the interpretation of the data, this type of instrument is limited in its application.

3.2.4 In contrast to the retarding potential type of instrument, the hemispherical spectrometer to be described below has a resolution $\sim 30\text{meV}$ throughout the energy range, a direct energy distribution output from an electron multiplier which greatly increases sensitivity, as well as

comprehensive output facilities in terms of gain, filtering and spectrum scan speed. For these reasons the hemispherical spectrometer was chosen for the experimental measurements described here.

3.3.0 The hemispherical deflection spectrometer analyser.

3.3.2 The instrument is based upon the design of Kuyatt and Plummer [73] although certain changes have been made to accommodate the different experimental conditions. A general section through the spectrometer assembly is shown in fig (13a) whilst the electron optical layout is shown in greater detail in fig (13b). An overall view of the instrument and associated electronics is shown in fig (14). The basic instrument was already built when the present project work commenced although certain preliminary investigations with field emitting tips were necessary before embarking on the modifications described in 3.7.0. Accordingly, the various components of the spectrometer are briefly described in 3.3.2 to 3.6.3 in order to illustrate the general design philosophy and resulting performance of the instrument. Details of the modifications carried out for this project follow in 3.7.0 to 3.9.10.

3.3.2 The hemispherical deflecting element forms the heart of the spectrometer and the theory of this type of deflector was first given by Purcell [76]. Consider two concentric hemispherical elements of inner radius R_{IH} and outer radius R_{OH} , with an electron travelling in the plane of the paper and following the mid-radius R_0 as shown in fig (15). Let there be an outward radial field \underline{F} due to a charge $+Q$ on the inner hemisphere and $-Q$ on the outer hemisphere. Under these circumstances, the electron will be constrained to execute circular motion in the mid-plane (R_0) if:

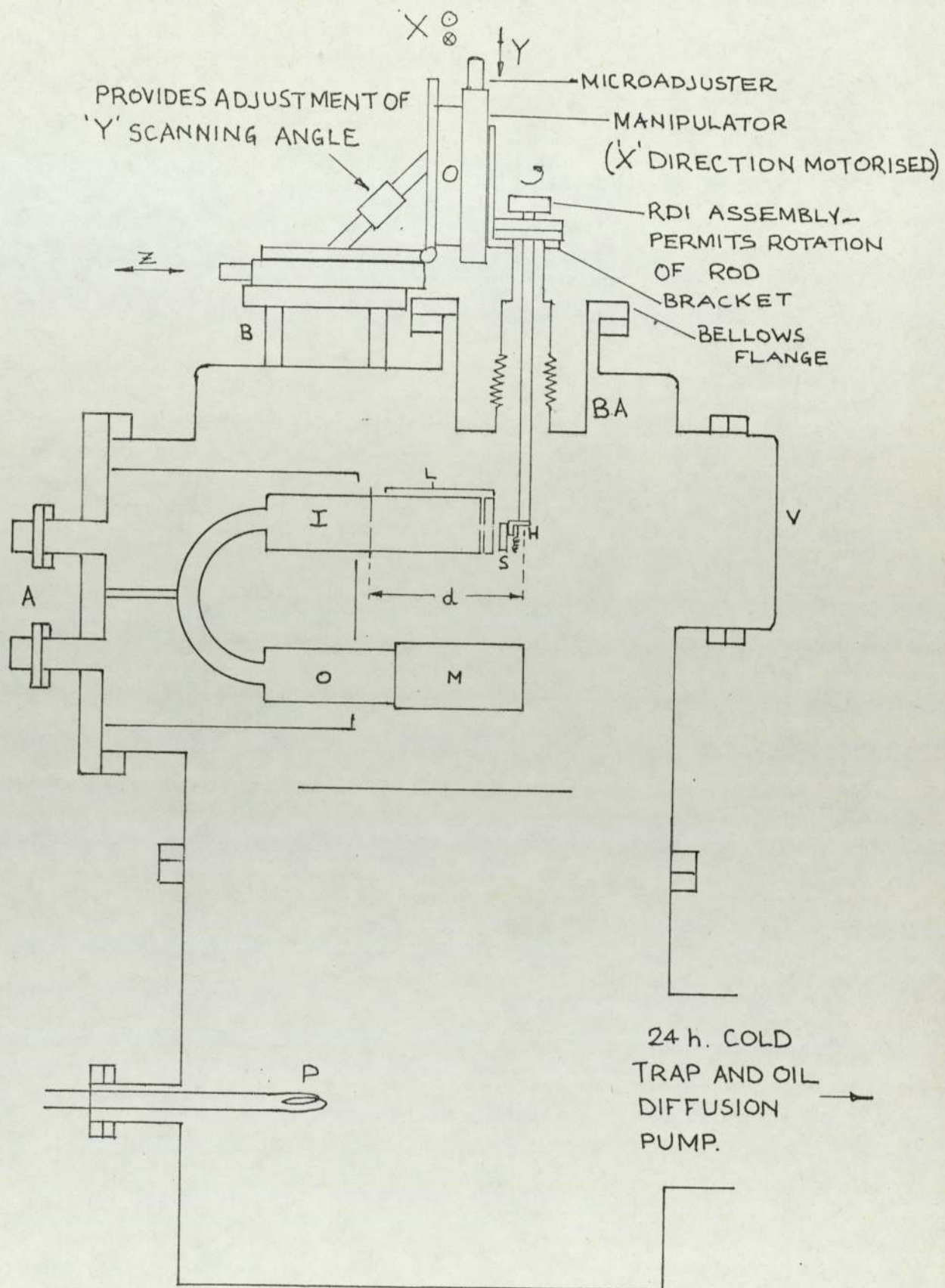


FIG 13(a) GENERAL SECTION THROUGH SPECTROMETER CHAMBER SHOWING MANIPULATOR ASSEMBLY ATTACHED.

A- SPECTROMETER ASSEMBLY AND OUTLET SOCKETS; I- INPUT LENSES; O- OUTPUT LENSES; M- ELECTRON MULTIPLIER; L- INTERFACING LENS; B- BASEPLATE TO SUPPORT MANIPULATOR ASSEMBLY; V- VIEWING PORT; BA- BELLOWS ASSEMBLY; P- SUBLIMATION PUMP; S- SPECIMEN; H- SPECIMEN HOLDER.

THE DIAGRAM SHOWS THE APPROXIMATE PATH OF A PARALLEL BEAM OF ELECTRONS ENTERING THE FIRST INPUT LENS. THE INTERFACING LENS WHICH SUPPLIES THIS BEAM IS SHOWN IN FURTHER DETAIL IN FIGS. 22, 23, 24 AND 26.

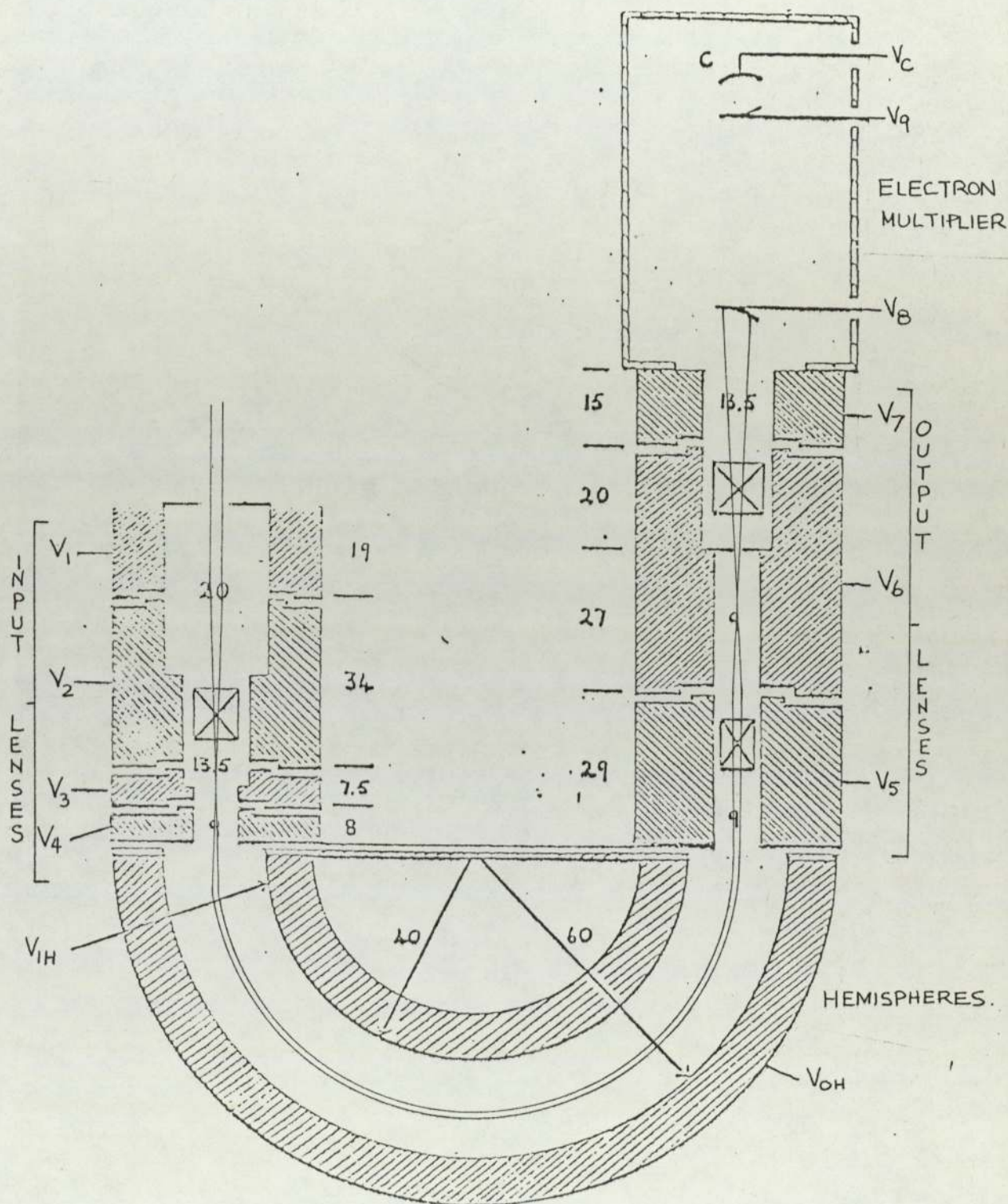
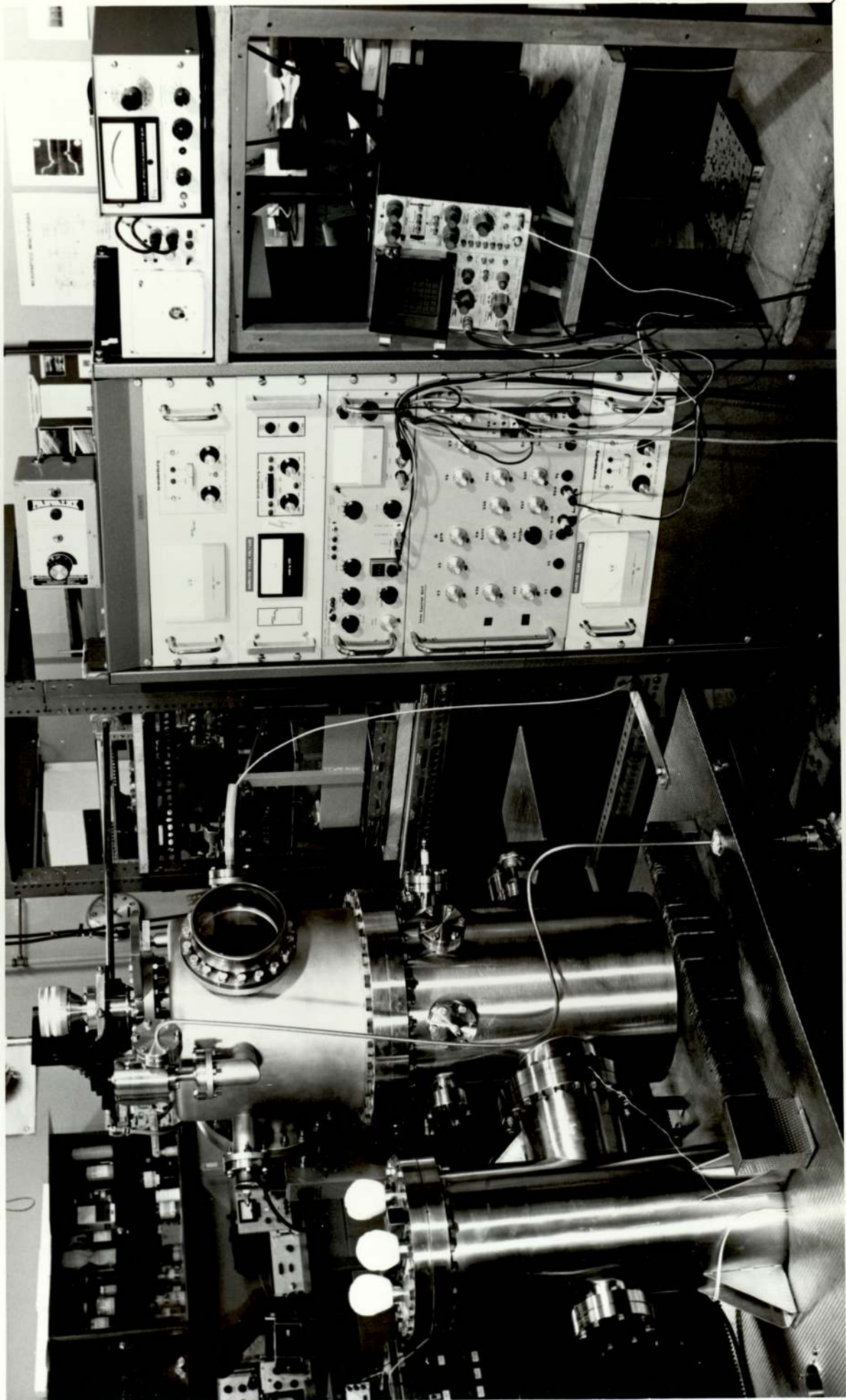


Fig 13(b) ESSENTIAL FEATURES OF THE ELECTRON OPTICAL SYSTEM OF THE SPECTROMETER.

THE FIGURES GIVE THE LENS DIMENSIONS IN MM.
ELEMENTS 2, 5 AND 6 CONTAIN DEFLECTION PLATES.

Fig 14
A general exterior view
of the
spectrometer and associated equipment



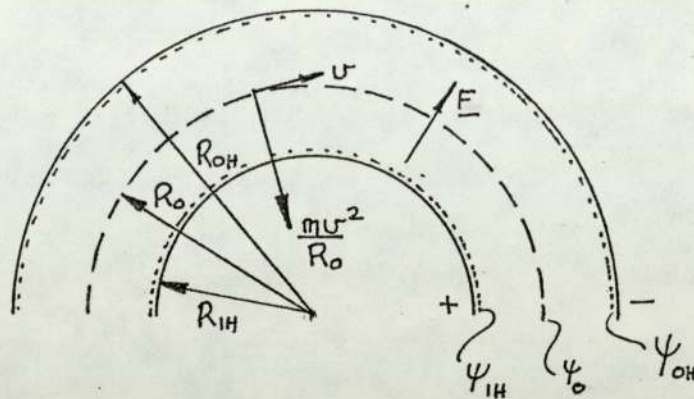


FIG 15. AN ELECTRON PASSING BETWEEN A CONCENTRIC PAIR OF HEMISPHERES ALONG THE MID-RADIUS, R_0 .

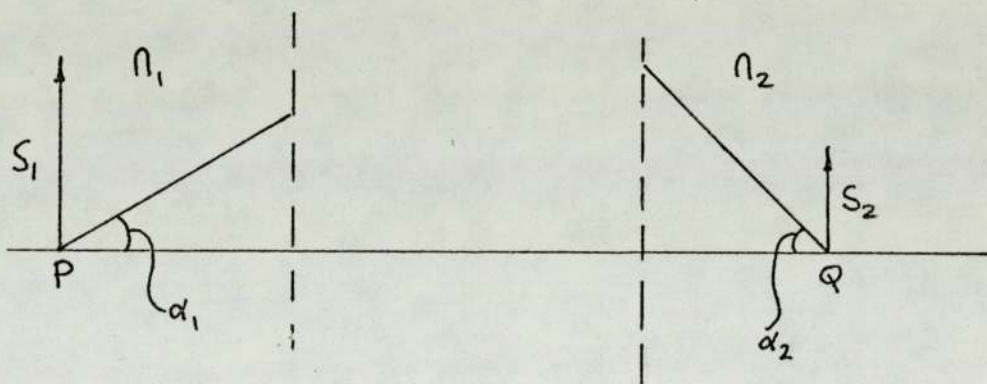


FIG 16. THE HELMHOLTZ-LAGRANGE THEOREM.

THE REGION BETWEEN THE DOTTED LINES REPRESENTS AN OPTICAL SYSTEM SYMMETRICAL ABOUT PQ. RAYS FROM AN OBJECT HEIGHT S_1 AT P PASS THROUGH THE SYSTEM AND ARE BROUGHT TO A FOCUS TO FORM AN IMAGE HEIGHT S_2 AT Q. FOR SMALL ANGLES α PARAXIAL RAYS

$$n_1 S_1 \alpha_1 = n_2 S_2 \alpha_2$$

WHERE n_1 AND n_2 ARE THE REFRACTIVE INDICES OF OBJECT AND IMAGE SPACES RESPECTIVELY.

FOR THE CASE OF ELECTRON OPTICS, $n \propto \sqrt{V}$, WHERE V IS THE VOLTAGE ON THE ELEMENT APPROPRIATE TO THAT REGION. THEREFORE:

$$S_1 \alpha_1 \sqrt{V_1} = S_2 \alpha_2 \sqrt{V_2}.$$

$$\frac{mv^2}{R_0} = (-e)(-F_0) \quad \text{assuming non-relativistic velocities of the electron.}$$

where m = electron rest mass

v = electron velocity ($v \ll c$)

$-e$ = charge on electron

F_0 = electric field between hemispheres at R_0 in direction shown.

$$\text{or: } mv^2 = R_0 e F_0$$

If the kinetic energy of the electron is ϵ_a then

$$\epsilon_a = \frac{mv^2}{2} = \frac{R_0 e F_0}{2} \quad (46)$$

Applying Gauss' electric flux theorem to a concentric spherical surface radius r ($R_{1H} < r < R_{0H}$) then:

$$\int_{\text{over sphere}} \underline{F}(r) \cdot \underline{n} \, ds = 4\pi r^2 F(r) = \frac{Q}{\epsilon_0}$$

where ϵ_0 is the permittivity of free space.

$$\therefore F(r) = \frac{Q}{4\pi\epsilon_0 r^2} = -\frac{\delta\psi(r)}{\delta r} \quad (47)$$

where $\psi(r)$ is the electric potential at a distance r in the field F , taking the usual convention that when $r = \infty$, $\psi = 0$.

Using equation (47) to specify the potential ψ_{1H} at a point just outside the surface of the inner hemisphere (i.e. in the gap),

$$\psi_{1H} = \frac{-Q}{4\pi\epsilon_0} \int_{\infty}^{R_{1H}} \frac{1}{r^2} dr$$

$$\therefore \psi_{1H} = \frac{Q}{4\pi\epsilon_0 R_{1H}} \quad (48)$$

$$\text{Similarly } \psi_{OH} = \frac{Q}{4\pi\epsilon_0 R_{OH}} \quad (49)$$

where ψ_{OH} is the potential at a point just outside the surface of the outer hemisphere (again in the gap).

Now from eqn (47)

$$F(r) = \frac{Q}{4\pi r^2 \epsilon_0}$$

$$\therefore \text{ at radius } R_0, F_0 = \frac{Q}{4\pi R_0^2 \epsilon_0}$$

Substituting this into (48) and (49)

$$\psi_{1H} = \frac{F_0 R_0^2}{R_{1H}} ; \quad \psi_{OH} = \frac{F_0 R_0^2}{R_{OH}}$$

$$\text{But from (46) } F_0 = \frac{2\epsilon_a}{R_0 e} \quad \text{and since } R_0 = \frac{R_{1H} + R_{OH}}{2}$$

$$\psi_{1H} = \frac{\epsilon_a}{e} \left[\frac{R_{OH}}{R_{1H}} + 1 \right] \quad (50)$$

Similarly,

$$\psi_{OH} = \frac{\epsilon_a}{e} \left[\frac{R_{1H}}{R_{OH}} + 1 \right] \quad (51)$$

Hence the voltage across the hemispheres required to allow the transmission of an electron of kinetic energy ϵ_a around a circular path of radius R_0 is:

$$\Delta V_H = \psi_{1H} - \psi_{0H} = \frac{\epsilon_a}{e} \left[\frac{R_{0H}}{R_{1H}} - \frac{R_{1H}}{R_{0H}} \right] \quad (52)$$

Equation (52) represents the first of the three main design equations for the deflection hemispheres, the other two being those for the resolution and for the maximum deviation of the beam.

3.3.3 The resolution of the hemispheres is given by [77]:

$$\frac{\Delta\epsilon}{\epsilon_a} = \frac{Z}{2R_0} + \frac{1}{2} (\alpha)^2$$

where ϵ_a is the analysing energy of the hemispheres; that is, the kinetic energy that the electrons must have in order to traverse the mid-path, R_0

$\Delta\epsilon$ is the maximum amount by which the electrons can exceed the analysing energy and still pass round the hemispheres (i.e. the hemisphere band width)

Z is the input and output slit width (assumed equal)

α is the angular spread of the input beam

Hence,

$$\Delta\epsilon = \epsilon - \epsilon_a = \epsilon_a \left[\frac{Z}{2R_0} + \frac{1}{2} \alpha^2 \right] \quad (53)$$

It is clear that to obtain the best resolution requires the smallest band width at a given analysing energy. Thus from equation (53) it is necessary for ϵ_a , Z and α to be small and R_0 to be large. There is a limitation on the minimum value for ϵ_a , since very low energy electrons can be difficult to control due to the increasing importance of stray magnetic field effects and the variation in surface potential. Decreasing the size of the apertures improves resolution but reduces transmission and so considerations of minimum detectable current puts a lower limit on this factor. Finally, provided $\alpha^2 < \frac{Z}{R_0}$ the effect of this factor is not too great since increasing α changes the shape of the transmission function

rather than increasing $\Delta\epsilon$.

3.3.4 In this instrument, an analysing energy of 2eV was chosen as being a reasonable compromise of the factors discussed. The designed resolution was $\sim 20\text{meV}$ for electrons entering the spectrometer (before retardation) of 2keV i.e. a resolving power of 10^5 . To minimise broadening of the hemisphere transmission function [77] it is usual to set

$$\alpha^2 = \frac{Z}{4R_0} \quad (54)$$

Thus from (53)

$$\alpha^2 = \frac{2}{5} \frac{\Delta\epsilon}{\epsilon_a} \quad (55)$$

Substituting (55) into (53)

$$0.8 \frac{\Delta\epsilon}{\epsilon_a} = \frac{Z}{2R_0} \quad (56)$$

3.3.5 The law of Helmholtz and Lagrange [78] can now be applied to the input electron beam of the spectrometer. Referring to fig (16)

$$S_1 \alpha_1 V_1^{\frac{1}{2}} = S_2 \alpha_2 V_2^{\frac{1}{2}} \quad (57)$$

For this spectrometer it was known that the tip would be positioned approximately 50mm from the front anode (dimension d in fig 13a) so that with an anode aperture of 0.5mm diameter, the effective half angle of the diverging beam from the tip (i.e. the part of the beam that passes into the analyser) is

$$\alpha_1 = \frac{2.5 \times 10^{-1}}{5 \times 10} = 5 \times 10^{-3} \text{ rad.}$$

Using this and equations (55), (56) in equation (57) and taking V_1 as the front anode potential and V_2 as the mid-potential of the hemispheres leads

to

$$\frac{\Delta\epsilon^3}{\epsilon_a^2} = \frac{1.2 \times 10^{-2}}{R_0^2}$$

If $\Delta\epsilon = 25\text{meV}$, $\epsilon_a = 2\text{eV}$ then

$$R_0 = 55.4\text{mm}$$

In fact, a value of $R_0 = 50\text{mm}$ has been used which slightly alters the value of $\Delta\epsilon$ to 27meV . From equation (56) a value for Z may now be derived:

$$Z = 1.6 \frac{\Delta\epsilon}{\epsilon_a} R_0 = 1.08\text{mm}$$

In practice, the input aperture is circular (1.0mm dia) and the output aperture is rectangular (1.1mm width); this gives improved transmission without markedly affecting the resolution [79].

3.3.6 A final property of the spherical deflector which is of interest is the maximum deviation Z_m of the beam in the deflector from the central path of radius R_0 . This constitutes the third analyser design equation and is given by [77]:

$$\frac{Z_m}{R_0} = \frac{\Delta\epsilon}{\epsilon_a} + \left[\alpha^2 + \left(\frac{Z}{2R_0} + \frac{\Delta\epsilon}{\epsilon_a} \right)^2 \right]^{1/2}$$

From equation (55)

$$\alpha^2 = \frac{2}{5} \frac{\Delta\epsilon}{\epsilon_a}$$

$$\therefore Z_m = 5\text{mm.}$$

In the final design of the spectrometer, $R_{OH} = 60\text{mm}$ and $R_{IH} = 40\text{mm}$

giving a gap of 20mm. Using these values with equation (52) gives the voltage across the hemispheres as:

$$\Delta V_H = 2 \left[\frac{60}{40} - \frac{40}{60} \right]$$

$$\Delta V_H = 1.67 \text{ volts.}$$

The path of the electrons around the hemispheres, and hence the analysing energy, will also be affected by the presence of stray magnetic fields, the most significant of these being the horizontal component of the earth's field. An electron of charge $-e$ travelling with velocity v at an angle θ to a field of magnetic induction B will experience a force F given by

$$\underline{F} = -e\underline{v} \times \underline{B}$$

The value of θ depends on the orientation of the analyser and for the "worst case" where the horizontal component of the earth's magnetic field is normal to the plane of motion of the electrons between the hemispheres (i.e. $\theta = \pi/2$), equation (46) becomes:

$$\frac{mv^2}{R_0} = eF_0 - evB$$

The new analysing energy ϵ_a^1 becomes

$$\epsilon_a^1 = \frac{eR_0}{2} (F_0 - vB)$$

so that,

$$\psi_{IH} = \frac{R_0^2}{R_{IH}} \left[\frac{2\epsilon_a^1}{eR_0} + vB \right]$$

$$\psi_{OH} = \frac{R_0^2}{R_{OH}} \left[\frac{2\epsilon_a^1}{eR_0} + vB \right]$$

and

$$\Delta V_H = \psi_{1H} - \psi_{0H} = \frac{\epsilon_a^1}{e} \left[\frac{R_{0H}}{R_{1H}} - \frac{R_{1H}}{R_{0H}} \right] + R_0^2 v_B \left[\frac{1}{R_{1H}} - \frac{1}{R_{0H}} \right] \quad (58)$$

The part of the spectrometer containing electrons of low energy is surrounded by a mu-metal shield which has a permeability of about $0.05W A^{-1} M^{-1}$ and thus $B \sim 8.5 \times 10^{-7}$ tesla. For electrons which pass through the mid-radius of the hemispheres,

$$\frac{1}{2}mv^2 = eV_a^1, \text{ where } eV_a^1 (= \epsilon_a^1) \text{ is the analysing energy in the presence of magnetic field } B.$$

Substituting for v , and putting values for the other parameters in (58) leads to

$$V_a^1 = 1.985 \text{ volts}$$

i.e. a change in analysing energy of $\sim 15\text{meV}$. The actual value of θ , variation in the local field and the presence of other fields in the laboratory will all affect this result. One method of reducing this field even further is by the use of three pairs of mutually perpendicular Helmholtz coils mounted around the spectrometer. Experiments on the effect of reducing the field around the spectrometer using such coils were carried out by Pearson [80]. He found no detectable change in the energy spectrum from the instrument when the field was reduced to $< 10^{-8}$ tesla. This gives supporting evidence to the theoretical analysis which indicates that the largest shift likely to be observed is 15meV ; since shifts of $\approx 10\text{meV}$ cannot be reliably detected it suggests that magnetic field effects are even less than assumed in the calculation. Consequently, the Helmholtz coils were felt to be unnecessary for the present investigations.

3.3.7 So far, a value has been calculated for ΔV_H for which electrons of a given kinetic energy, ϵ_a , will move along the mid-radius, R_0 . In order to obtain the energy distribution of the electrons arriving at the hemispheres, the mid-potential, ψ_0 , must be set to a pre-determined value. The reason for this is discussed in the section on scanning (3.5.0) and an expression for ψ_0 is obtained as follows. Referring to equation (47), the mid-potential ψ_0 is given by:

$$\psi_0 = \frac{Q}{4\pi R_0 \epsilon_0} = F_0 R_0 = \frac{2\epsilon_a}{e} \quad (59)$$

It is important to note that this is an electrostatic potential which, using the common convention, is measured with reference to the potential at infinity. In a practical case this potential must be referred to that of another electrode so that ψ_0 can be established in terms of applied voltages. This is done by referring ψ_0 to ψ_{1H} and ψ_{0H} . Thus using equations (50), (51) and (59)

$$\begin{aligned} V_{1H} &= \psi_{1H} - \psi_0 = \frac{\epsilon_a}{e} \left[\frac{R_{0H}}{R_{1H}} + 1 \right] - \frac{2\epsilon_a}{e} = \frac{\epsilon_a}{e} \left[\frac{R_{0H}}{R_{1H}} - 1 \right] \\ &= V_a \left[\frac{3}{2} - 1 \right] = 1.0 \text{ volts} \end{aligned}$$

Similarly,

$$V_{0H} = \psi_0 - \psi_{0H} = \frac{\epsilon_a}{e} \left[2 - \left(\frac{R_{1H}}{R_{0H}} + 1 \right) \right] = 0.67 \text{ volts}$$

Since ψ_{1H} and ψ_{0H} have been defined as the potentials just outside the hemisphere surfaces fig (15), the potential on the hemisphere elements themselves will differ from this value by an amount ϕ_c , which is approximately equal to the work function of the elements. (Strictly, the work function is the work done in slowly removing an electron from the Fermi level in the bulk of the metal to a point infinitely far away, rather than

to a point just outside the surface).

3.3.8 The conditions evaluated for the hemispheres may now be established in practical terms by means of the resistors R_1 and R_2 as shown in fig (17). The voltage across the hemispheres, ΔV_H , is set equal to $(V_{1H} + V_{0H})$ by adjusting the resistors R_1 and R_2 to give a voltage drop of V_{0H} and V_{1H} respectively. By setting the voltage between these resistors to a value of $(\psi_0 + \frac{\phi_c}{e})$ with reference to earth in fig (17), it can be seen that this will then give the required potentials just outside the hemisphere surfaces. Further, if the point between the resistors is connected to the electrode L_4 -positioned in front of the hemisphere entrance slit - then the potential for the electrons arriving inside L_4 will also be ψ_0 .

3.4.0 The input and output lenses.

3.4.1 The input lens system of the analyser has to fulfill two main criteria:

- i) to decelerate the electrons from an energy of $\sim 2\text{keV}$ at the anode to $\sim 2\text{eV}$ at L_4 i.e. a ratio of about 10^3 , and
- ii) to provide an image magnification of $2x$, since the input aperture of the lens is 0.5mm diameter whilst that of the hemispheres is 1.0mm .

The actual deceleration ratio will vary somewhat according to the operating conditions but it is necessary for the focal properties to remain constant throughout the range of values (typically $1 - 4\text{kV}$) that may be used. These criteria necessitate the use of a lens of at least three elements whereby the centre element can be adjusted to give the correct focus for any desired overall voltage ratio. Consequently, a three element lens designed in accordance with the method described by

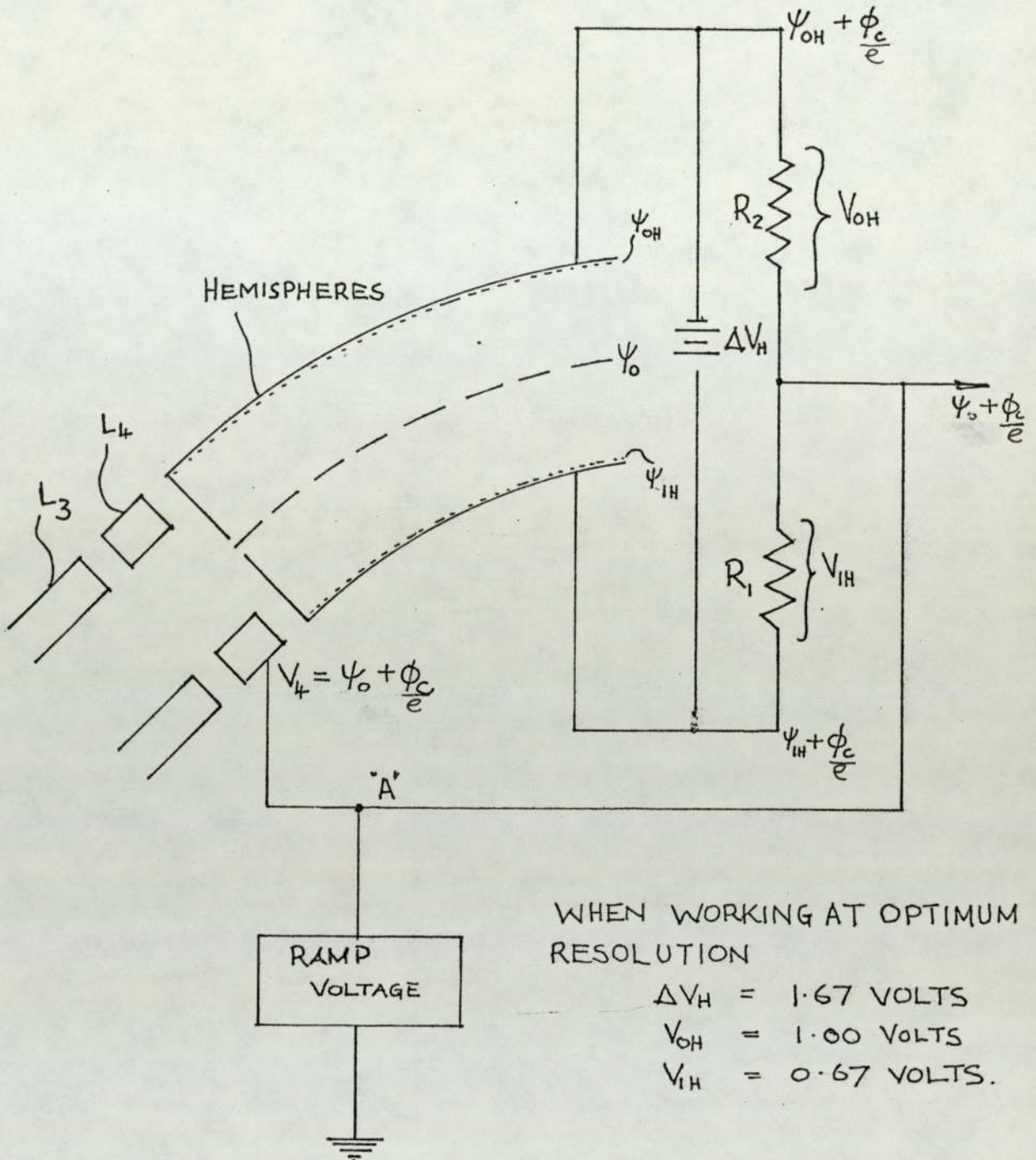


Fig 17. THE CIRCUIT USED TO OBTAIN THE REQUIRED MID-POTENTIAL OF THE HEMISPHERES, ψ_0 .

SINCE THE POTENTIAL INSIDE V_4 IS ALSO ψ_0 , APPLYING A RAMP VOLTAGE AT "A" ALLOWS ELECTRONS OF VARYING ENERGIES TO TRAVERSE THE MID-PATH AND SO BE TRANSMITTED BY THE HEMISPHERES. SINCE ΔV_H REMAINS CONSTANT, THE RESOLUTION IS UNALTERED THROUGHOUT THE SCAN.

Heddle [79] was adopted, followed by a fixed ratio lens. The component lenses have different diameters so that the lens elements are a reasonable length, varying between 9 and 20mm, the total length being 70mm. The operational mode is shown by the electron trajectories of fig (13b) where the focusing characteristics are adjusted by varying the potential (V_2) of element 2. This element also contains a set of x - y deflector plates for fine beam steering.

3.4.2 The function of the output lens system is to re-accelerate the electron beam leaving the hemispheres and at the same time to collimate it to the electron multiplier. Lens L_5/L_6 accelerates the electrons onto a rectangular aperture where the image magnification is 0.5. A set of deflector plates in L_5 is used for steering the beam through this aperture. The emergent beam is then accelerated to approximately 200ev by lens L_6/L_7 so as to impinge diffusely onto the first dynode of the electron multiplier, thus reducing the effect of spatial variation in sensitivity on the multiplier surface. The multiplier used is a 14 dynode Twentieth Century type ED525. The gain is quoted as 2.5×10^5 at 4kV and the maximum output current is $10\mu\text{A}$. The dynode surfaces are beryllium copper and must be kept free of contamination particularly pump oil; lengthy exposure to damp air must also be avoided. As the electrons leaving the hemispheres are at a low positive voltage the last dynode of the electron multiplier is at a high voltage and the output signal is floating.

3.4.3 The lens elements of the electron optical system were constructed from non-magnetic stainless steel and accurately positioned by the use of sapphire spheres. A Mumetal can surrounds the low energy region of the system thus reducing the effect of external magnetic fields on the electron path.

3.4.4 The electronic system for the analyser comprises a voltage supply for the lenses and electron multiplier, a ramp generator for scanning, and amplifiers to handle the output from the multiplier. Display is usually via a storage oscilloscope but there is provision for an x - y recorder. The layout of the various units is shown in fig (18).

3.4.5 The lens voltages are applied using two Brandenburg alpha series 0 - 5kV power units, one of these providing the voltage for lenses $L_1 - L_6$ by means of a resistor chain, individual adjustment being available through a wide range for each lens. This arrangement has the advantage that the lens voltage ratios are independent of the magnitude of the anode voltage V_1 , so that the focusing properties of the lenses are largely unaffected by changes in V_1 over the operating range of the instrument (1 - 4kV). The second power unit supplies the 4kV for the electron multiplier and the required voltage for V_7 , this again being adjustable. In-line jack sockets are also provided on the resistor chain for individual lens voltage and current measurements using D.V.M. and electrometer. The hemisphere voltages are provided by a floating supply driven by batteries which gives a low drift, low noise value of ΔV_H during variation of V_1 . In fact, ΔV_H can be varied to give a range of analysing energies from 2 to 18eV. The former is required for high resolution operation whereas the latter offers a greater output signal at low resolution for the initial beam alignment procedure. Separate adjustments are also provided for setting each hemisphere voltage relative to the hemisphere mid-potential.

3.4.6 The signal amplifier is in two parts and consists of a head unit mounted directly onto the vacuum flange which contains the electrical leadthroughs, and a second rack-mounted unit. The head unit contains switched collector resistors (1 K Ω - 10 M Ω) and an isolation amplifier

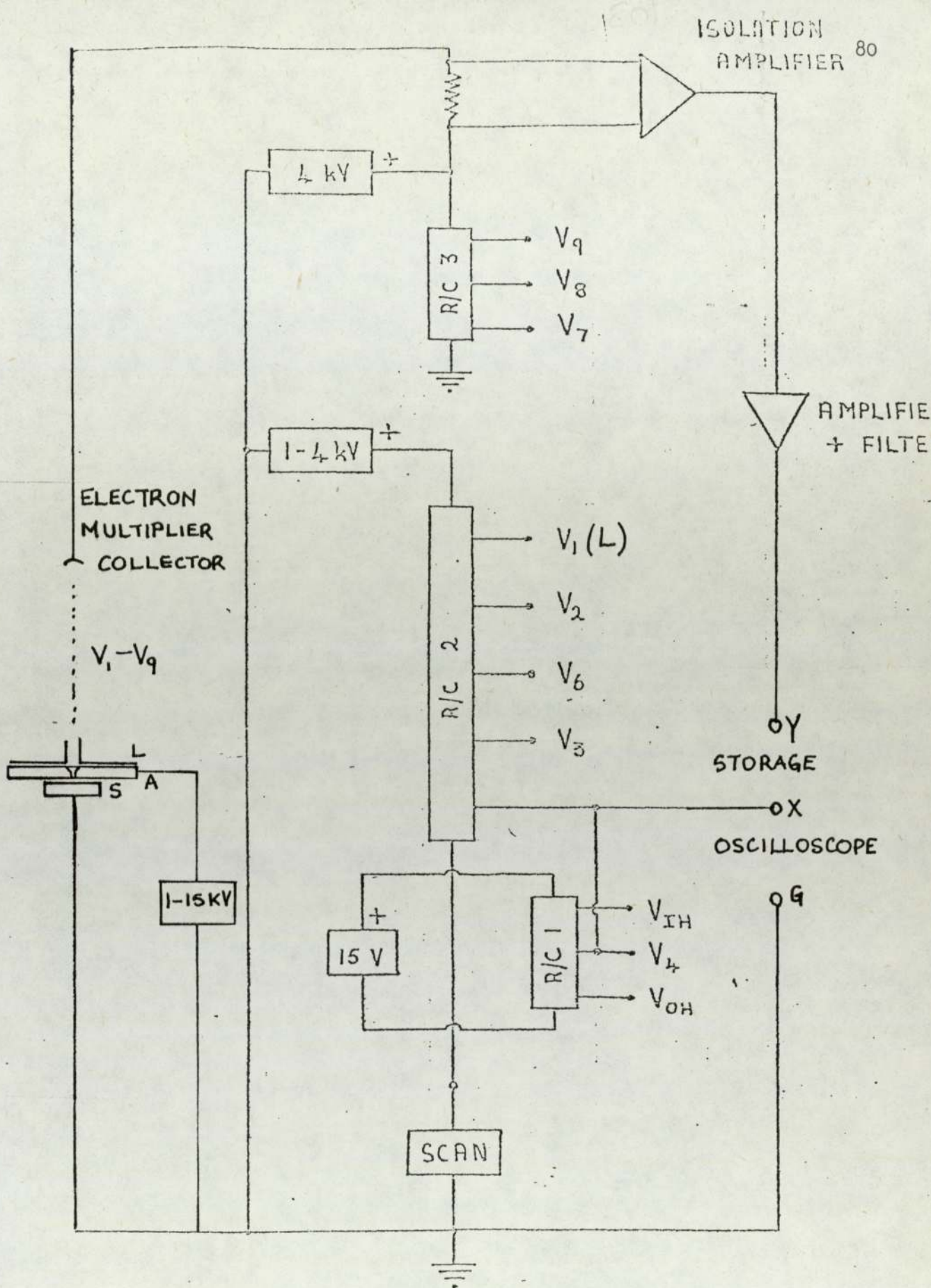


FIG 18. VOLTAGE SUPPLY ARRANGEMENTS OF THE SPECTROMETER. SUPPLIES FOR THE DEFLECTION PLATES (NOT SHOWN) ARE TAKEN FROM A SEPARATE RESISTOR CHAIN.

AD273K. This amplifier can withstand 5kV in both common and differential modes. It has a gain of 1.00 and a linearity of 0.2% up to 2V. The second rack mounted amplifier has been purpose-built and amplifies the signal into the oscilloscope or recorder. It has a continuously variable gain between 5 and 5000 and incorporates a low pass filter (40dB per decade roll off, time constant variable between 10 μ s and 300ms). This filter is normally used on slow scanning to reduce mains hum or spurious noise. The output is fed to a panel meter, and an oscilloscope or x - y recorder. The output on the panel meter is scaled 0 \rightarrow 10V and the electron multiplier output current for full scale is given by

$$I_{\text{fsd}} = \frac{10^{-5}}{(R_c \times \text{gain})} \text{ amps}$$

where R_c = collector resistor in M Ω .

Thus the minimum current for fsd, assuming a multiplier gain of 10^5 , is $\sim 10^{-15}$ A. The noise current is given by

$$I_{\text{noise}} = \sqrt{2(eI_c \Delta f)}$$

where I_c is the input current

Δf is the bandwidth of the noise (100 Hz)

so that $I_{\text{noise}} = 1.8 \times 10^{-15}$ A or 2% of the input current. Thus, satisfactory operation is possible down to 10^{-12} or 10^{-13} A. Pulse counting would be required for lower current levels.

3.4.7 The ramp generator provides a switched energy scan of 1, 2, 5, or 10V; this voltage can be precisely set using preset potentiometers inside the unit. The actual voltage of starting the scan can also be adjusted so that V_4 may be scanned through any of the pre-set ranges between 0 and 20V. The scan period is continuously adjustable between

10ms and 100s and continuous or single-shot operation is also provided. In addition there is a manual scan facility and the provision for holding the scan at any position.

3.5.0 Energy scanning

3.5.1 The method of obtaining an energy distribution will now be described. Suppose that the emitter is earthed and has a Fermi level ζ and work function ϕ_E (fig 19). Electrons that are field emitted will be accelerated towards the anode, after which they will be decelerated to the element L_4 . If L_4 is also earthed (fig 20) then the Fermi level of L_4 will be equal to that of the emitter. If now a positive voltage $V_4 (= \phi_{c/e})$ is applied to L_4 (fig 21), then the potential in the free space inside L_4 will be equal to the emitter Fermi level. In such a situation, an electron field emitted at the Fermi level would experience no net change in kinetic energy in moving to L_4 - or to the mid-path of the hemispheres, since by the resistor arrangement these are at the same potential.

3.5.2 Suppose now that V_4 is increased by an amount ψ_0 so that $V_4 = \frac{\phi_c}{e} + \psi_0$; the kinetic energy gained by a field emitted electron in moving from the emitter to L_4 will, at some value of ψ_0 just be equal to eVa (the kinetic energy required to traverse the mid-path of the hemispheres). Consequently, if V_4 is slowly increased from zero, then in the idealised case where a metallic emitter is maintained at a temperature of absolute zero, the first electrons to gain energy eVa due to the potential at L_4 will be those from the Fermi level. Therefore, for Fermi level electrons,

$$\psi_0 \quad (\text{at the Fermi level}) = \frac{\epsilon_a}{e}$$

or

$$V_4 - \frac{\phi_c}{e} = \frac{\epsilon_a}{e}$$

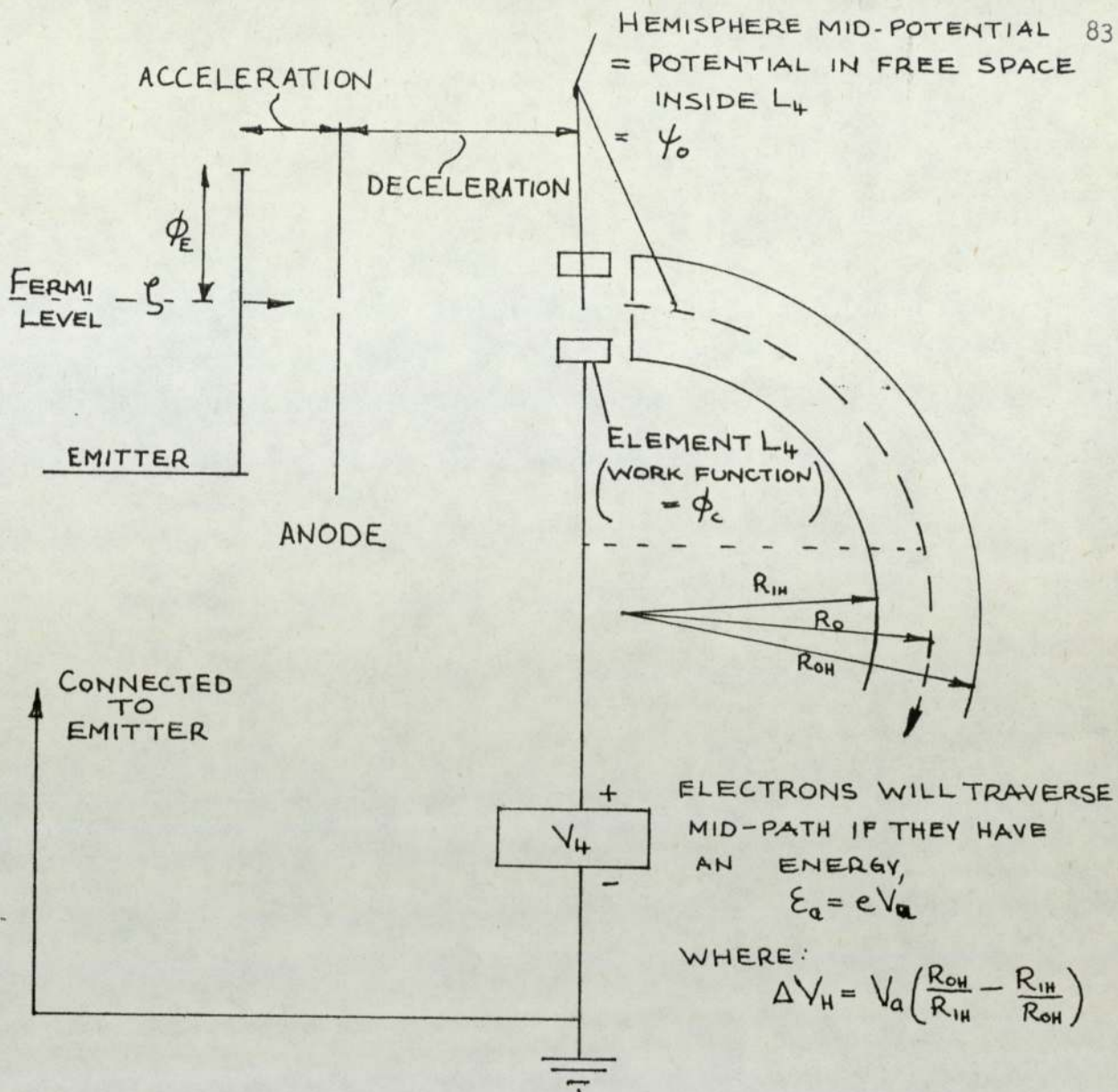


FIG 19. MEASURING THE ENERGY OF EMITTED ELECTRONS.
 IF $V_4 = \phi_c/e$ THEN FOR ELECTRONS EMITTED FROM THE FERMI LEVEL, ξ , THERE WILL BE NO NET GAIN OR LOSS IN ENERGY WHEN ARRIVING AT L_4 . AT SOME LARGER VALUES OF V_4 , HOWEVER, THE FERMI LEVEL ELECTRONS WILL HAVE GAINED AN ENERGY eV_a WHEN REACHING L_4 WHICH MEANS THEY WILL PASS AROUND THE HEMISPHERES. SIMILARLY FOR EACH ENERGY LEVEL ABOVE AND BELOW ξ THERE WILL BE A CORRESPONDING VALUE OF V_4 WHICH GIVES THE ELECTRONS OF THAT LEVEL AN ENERGY OF eV_4 AT L_4 . HENCE RAMPING V_4 AND MEASURING THIS AGAINST THE ELECTRON CURRENT TRANSMITTED THROUGH THE HEMISPHERES GIVES THE ELECTRON ENERGY DISTRIBUTION.

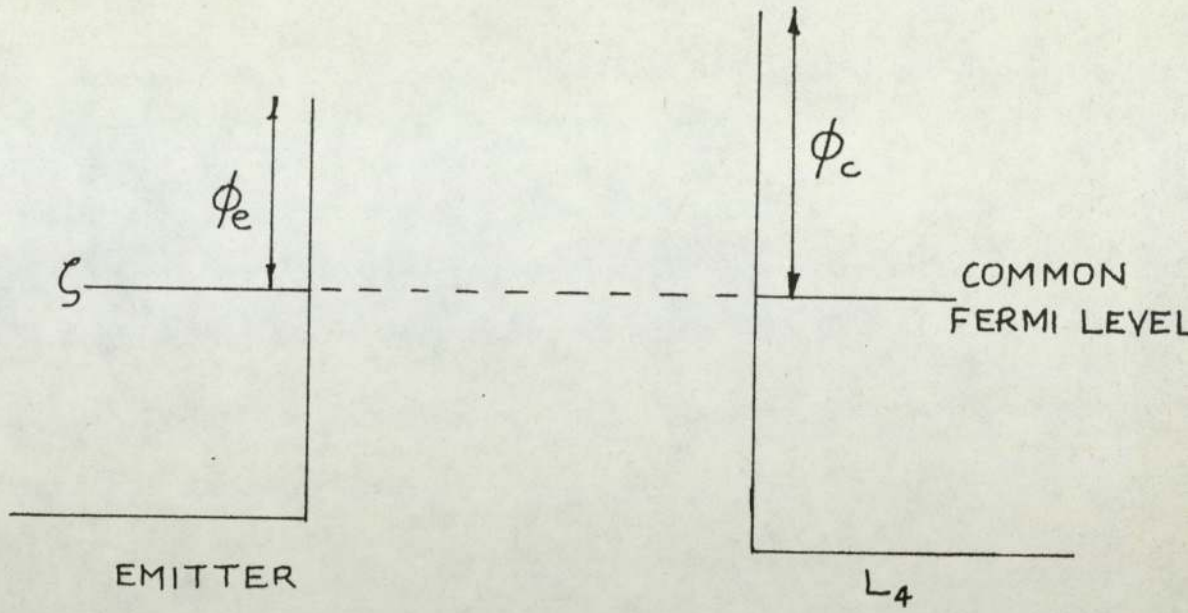


FIG 20. Emitter and L_4 earthed.

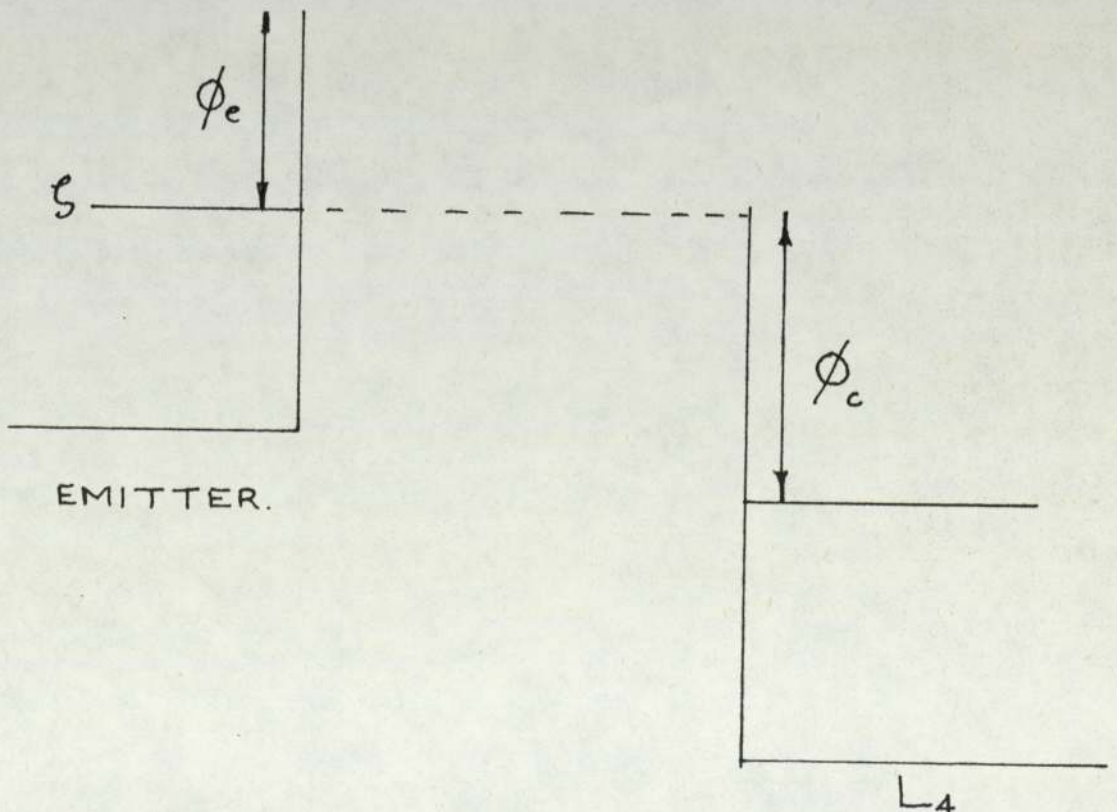


FIG 21. Emitter earthed, $V_e = \phi_c / e$.

Since ϵ_a is known (from ΔV_H and the dimensions of the hemispheres, eqn (52)) and V_4 can be measured, ϕ_c can be determined. In practice, Young [50] has described a method whereby Fermi level electrons may be identified on a distribution even though the emitter is above absolute zero. This method is explained later in 3.6.1. If V_4 is now further increased, then ψ_0 will correspondingly pass through a further range of values; thus for each electron energy below the Fermi level a value of ψ_0 will be reached such that the electron acquires kinetic energy eV_a on reaching L_4 and will consequently be transmitted by the hemispheres along the mid-path. Since no energy is lost or gained by an electron in the barrier tunnelling process, the number of electrons passing through the hemispheres plotted against V_4 will correspond to the distribution in total energy of the electrons at the surface of the emitter.

3.5.3 It should be noted that since ΔV_H is strapped to V_4 through the resistors R_1 and R_2 , the resolution and pass kinetic energy, ϵ_a , of the hemispheres remains constant throughout the scan of V_4 . Reference to fig (18) shows how V_4 is varied in practice by inserting a ramp generator between the bottom of the lens resistor chain and earth. This means that slight lens defocusing occurs during scanning since the voltage ratios change. However, this effect is found to be insignificant as a detailed distribution is usually $\leq 5V$ base width.

3.6.0 Calibration

3.6.1 In order to calibrate the analyser it is necessary to identify the position of the Fermi level on a particular energy distribution. This is done using an atomically clean metallic emitter at a temperature of 300K. According to Young [50] the Fermi level on such a distribution occurs 73% up the high-energy slope. The value of V_4 corresponding to this

position is measured and this value always corresponds to the Fermi level of any emitter used in the instrument.

3.6.2 There are, however, some important conditions that must be fulfilled to ensure an unambiguous interpretation. Firstly, Braun et al [74] have suggested that there are problems in obtaining a 'calibration' standard tungsten tip which may be assumed reproducible from one laboratory to another. However, as will be shown in chapter 6, the Fermi level position on an energy distribution does not seem to be dependent on tip cleanliness and so even a tip which is not atomically clean may be used for calibration purposes (the determination of analyser resolution is, however, critically dependent on tip cleanliness). Secondly, the emitter and L_4 must be earthed at the same point to avoid any possibility of a voltage arising between the emitter and L_4 when $V_4 = 0$. Similarly, if there is any voltage drop down the emitter between the earthing point and the emitting point during the emission process (e.g. an "iR" drop) then this will result in a shift in the value of V_4 at which the Fermi level occurs. Finally, it cannot always be assumed that the Fermi level at the surface of the emitter is identical to that in the bulk. If it is not, then it is still only possible to identify the position of the Fermi level in the bulk of the emitter.

3.6.3 A calibration has been carried out on the analyser described here on two separate occasions using different tungsten emitters. It has resulted in a value of

$$V_4 = 6.23 \pm 0.03 \text{ volts}$$

for the position of the Fermi level.

3.7.0 Modifications to spectrometer

3.7.1 In order to use the spectrometer described in the previous sections for field emission studies on broad area electrodes, certain modifications were necessary to accommodate the different experimental conditions.

Principally, these were

(i) An addition to the input lens system to allow for the higher anode potentials frequently required with broad area electrodes.

and

(ii) A manipulator stage of far greater flexibility to permit the necessary alignment and movement for the broad area specimen when initially locating an emission site on the surface.

3.8.0 The interfacing input lens

3.8.1 When the field emission spectrometer is used for measurements on fabricated tip specimens, anode voltages are typically 1 - 3kV and the tip is usually mounted several centimeters from a fluorescent screen anode. Electrons from the tip impinge normally on the screen and so an approximately paraxial electron beam passes through the anode probe hole into the spectrometer. In contrast, to obtain emission from broad area specimens, typical anode voltages are in the range 5 - 10kV when using a specimen-anode gap of $\sim 0.5\text{mm}$. In addition, there are electron optical problems with this geometry since the high gap field penetrates through the anode aperture distorting the electron beam. Consequently, an interfacing lens had to be designed in order to use the spectrometer with broad area specimens. The main design criteria were:

(i) To reduce the energy of the electrons from $\sim 8\text{keV}$ when in the gap to the $\sim 2\text{keV}$ requirements of the spectrometer,

and

(ii) To re-focus the beam after passing through the anode aperture to give

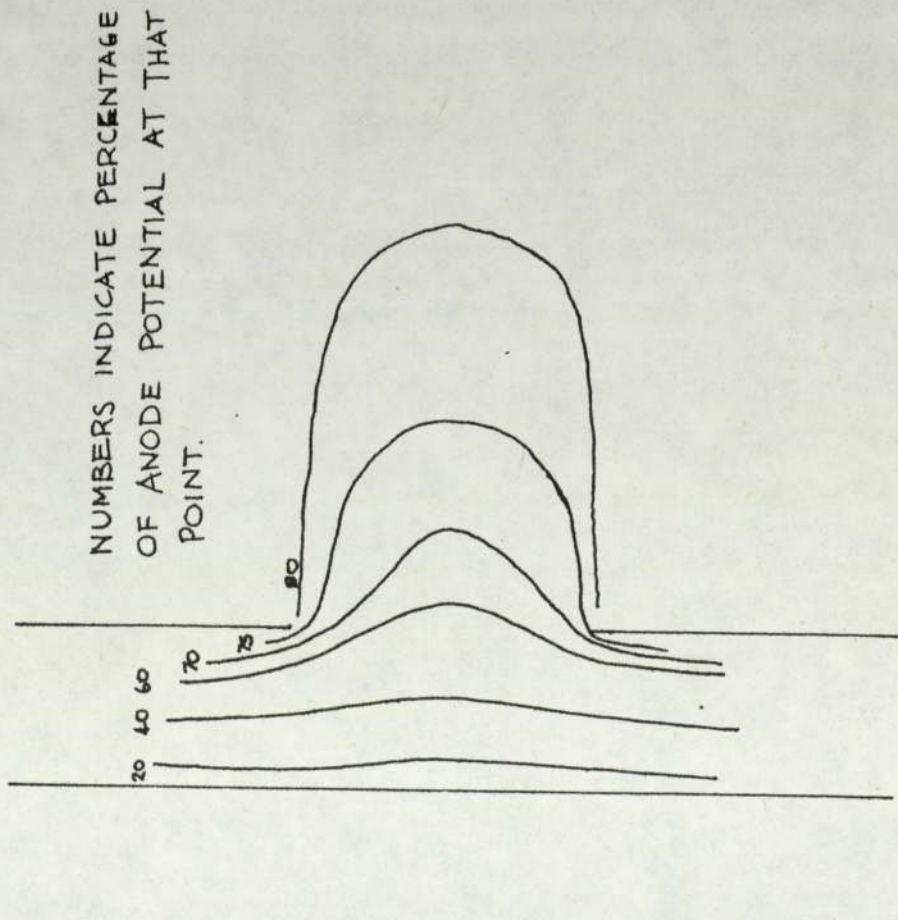
a paraxial input to the spectrometer.

Figure 13(a) shows a general section through the spectrometer; the dimension, d , is the normal distance when using the instrument with a fabricated tip emitter. However, the anode must be $\sim 0.5\text{mm}$ from a broad area specimen and so this determined the overall length of the lens.

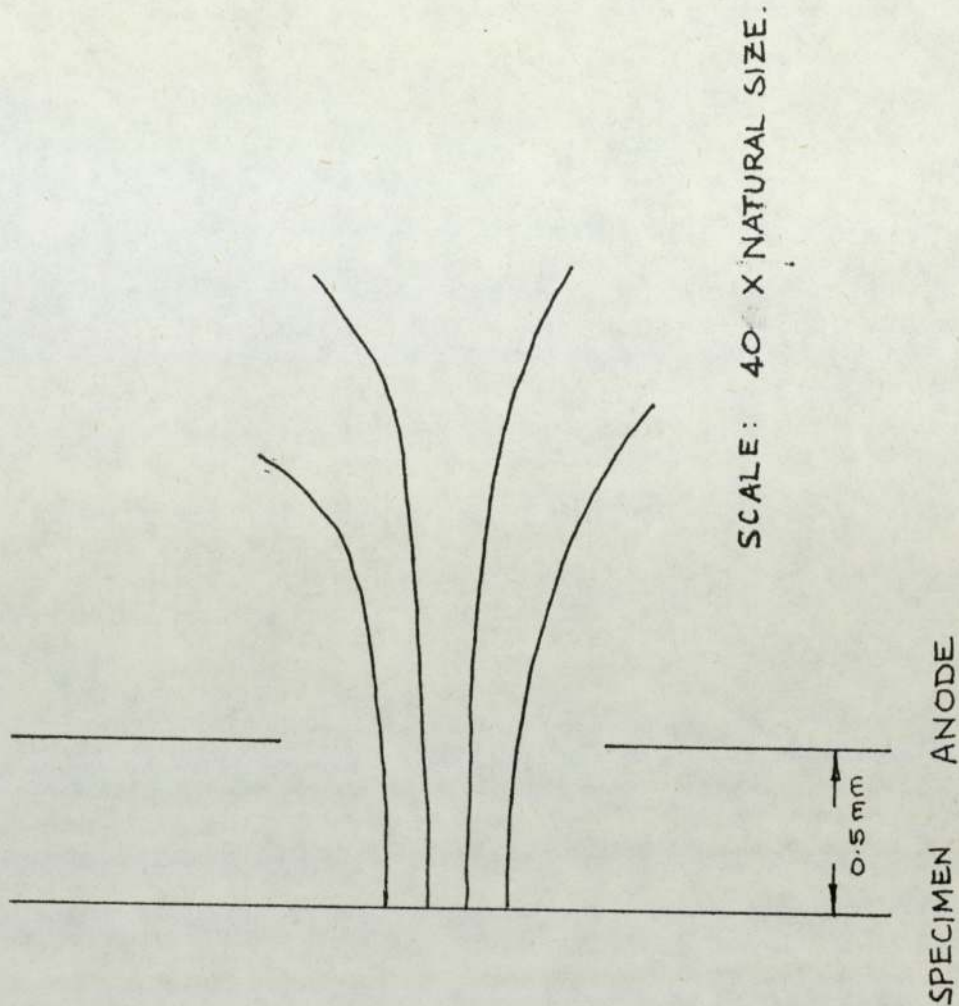
3.8.2 In the past, electron gun design has been based upon a thermionic tip as emission source, or, exceptionally, a field emitting source such as a tungsten tip [81]. The electron optics of focusing these sources cannot be applied in the present case, however, since the geometry, and hence the electric field characteristics, are quite different. Accordingly, it was decided to investigate the electric field properties of the inter-electrode gap using electrically conducting paper. This gives a first order approximation of the field and electron trajectory paths can subsequently be plotted.

3.8.3 Fig 22(a) shows the equipotential plot of the field between an anode and cathode using a typical gap size and anode aperture diameter (40 x natural size). Figure 22(b) shows the electron trajectories plotted from the equipotentials using the graphical Snell's law technique [82]. This shows that even electrons close to the centre of the aperture are deviated considerably and would result in an undetectably small current passing into the spectrometer. The broad area electrode requirement of a test gap size of $\sim 0.5\text{mm}$ automatically determined the position of the anode, which formed the first element of the lens. Also, the voltage on this element would typically be 5 - 8kV, and the voltage on the second lens was governed by the entrance requirements to the analyser (i.e. 1 - 2kV). Therefore, the only variable parameters in the lens design were the gap between the elements, the position of the gap and the diameter of the elements themselves.

Fig 22. (a) EQUIPOTENTIAL PLOT BETWEEN SPECIMEN AND ANODE SHOWING PENETRATION OF FIELD LINES.



(b) ELECTRON TRAJECTORIES CALCULATED FROM (a). THE DIVERGENCE MEANS THAT NO SIGNIFICANT PART OF THE BEAM WILL REACH THE FIRST LENS OF THE SPECTROMETER.



Consequently, a number of two element aperture and cylinder lenses were investigated using the graphical technique. The equipotential plot of the final design is shown in fig 23. Fig 24 shows the associated trajectory plot indicating that with this design electrons close to the axis will be undeviated presenting an approximately parallel input beam to the spectrometer. In addition, some adjustment of the focusing of the lens can be carried out by varying the voltage on L - this is directly connected to the first lens element of the spectrometer and so may be set within the range $\sim 1 - 2\text{kV}$.

3.8.4 Fig 25 shows a section through the final design of the lens which bolts on to the first input lens of the spectrometer in place of the fluorescent screen anode. Also shown in fig 25 are the details of the main elements of the lens. The metal components were constructed of stainless steel and, where possible polished to obtain a smooth profile. The gap between the anode, A, and the second element, L, is maintained by a machined ceramic insulator. The lens is illustrated in fig 26 and fig 27 shows the lens fitted onto the spectrometer. In early tests, the aperture at the rear of the lens was $\sim 10\text{mm}$ to provide maximum current input into the analyser. Subsequently, (for all the results reported here) this was reduced to 1mm to closely simulate the conditions when operating the spectrometer with the fluorescent screen anode. After assembling the components of the lens, and prior to fitting onto the spectrometer, alignment of front and rear apertures was checked using a laser beam.

3.8.5 Tests carried out with the lens showed that the focusing condition did not always correspond to the design voltage ratio; it is thought that the explanation for this effect lies in the presence of a more divergent input beam than that predicted from the equipotential plot due to micro-

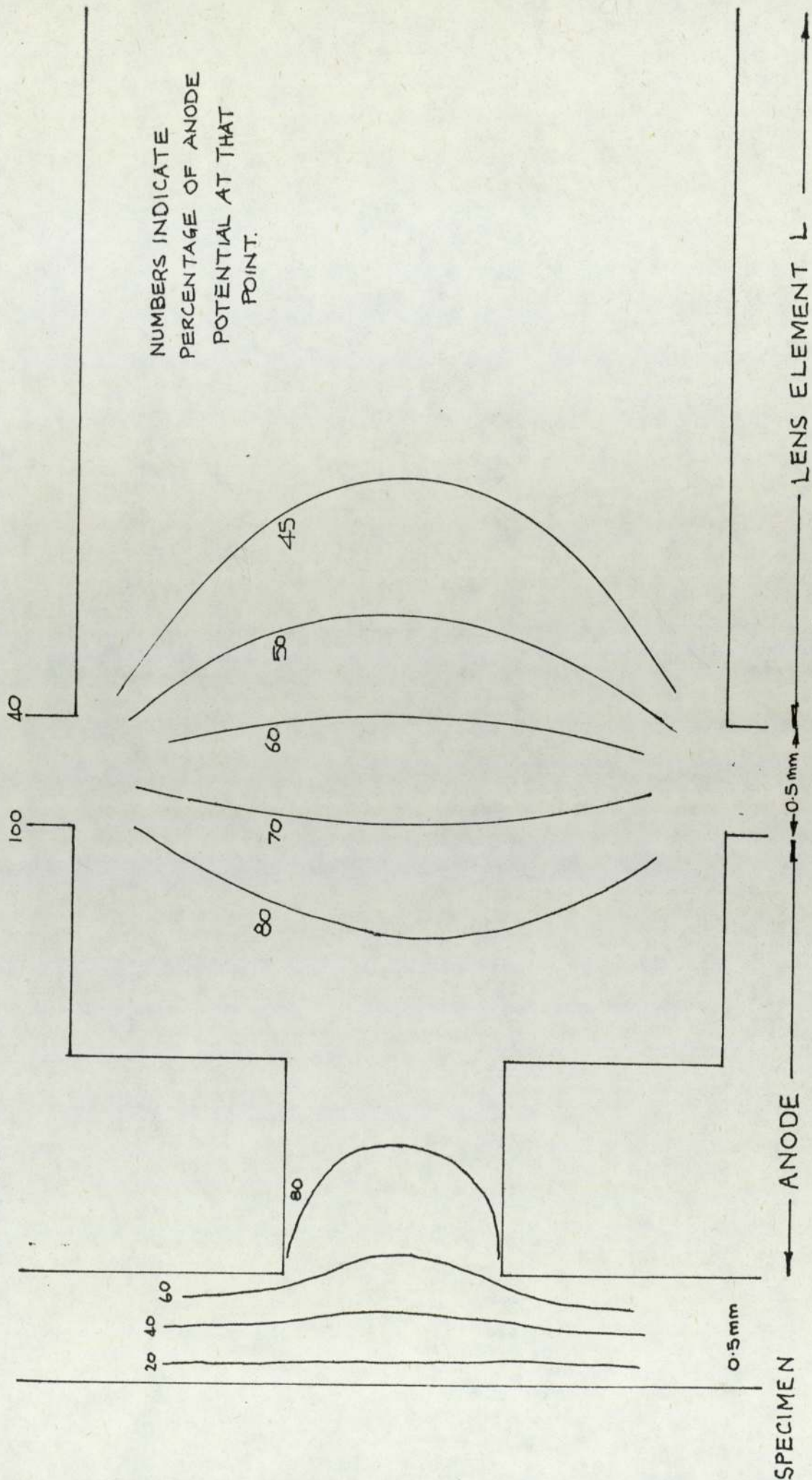


Fig 23. EQUIPOTENTIAL PLOT OF INTERFACIAL LENS.

SCALE: 40 X NATURAL SIZE
ELEMENT L IS HELD AT A
POTENTIAL 40% OF THAT ON THE
ANODE.

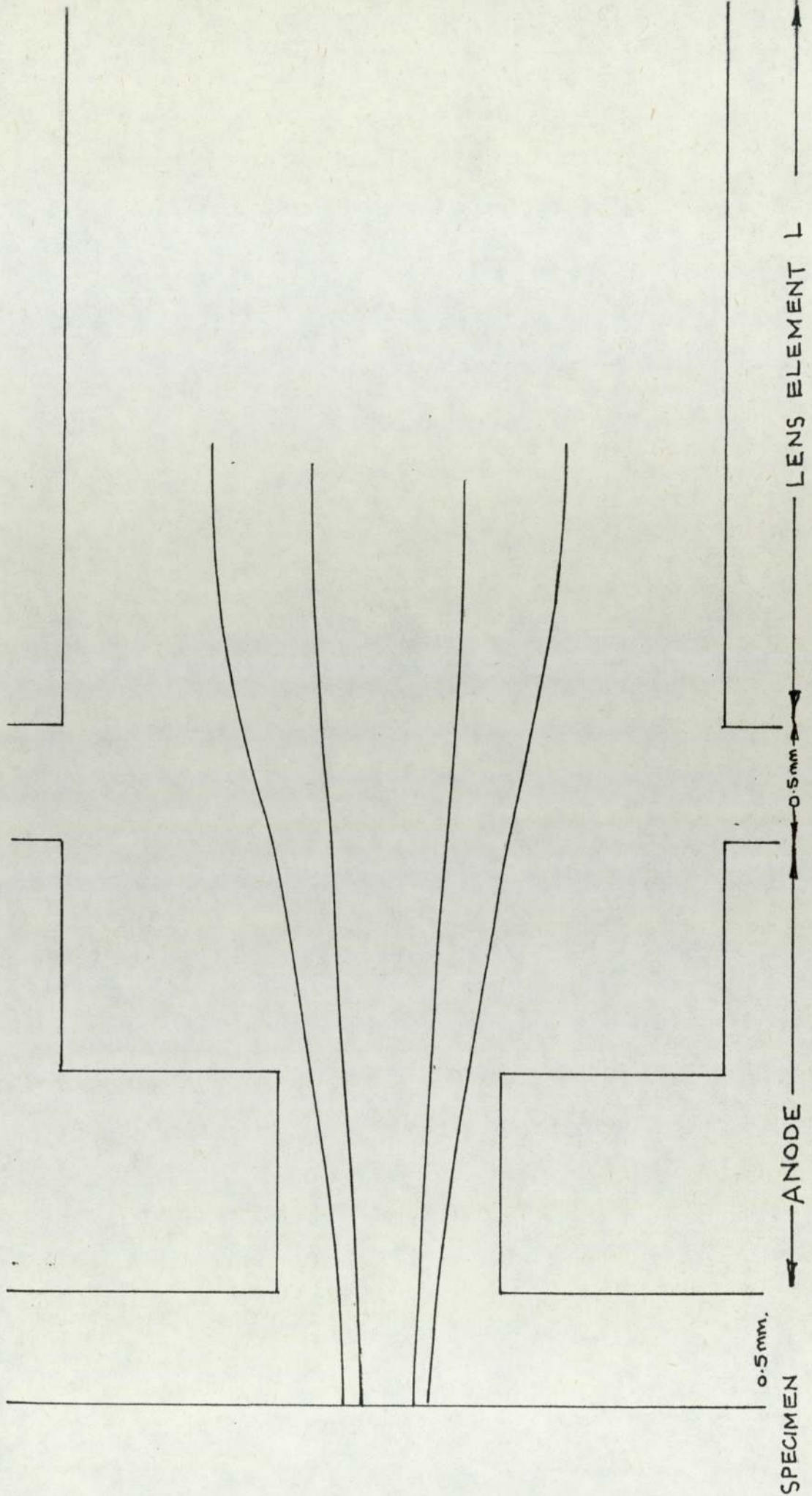
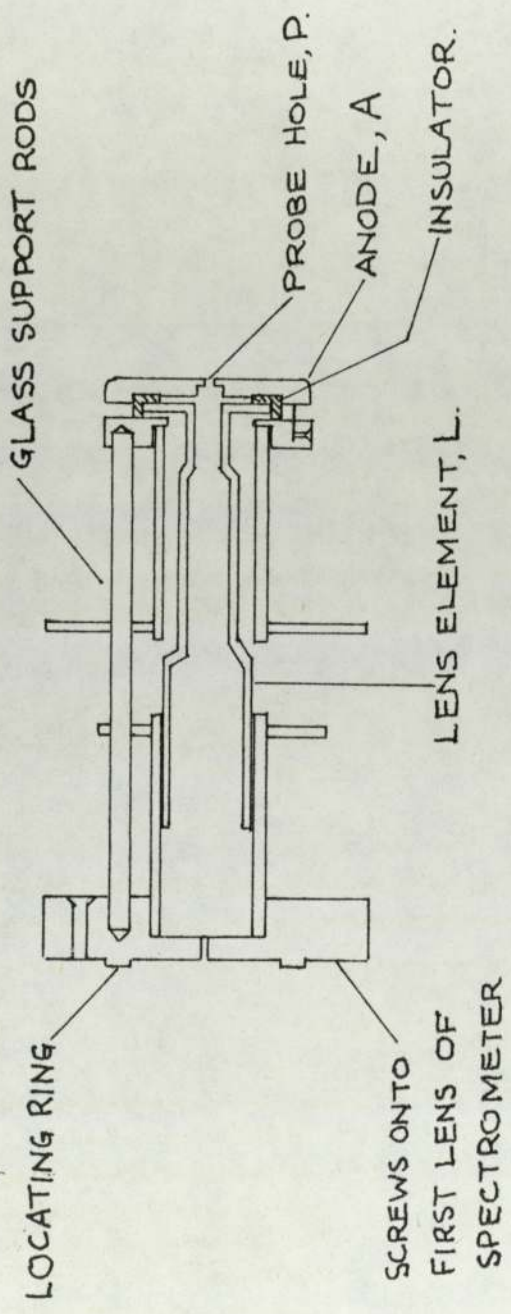


FIG 24. ELECTRON TRAJECTORY PLOT OF THE INTERFACING LENS. SCALE: 40 X



SECTION THROUGH INTERFACING LENS.

FULL SCALE.

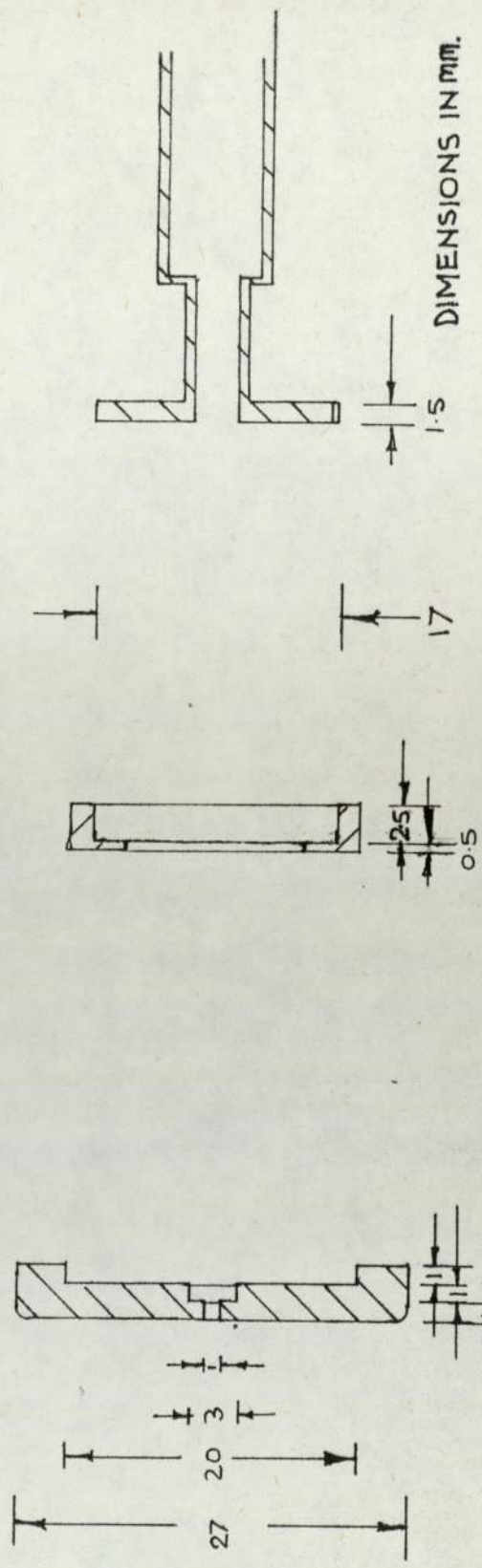


FIG 25. THE INTERFACING LENS.

LENS ELEMENT, L
TWICE FULL SIZE.

Fig 26

A close-up view of the interfacing lens showing the front anode, insulator and the rest of the assembly. The lens element, L, can be seen projecting from the assembly.

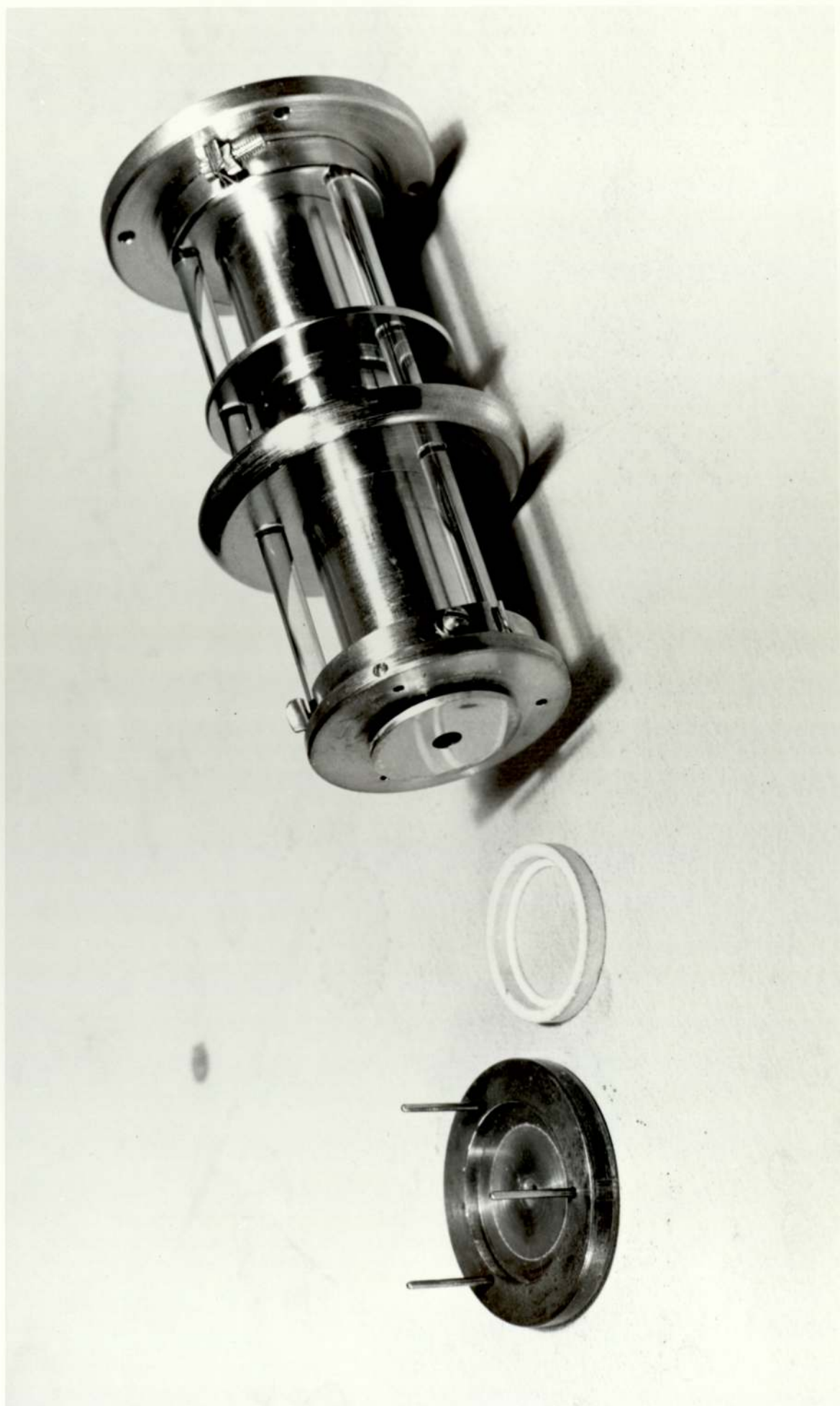
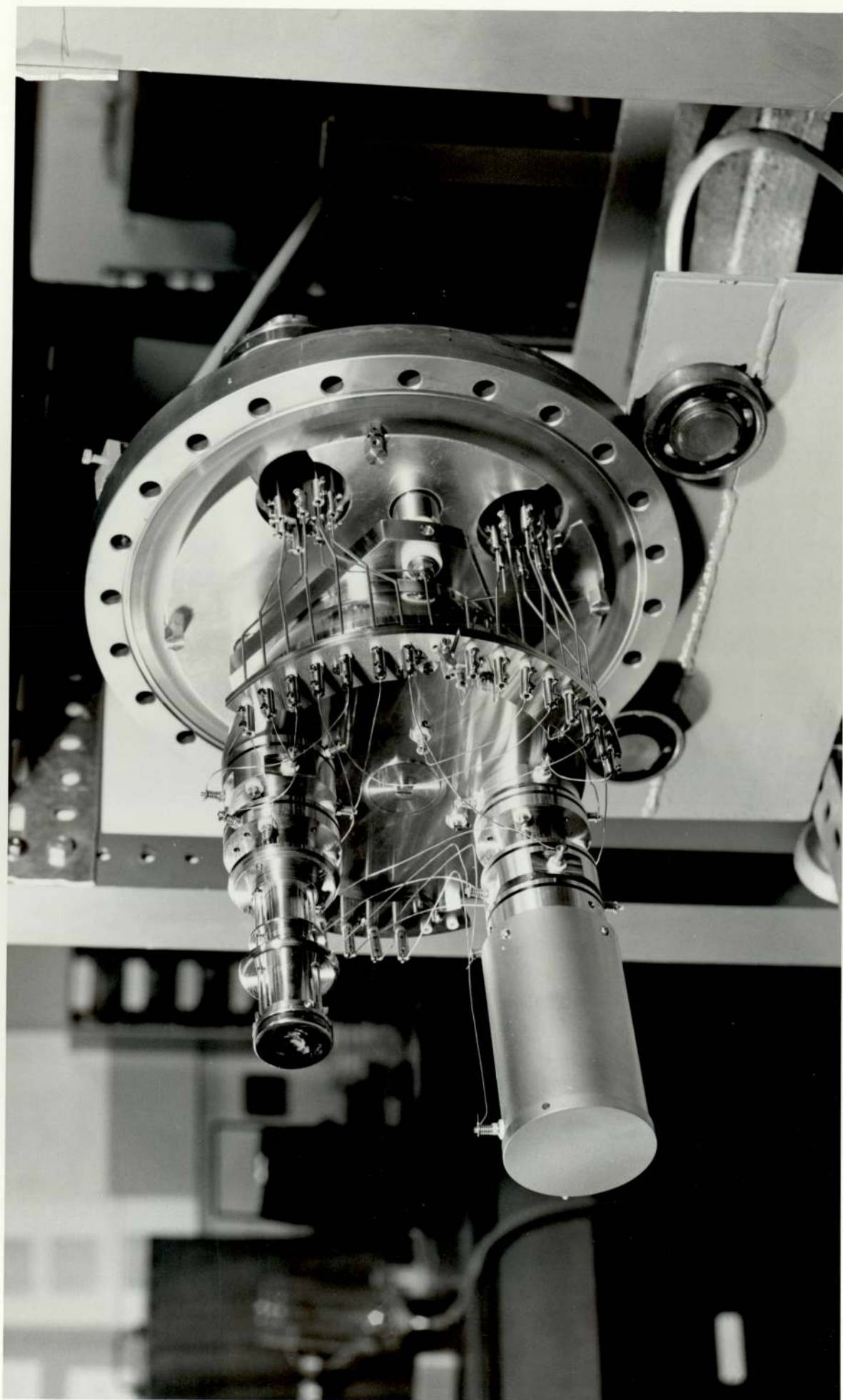


Fig 27

The interfacing lens attached to the spectrometer.
The mu-metal shield surrounding the hemisphere
elements has been removed for this photograph, to
show the various components in greater detail.



scopic field distortions in the region of the emitting site. However, focusing was always found to be critical, a variation of $\pm 5\%$ in the voltage at (L) being sufficient to completely de-focus the lens.

3.8.6 No separate experiments were carried out to determine the aberrations of the lens, but since it was successfully focusing the beam into the 1mm central rear aperture any such effects were apparently not serious. This is supported by measurements which showed that an electron current of only $\sim 3 \times 10^{-10}$ A passed into the analyser for an input current of $\sim 10^{-7}$ A, confirming that only paraxial electrons were collected for which aberration effects would be minimal.

3.9.0 The Manipulator Assembly

3.9.1 When using field emitting tips with the spectrometer, an emission pattern is normally obtained on the fluorescent screen anode and the part of the pattern to be analysed is centred over the probe hole. Usually, slight rotation or tilt of the specimen and re-centering of the area of interest over the probe hole is sufficient to ensure that the electrons enter the spectrometer in a paraxial beam. Alternatively, beam positioning may be carried out using deflector plates in front of the emitting tip. Such a technique is not feasible when using broad area electrodes where there is a very small inter-electrode gap. Consequently, a more versatile manipulator had to be designed for the spectrometer which would systematically scan the surface of a specimen in front of the anode probe hole.

3.9.2 One of the main criteria in the design of the manipulator was the size of specimen to be used. One important series of specimens to be examined were the switch contacts used in the Central Electricity Generating Board vacuum circuit breakers (discussed in chapter 5). These

contacts are $\sim 14\text{mm}$ in diameter and 4mm thick; they also have a 4mm diameter central hole. It was felt, therefore, that the manipulator assembly should be designed to accommodate this size of specimen and that other specimen materials could be machined to these dimensions.

Therefore, the design criteria were

- (i) Horizontal and vertical movement of at least 14mm in each direction
- (ii) Manipulation to allow alignment of the specimen surface parallel to the anode
- (iii) Manipulation to ensure a constant inter-electrode gap during scanning
- (iv) Manipulation to vary the inter-electrode gap

It was felt that the most logical arrangement was to have the complete manipulator assembly mounted outside the spectrometer vacuum chamber with a single central rod passing through a U.H.V. bellows with a suitable specimen holder assembly mounted at the lower end.

3.9.3 The general layout of the manipulator and bellows unit when mounted on the spectrometer vacuum chamber is shown in fig 13(a). The xyz manipulator consists of "Micro-controlle" type MR translation stages, modified as described in the following sections, having 25mm of travel in each direction. The bellows is a Vacuum Generators UMDI unit which can accommodate the required amount of translational motion. The control rod fitted to the manipulator is a Vacuum Generators RDI unit which can be rotated through 360° . The rod passes through the bellows unit and the specimen holder is attached to its lower end. The alignment of the specimen is carried out by adjusting three variables of the manipulator system,

- (i) the rotation of the RDI rod
- (ii) the angle between the (xy) and z manipulators using the adjustable bracket (fig 13a)

(iii) the angle of scan, by rotating the whole of the manipulator assembly (fig 28).

3.9.4 Correct alignment involves obtaining a parallel interelectrode gap, measuring the gap and ensuring that this remains constant during scanning. The alignment of the gap is measured using an auto-collimating telescope. Initially this is adjusted to obtain normal incidence/reflection from the highly polished anode face of the interfacing lens (fig 29). The rear of the specimen holder is also highly polished and forms the second reference face for the alignment. When a specimen is mounted in the holder it is known that the front face of the specimen is accurately parallel to the rear of the holder. The alignment is carried out as shown in fig 29. The specimen holder assembly is moved into the beam of the telescope and the assembly is then adjusted in the vertical and horizontal planes until normal reflection is obtained from the rear face of the holder. Vertical adjustment (see fig 29(b)) is achieved using the variable angle bracket on the manipulator assembly (illustrated in fig 30). Horizontal adjustment is by rotation of the EDI rod.

3.9.5 The interelectrode gap is determined by measuring the capacitance between the anode and specimen using an E.C.D. 100 digital capacitance meter. This instrument measures the time constant for charging up the unknown capacitor when in parallel with a known resistor and gives a reading directly in capacitance to a limit of 0.1pF with an accuracy of 1%. As this is a d.c. method of measurement it eliminates problems of stray reactance encountered when using an a.c. bridge technique. Figure (31) shows a graph of capacitance versus the Z co-ordinate which establishes the position of zero gap. This method has the advantage that no contact is made between anode and cathode, eliminating the

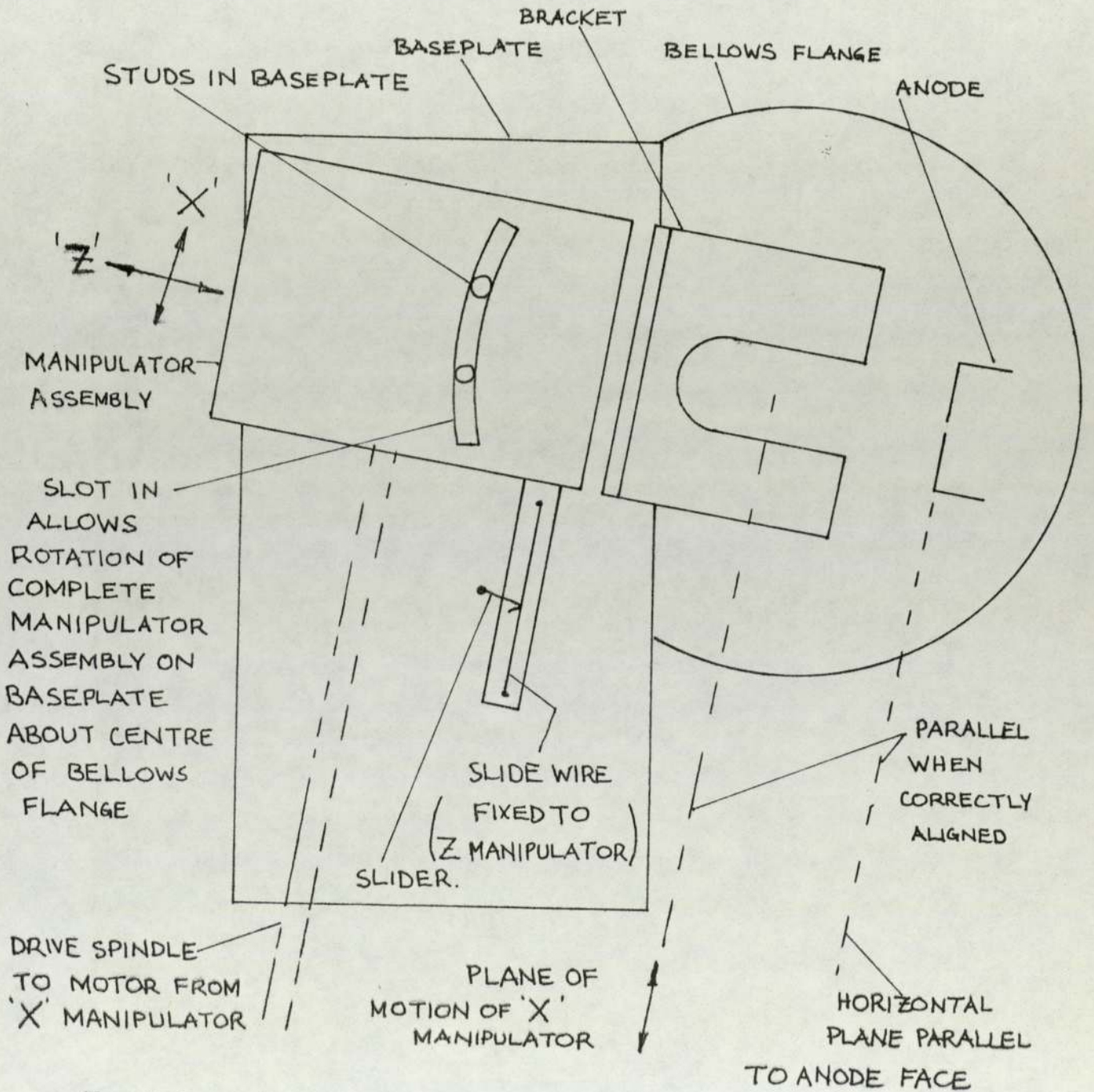
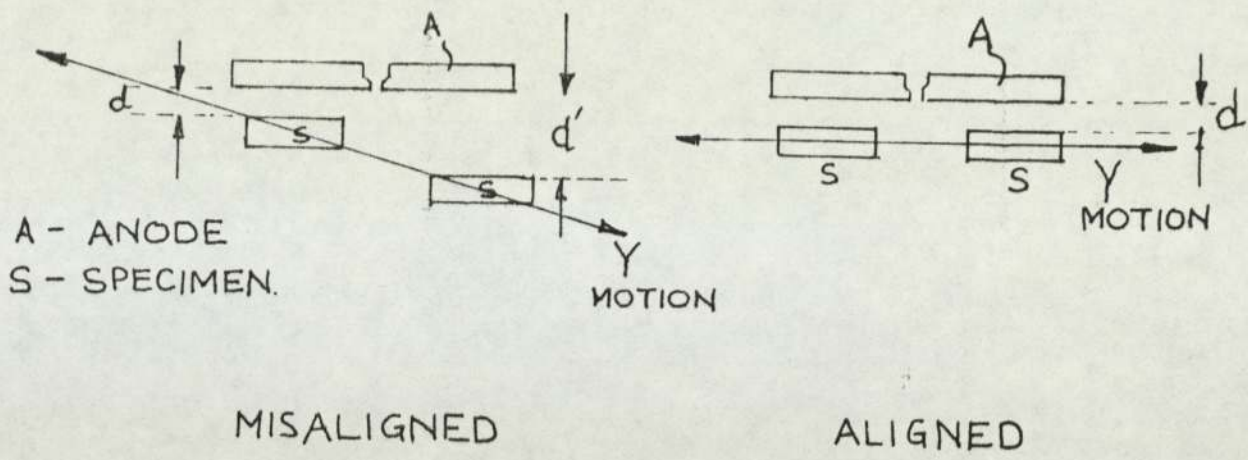


Fig 28 . ROTATION OF COMPLETE MANIPULATOR ASSEMBLY ON BASEPLATE.



CHANGE IN DIRECTION OF Y-MOTION ACHIEVED BY ROTATION OF COMPLETE MANIPULATOR ASSEMBLY ON BASEPLATE.

(b) VERTICAL PLANE: ALIGNMENT OF SCAN DIRECTION AND SPECIMEN SURFACE.

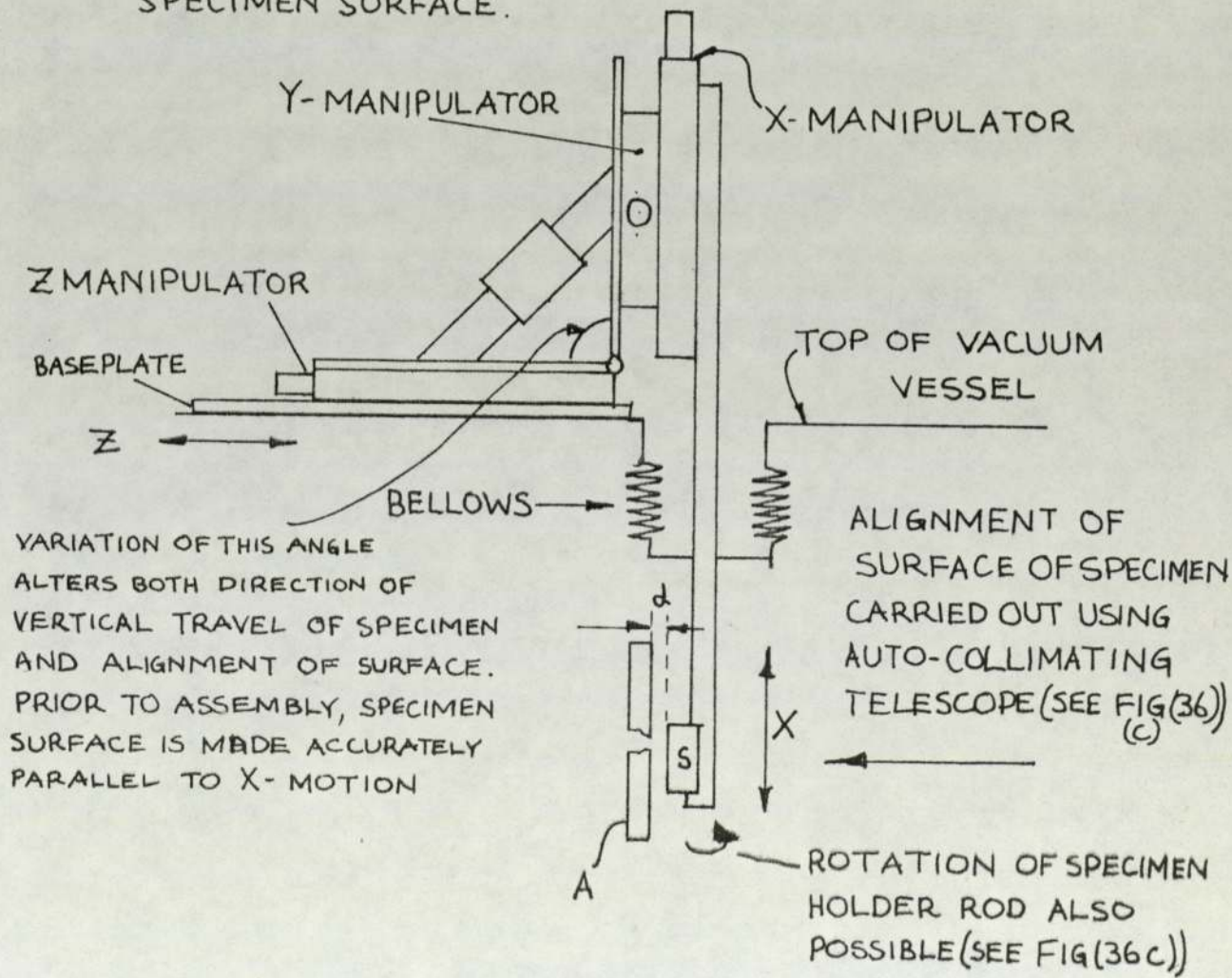
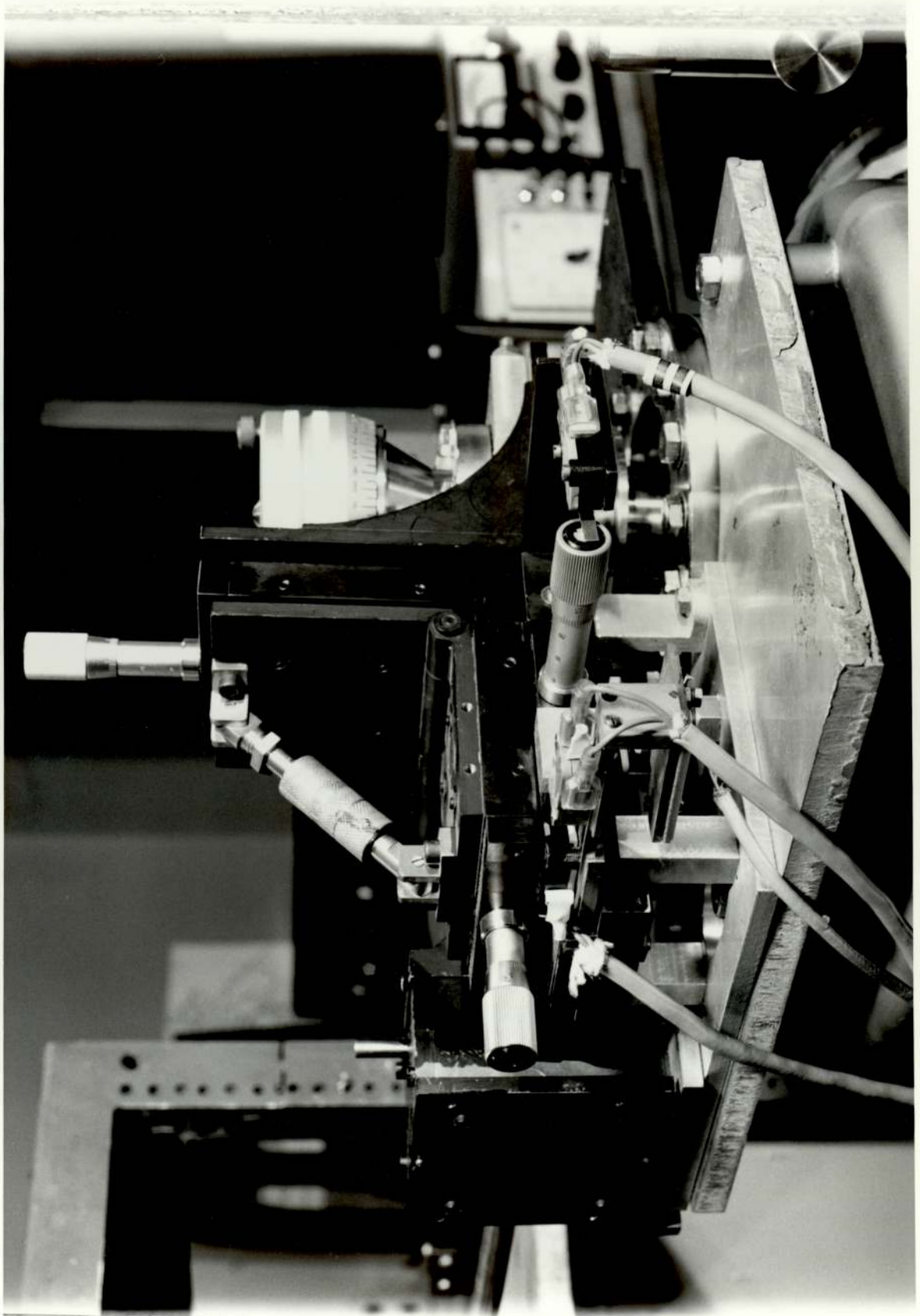


FIG 29 (a) AND (b). ALIGNMENT PROCEDURES.

Fig 30

The manipulator assembly mounted on the spectrometer



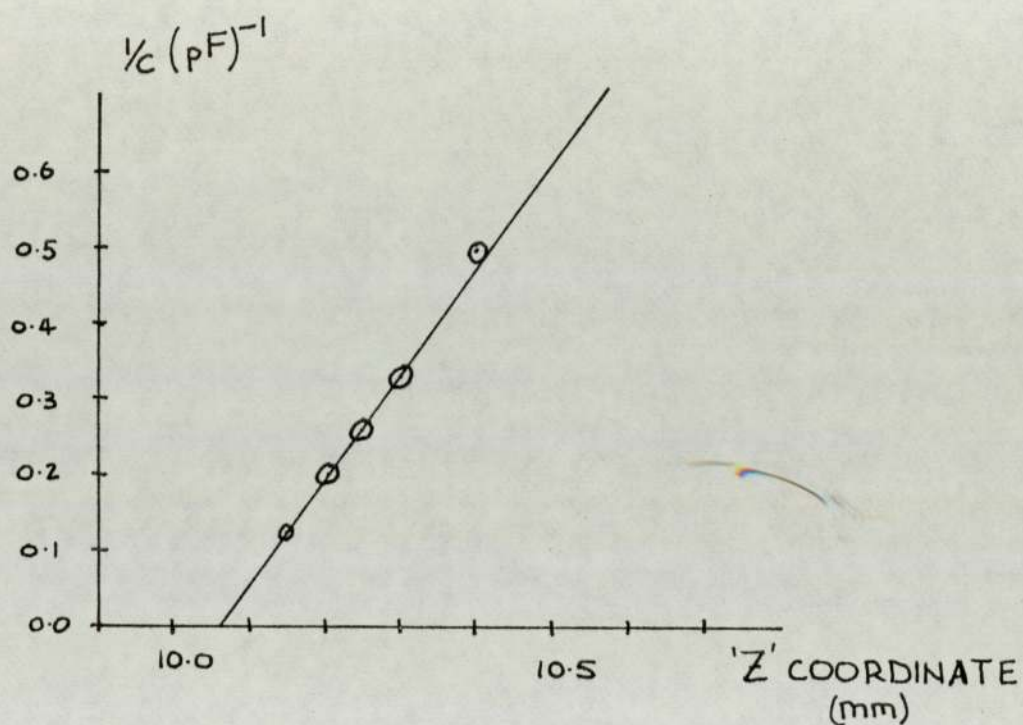


FIG 31. VARIATION IN INTER-ELECTRODE CAPACITANCE WITH GAP. IN THIS CASE, ZERO GAP CORRESPONDS TO $Z=10.06$ (mm).

possibility of surface micro-damage.

3.9.6 The third alignment procedure is to ensure a constant gap during scanning. This is achieved automatically in the vertical plane when aligning the specimen, as shown in fig 29(b). The correct setting for the horizontal plane is achieved by rotating the whole manipulator assembly about the RDI rod, as shown in fig 28.

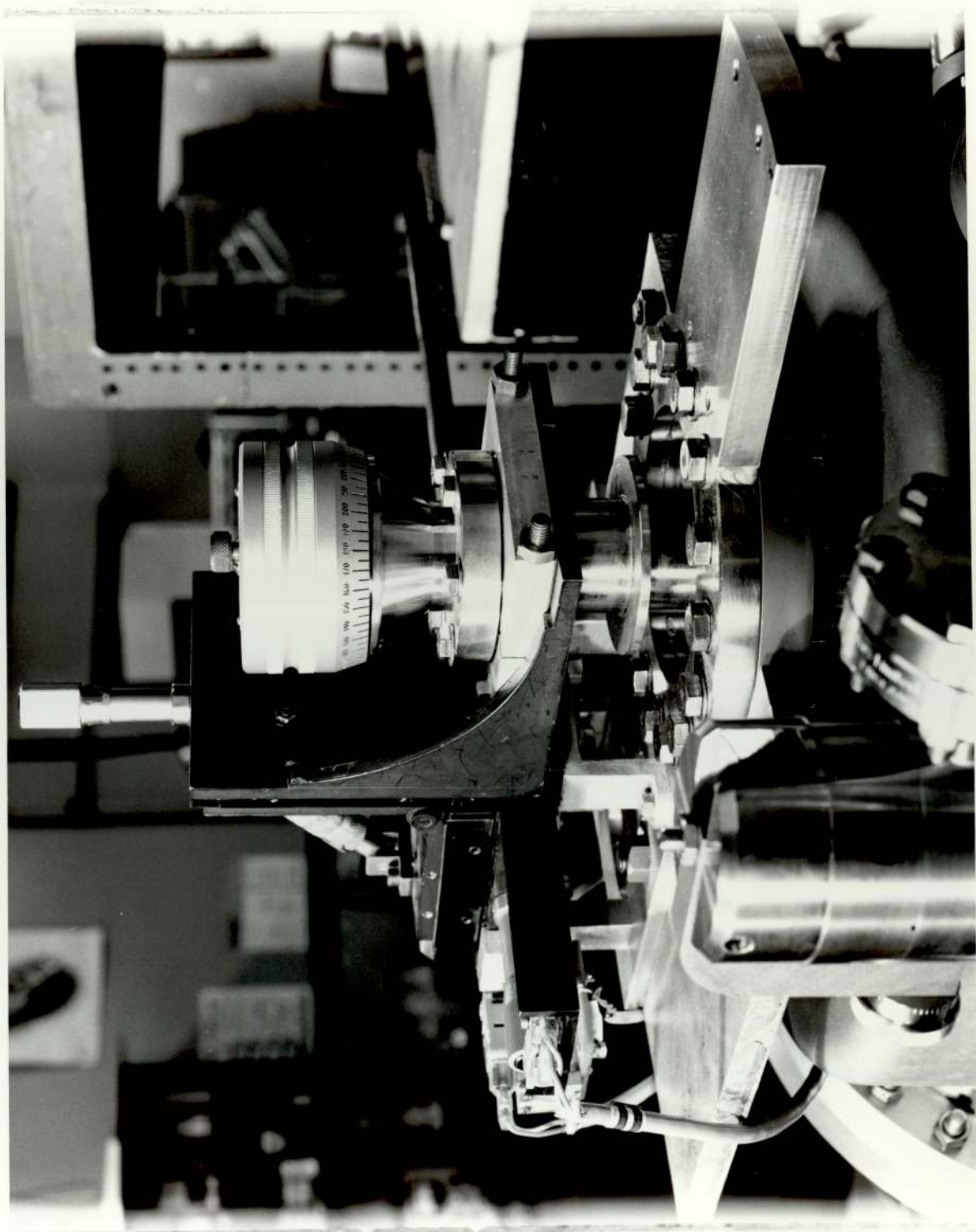
A flange on the bellows unit (which can be seen on the illustration of fig 32) supports the bellows assembly while the manipulator is being rotated. This is also used to support the bellows when the manipulator assembly is removed during system bakeout.

3.9.7 To check the scan alignment, a voltage is applied between anode and cathode until a steady pre-breakdown current of $\sim 10^{-6}$ A is obtained. If the scan alignment is correct this current will remain steady throughout the x scan. Once this position has been found and marked, it can usually be readily re-located whenever the manipulator unit is removed and replaced, and rarely needs re-adjustment. If some adjustment is required, however, then subsequent re-adjustment of specimen alignment and gap spacing may also be necessary.

3.9.8 A diagram of the specimen holder attached to the end of the RDI rod is shown in fig 33. The holder is insulated from the rod and a clamp ring holds the specimen. The holder also supports an outgassing filament made from 100 μ m diameter tungsten wire. This has the dual purpose of outgassing both the specimen and the anode. By siting the filament behind the specimen, outgassing can be carried out without bombarding the surface, thus avoiding possible surface microdamage. During outgassing, the specimen surface is normally turned through 180° to face away from the anode to minimise cross contamination between

Fig 32

The front of the manipulator assembly showing the bracket supporting the RDI rod and the top of the bellows unit.



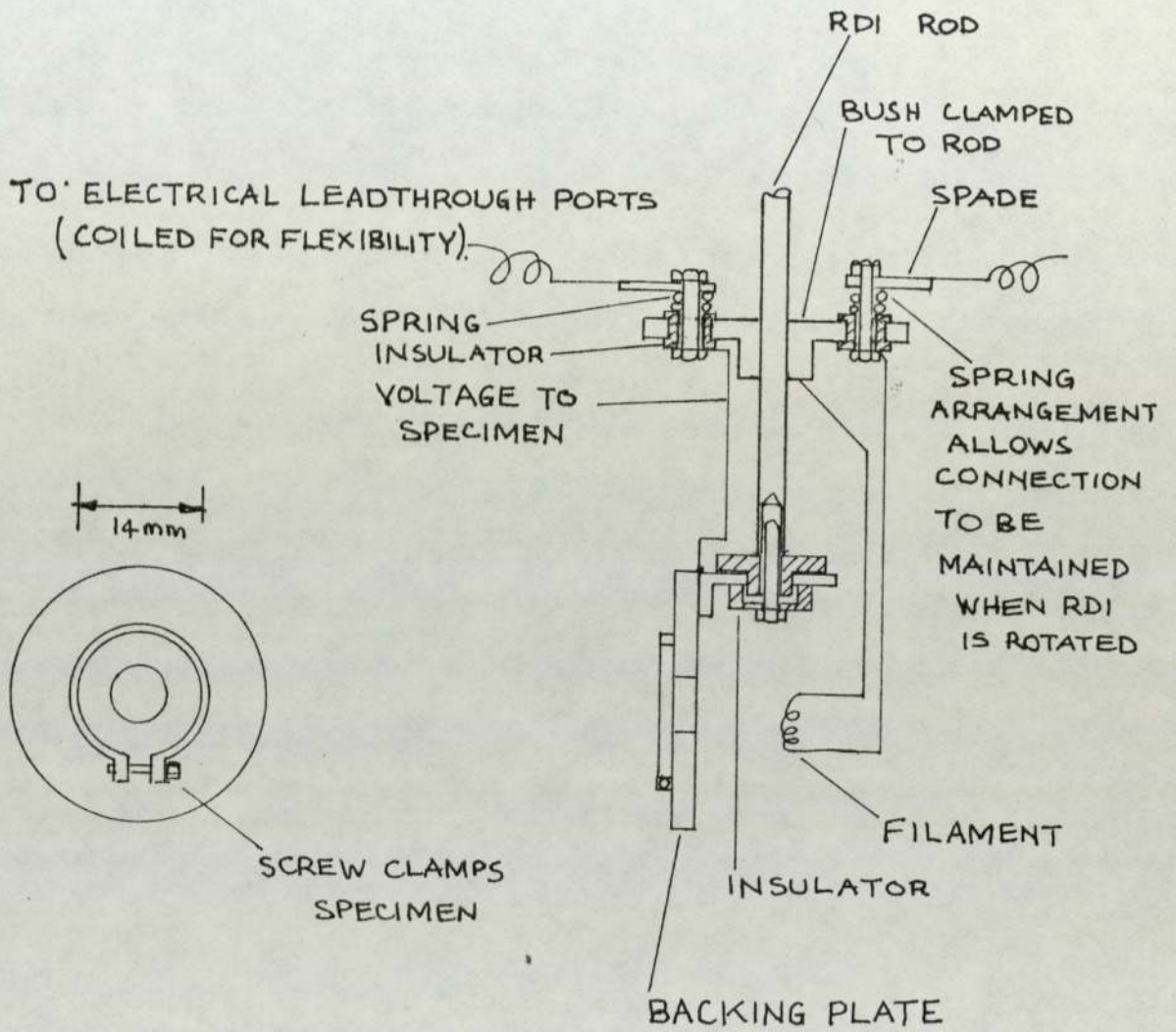


FIG 33. THE SPECIMEN HOLDER

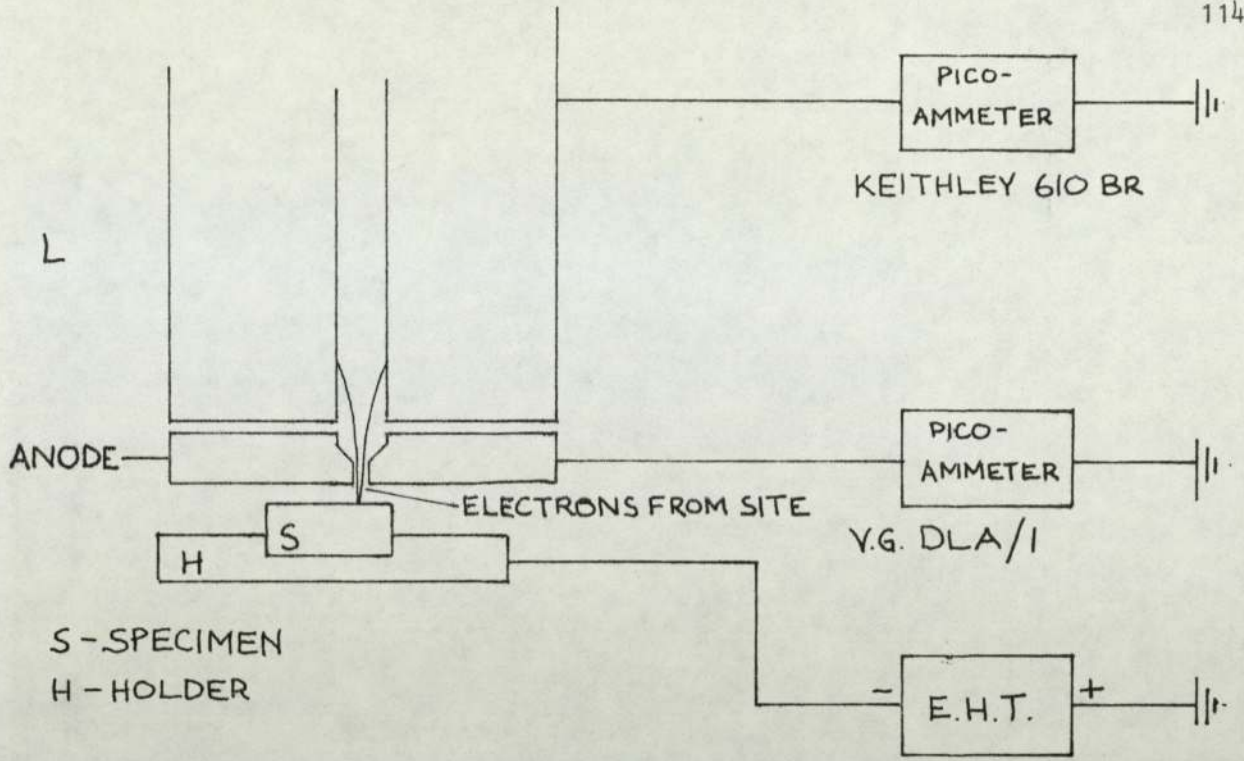
specimen and anode. Electrical connections are introduced through two separate electrical leadthrough ports using Vacuum Generators EFT1A components which are insulated for voltages up to 15kV. Special contacts are necessary at the top of the holder to allow rotation of the specimen (for example, during outgassing) without undue strain on the connecting wires. This is achieved by a coiled spring underneath a spade terminal which allows the terminal to rotate whilst still maintaining good electrical contact. Special insulators isolate the terminals from the supporting assembly. A central hole in the holder backing plate provides three functions; it minimises the mass of the assembly allowing higher outgassing temperatures to be reached, it allows more direct heating of the specimen, and finally it enables site co-ordinates to be specified when using the various electrodes as described in 3.10.1. As mentioned earlier, the rear face of the backing plate is highly polished in order to carry out the specimen alignment procedure. An illustration of the holder containing a copper specimen is shown in fig 34.

3.9.9 The scanning technique adopted was to use a raster pattern with horizontal scans and 0.5mm vertical steps. With the 1.0mm diameter anode probe hole it was felt that this would adequately cover the whole of the specimen surface area and enable any sites present to be detected. To facilitate scanning, the x motion of the manipulator was motorised. The main criterion when designing this system was to ensure that the scanning speed was sufficiently slow so that any emission site passing the probe hole would be detected. Electron emission from a site can be detected as shown in fig 35, by defocusing the input lens and measuring the current arriving at the second lens element, L, with a picoammeter. The response time for the Keithley 610 BR is ~ 0.5 second for a current

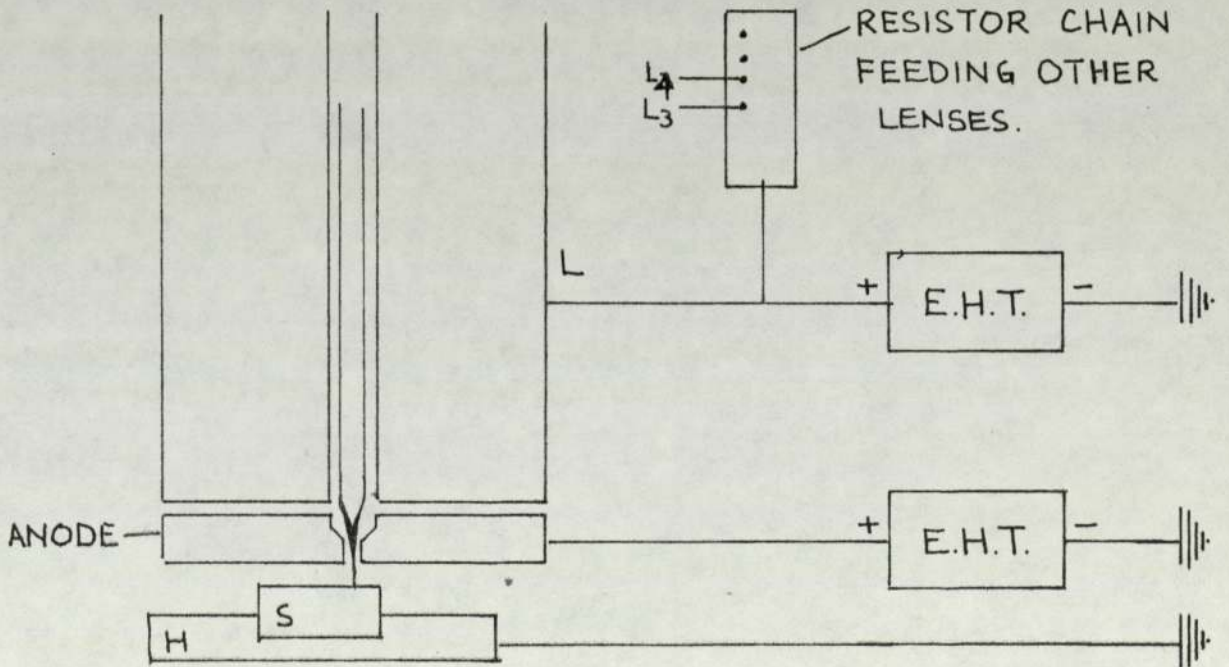
Fig 34

The lower part of the bellows assembly showing the end of the RDI rod to which is attached the specimen holder and a copper specimen.





(a) DETECTING A SITE AND MEASURING THE $i-V$ CHARACTERISTIC.



(b) OBTAINING THE ENERGY DISTRIBUTION OF A SITE BY APPLYING A VOLTAGE TO L AND SO FOCUSING THE BEAM.

FIG 35. ELECTRICAL CONNECTIONS TO DETECT AND FOCUS A SITE.

of 10^{-10} A reducing to 0.003 second for a current of 10^{-6} A. With a scan of 16mm and a probe hole diameter of 1.0mm, a scan time of about 8 seconds would be required to detect 10^{-10} A. In practice, it is desirable to provide for scanning at considerably slower speeds to allow for centralisation of a site with respect to the probe hole prior to final manual adjustment. Consequently, a variable speed d.c. motor was chosen, a ParValux SDI SS with 3168 : 1 gearbox and thyristor d.c. controller. This gave a maximum rotational speed of 1 rev/min. which could be reduced with the controller to $\sim 1/25$ rev/min. The available torque was adequate at 35lb ins.

3.9.10 A converter was designed to translate the rotational motion of the motor to the required translational motion of the x manipulator. The principles of the final design are shown in fig 36 and the unit is illustrated in fig 37. It consists of two gimbal bearings, one mounted inside the other. The pivots of the outside gimbal are vertical and those of the inside are horizontal. The inside gimbal ring is a roller bearing and the centre of this bearing is rigidly fixed to a central spindle at an angle of $\sim 30^\circ$. As the spindle rotates, the transverse motion of the inner bearing is transmitted to the outer bearing which carries out a reciprocating motion in the horizontal plane. The x manipulator is coupled to the outer bearing with a connecting rod and rotation of the spindle in the bearing unit results in a forward and backward motion of the x manipulator. This system has the advantage of providing direct drive in both directions and does not depend on return springs. The return springs of the x manipulator were therefore removed and in normal scanning the micrometer screw of this manipulator is backed right off. It can, however, be used for providing an x-co-ordinate of the site and also for micro-manipulation in the x direction for precise

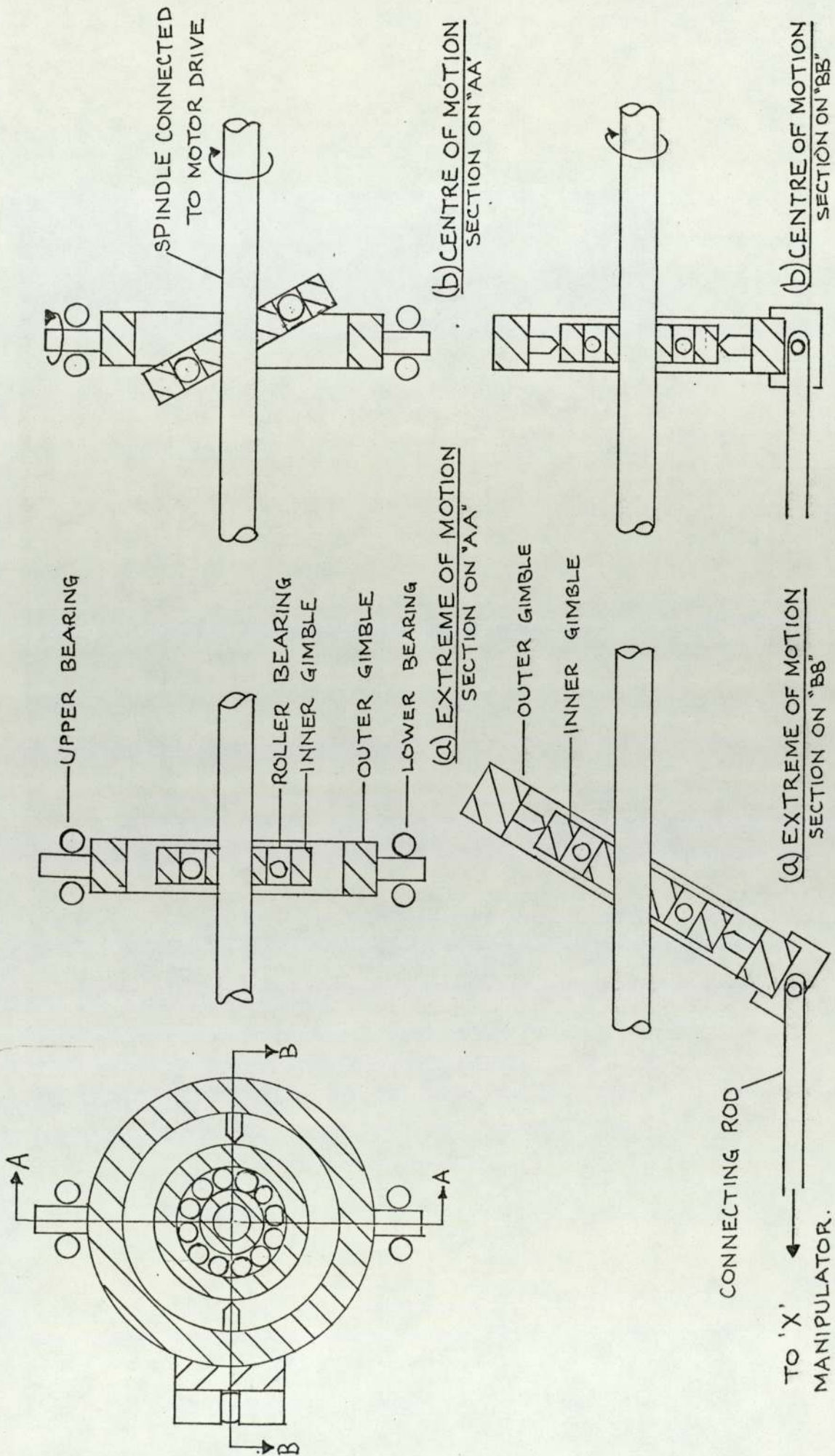
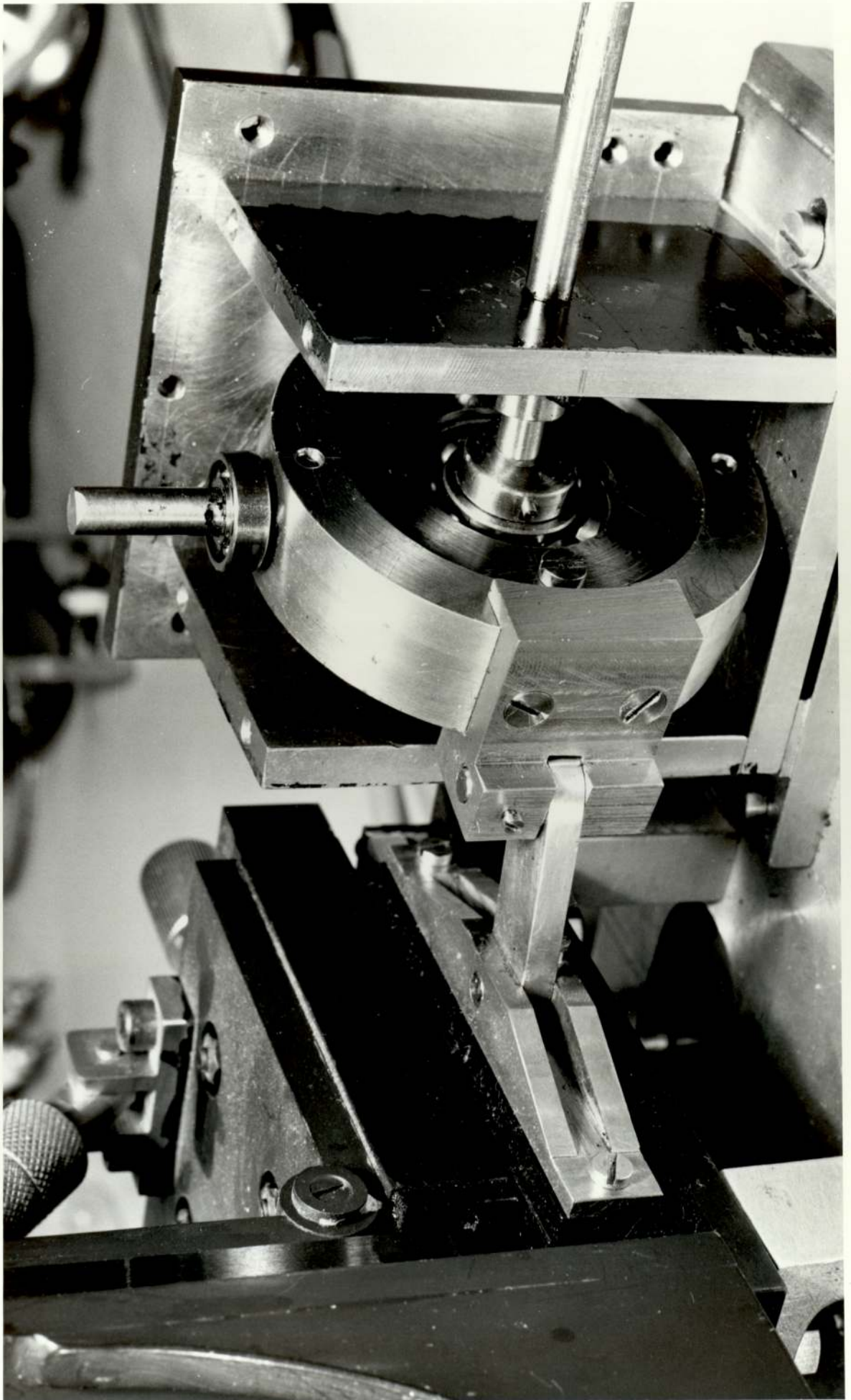


FIG 36. SCHEMATIC DIAGRAM SHOWING PRINCIPLES OF OPERATION OF GIMBLE BEARING CONVERTER UNIT.

Fig 37

A close-up of the gimble bearing unit for converting the rotary motion of the motor drive to reciprocating motion for the x-scan. The cover has been removed for this photograph to show the detail.



site location. The motor unit was fitted onto a trolley shelf which was rigidly affixed to the framework of the spectrometer equipment. The motor uses a solid coupling to the converter unit and this is illustrated in fig 38. Microswitches are fitted to the x manipulator to switch off the motor drive at the end of each scan, fig 39. A microswitch is also incorporated to prevent actuation of the scanning motor when the x manipulator micrometer screw is not in the fully backed off position, fig 39.

3.10.0 Obtaining the energy distribution of an emission site

3.10.1 Two classes of specimen were used in these investigations. The "planar" electrodes, which had a freshly machined or diamond polished surface finish with a smoothly profiled edge, typically representing the type of electrode encountered in "passive" applications. The other electrodes were switch contacts which had a heavily arced irregularly shaped surface. The latter type are discussed fully in chapter 5. The planar electrodes are prepared for examination by Spirit cleaning in an ultrasonic bath. After assembly in the spectrometer, the system is evacuated and baked for 18 hours at $\sim 230^{\circ}\text{C}$. Subsequent cooling and filling of the liquid nitrogen cold trap gave a chamber pressure of $\sim 2 \times 10^{-10}$ torr. Prior to taking measurements, the specimen and anode are outgassed (using the filament on the specimen holder) with 1keV electrons at 50mA current. The duration of this treatment is usually 2 - 3 minutes which is sufficient to bring the specimen to dull red heat - a temperature of $\sim 700^{\circ}\text{C}$ - and to raise the pressure to $\sim 8 \times 10^{-8}$ torr. By bombarding the rear of the specimen with electrons, there is no direct surface damage whilst the temperatures reached were sufficient to cause considerable thermal activation of the surface atoms. After the specimen and anode have been outgassed and then correctly aligned,

Fig 38

Showing the motor, reduction drive, and solid coupling rod to the manipulator assembly.

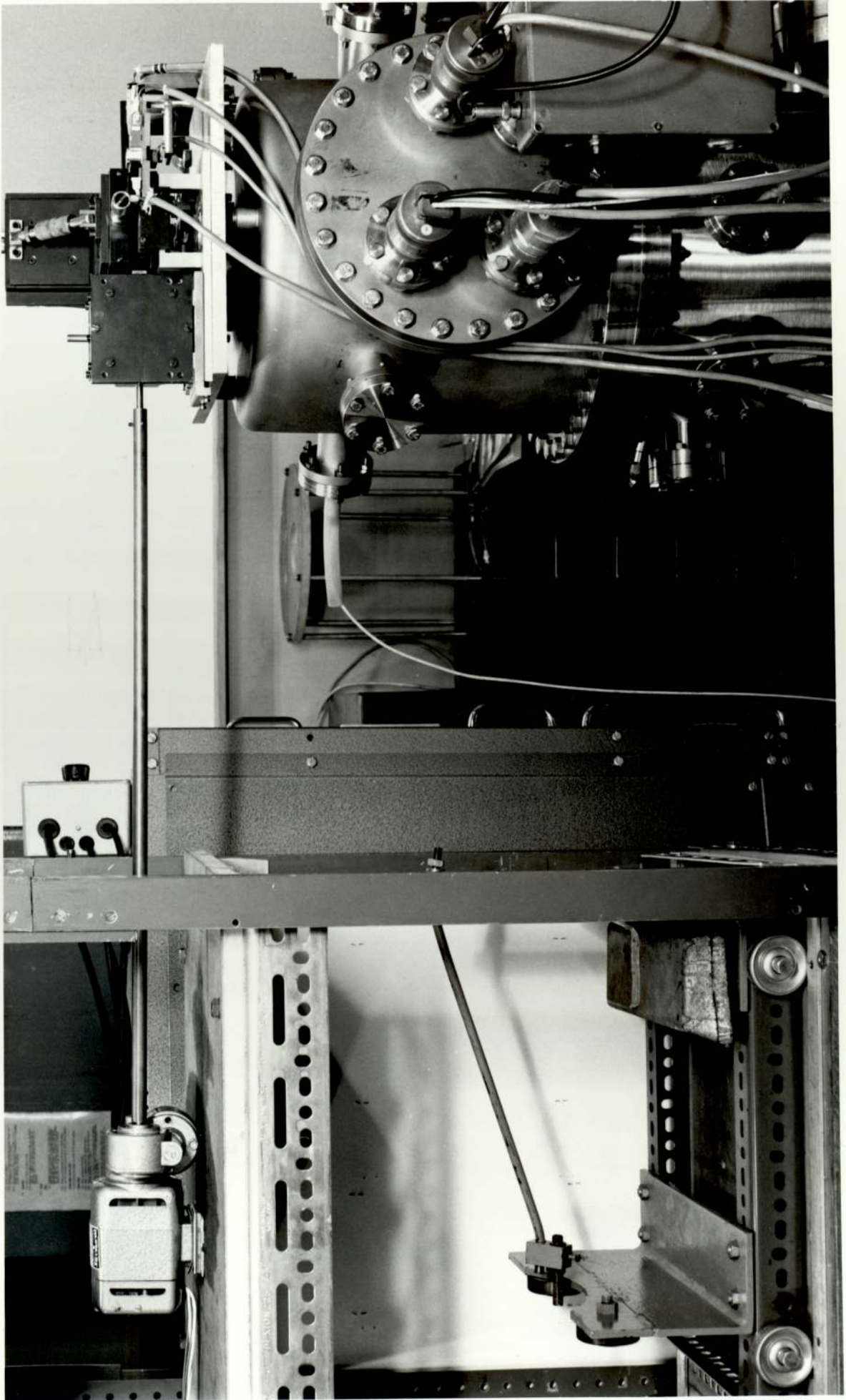
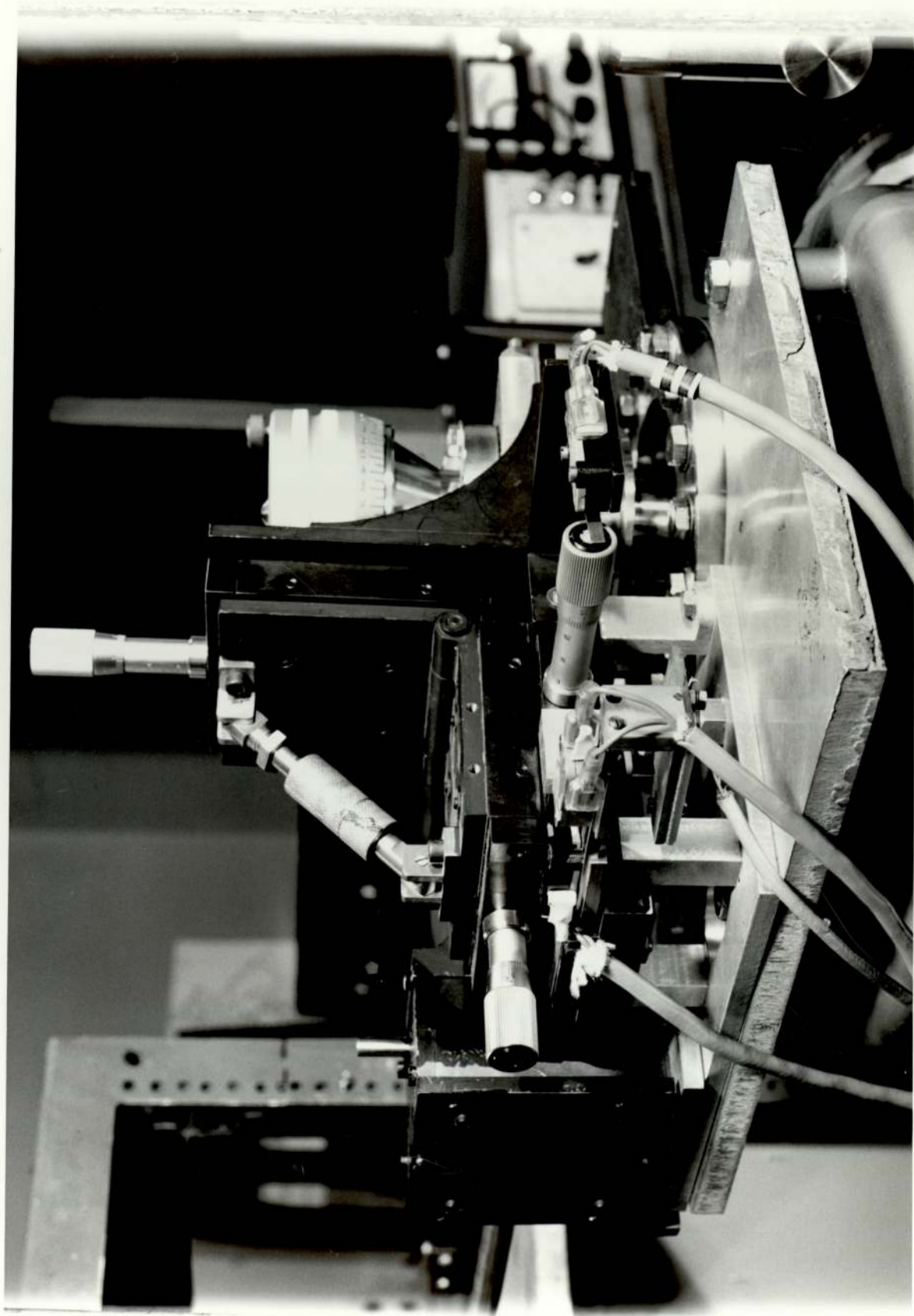


Fig 39

A close-up of the manipulator assembly
showing microswitches and slide wire.



reference co-ordinates can be established for the specimen in order to be able to define the position of any emission sites that are found. To do this, a cathetometer is set up so that by observation through the view port, the anode probe hole is in the centre of the field of view. The specimen is then moved into position so that its centre (easily identifiable from the machining marks) then corresponds to the centre of view of the cathetometer. Reference co-ordinates corresponding to the specimen centre can then be read off the x and y manipulators. In the case of the chromium-copper specimens it is necessary to determine the centre of the hole by measuring the co-ordinates of the hole edges. In either case this centre can be re-located if the specimen is subsequently examined in an electron microscope. The main source of error in this procedure is in re-setting the orientation of the specimen but it is estimated that the accuracy of re-location is $\pm 20\mu\text{m}$.

3.10.2 The circuit for detecting an emission site is shown in fig 35. It is convenient to use a log-scale picoammeter on the anode to readily observe order of magnitude changes without frequent range changing. The picoammeter connected to L is a more precise instrument for accurate current measurement. An increasing negative voltage is then applied to the specimen to determine whether there is a site present that will emit within the available field range; this is limited by a maximum gap voltage of $\cong 10\text{kV}$ that, typically, can only be sustained across gaps $\geq 0.5\text{mm}$ if flash-over is to be avoided. Normally, if a site is present, a voltage is set which corresponds to an anode current of $\sim 1\mu\text{A}$. The specimen is then scanned in a raster pattern in front of the anode probe hole until an emission current is registered at L. If this is caused by a genuine site then the increase in current at L will correspond to a decrease in current at the anode. Microadjustments can then be made to both the horizontal and vertical positions of the specimen to obtain the

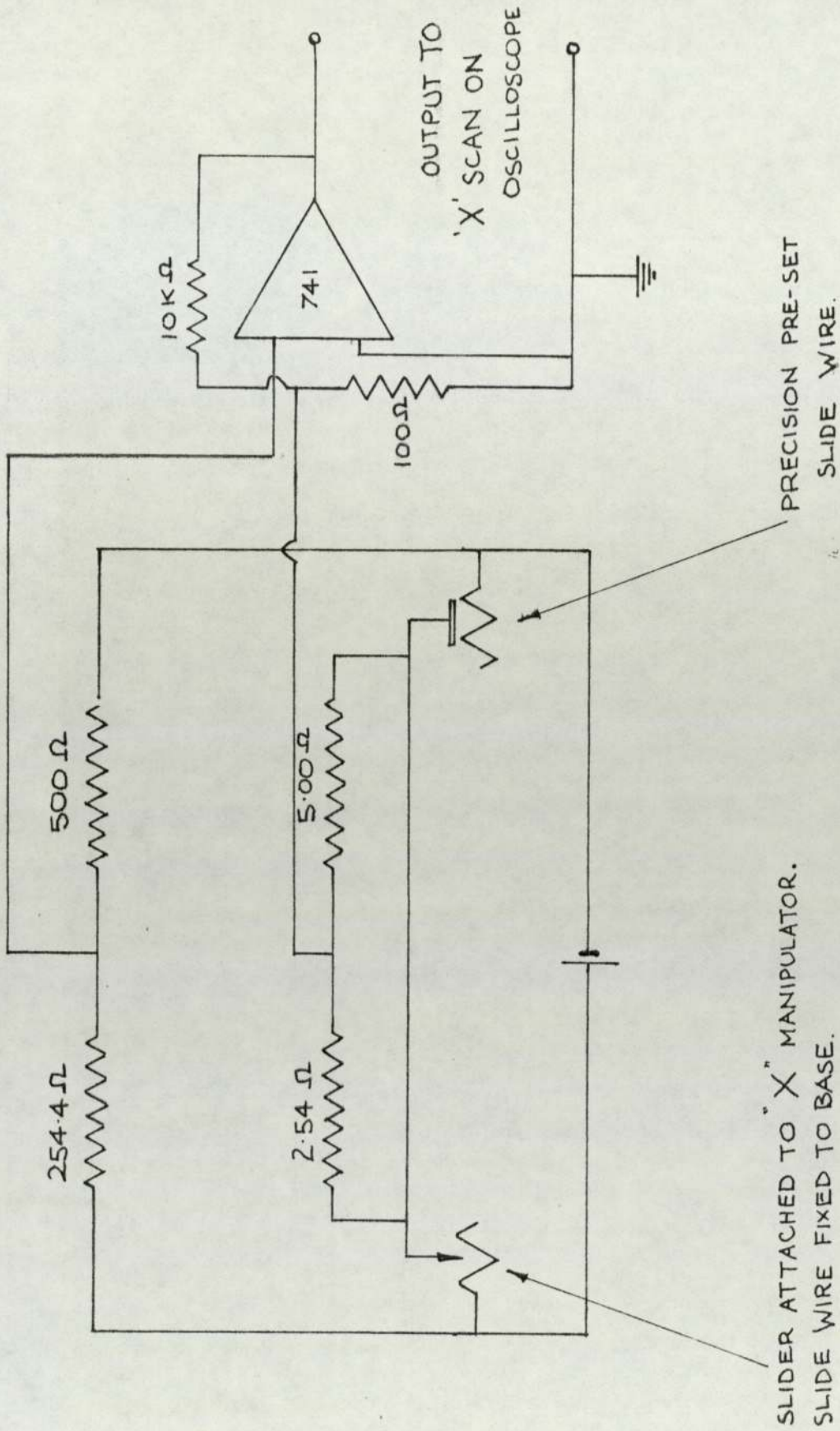


Fig 4.0. CIRCUIT TO PROVIDE VOLTAGE FOR 'X' INPUT OF OSCILLOSCOPE PROPORTIONAL TO 'X' POSITION OF SPECIMEN.

maximum current at L. When the site is correctly centralised, virtually all the current is picked up at L, and typically < 1% is lost to the anode. Thus the relative proportions of the two currents will indicate whether the site obtained is the only one on the specimen or if there are likely to be others. In practice, a current of $\sim 10^{-9}$ A is required at L in order to readily detect the energy spectrum of the electrons through the spectrometer. This is because the input aperture to the analyser selects only a small part of the total current ($\sim 1/300$).

3.10.3 During scanning the meter at L can be observed for the appearance of a signal but an automatic facility was incorporated to allow greater operational freedom. To obtain a signal proportional to the x position of the manipulator, the resistance change of a slide wire was used. The slide wire is fixed and the slider is attached to the x manipulator as shown in fig 39. The slider and one end of the wire are connected to a Kelvin bridge circuit as shown in fig 40. As the x manipulator moves, the change in resistance gives a proportional change in the out-of-balance voltage from the bridge. This is then fed to a d.c. amplifier with a gain of 100x; the output of this amplifier is then connected to the x plates of a storage oscilloscope or plotter.

3.10.4 The meter connected to L has an output of 0 - 3V corresponding to 0 - f.s.d. on the front meter reading. This output is therefore connected to the Y plates of the oscilloscope or recorder to give a displacement corresponding to a current at L. Thus it is only necessary to observe the storage oscilloscope at the end of each scan to see if a signal corresponding to an emission site has been registered during that scan.

3.10.5 To measure the energy distribution (spectrum) of the site, the interelectrode voltage is reduced to zero and the specimen is connected to earth. A positive voltage is then applied to the anode which previously corresponded to a site current of $\sim 10^{-7}$ A. With suitable voltages on the various analyser lenses (table 2) an increasing voltage is applied to L until a distribution is obtained at the output of the spectrometer, which corresponds to correct focusing of the interfacing lens. Occasionally, the focusing voltage at L may correspond to a value outside the normal operating voltage of the spectrometer (e.g. < 1 kV). In such a case, it may be necessary to alter the interelectrode gap (thus changing the voltage required on the anode) to restore the focussed value of L into the normal operating region. Generally a number of adjustments are required to the spectrometer input lens voltages, and the position of the specimen, to obtain an optimum signal. Variation of the interelectrode gap also provides a method of observing any changes in the energy spectrum with field, without affecting any of the focusing of the spectrometer.

3.10.6 Finally, when the position of the specimen has been optimised and the required spectra taken, a Fowler-Nordheim graph can be plotted from the measured i/V characteristic of the site, reverting to the electrical connections of fig 35(a).

Table 2

Typical conditions for the operation of the spectrometer when obtaining the distributions was as follows:

V_1 (L)	2kV
V_2	158V
V_3	14V
V_4	2, 5, or 10V scan. For 5V scan typically 5 - 10V
V_5	as V_4
V_6	17
V_7	200V
V_8	200V.

4.0.0 Experimental Results

4.1.0 Introduction

4.1.1 As mentioned in the introductory chapter, measurements have been made on electrode materials which are of interest in both the "passive" and "active" high voltage applications. In this chapter, results are given for the electrode materials in the first of these two categories where the measurements have been confined to the electron spectrometry technique already described. For the electrode material used in the "active" application of high voltage vacuum switching, two additional facilities have been used to gain further information on the nature of the emission sites; these are electron microscopy and elemental X-Ray analysis of the emitting area. Consequently, a description of these techniques and the results obtained from this special electrode material are given separately in Chapter 5.

4.2.0 Spectrometer Performance

4.2.1 The performance of the spectrometer when used in the "normal" mode to measure energy spectra from specially fabricated field emitting tips has already been discussed in detail by Braun et al [74]. Essentially the authors found that absolute calibration of the instrument was difficult because of the rather unsatisfactory nature of a tungsten tip as reference source. However, measurements indicated an instrument resolution $\approx 30\text{meV}$ and an identification of the emitter Fermi level was also carried out (see 3.6.3). A primary requirement of the present investigation was to establish that the addition of the interfacing lens had not influenced the performance of the analyser, particularly in respect of the resolution. Accordingly, the next section deals with assessing the performance of this modified analyser and gives the

results from measurements carried out on the instrument used in this work.

4.2.0 The Performance of the Modified Spectrometer

4.2.1 This may be assessed under three different headings:

- (i) Resolution
- (ii) Sensitivity and signal to noise ratio
- (iii) Dependence on position of emission source

The determination of the resolution of field emission energy spectrometers has been discussed in detail by Young and Kuyatt [83]. They assume that an energy analyser has a Gaussian transmission function given by:

$$G(E) = \frac{0.939438}{\Delta E_{1/2}} \exp\left(-\frac{2.772588}{(\Delta E_{1/2})^2} E^2\right) \quad (60)$$

where $\Delta E_{1/2}$ is the full width at half maximum of the transmission function.

The effect of the analyser is calculated by folding the assumed Gaussian transmission function into the field emission energy distribution $P(E)$, as given by eqn, 20(a).

$$P(E) = C \frac{\exp(E/d)}{\exp[(E - \zeta)/kT] + 1} \quad (61)$$

where C is a constant

Thus

$$J(E) = \int P(E^1) G(E^1 - E) dE^1 \quad (62)$$

The function $P(E)$ is normalised so that at $T = 0K$ its peak value is 1.

This requires that

$$C = \exp(-\zeta/d)$$

and

$$P(E) = \exp[(E-\zeta)/d] / \exp[(E-\zeta)/kT] + 1$$

Calculations were carried out at various temperatures between 0K and 300K and for each temperature the functions P and G were calculated at intervals of 0.001eV or 1% of ΔE , whichever was smaller. Equation (62) was evaluated at intervals of 0.001eV using numerical integration by Simpson's rule. Fig (41) shows the curves obtained by Young and Kuyatt at 77K (note that energy is increasing from left to right). Since the high energy edge is particularly sensitive to variation in the half width of the spectrometer transmission function, the authors chose as a pertinent parameter in defining the resolution of the spectrometer the difference in energy between the 10% and 90% points on the high energy edge ($\Delta J(E)$). Fig (42) shows the variation in $\Delta J(E)$ with FWHM of the spectrometer at various temperatures whilst fig (43) shows how the energy distribution width (F.W.R.M.) varies with spectrometer F.W.H.M at these temperatures. It can be seen from these figures that this method of determining analyser resolution is far more meaningful at low temperatures.

4.2.2 Fig (57) shows an energy distribution obtained from a broad area stainless steel electrode using the modified spectrometer described in Chapter 3. In this and all other experimental curves measured on this equipment, energy is decreasing from left to right. It will be seen that the energy width $\Delta J(E)$ is $\sim 0.120\text{eV}$ (this represents the sharpest high energy slope obtained from the various specimens studied). Using the results of Young and Kuyatt, this corresponds to a maximum bandwidth of $\sim 80\text{meV}$. Whilst this is a higher value than the best result obtained by Braun et al ($\sim 50\text{meV}$) [74] on this instrument using a field emitting

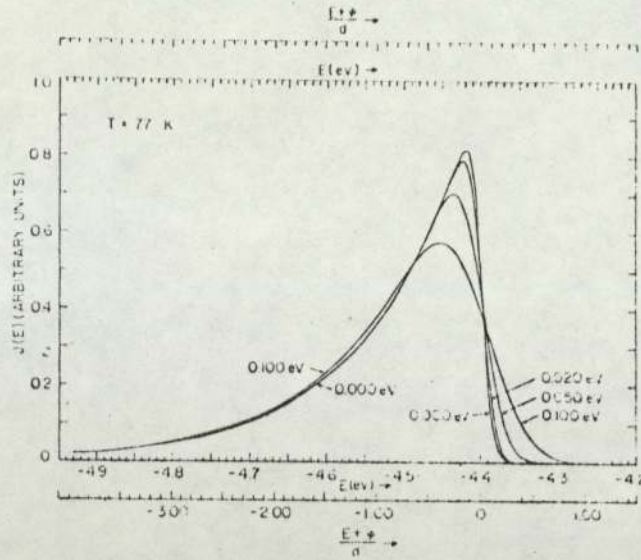


FIG 41. THE EFFECT OF ANALYSER TRANSMISSION FUNCTION ON ENERGY DISTRIBUTION MEASUREMENTS. $T=77\text{K}$, TRANSMISSION FUNCTION: $0.000 \rightarrow 0.100\text{eV}$.

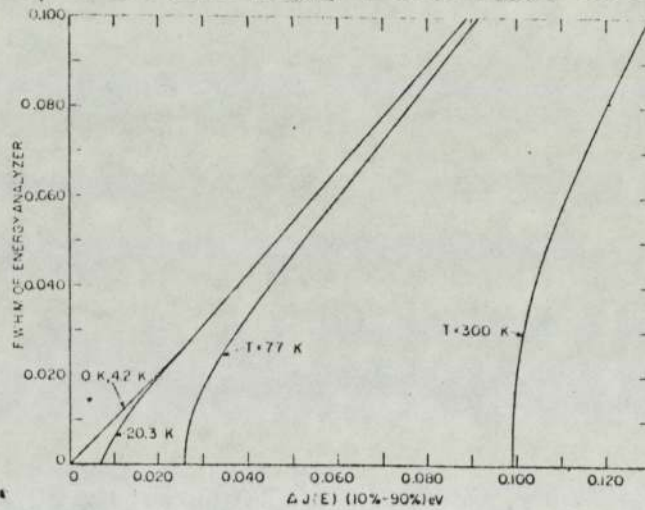


FIG 42. F.W.H.M. OF ENERGY ANALYSER AS DETERMINED FROM THE HIGH ENERGY EDGE OF THE MEASURED ENERGY DISTRIBUTION

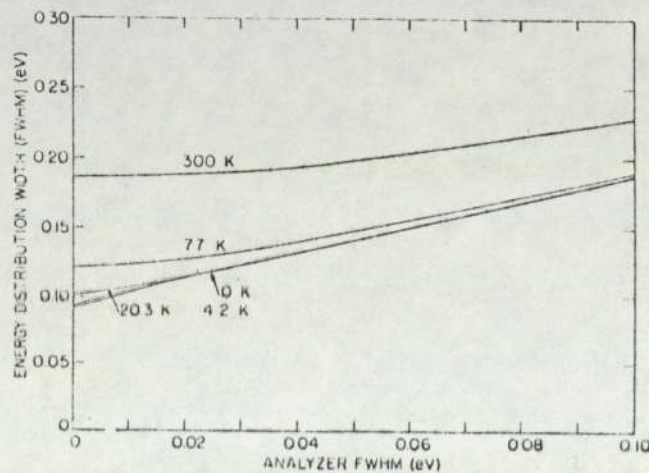


FIG 43. ENERGY DISTRIBUTION WIDTH AS A FUNCTION OF ANALYSER F.W.H.M.

tungsten tip, there is a difference in the experimental conditions in the two cases. It is possible to attain a far greater level of surface cleanliness with a specially fabricated emitter than has so far been possible with the present experimental arrangement using broad area electrodes. The earlier results of [74] show that the high energy slope width is critically dependent upon the level of surface contamination. There must inevitably be an impurity layer on the surface of the electrode being studied (discussed further in 6.5.5) and it therefore seems probable that the increased width of the high energy slope is due to these surface conditions rather than any deterioration in the performance of the spectrometer in its modified form with the interfacing lens. Moreover, even this somewhat higher measured value of bandwidth does not affect the conclusions which may be drawn from the spectra presented in chapters 4 and 5.

4.2.3 Measurements were next carried out to determine the minimum usable current for the spectrometer. To do this the voltage between specimen and anode was steadily decreased and the gain of the spectrometer amplifiers progressively increased until reaching the maximum acceptable noise level compatible with proper analysis of the signal. At this setting the voltages were removed from input lenses ($L_2 \rightarrow L_4$) and the inner and outer hemispheres. The elements were then connected via a small e.m.f. to a picoammeter (fig 44). With the voltages on the anode and element L remaining unchanged, the current into the spectrometer remained constant and its value could be read on the picoammeter. The minimum acceptable input level corresponded to an input current of $\sim 10^{-10}$ A, at which the signal to noise ratio was ~ 35 db.

4.2.4 Another important effect sometimes noted when varying the input current, was shifting of the spectrum - a phenomenon not usually encountered with metallic emitters, although common in semi-conductors where

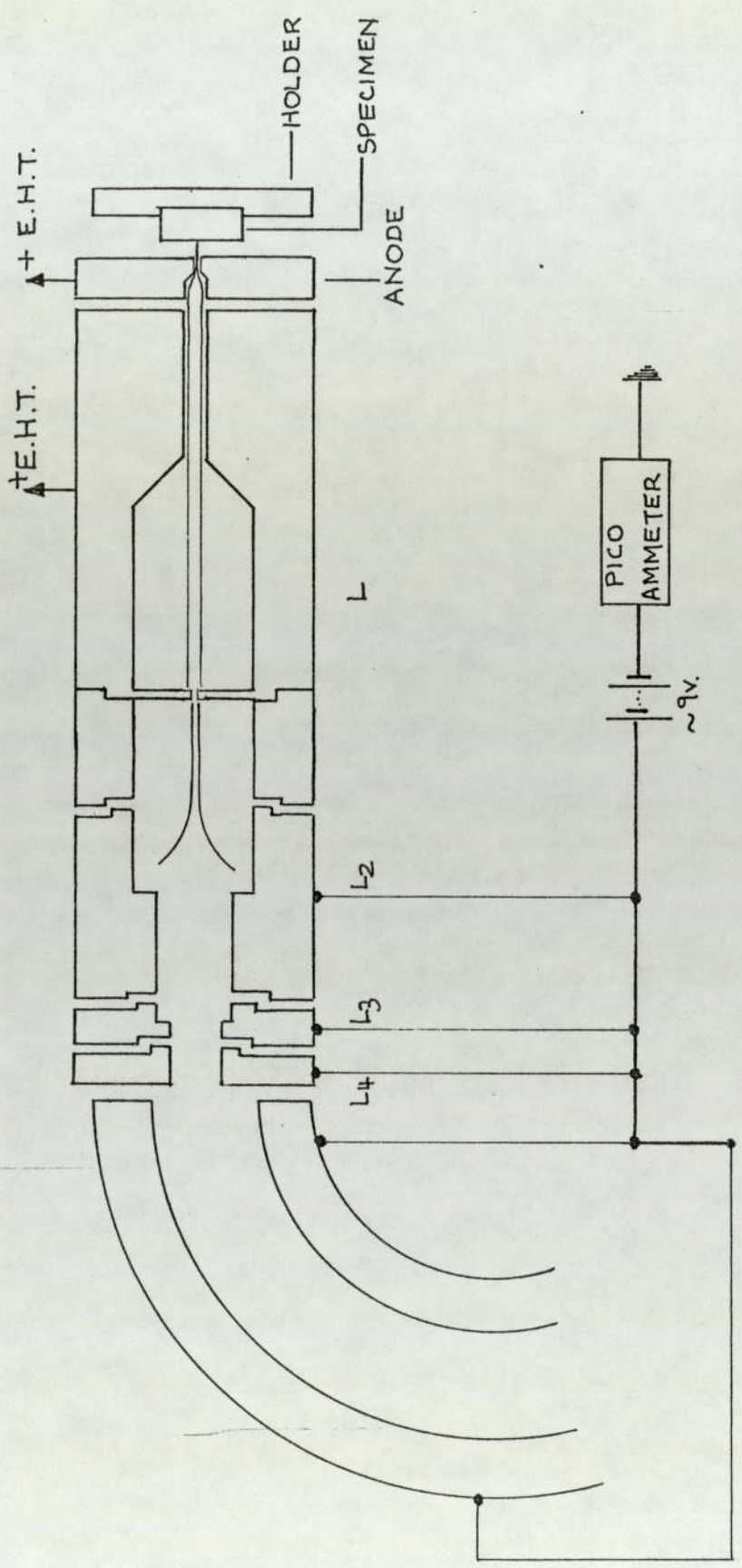


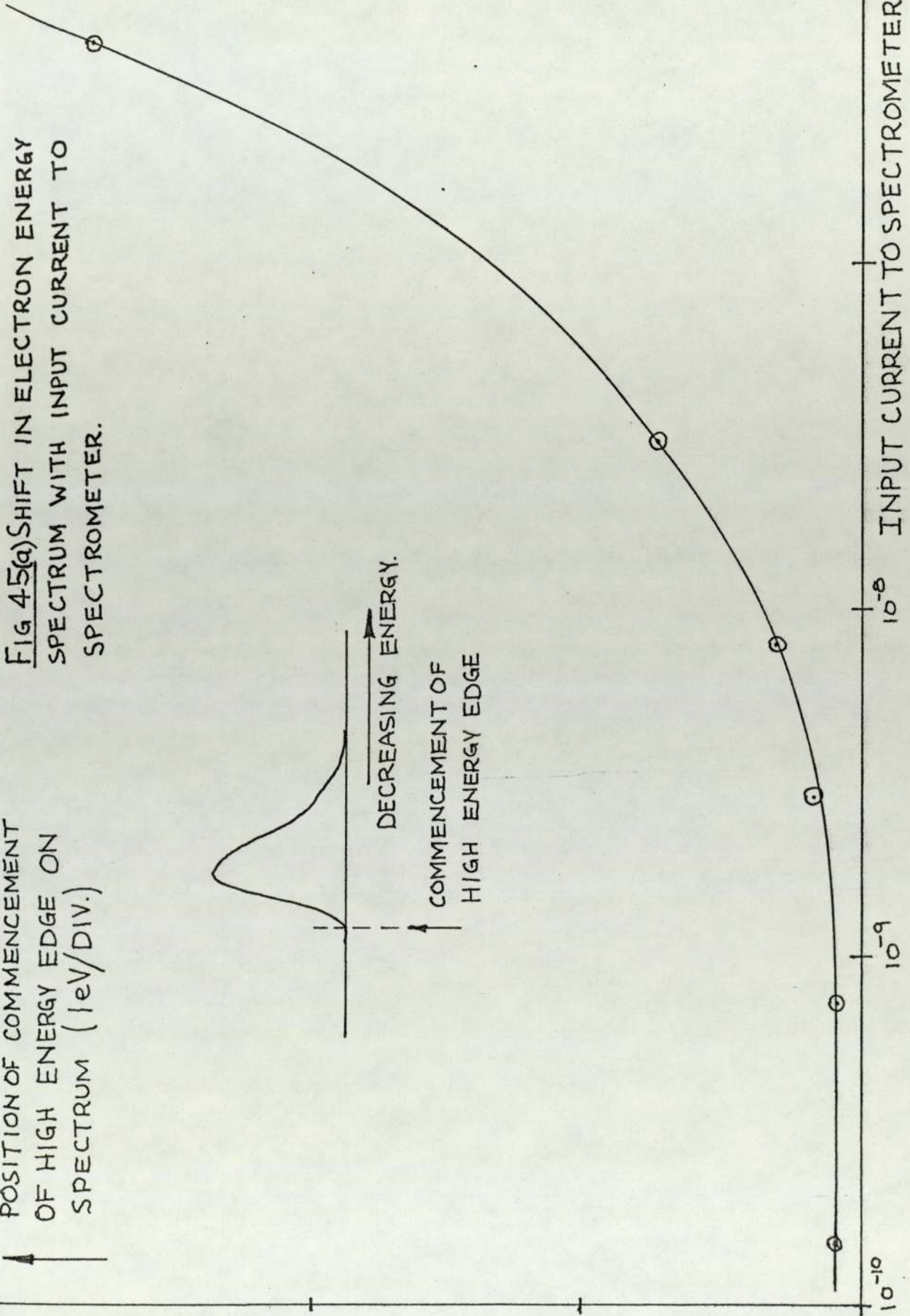
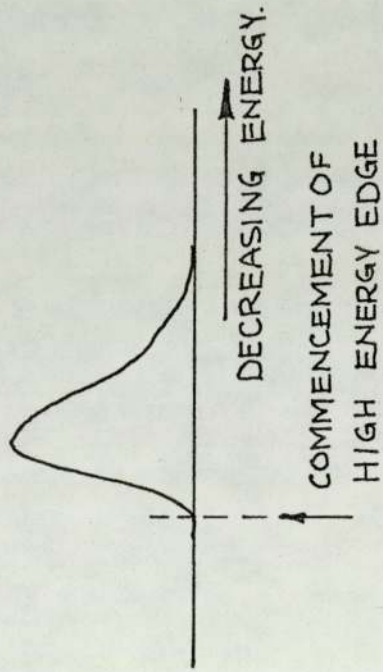
FIG 44. LENS ELEMENT CONNECTIONS TO MEASURE INPUT CURRENT INTO SPECTROMETER.

the resistivity of the material can lead to an appreciable voltage drop down the emitter shank. Consequently, a series of measurements were carried out to determine the extent of this shift with varying input currents to the spectrometer. In fig 45(a) the position of the commencement of the high energy edge is plotted against input current for one particular copper specimen. It will be seen that for an input current of $< 10^{-9}$ A, there is no significant shift in the distribution. Accordingly, all the distributions given here were measured at current levels in this regime and in each case it was specifically checked that variations in input current of 10x did not shift the position of the distribution. In many cases, however, no shift in spectrum was detectable over the whole pre-breakdown current range investigated (i.e. up to $\sim 10\mu\text{A}$). Fig 45(b) shows the variation in the distribution F.W.H.M. with macroscopic field across the interelectrode gap.

4.2.5 Tests were also carried out to examine the effect on the distribution of horizontal and vertical movement of the specimen. In every case it was found that shifting the specimen in this way only changed the magnitude of the distribution peak and did not distort the shape or position of the peak in any way. Measurements were also made to determine the variation in current passing through the probe hole with shifting of the specimen. This current was detected, as described in Chapter 3, by removing the voltages on lenses L - L₄ and then measuring the current at L with a picoammeter.(fig 35(a)). Figs (46) and (47) show the variation in this current for shifts of the specimen in x and y directions. The change in x or y to completely lose a spectrum was dependent upon the current distribution of the site but typically was within $\pm 50\mu\text{m}$.

POSITION OF COMMENCEMENT
OF HIGH ENERGY EDGE ON
SPECTRUM (1eV/DIV.)

FIG 45(a) SHIFT IN ELECTRON ENERGY
SPECTRUM WITH INPUT CURRENT TO
SPECTROMETER.



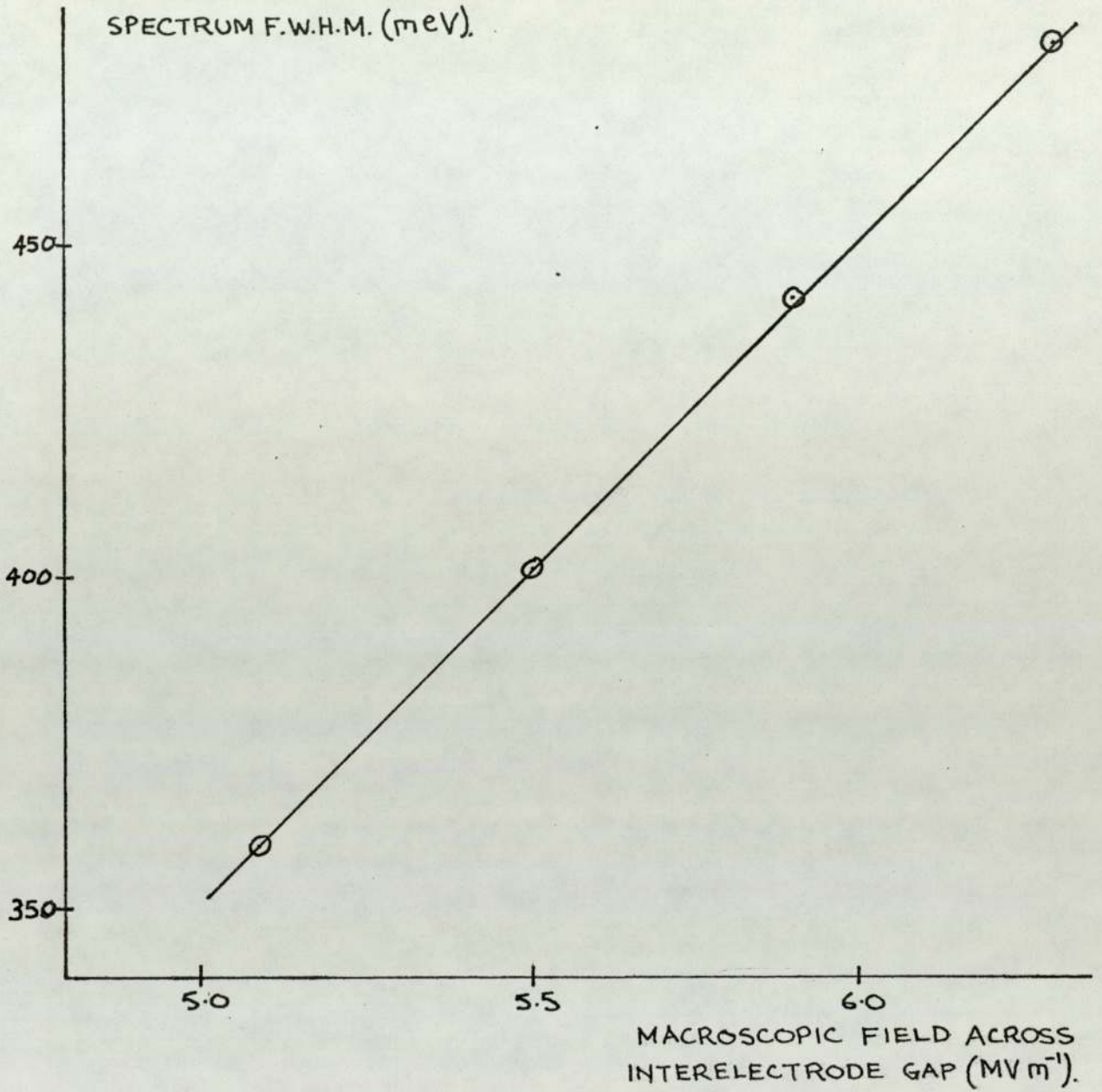


Fig 45(b) VARIATION IN SPECTRUM F.W.H.M. WITH
MACROSCOPIC FIELD ACROSS THE INTERELECTRODE GAP

FIG 46. VARIATION OF CURRENT INTO ANODE PROBE HOLE WITH 'X' POSITION OF SPECIMEN.

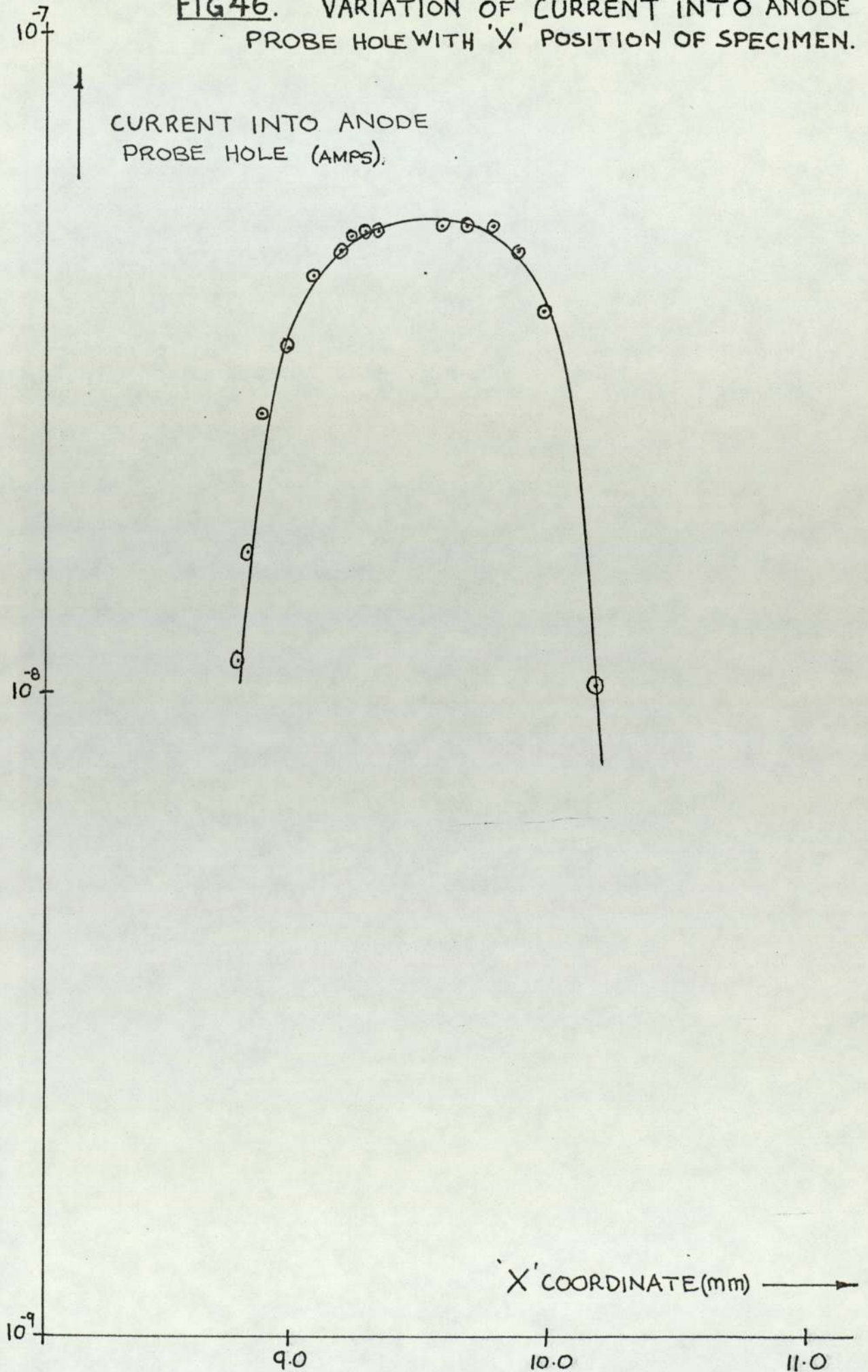
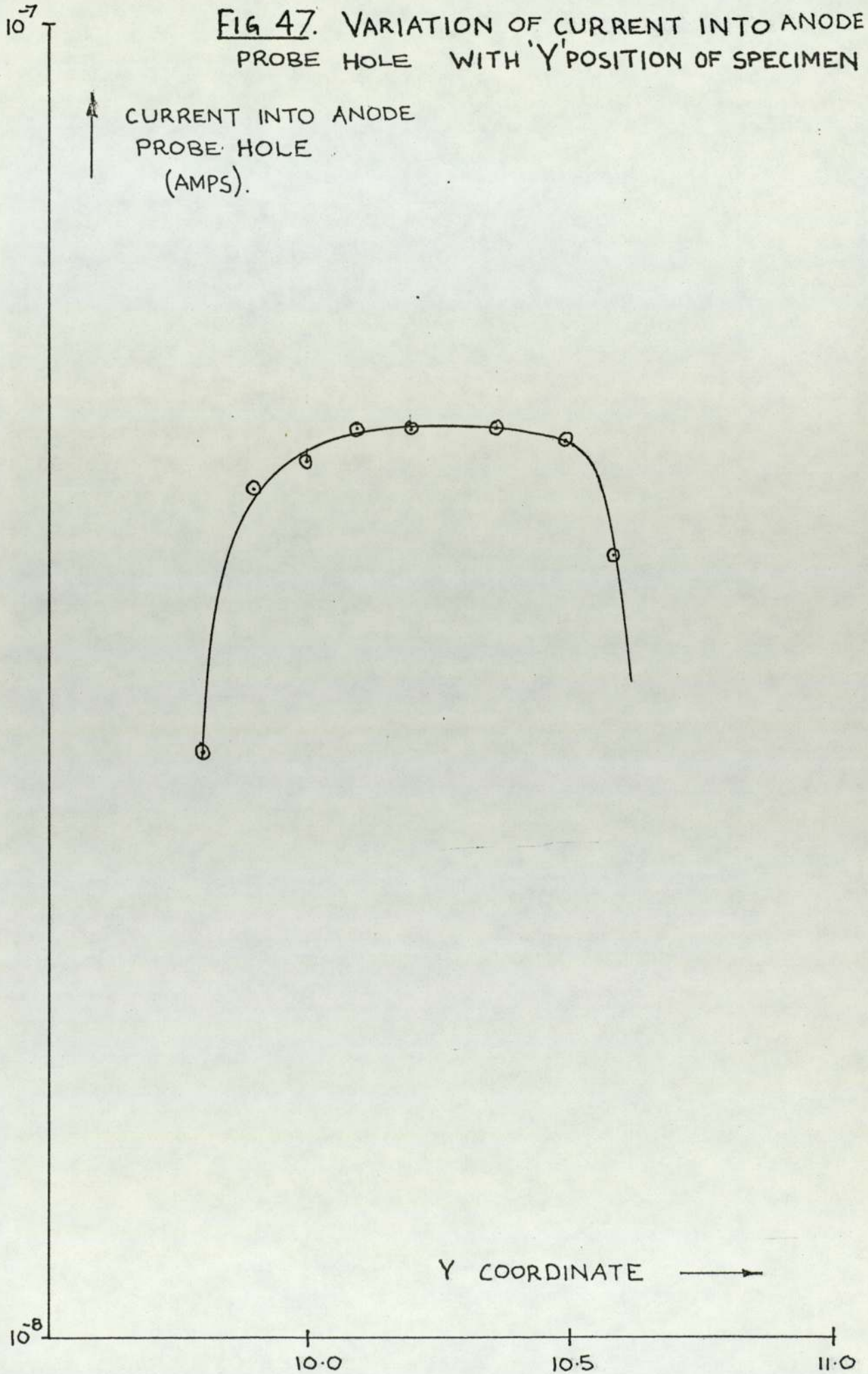


FIG 47. VARIATION OF CURRENT INTO ANODE PROBE HOLE WITH 'Y' POSITION OF SPECIMEN



4.3.0 Description of measurements taken on each sample

4.3.1 As indicated in Chapter 2, there are certain features which are important for the interpretation of FEED data. Specifically these are:

- 4.3.1.(1) The position of the emitter Fermi level. This gives information on the electron supply function by revealing whether electrons are emitted from above as well as below this level. The relevant tables accompanying the distributions give the difference in energy between the position of the Fermi level on a metallic emitter - 73% up the high energy slope at 300K (50) - and the 73% position obtained on the actual distribution.
- 4.3.1.(2) The shape and half-width, $\Delta E_{\frac{1}{2}}$, of the distribution. This gives an indication of the state of the surface at the point of emission. A narrow distribution with a steep high energy edge with the Fermi level in the 73% position indicates emission from a clean metal surface; under these circumstances the distribution can be used to give a value for the work function of the surface (see Chapter 2). A broader distribution can be attributed to either surface contamination and a lowered work function or a high electric field at the surface (see eqn. 28 and Fig 45(b)). Contaminants may also give rise to a more complicated potential barrier and possibly a modified electron supply function if any field penetration is present at the surface. This latter point is discussed in greater detail in Chapter 6. Changes in the potential barrier can give rise to extra peaks or structure in a distribution on the model of "resonance tunnelling" originally proposed by Duke and Alferieff [84] and later developed by others [85], [86].
- 4.3.1.(3) The slope of the high energy edge of the distribution, $\Delta J(E)$. A steep slope indicates a rapid rise from empty to full

electronic levels typical of a metal at relatively low temperature with the electrons obeying Fermi-Dirac statistics. A shallower high energy slope is characteristic of a more gradual change from empty to full levels, possibly due to the presence of "hot" electrons. This may be caused by contamination, such as observed by Braun et al [74] and discussed further in Chapter 6.

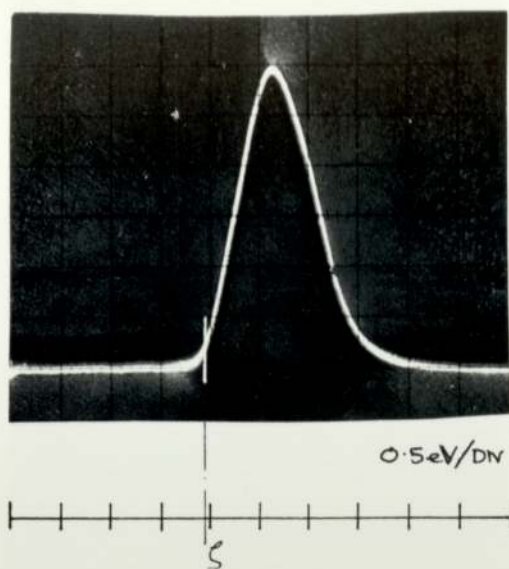
- 4.3.1.(4) Finally, the measurement of the voltage current characteristics associated with an energy distribution. Plotting this according to the Fowler-Nordheim equation (viz: $\log i/V^2$ v. $1/V$) may provide information on whether the emission obeys this law, and if so, in assisting in the evaluation of β or ϕ (as indicated in Chapter 2).

4.4.0 The Distributions obtained from the Test Specimens

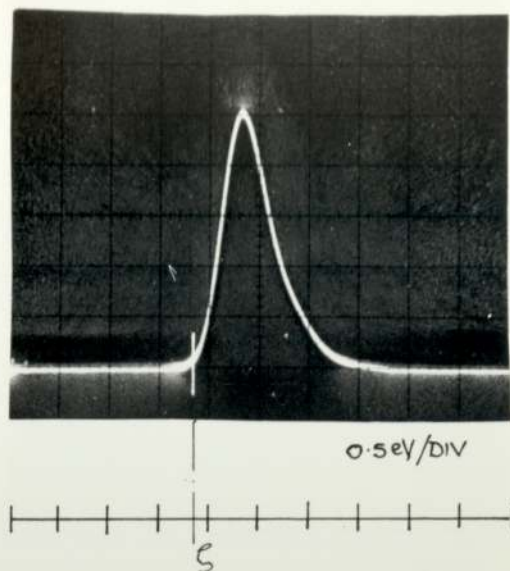
4.4.1 Measurements were carried out on three different electrode materials which are of particular interest in "passive" high voltage applications. These are copper, stainless steel and titanium alloy. Copper is of interest because it is well known to have a particularly poor high voltage performance. It was therefore ideal as an initial test specimen since it will readily produce emission from one or more sites on the electrode surface. In contrast, both stainless steel and the titanium alloy are used extensively in high voltage technology because the occurrence of field emission sites seems to be inhibited. Indeed, under test conditions it is sometimes found that no steady pre-breakdown current can be obtained, in which case the electrode material suddenly breaks down with the occurrence of a microdischarge thought to be of microparticle origin.

4.4.2 The results obtained from the first copper specimen (No. 1) are shown in fig (48). On this and subsequent spectra, the position of the emitter Fermi level, ζ , - determined as described in 3.6.0 - is marked by a vertical white line. Tests on this specimen were carried out primarily to determine the effect of outgassing on the electron distribution. The details of each treatment are given in table (3). The distribution was measured ~ 10 minutes after each outgassing treatment when the pressure had returned to the base value of $\sim 2 \times 10^{-10}$ torr.

4.4.3 Fig (49) shows the results on the second copper specimen (No. 2). Again, the effects of outgassing were investigated together with a more prolonged exposure to U.H.V. (15hrs.). In addition an i-v characteristic was taken of this site shortly after the outgassing and the resulting F-N plot is shown in fig (50). Table (4) gives the relevant details of the distribution together with the value of β obtained from the F-N plot. The distributions obtained from a third copper specimen are shown in fig 51(a) and (b). This specimen exhibited the feature of a second, lower energy, peak on some of the distributions, the presence of this peak apparently dependent on the precise surface conditions at the time of making the measurement. Where relevant, the separation between the peaks is included with the other data in Table (5). After making several measurements on this specimen a microdischarge occurred in the chamber, but afterwards there was still emission from the site. The fourth copper specimen differed from the others in that three separate sites were found, each of which was separately analysed. Fig 52(a) and (b) shows the spectra and Table (6) gives the relevant details. Unlike all the other sites reported on in this chapter, sites 1 and 2 of this specimen exhibited a marked distribution shift with variation in emission current. In the case of site 1 the shift was not apparent until the

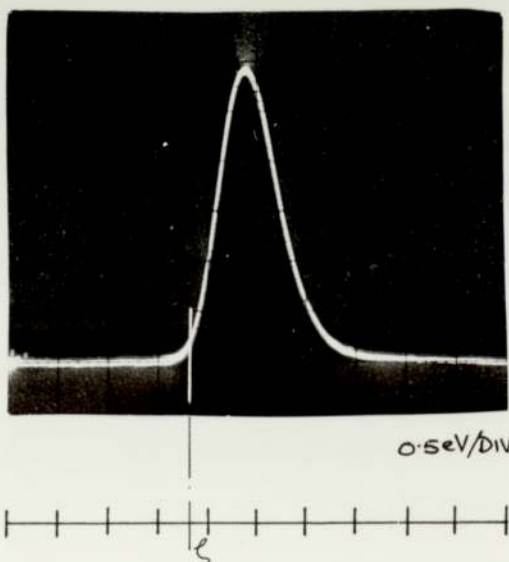


(A) NO TREATMENT.

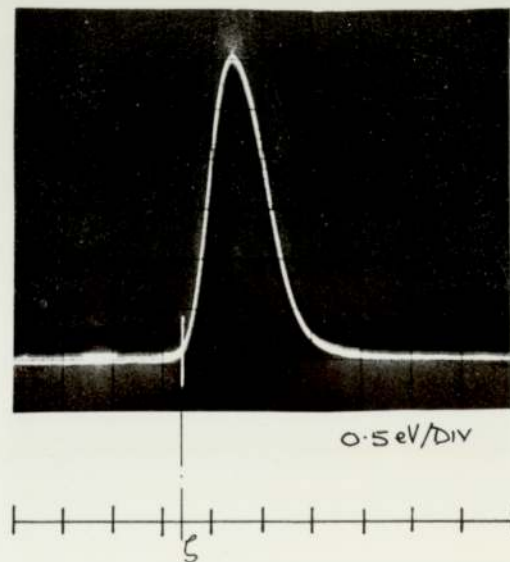


(B) 1 MINUTE OUTGAS.

$\xrightarrow{\hspace{1.5cm}}$
 DECREASING ENERGY.



(C) A FURTHER 2 MINUTE
OUTGAS.

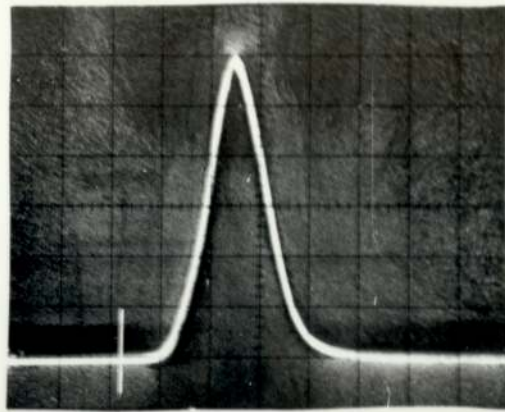


(D) A FURTHER 4 MINUTE
OUTGAS.

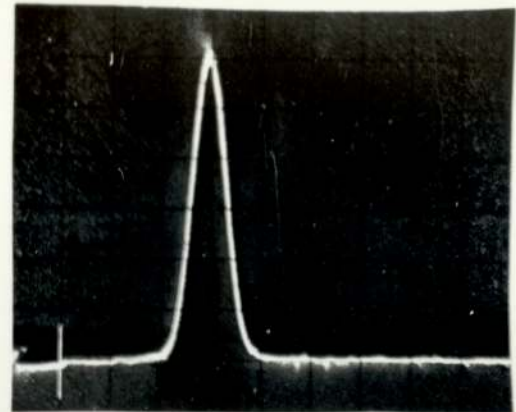
FIG48. ENERGY DISTRIBUTIONS OF FIRST COPPER SPECIMEN. THE POSITION OF THE EMITTER FERMI LEVEL IS SHOWN IN EACH CASE. ELECTRON ENERGY IN eV, 0.5eV/DIV IS X AXIS (GOING FROM HIGH ENERGY TO LOW ENERGY LEFT TO RIGHT). ELECTRON CURRENT PER UNIT ENERGY IS Y AXIS.

Table 3 Copper Specimen 1 at ambient temperature of 300K

Outgas treatment at 50W	F.W.H.M. ($\Delta E_{\frac{1}{2}}$) (meV)	High energy slope width $\Delta J(L)$ (meV)	Distribution shift (meV)
None	900	550	450
1 minute	600	300	300
Further 2 minutes	700	350	300
Further 4 minutes	650	350	300
Theoretical value for a metal	230	100	NIL

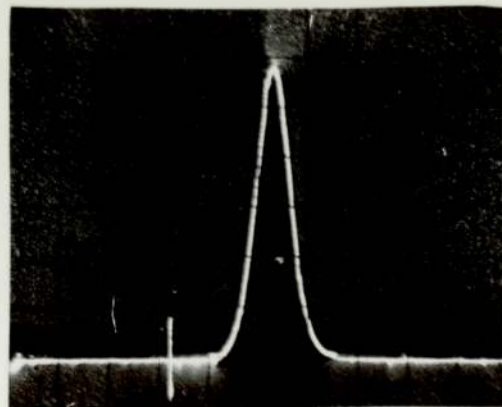


(A) NO TREATMENT.



(B) 2 MINUTE OUTGAS

→
DECREASING ENERGY.



(C) LEFT 15 HOURS UNDER U.H.V.

FIG.49 ENERGY DISTRIBUTIONS OF SECOND COPPER SPECIMEN. THE POSITION OF THE EMITTER FERMI LEVEL IS SHOWN IN EACH CASE. ELECTRON ENERGY IN eV, 0.5 eV/DIV IS X AXIS (GOING FROM HIGH ENERGY TO LOW ENERGY LEFT TO RIGHT). ELECTRON CURRENT PER UNIT ENERGY IS Y AXIS.

FIG 50. FOWLER-NORDHEIM PLOTS OF COPPER SPECIMENS.

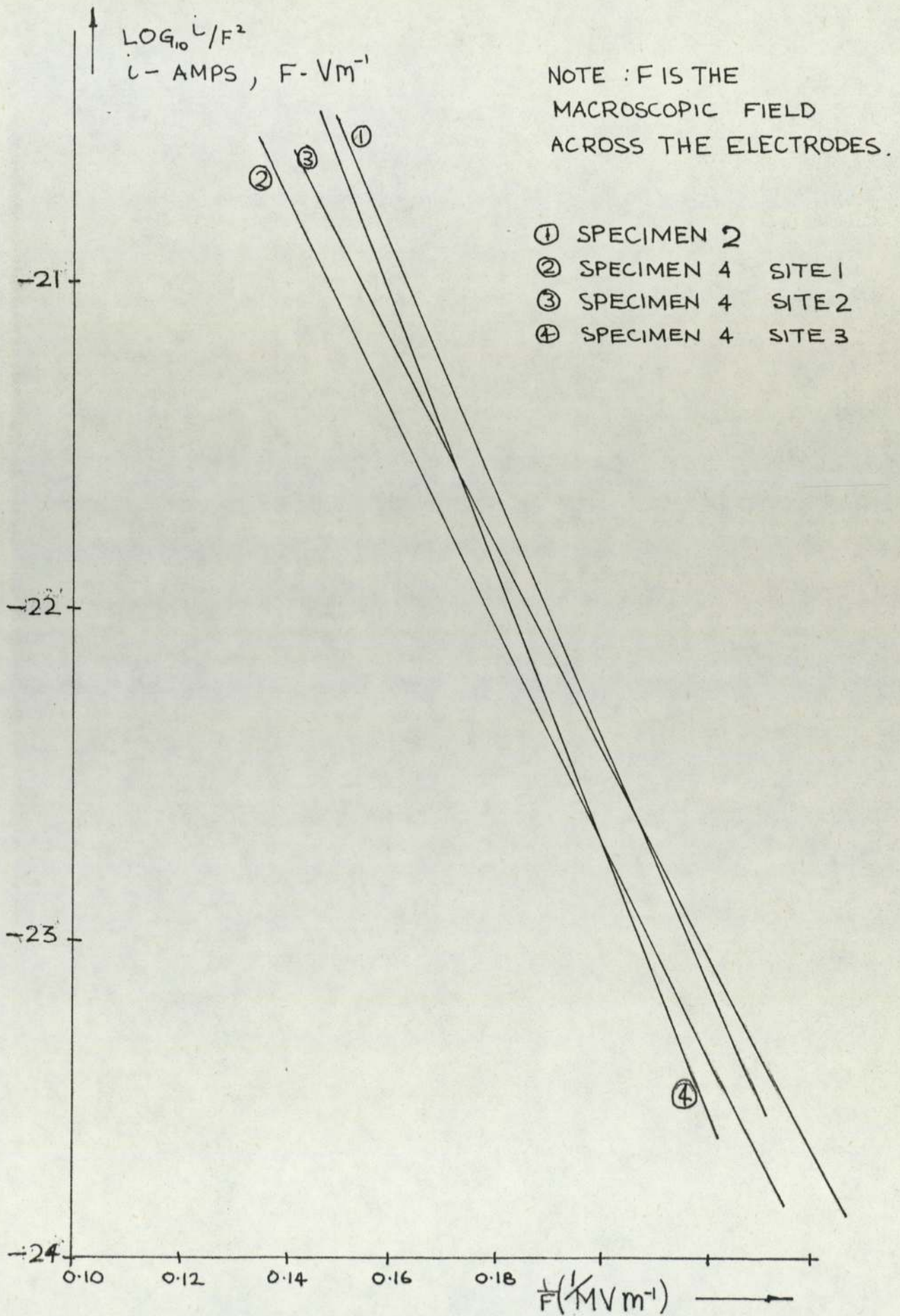
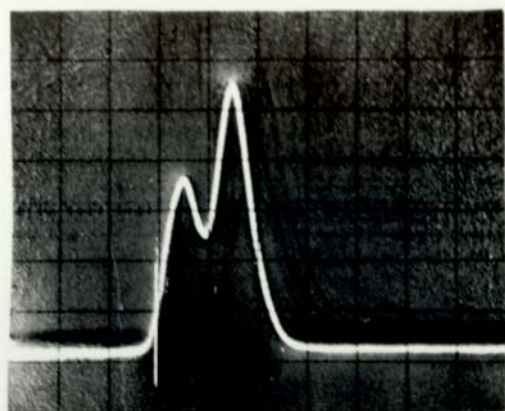


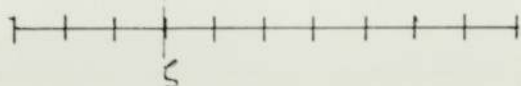
Table 4
Copper Specimen 2 at ambient temperature of 300K

Treatment	V_a (kV)	Gap (mm)	F.W.H.M. ($\Delta E_{\frac{1}{2}}$) (meV)	High energy slope width $\Delta J(E)$ (meV)	Distribution shift (meV)	Field enhancement β , from slope of F-N graph (*)
None	6.4	1.11	650	450	1000	-
2 minute outgas at 50W	5.0	1.11	400	300	1350	800
Left a further 15 hours under U.H.V.	4.4	1.11	400	250	950	-
Theoretical value for a metal			230	100	NIL	

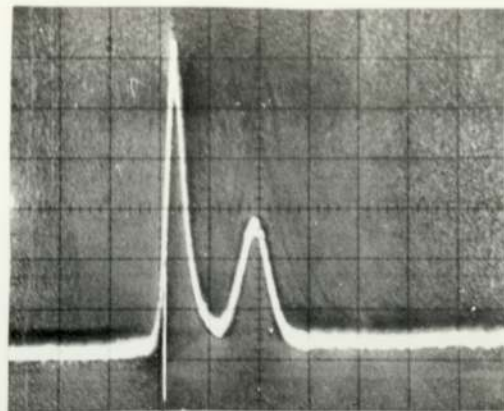
(*) Assuming $\phi = 4.5\text{eV}$.



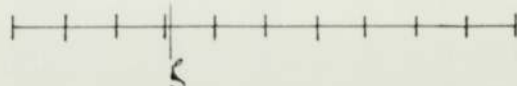
0.5 eV/div



(A) NO TREATMENT

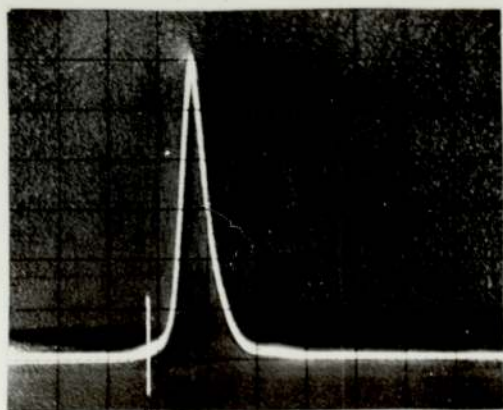


0.5 eV/div

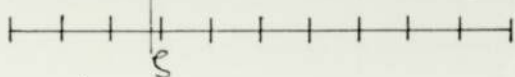


(B) LEFT 15 HOURS UNDER U.H.V.

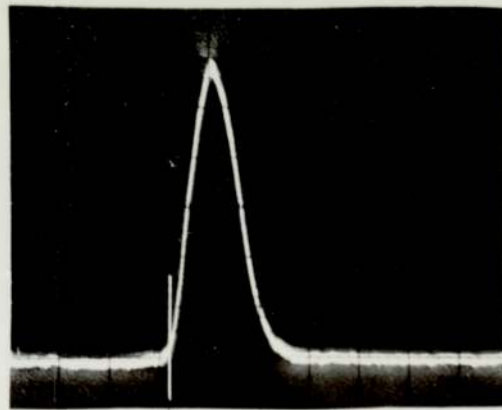
→
DECREASING ENERGY.



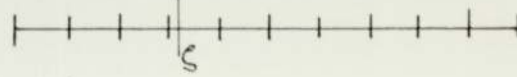
0.5 eV/div



(C) LEFT A FURTHER 5 HOURS UNDER U.H.V.

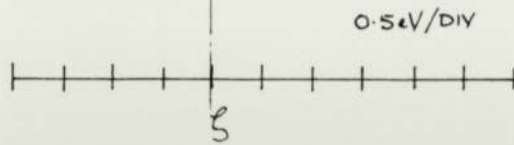
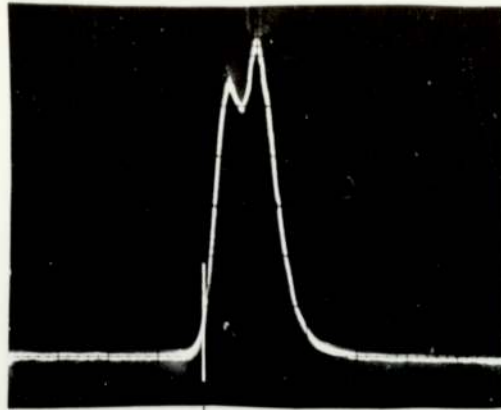


0.5 eV/div



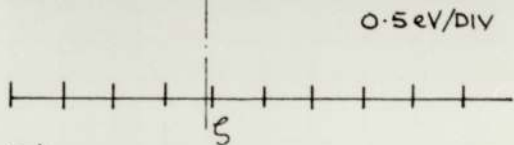
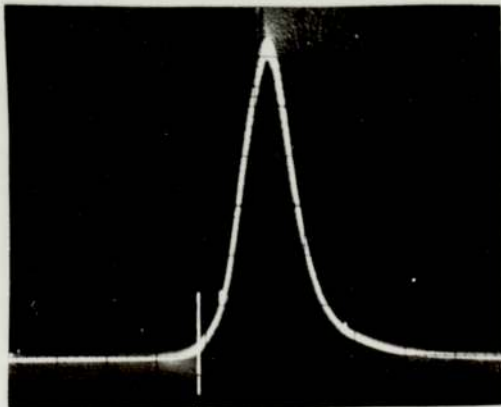
(D) LEFT A FURTHER 63 HOURS UNDER U.H.V.

FIG 51(a) ENERGY DISTRIBUTIONS OF THIRD COPPER SPECIMEN. THE POSITION OF THE EMITTER FERMI LEVEL IS SHOWN IN EACH CASE. ELECTRON ENERGY IN eV, 0.5 eV/DIV, IS X AXIS (GOING FROM HIGH ENERGY TO LOW ENERGY, LEFT TO RIGHT). ELECTRON CURRENT PER UNIT ENERGY IS Y AXIS.



(E) OUTGASSED FOR 4 MINUTES
AT 50 WATTS.

→
DECREASING ENERGY.



(F) AFTER MICRODISCHARGE
IN CHAMBER.

FIG 5(b). ENERGY DISTRIBUTIONS OF THIRD COPPER SPECIMEN. THE POSITION OF THE EMITTER FERMI LEVEL IS SHOWN IN EACH CASE. ELECTRON ENERGY IN eV, 0.5 eV/DIV IS X AXIS (GOING FROM HIGH ENERGY TO LOW ENERGY LEFT TO RIGHT). ELECTRON CURRENT PER UNIT ENERGY IS Y AXIS.

Table 5

Copper Specimen 3 at ambient temperature of 300K

Treatment	V_a (kV)	Gap (mm)	F.W.H.M. ($\Delta E_{\frac{1}{2}}$) (meV)	High energy slope width $\Delta J(E)$ (meV)	Distribution shift (meV)	Peak Separation (meV)
None	4.7	0.4	-	250	150	500
15 hrs under U.H.V.	4.7	0.4	-	150	NIL	800
Further 5 hrs under U.H.V.	4.7	0.4	250	200	400	-
Further 63 hrs under U.H.V.	4.8	0.4	550	300	250	-
Outgassed for 4 mins at 50W	4.8	0.4	-	200	150	300
Microdischarge in chamber	4.8	0.4	600	400	550	-
Theoretical value for metal			230	100	NIL	

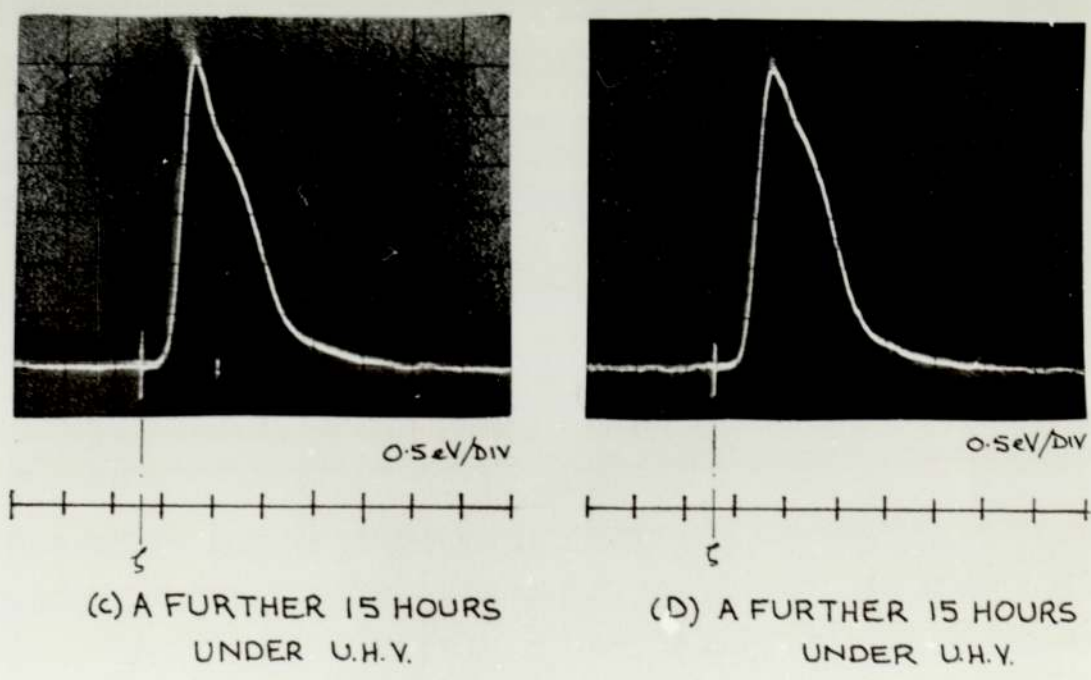
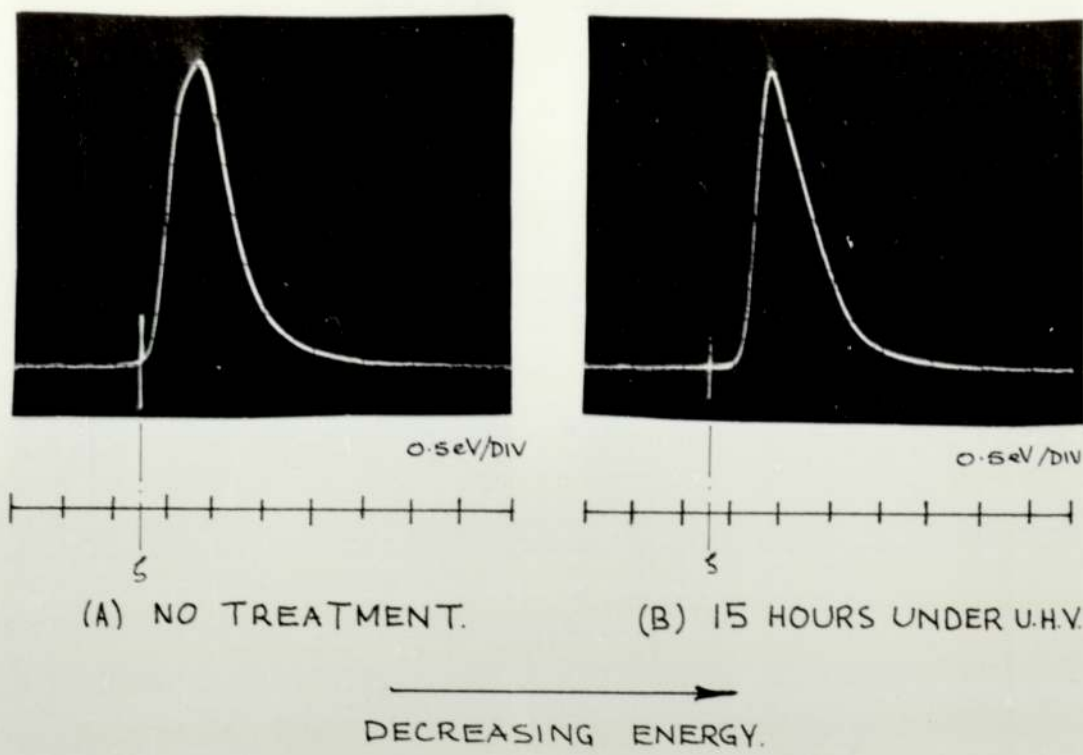
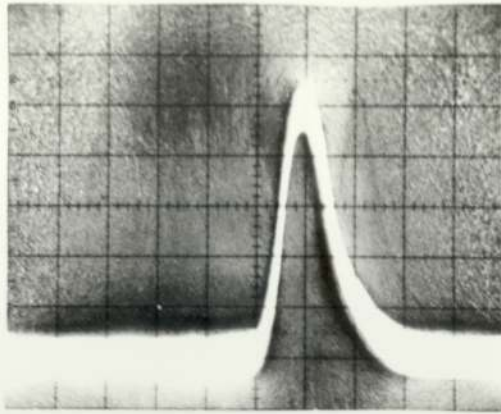
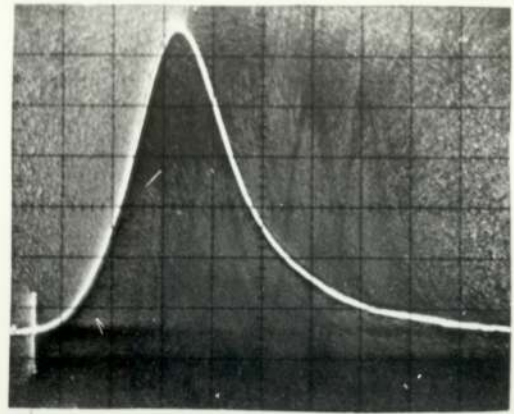


FIG 52(a) ENERGY DISTRIBUTIONS OF FOURTH COPPER SPECIMEN (SITE I). THE POSITION OF THE EMITTER FERMI LEVEL IS SHOWN IN EACH CASE. ELECTRON ENERGY IN eV, 0.5eV/DIV, IS X AXIS (GOING FROM HIGH ENERGY TO LOW ENERGY LEFT TO RIGHT). ELECTRON CURRENT PER UNIT ENERGY IS Y AXIS.

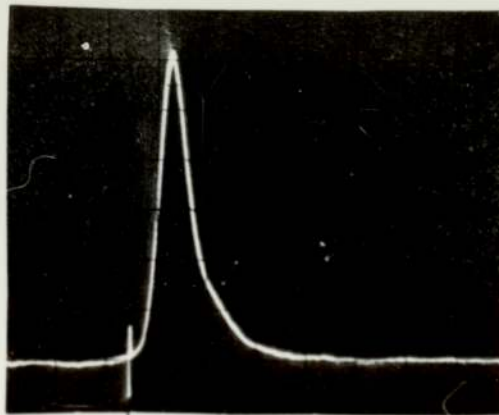


SITE 2. NO TREATMENT.



SITE 3. NO TREATMENT.

→
DECREASING ENERGY.



SITE 3. 15 HOURS UNDER U.H.V.

FIG 52(b) ENERGY DISTRIBUTIONS OF FOURTH COPPER SPECIMEN. THE POSITION OF THE EMITTER FERMI LEVEL IS SHOWN IN EACH CASE. ELECTRON ENERGY IS X AXIS (GOING FROM HIGH ENERGY TO LOW ENERGY LEFT TO RIGHT). ELECTRON CURRENT PER UNIT ENERGY IS Y AXIS.

Table 6 Copper Specimen 4 at ambient temperature of 300K

Treatment	V _a (kV)	Gap (mm)	F.W.H.M ($\Delta E_{1/2}$) (meV)	High energy slope width $\Delta J(E)$ (meV)	Distribution shift (meV)	Field Enhancement β , from slope of F-N graph (*)
<u>Site 1</u>						
None	5.2	0.85	650	250	350	
15 hrs under U.H.V.	7.4	1.30	600	350	400	
Further 15 hours under U.H.V.	7.5	1.35	700	300	450	
Further 15 hours under U.H.V.	7.5	1.35	750	350	450	850
<u>Site 2</u>	8.0	1.39	1000	500	see text	900
<u>Site 3</u>						
None	9.4	1.32	450	750	400	
15 hours under U.H.V.	9.6	1.30	350	200	300	700
Theoretical value for metal			230	100	NIL	

(*) Assuming $\phi = 4.5\text{eV}$.

field had been increased by $\sim 10x$ from that at which the spectra were measured. Site 2 was quite different, however, in that even at low fields the spectrum was shifted to lower energies by several volts, indicating a considerable "iR" drop. In view of this unusual behaviour it is clear that some rather exceptional phenomenon was being observed in this instance, perhaps a gross dust particle, similar to that observed by Cox and Williams [36]. However, the F-N plot showed no unusual characteristics (fig 50). Finally, fig (53) shows the energy distribution from site 3 on this copper specimen compared with that obtained from a reference tungsten emitter. The shift in the copper spectrum is clearly evident.

4.4.4 Following the work on copper, a titanium alloy specimen was examined in the spectrometer. This alloy is manufactured by T.I.L.^{TD}. The resulting spectra from one site are shown in fig 55(a) and (b) and their associated details are given in Table (7). It will be seen that although initially a single peaked spectrum was obtained, after some time under U.V. conditions this split into two peaks. Due to filament failure it was not possible to investigate the effect of outgassing.

4.4.5 The final specimen examined was of stainless steel. Initially there were problems obtaining a stable pre-breakdown current from this material. It was found that a steadily increasing interelectrode voltage would produce no emission current, until at some critical value a micro-discharge would occur in the chamber. However, on one particular sample, a stable site was found and the energy distribution is shown in fig (57). The corresponding spectra details are given in Table (8) and the F-N plot in fig (56).

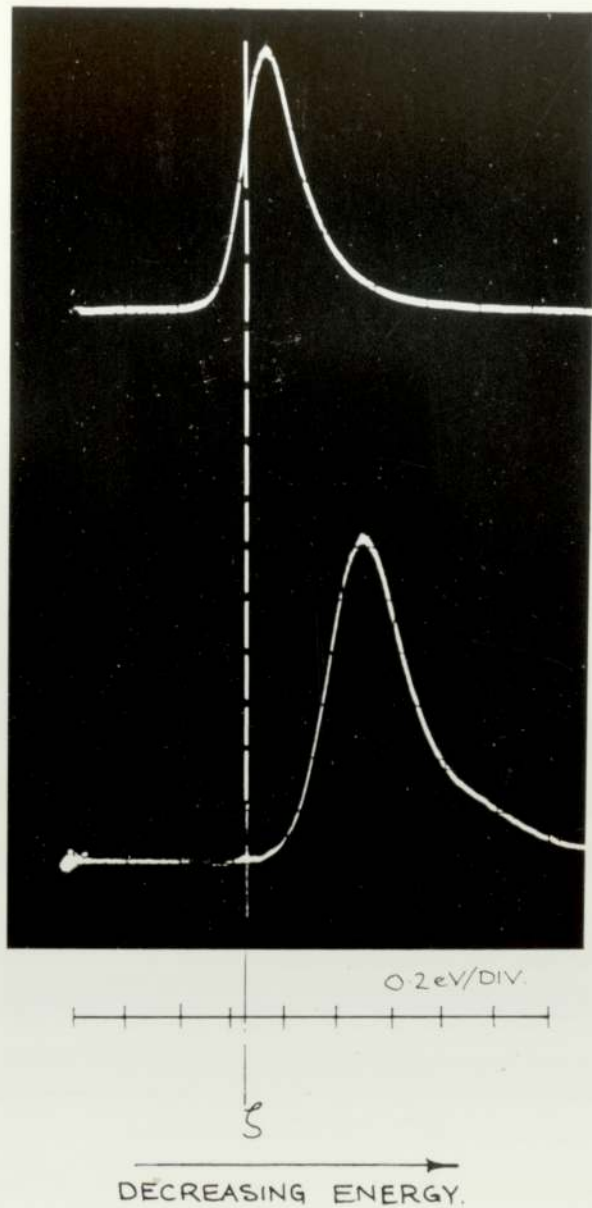
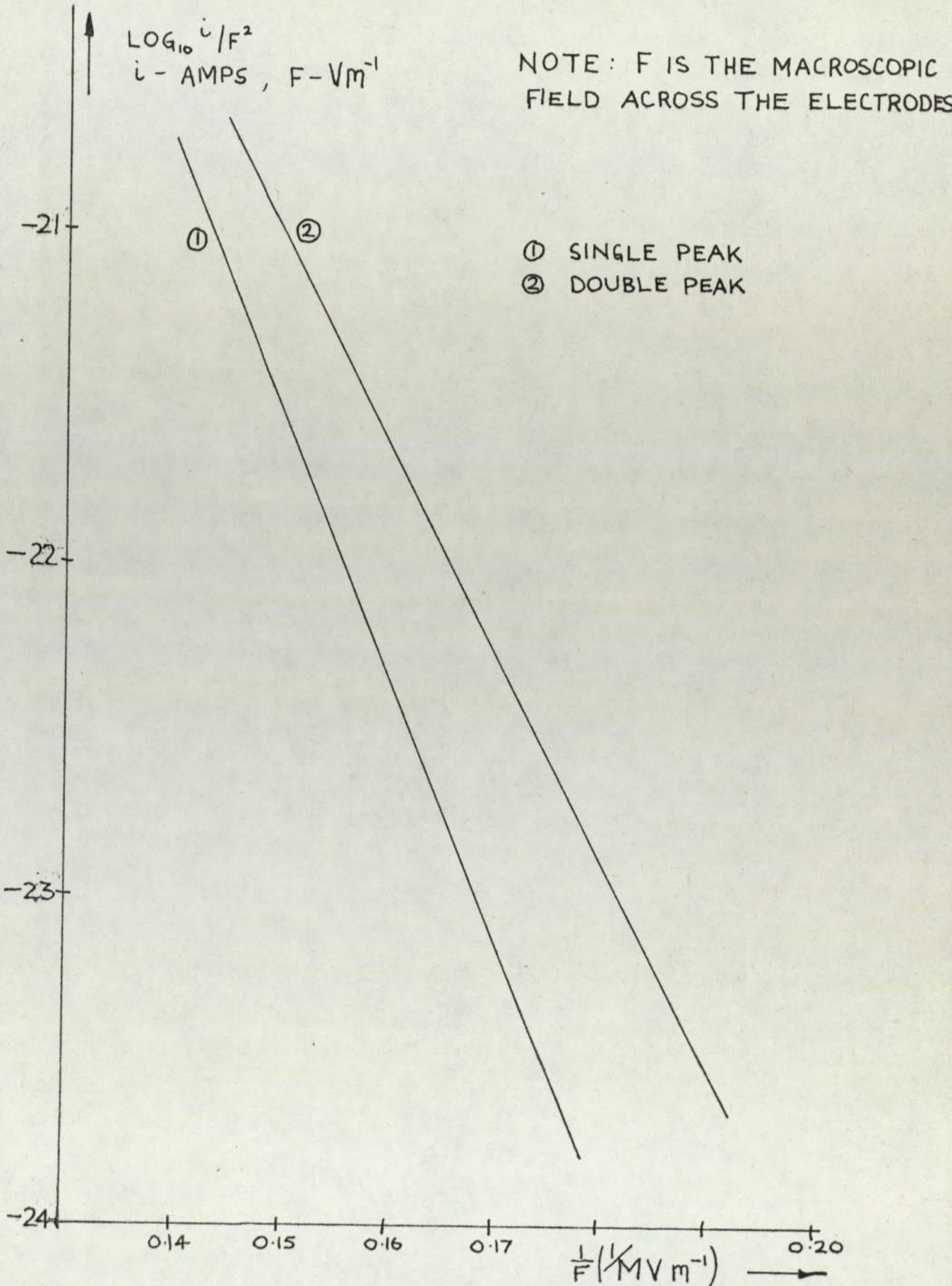
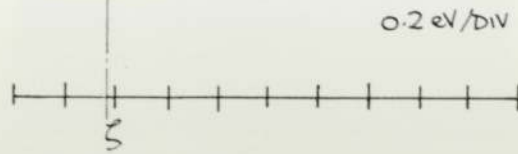
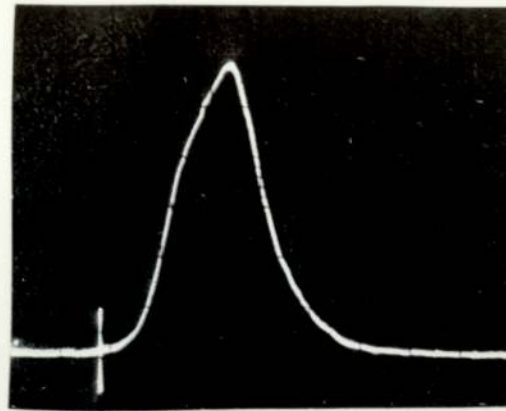


FIG 53. THE ELECTRON ENERGY DISTRIBUTION OBTAINED FROM A REFERENCE TUNGSTEN EMITTER (UPPER CURVE) COMPARED WITH THAT FROM THE COPPER SPECIMEN OF FIG 52 (SITE 3). ELECTRON ENERGY IN eV, 0.2 eV/DIV IS X AXIS (GOING FROM HIGH ENERGY TO LOW ENERGY LEFT TO RIGHT). ELECTRON CURRENT PER UNIT ENERGY IS Y AXIS. THE POSITION OF THE FERMI LEVEL IS SHOWN.

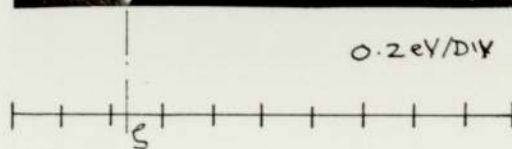
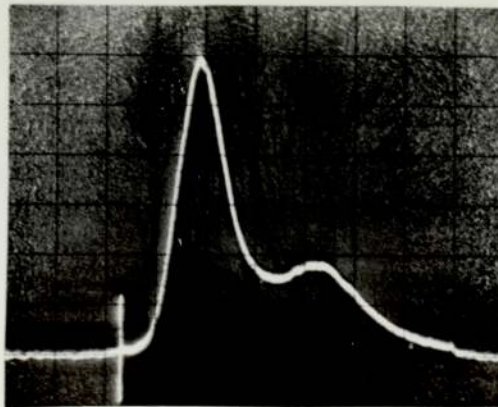
FIG 54. FOWLER-NORDHEIM PLOTS OF TITANIUM ALLOY SPECIMEN.





(A) NO TREATMENT.

→
DECREASING ENERGY.



(B) 18 HOURS UNDER U.H.V.

FIG 55. ENERGY DISTRIBUTIONS OF TITANIUM ALLOY SPECIMEN. THE POSITION OF THE EMITTER FERMI LEVEL IS SHOWN IN EACH CASE. ELECTRON ENERGY IN eV, 0.2 eV/DIV IS X AXIS (GOING FROM HIGH ENERGY TO LOW ENERGY LEFT TO RIGHT). ELECTRON CURRENT PER UNIT ENERGY IS Y AXIS.

Table 7 Titanium alloy specimen at ambient temperature of 300K

Treatment	V_a (kV)	Gap (mm)	F.W.h.M. (ΔE_t) (meV)	High energy slope width $\Delta J(E)$ (meV)	Distribution shift (meV)	Peak Separation (meV)	Field enhance β , from slope of F-N graph (*)
None	10.8	1.76	400	700	350	-	800
16 hours under U.V.	8.3	1.90	-	350	250	500	400
Theoretical value for a metal			230	100	NIL		

(*) Assuming $\phi = 4.1\text{eV}$.

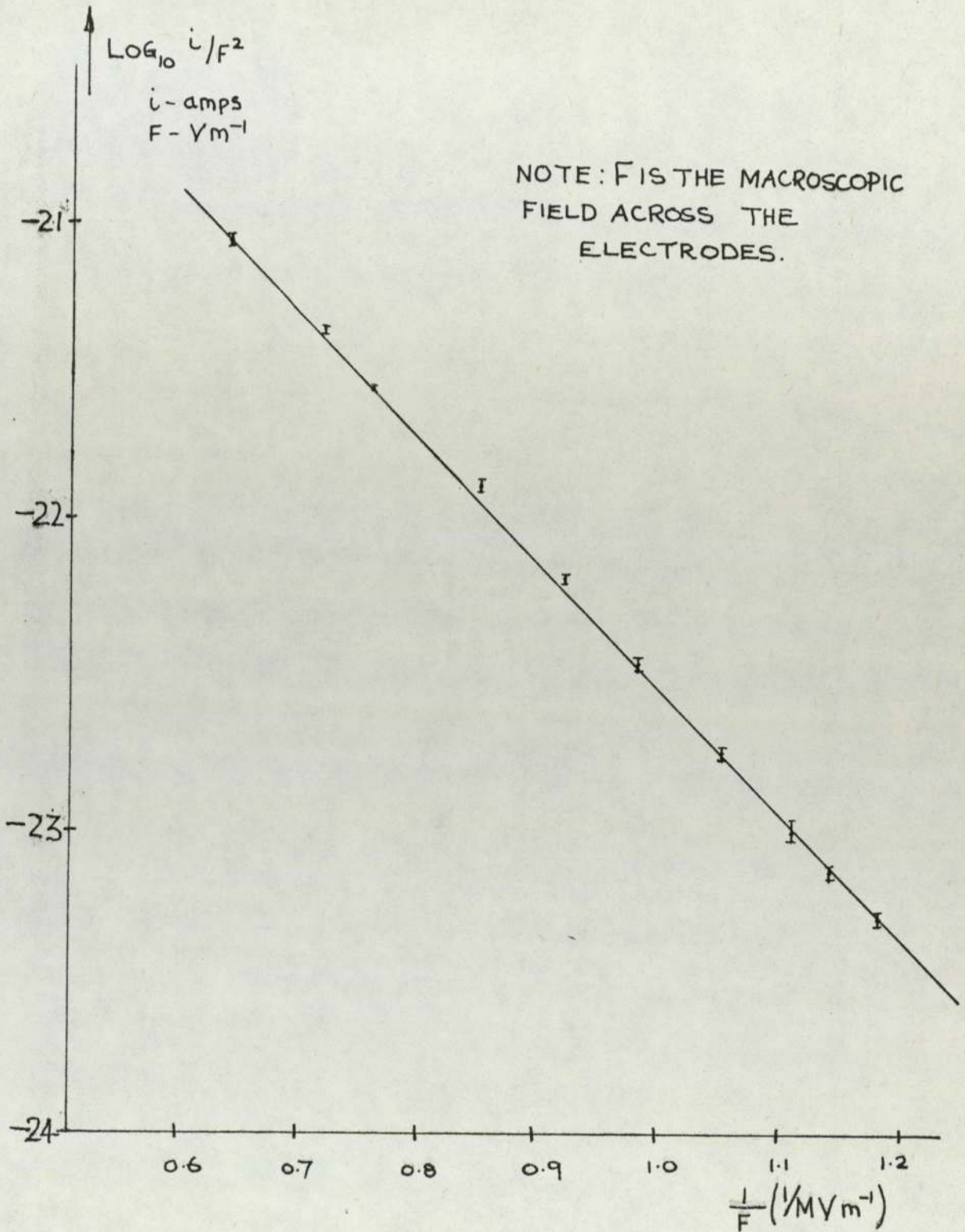
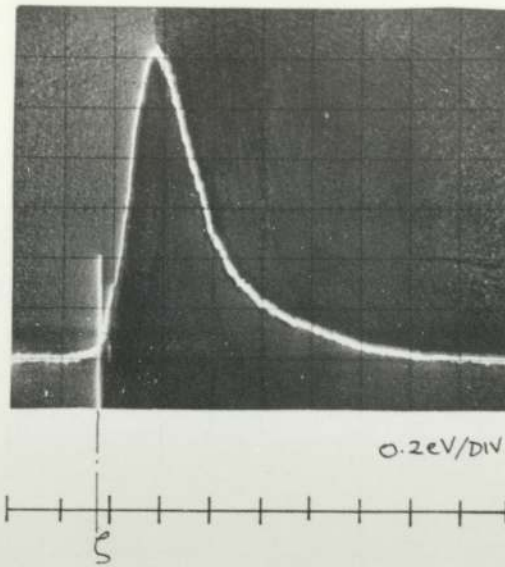
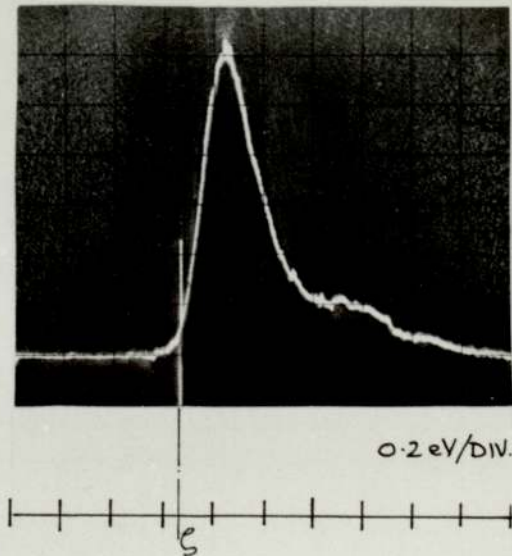


FIG 56. FOWLER-NORDHEIM PLOT OF STAINLESS STEEL SPECIMEN.



(A) NO TREATMENT.

→
DECREASING ENERGY.



(B) 18 HOURS UNDER U.H.V.

FIG 57. ENERGY DISTRIBUTIONS OF STAINLESS STEEL SPECIMEN. THE POSITION OF THE EMITTER FERMI LEVEL IS SHOWN IN EACH CASE. ELECTRON ENERGY IN eV, 0.2 eV/DIV IS X AXIS (GOING FROM HIGH ENERGY TO LOW ENERGY LEFT TO RIGHT). ELECTRON CURRENT PER UNIT ENERGY IS Y AXIS.

Table 8

Stainless steel specimen at ambient temperature of 300K

Treatment	V_a (kV)	Gap (mm)	F.W.H.M. ($\Delta E_{1/2}$) (meV)	High energy slope width $\Delta J(E)$ (meV)	Distribution shift (meV)	Field enhancement β , from slope of F-N graph (*)
None	4.5	0.6	300	150	100	
18 hours under U.H.V.	4.5	0.75	300	120	100	400
Theoretical value for a metal			230	100	NIL	

(*) Assuming $\phi = 4.4\text{eV}$.

4.4.6 The most striking feature which is common to all but one of the emission sites is the displacement of the spectrum to lower energies compared to that normally expected from a metallic emitter, with the result that all electrons are emitted from below the Fermi level. Examining these shifts in more detail, site 2 on copper specimen 4 can be singled out as a special case since there was such a large and critical dependence of the shift on the applied field. Of the remaining copper spectra, the average shift is 450meV with a standard deviation of ~ 300 meV. However, the shifts on specimen 2 were much higher than average whilst some of those from specimen 3 were particularly low, which results in the high standard deviation. Considering, therefore, the single site on specimen 1 and sites 1 and 3 on specimen 4 gives an average shift of 370mV with a standard deviation of 64. The more limited results of titanium and stainless steel give average shifts of 300mV and 100mV respectively.

5.0.0 Studies on high voltage vacuum switch contacts

5.1.0 Introduction

5.1.1 This chapter presents the results of investigations into a material used in an "active" high voltage situation - that of high voltage switching. This particular investigation was carried out as a collaborative venture in which the electron spectrometry technique at Aston was combined with the electron microscopy facility of the vacuum switchgear group at C.E.C.B., Marchwood.

5.1.2 The objective of this special investigation was to identify emission sites on an electrode surface, examine them microscopically at Marchwood and then to transfer the electrodes to Aston in order to recover and examine the sites in the electron spectrometer. In this way it was possible to considerably increase the scope of the examination into the origin of the sites. However, before describing the microscope facility, additional investigations and results in detail, the nature of the vacuum switch problem will be briefly discussed.

5.2.0 High voltage vacuum switches

5.2.1 A discussion of the problems in high voltage switchgear has been given by Gardner et al [87]. The contacts of a mechanical switch have a basically similar function whatever the levels of voltage or current that must be interrupted. Ideally, they should act as a good conductor when closed and provide a good insulating gap when open. When closed, they should be able to open promptly and interrupt their design current without generating excessive over-voltages. When open, they should be able to close promptly, perhaps to pass a very high, short-circuit current, without risk of welding together or suffering other serious

degradation. The flexibility and reliability of the C.E.G.B. transmission system depends on the efficient performance of the large numbers of such mechanical breakers that are used for circuit selection and protection.

5.2.2 For most of their life, these devices are primarily required to switch or carry normal load currents, but they must also be able to interrupt fault currents more than twenty times normal without damage to either themselves or the supply circuit. Currents approaching 60kA at 400kV must be reliably interrupted within 40 milliseconds - barely two cycles of the supply frequency - by equipment using fairly massive moving contacts and it is this occasional, exceptional duty which largely governs their design.

5.2.3 At first sight, the breaking of a circuit carrying current seems a simple matter and, at ordinary domestic power levels, so it is. As soon as the switch contacts begin to separate, a small arc is drawn between them and current continues to flow until the next zero of the supply frequency when the arc is extinguished. The current thus falls smoothly to zero. Were it not for the arc, the rapid interruption of an appreciable current could give rise to dangerously high inductive voltages, since from Faraday's law of electromagnetic induction,

$$V = -L \frac{di}{dt}$$

where L is the inductance of the circuit and $\frac{di}{dt}$ is the rate of change of current.

Should the arc become unstable and collapse while a finite current is flowing, inductive voltages still appear. This behaviour is known as current chopping and its avoidance is an important consideration in high power switch design, especially where the current in inductive loads is to be interrupted.

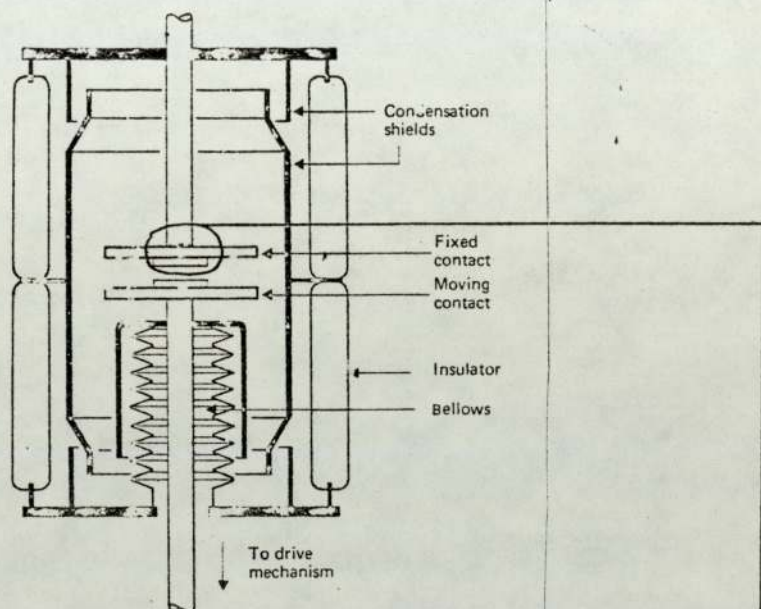
5.2.4 At voltages beyond the domestic level, the useful properties of the switching arc become a disadvantage under atmospheric conditions. Instead of remaining extinguished the arc may re-ignite if voltage builds up again too rapidly before the dielectric strength of this gap has recovered. Re-ignition can be inhibited by causing the arc to extinguish sooner in advance of current zero by using several gaps in series or by drawing the contacts further apart until the available voltage can no longer sustain the discharge. However, at kilowatt levels arc lengths become too great for this to be practical and extinction must be achieved by other means. In practice, therefore, the presence of an arc on opening the switch is accepted; the main design task is to ensure controlled collapse of the arc - primarily by being able to cool it well enough for it to extinguish near current zero - and then to build up sufficient dielectric strength in the gap to prevent re-ignition.

5.2.5 At present the most successful high voltage switch is the gas-blast type using SF_6 gas. In this design a sheath of high pressure insulating gas is directed along the current path of the arc to extract heat by forced convection; the aim is to remove the arc energy and to achieve minimum residual ionisation at current-zero. Post-zero dielectric strength then depends on the insulating properties of the high pressure gas. Although such switches are meeting the present demand for circuit interrupters at the highest voltage levels - up to 400kV - they are, however, still complex in design and expensive to produce.

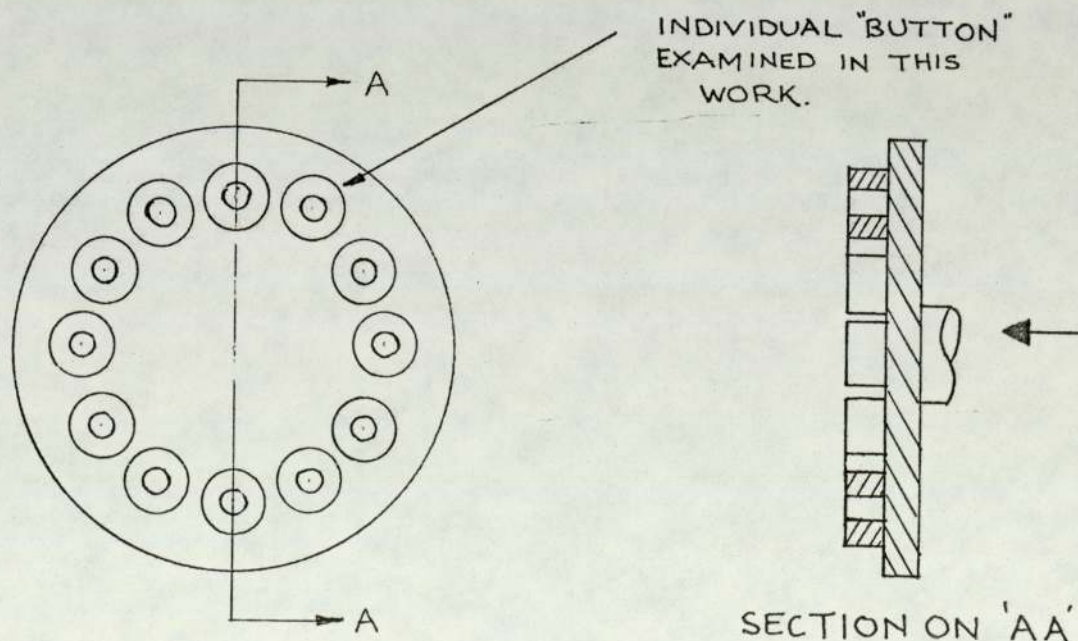
5.2.6 In theory, a far more elegant and much less expensive solution to the problem would be to use a vacuum switch. A vacuum switch consists of two contacts sealed into an evacuated, insulating envelope. One contact is mounted on a bellows so that it can be withdrawn to break the circuit. Deposition of evaporated electrode material on the insulator

is prevented by a shield. A schematic diagram of such a switch is shown in fig (58). Contact motion is relatively small - typically 10 - 20mm - and the arc plasma forms from vaporised electrode material. At the instant of contact separation, all the current flows through a few final points of contact, which are heated and partially vaporised. Subsequently, the supply of vapour is replenished from the "arc spots" - the intensely hot localised areas at which the arc joins the cathode. The gap normally recovers the dielectric properties of vacuum in ~ 10 microseconds. The rapidity of the recovery processes means that vacuum switches are generally capable of sustaining much more rapid rates of rise of recovery voltage than other types of switchgear.

5.2.7 The average vacuum switch, with a contact separation of 10 - 20mm has a reliable voltage rating of only $\sim 20\text{kV(rms)}$ while a 10mm gap between polished plane electrodes will typically hold off 300kV. Since the breakdown voltage for plane electrodes increases as the square root of the gap, it might at first appear that switch ratings could be improved by increasing the contact clearances. Apart from making the switches rather cumbersome, such an increase could lead to poor dielectric recovery performance as a result of the increased distances that vapour molecules would have to travel before clearing the arc space. The object of the present investigations, therefore, is to try to identify the fundamental performance limitations of the vacuum switch to see if they can be overcome with improved design or materials. Of greatest interest are the limitations of the vacuum switch in the ability to interrupt fault currents and also the ability to withstand the re-imposition of voltage across the gap once the switching arc has collapsed. Accordingly, a considerable research effort has been devoted to determining the cause of breakdown in a vacuum switch when the opened



(a) SECTION THROUGH COMPLETE SWITCH.



(b) DETAIL OF CONTACTS.

FIG.58 SCHEMATIC DIAGRAM OF A VACUUM SWITCH (FROM GARDNER et al [87]). ARC EXTINCTION AT CURRENT ZERO DEPENDS ON THE CONDENSATION OF ELECTRODE VAPOUR ON ELECTRODES AND METAL SHIELDS. THE SHIELDS ALSO PROTECT THE INSULATING ENVELOPE FROM CONTAMINATION.

contacts are subjected to an increasingly high voltage. In common with the "passive electrode" situation, it is believed that the cause of such breakdown may be identified with the existence of pre-breakdown currents from localised sites on the cathode surface. As shown in the inset of fig (58), a modern vacuum switch does not have a single planar surface for each electrode, but a series of circular "buttons" arranged in an annular ring. The reason for the arrangement is to facilitate the movement of the arc prior to its collapse, this helps to prevent excessive heating and damage to a particular area of the electrode surface which would otherwise occur if the arc was allowed to "root" only on one spot. Commercial electrode materials are usually a compromise of the various requirements and are commonly based on copper with certain additions to prevent their welding together. The present studies are concerned with a chromium-copper alloy currently used in vacuum switches.

5.2.8 The electron microscope facility at Marchwood laboratories was designed to identify and measure electron emission sites on individual contact "buttons" and subsequently to observe the surface topography in the region of the emission site. This facility was developed by Cox [34] and was used by the present author for the studies reported here.

5.2.9 Fig (59) highlights the complementary nature of the experimental facilities at Aston and Marchwood and the similarity of the scanning technique and position co-ordinates.

5.3.0 Description of the microscope facility

5.3.1 The microscope used in this facility was a Vacuum Generators Miniscan scanning electron microscope (S.E.M.) with a resolution $\approx 100\text{nm}$ operating at $\approx 10^{-8}$ torr. A low magnification micrograph of a switch-

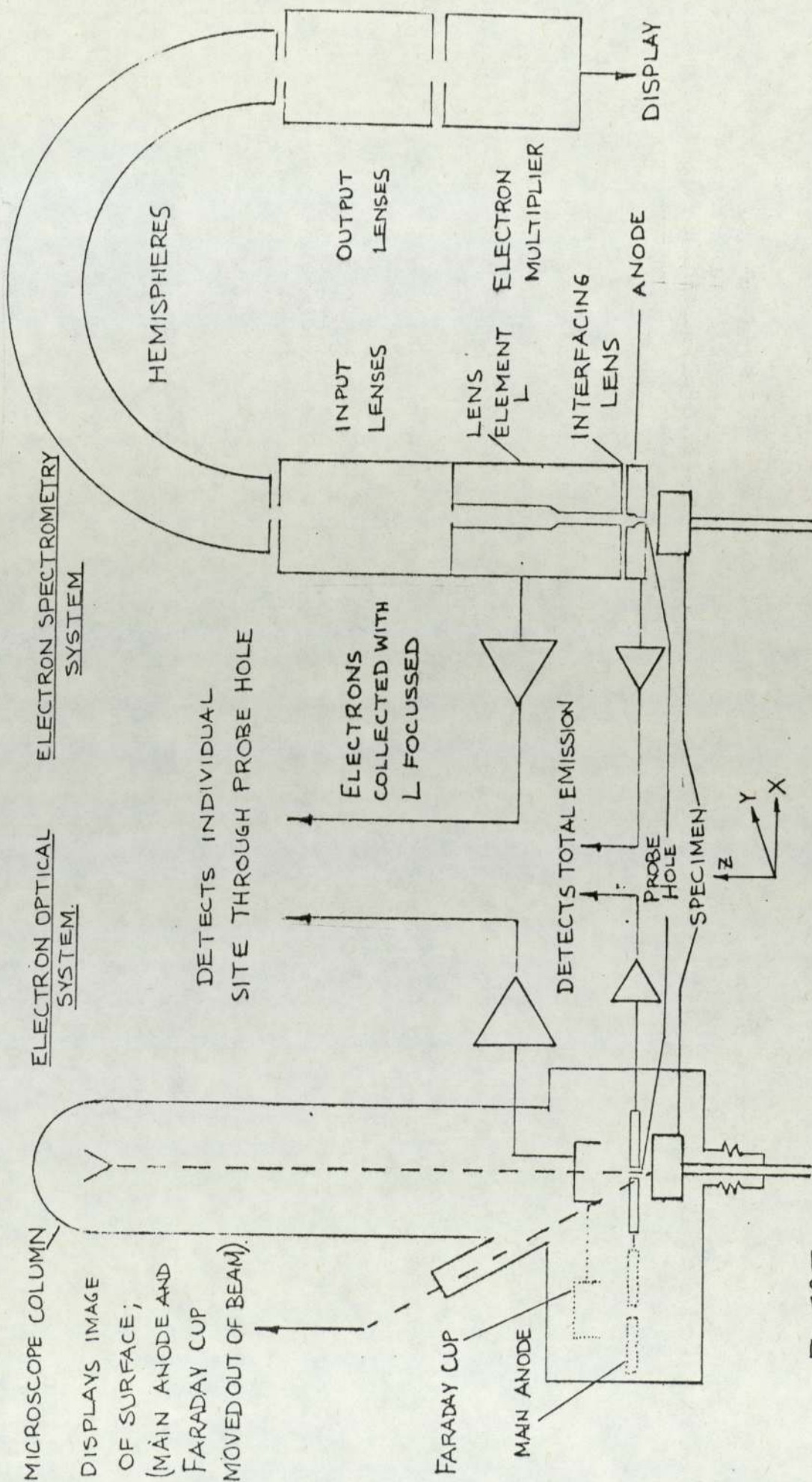


FIG. 59. THE COMPLEMENTARY SYSTEMS FOR INVESTIGATING ELECTRON EMISSION SITES ON BROAD AREA ELECTRODES.

contact specimen inside the microscope, showing the outline of probe and main anodes is shown in fig (60). The facility is basically similar to the earlier probe method of Cox and Wort [30] but in this case the specimen is scanned with respect to the stationary anode. The stainless steel anode has two sizes of probe hole; one is 500 μ m in diameter for rapid and coarse location of the emission sites and the other is \sim 5 μ m in diameter for precise location of the site and detailed mapping of its emission pattern. The probe anode, which is a flat plate inside a Faraday cup, is also moveable to allow it to be positioned either over the probe anode hole to detect any current passing through, or to be pulled clear of the hole for electron microscopy. Fig (61) is a close up of the exterior of the complete instrument showing the probe anode manipulator which allows 3 degrees of translational motion.

5.3.2 The specimen is moved by means of the microscope manipulator assembly which allows rotation $\pm 90^\circ$ tilt and three degrees of translational motion, reproduceable to better than 10 μ m. An electric motor drives one of the translational movements and a potentiometer connected to the common drive shaft provides an electrical analogue of the specimen position for feeding a mechanical x - y plotter. An insulator on the specimen stage allows the specimen potential to be raised to 20kV with respect to earth. As with the spectrometer system described in Chapter 3, the specimen is moved in a raster pattern beneath the main anode so that all parts of the surface pass beneath the probe hole. A similar alignment procedure is therefore required to make the specimen surface parallel to the polished face of the main anode, and to maintain a constant gap between them throughout the scan. Alignment to achieve a constant gap is carried out using a cone shaped copper specimen. This specimen is

Fig 60

Low magnification micrograph of a switch contact "button" inside the scanning electron microscope. The outline of the main anode can be seen in the lower half of the picture whilst the outline of the probe anode shield is in the top left hand part of the picture.

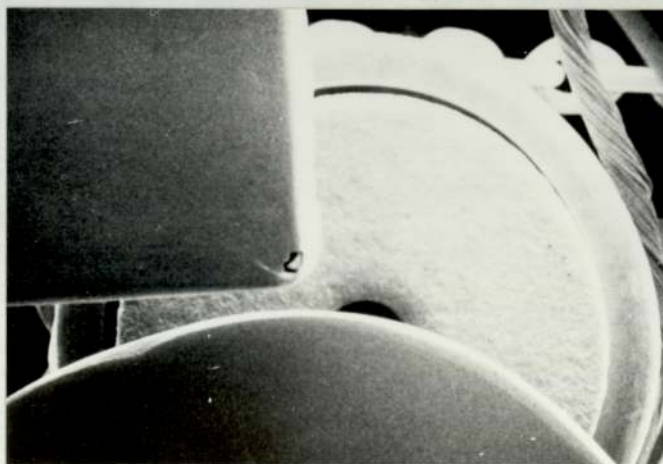
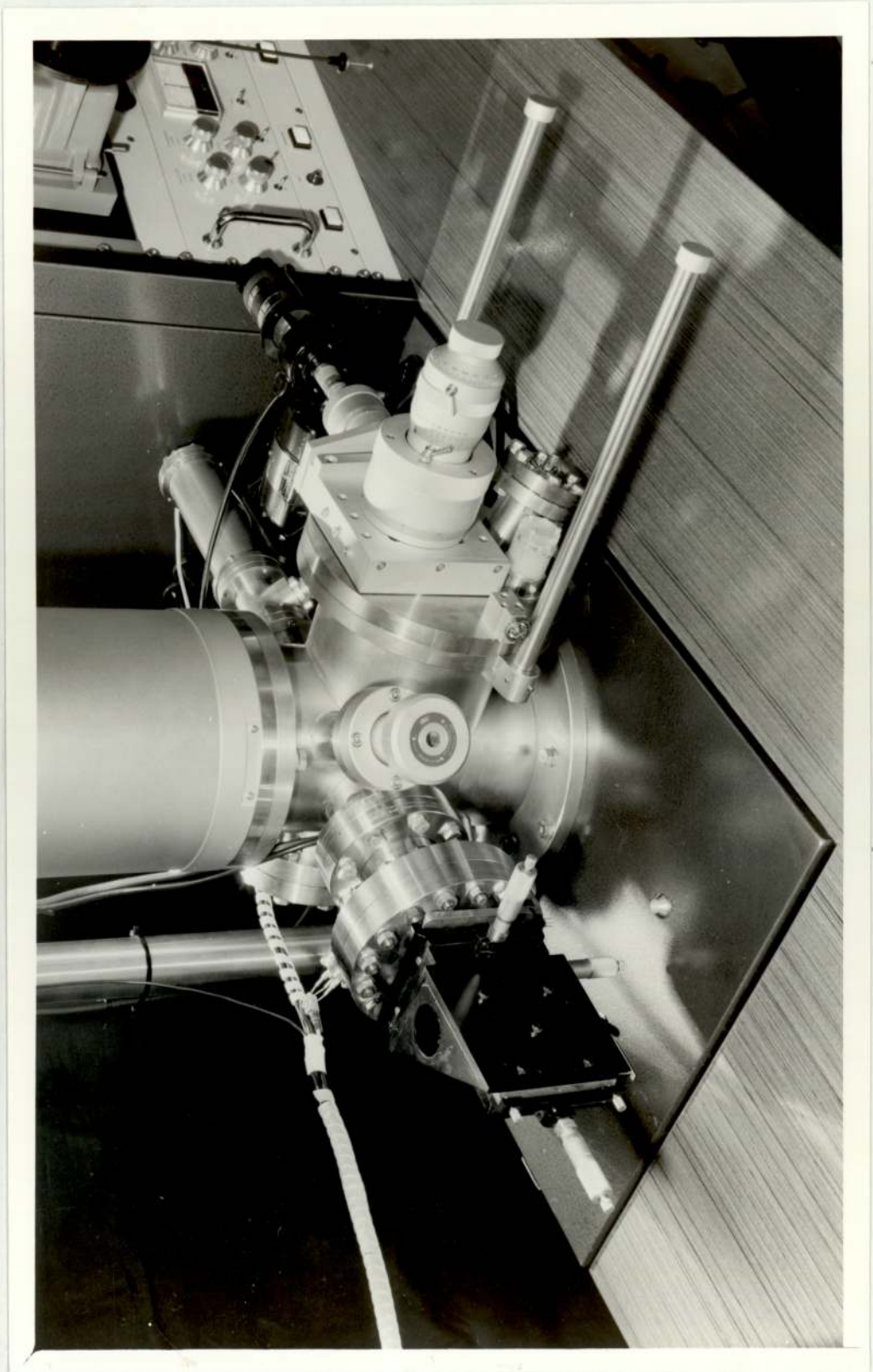


Fig 61

A close-up of the exterior of the microscope
showing the specimen and main anode
manipulator assemblies.

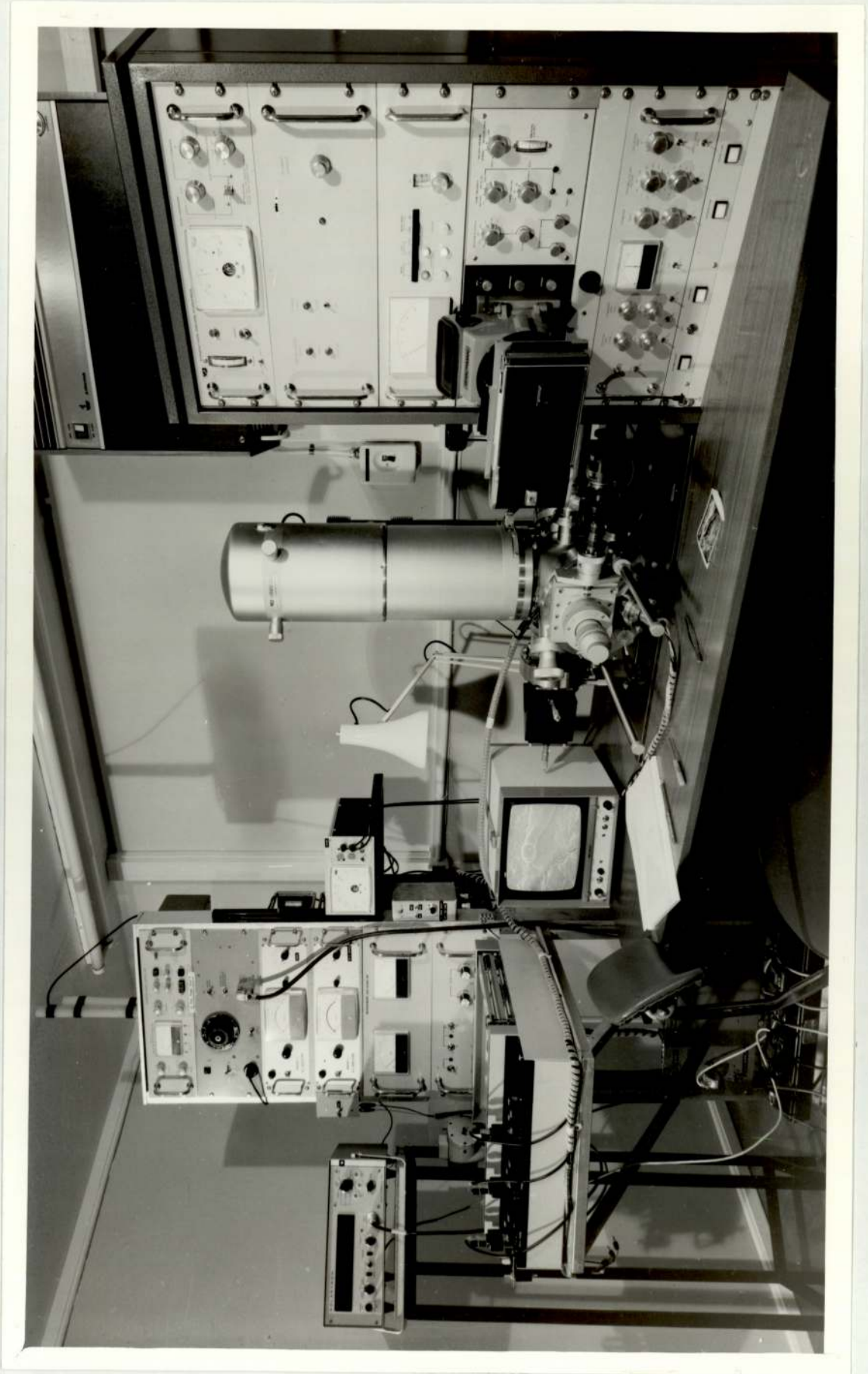


moved to the four extreme positions of the scan and at each position in turn the main anode is lowered down until electrical contact is just made. The height of the main anode is noted in each case and adjustments to the anode can be carried out until all four readings are identical; the scan plane is then parallel to the anode surface. The cone specimen is then removed and the real specimen to be examined is substituted in its place. The alignment of the scan plane automatically makes the x-plane of the specimen parallel to the anode; the y-plane is aligned using the tilt adjustment on the specimen manipulator. The specimen is tilted in each direction until electrical contact is made with the anode; the degree of tilt in each direction is noted. The centre position between these two angles is then set and the anode lowered closer to the specimen. The specimen is then again tilted in either direction and then set in the mid-position. By repeating this procedure down to very small anode-specimen gaps the final position will be accurately parallel to the anode surface. A disadvantage of this system of alignment when compared to that used in the spectrometer is that since interelectrode contact takes place, local surface damage may occur altering the surface topography that is to be examined.

5.3.3 The probe, main anode and specimen can be separately outgassed by electron bombardment from a filament mounted on, but electrically insulated from, the probe manipulator. Electron energies of 1keV are normally used and temperatures in the range 700 to 900°C attained. The specimen chamber is baked to $\sim 120^{\circ}\text{C}$ and all of the electrodes are outgassed prior to making any field emission measurements. The equipment - an overall view of which is shown in fig (62) - is housed within a "clean room" where special air filtering and circulation procedures have been followed in order to minimise dust contamination on the

Fig 62

An overall view of the
scanning electron microscope.



surfaces of specimens prior to their insertion in the S.E.M. Thus, although not as low as normally used for such measurements, the pressure and also the cleanliness of the electrode surfaces are very comparable to those in a vacuum switch.

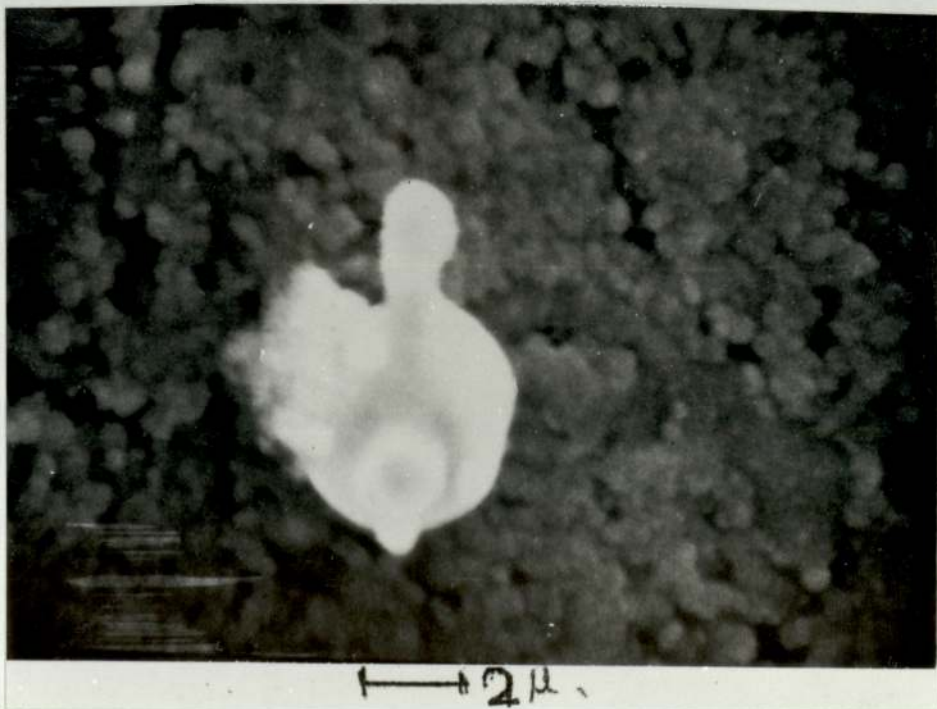
5.4.0 Experimental procedure

5.4.1 The experimental procedure is to spirit clean the specimen in an ultrasonic bath before inserting it into the S.E.M.; in transferring the specimen from the bath to the microscope the surface is kept covered to protect it from atmospheric dust. The surface of the specimen is then examined in the microscope for the presence of any obvious dust particles; these are frequently found despite all the precautions taken and fig (63) shows a typical example of such a particle. Very often they are found to be strong field emitters (see, for example, Cox and Williams [36]) and are characterised by having high β factors. Whilst obviously of interest in themselves this type of emitter tends to be rather transitory in nature and can easily be destroyed on removal from the S.E.M. Since the object of this investigation was to examine sequentially a site in both the S.E.M. and the electron spectrometer it was clearly desirable to have a site which was sufficiently permanent and stable to withstand removal and transit from one experimental facility to the other. Therefore, if any dust particles were observable on the specimen surface when in the S.E.M., the specimen was removed and re-cleaned in the ultrasonic bath - several times if necessary - until all dust particles had been eliminated.

5.4.2 When a dust free surface had been obtained the main and probe anode were moved into position and the microscope beam was then switched off. The specimen was then aligned with the main anode in the manner

Fig 63

An electron micrograph of the type of "dust particle" which is frequently found on the electrode surface. As frequently happens with such particles, this one was found to be a strong field emitter.



already discussed. Field emission measurements were then carried out by applying a suitable negative voltage to the specimen to give a pre-breakdown field emission current of a few microamperes at the "earthy" main anode. With the large probe hole on the optical axis of the electron microscope and the probe anode immediately above this, the specimen was then scanned in a raster pattern in a similar way to that used on the electron spectrometer. If an emitting region passed beneath the hole, electrons passed through it, were collected by the probe and fed a signal to the y axis of the mechanical plotter. When the site was positioned centrally beneath the hole - i.e. the position of maximum current collection - a current-voltage characteristic of the site was measured so that a Fowler-Nordheim analysis of the emitter could be carried out. A possible criticism of this technique is that no allowance is made for the lens effect of the main anode probe hole which is exactly analagous to that of the spectrometer system and illustrated in figs 22(a) and (b). Consequently, not all the emission current may be collected at the probe anode which would have the effect of reducing the predicted value of β .

5.4.3 The next step was to accurately position the site to ensure that the microscope examined the correct area of the specimen. To do this, the microscope filament was again switched on and the probe temporarily pulled away from the beam. The small hole on the main anode was then placed centrally in the beam, this being verified by varying the magnification of the microscope from minimum to maximum and ensuring that the hole remained central in the microscope image. This adjustment was very critical since it was essential to ensure that the microscope was imaging the precise area directly beneath the anode hole at all magnifications. It was found necessary to have the microscope beam on for a warm-up

period of 15 - 30 minutes before making this adjustment, after which the setting remained stable. The probe anode was then returned to its position above the main anode hole and the microscope filament was switched off.

5.4.4 Because of the roughness of the arced surfaces, the electric field can be considerably distorted in the region of an emitting site giving rise to some lateral displacement in the trajectory of emitted electrons. A trajectory plotting technique was therefore used for precisely locating the position of emitters under these conditions. Using the small hole in the main anode the specimen was positioned such that the current collected by the probe was a maximum. This procedure was then repeated at gradually reducing separations, and the position of the specimen at maximum current plotted as a function of separation. This effectively gave the trajectory of the centre of the electron beam and extrapolation to zero gap gave the co-ordinates of the emitter. The specimen was then set to these co-ordinates and the microscope filament was again switched on. After warm-up the probe anode was withdrawn and a final check made that the small hole in the main anode was central in the microscope image at all magnifications. This anode was then pulled clear and the microscope used to examine the predicted area at the appropriate magnification.

5.4.5 One further measurement that could be made was to replace the main and probe anodes and, using the small hole, determine the co-ordinates of the positions of constant current. In this way a current contour map of the emission site could be constructed, reflecting the shape of the site itself.

5.5.0 Results

5.5.1 A number of specimens were examined in the S.E.M. with a view to finding sites which could be later examined in the electron spectrometer. In spite of the large number of surface microfeatures which were present on the electrodes only one or two emission sites were found on each specimen examined. Although these were highly stable and remained unchanged when under vacuum, removal and exposure to atmospheric pressure could sometimes result in the loss of a site. Therefore, an endeavour was made to select a site which would be reproduceable in both the S.E.M. and the electron spectrometer.

5.5.2 Fig (64) shows a series of electron micrographs taken in the S.E.M. of the electrode surface area containing such an emission site whose characteristics were examined in both instruments. Fig (65) curve (1) shows the corresponding F-N plot taken from the i/V measurement of the site and fig (66) shows the trajectory plots for the x and y co-ordinates.

5.5.3 Following the measurements the specimen was then transposed to the spectrometer system in a dust free capsule and mounted at the same orientation as in the S.E.M. The specimen was then aligned in the spectrometer and using the position co-ordinates obtained from the microscope and transferring these to the spectrometer as described in Chapter 3, the emission was again detected.

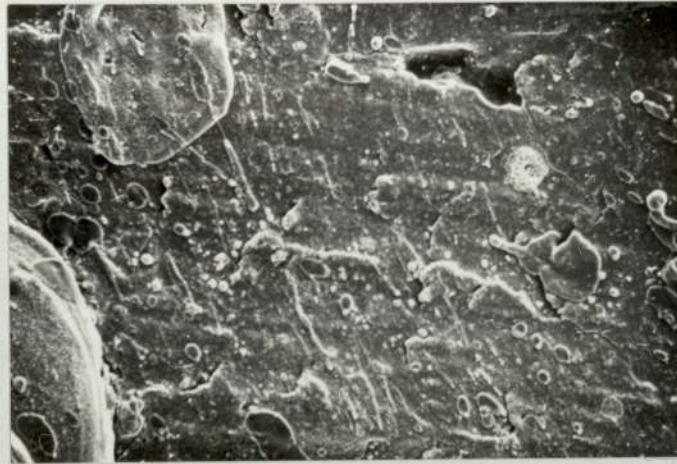
5.5.4 The first spectrum obtained from the site when initially mounted in the spectrometer is shown in fig 67(a) and the corresponding F-N graph taken from the measured i/V characteristic is shown in fig (65), curve 2. Further spectra measured at regular intervals revealed a gradual reduction in the low energy peak until, after 24 hours, only the high energy peak remained (curves (B) and (C)). The F-N plot of the measured $i-V$

Fig 64

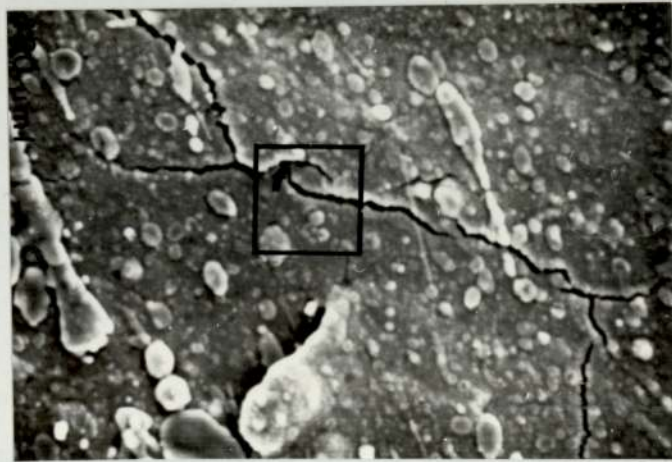
A series of micrographs taken in the V.G. scanning electron microscope showing the predicted area of the field emission site (20μ square). The arrow indicates the surface crack where the anomalous X-Ray spectrum was found when the specimen was later examined in the Cambridge microscope (see also fig 68).



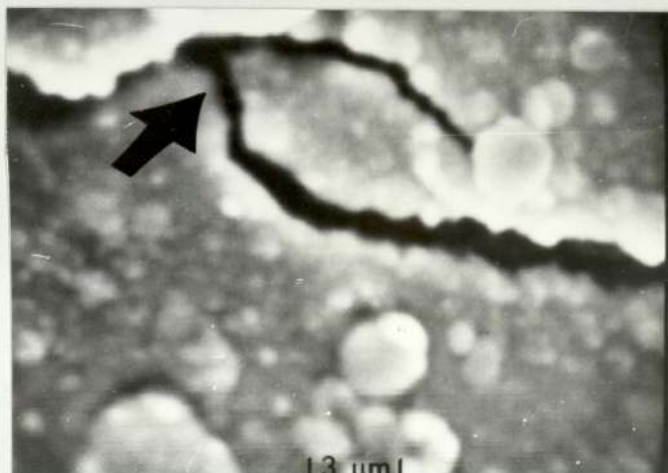
100 μm



100 μm



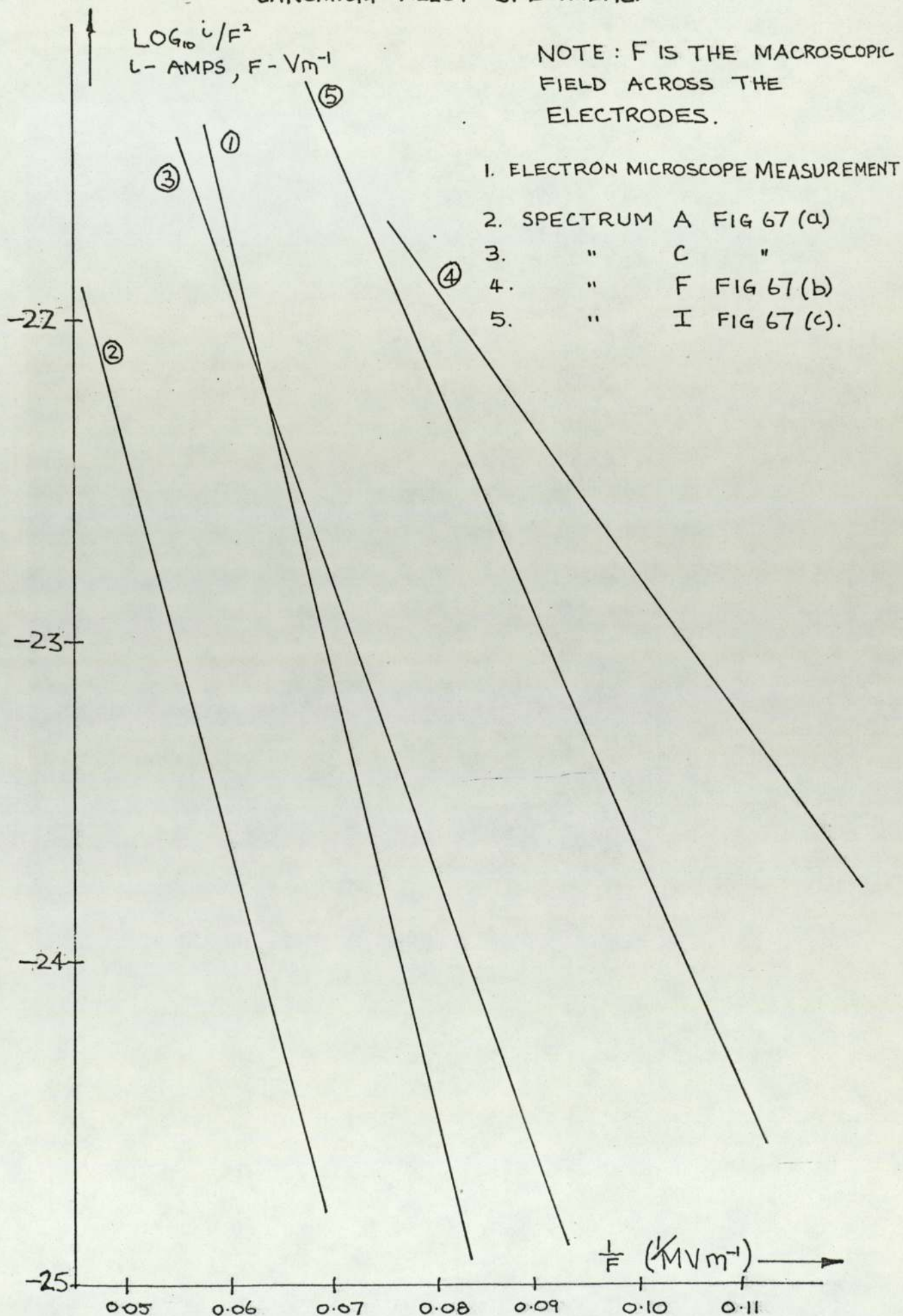
20 μm



3 μm

13 μm

FIG 65. FOWLER-NORDHEIM PLOTS OF COPPER-
CHROMIUM ALLOY SPECIMENS.



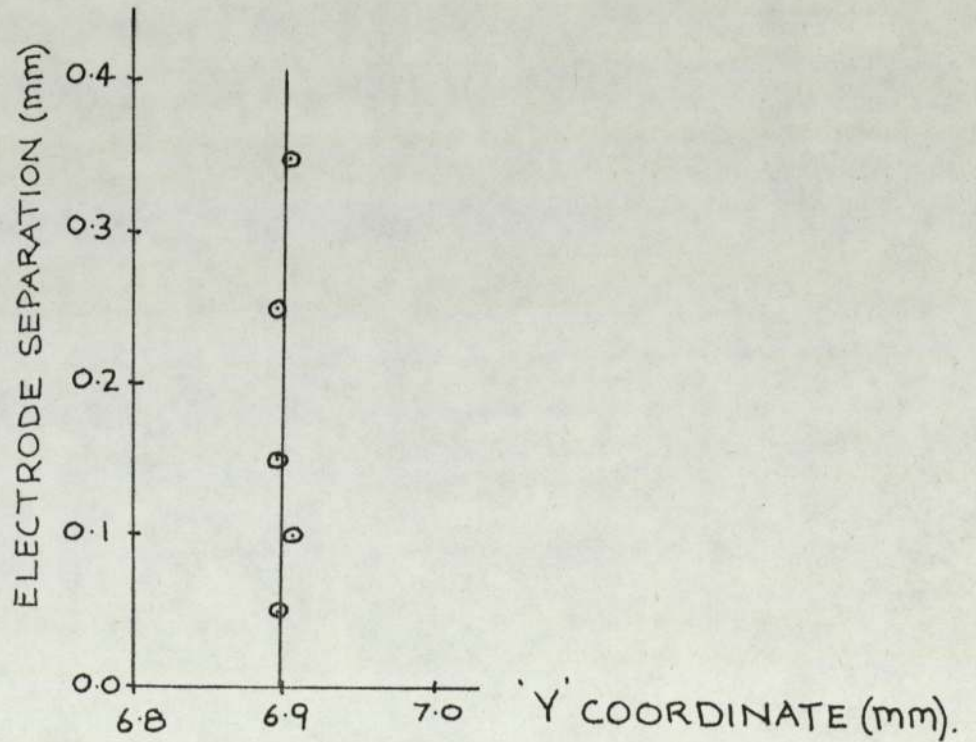
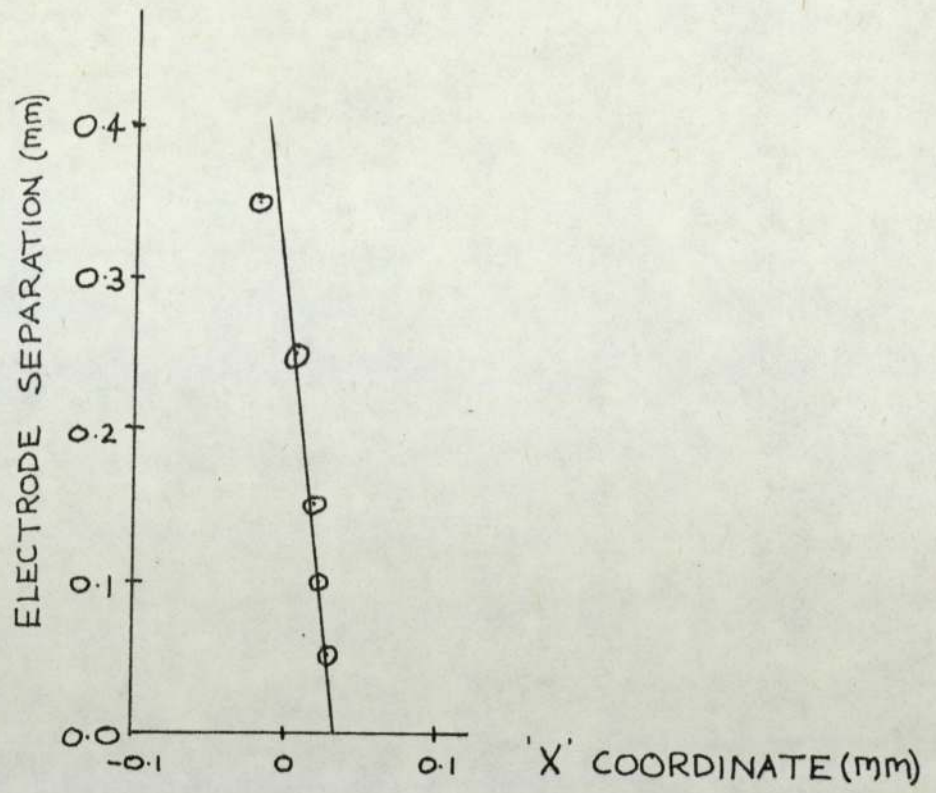


FIG 66. TRAJECTORY PLOTS OF THE ELECTRON EMISSION SITE ON THE CHROMIUM-COPPER SPECIMEN.

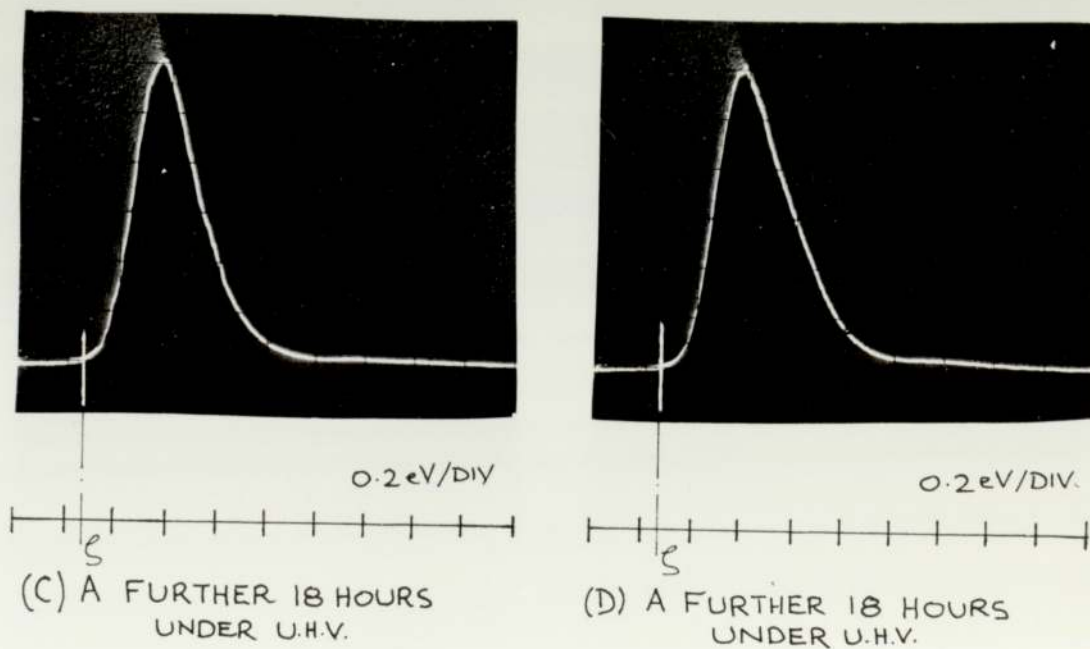
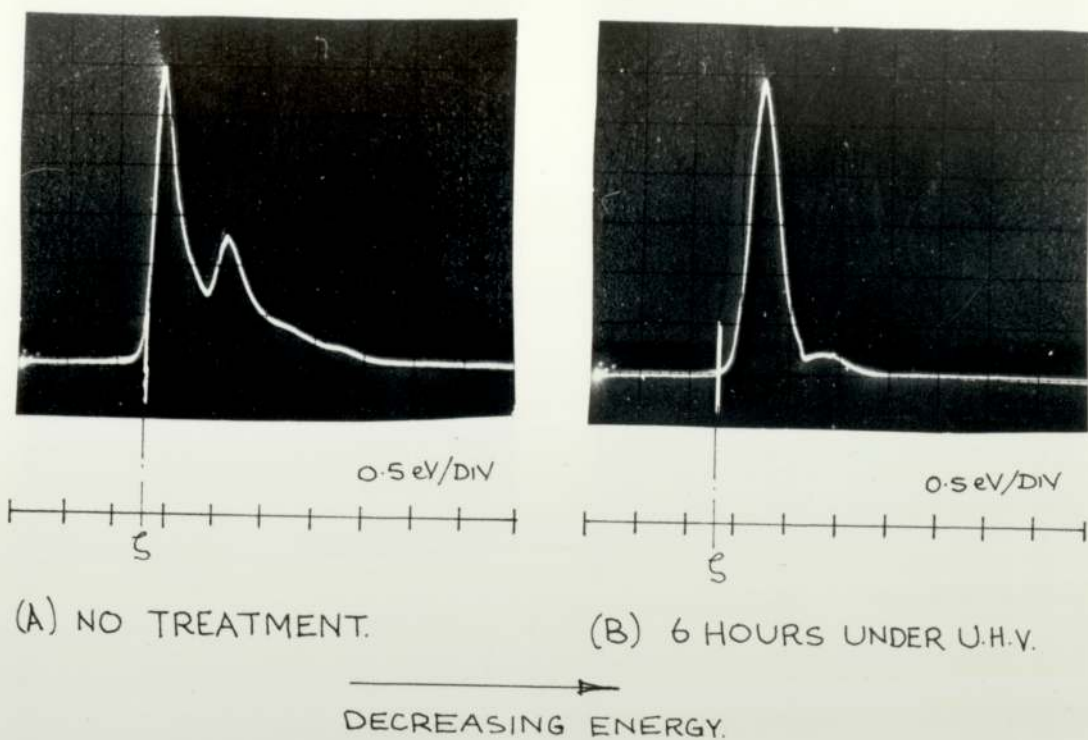
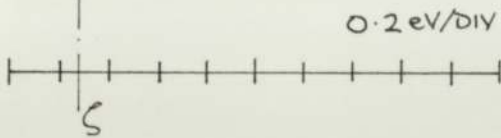
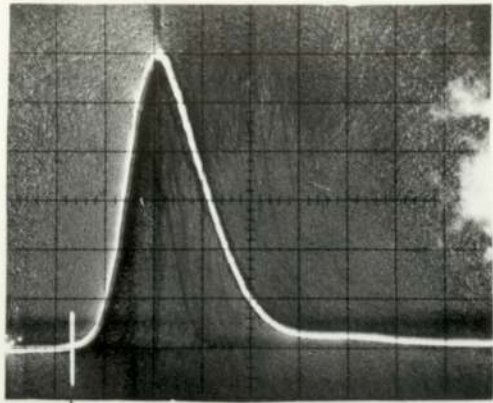


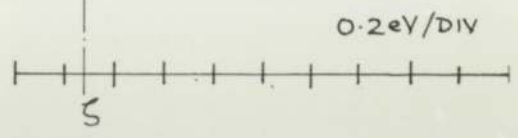
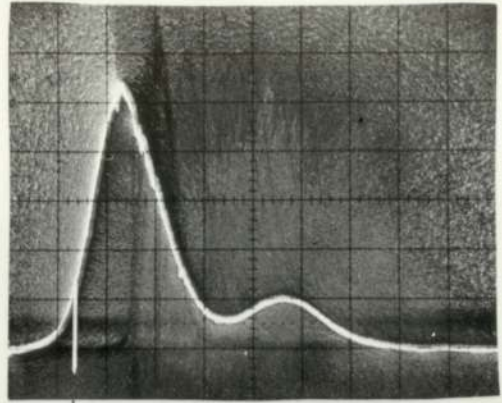
Fig 67(a). ENERGY DISTRIBUTIONS OF CHROMIUM - COPPER ALLOY SPECIMEN. THE POSITION OF THE EMITTER FERMI LEVEL IS SHOWN IN EACH CASE. ELECTRON ENERGY IS X AXIS (GOING FROM HIGH ENERGY TO LOW ENERGY, LEFT TO RIGHT). ELECTRON CURRENT PER UNIT ENERGY IS Y AXIS.

characteristic of (C) is shown in fig (65) curve 3. No further changes occurred when the spectrum was left untreated for a further 36 hours (fig 67(a)(D) and fig 67(b)(E)). The specimen was then outgassed using 1keV electron bombardment at a dissipation of 50W for 2.5 mins., the temperature rising to $\sim 700^{\circ}\text{C}$. An energy spectrum obtained about 10 mins. after this treatment is shown in fig 67(b)(F) and it is seen to have returned to the earlier double peak of curve (A). The corresponding F-N plot, taken from the i-V characteristics at this stage, is shown in fig (65) curve (4). After a further outgassing for 2.5 mins. there was no substantial change in the spectrum (fig 67(b)(G)) but after being left under vacuum for a further 30 mins. the distribution again returned to the single peak shown in fig 67(b)(H). Finally, the spectrum obtained after the specimen was left under vacuum for a further 18 hours is shown in fig 67(c)(I); the corresponding F-N plot is shown in fig (65) curve (5). Full details of the parameters of each of the spectra is given in Table (9).

5.5.5 To provide further information about the nature of the emission site, the specimen was removed from the spectrometer and inserted in a conventional scanning electron microscope - a Cambridge S.E.M. 2. This instrument also had a Kevex X-Ray analysis attachment for determining the elemental composition of the specimen area being viewed. The area of the specimen containing the emission site was examined and electron micrographs of this region are shown in fig (68). These show that the specimen had suffered no evident changes from the earlier micrograph shown in fig (64). Having confirmed this, the instrument was switched to a manual scan of the 20kV, 10nA and 25nm diameter electron probe so that the X-Ray facility could be used to study selected points within the predicted emission area. It was found that whilst the region was generally characterised by the spectrum of fig 69(a) with the anticipated strong copper and chromium peaks reflecting the alloy composition of the bulk

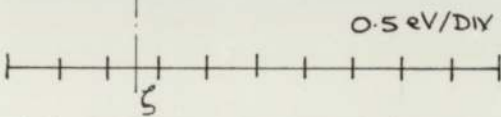
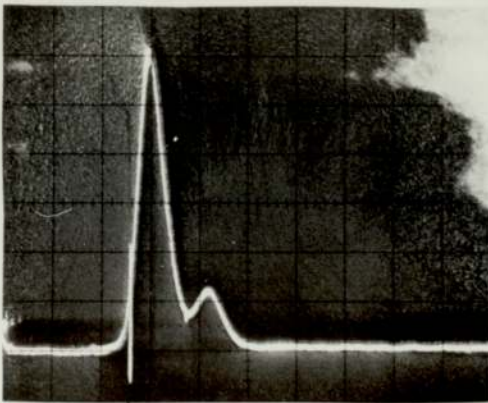


(E) A FURTHER 18 HOURS
UNDER U.H.V.

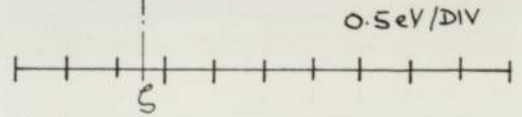
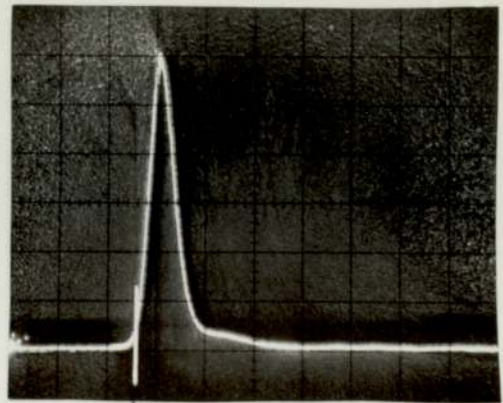


(F) AFTER 2½ MINUTE OUTGAS
AT 50W.

→
DECREASING ENERGY.



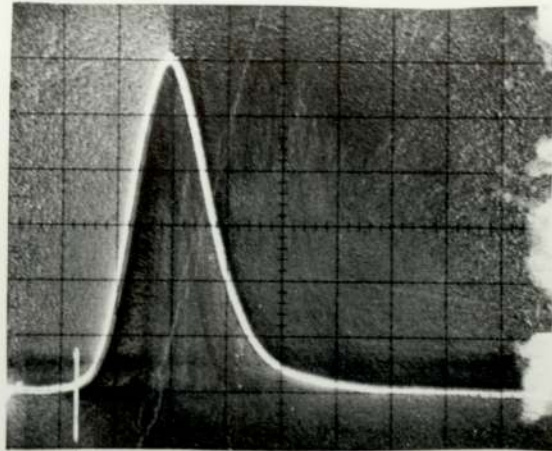
(G) AFTER A FURTHER
OUTGAS FOR 2½ MINUTES
AT 50W.



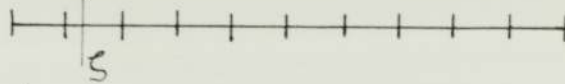
(H) 30 MINS AFTER (G)

FIG 67(b) ENERGY DISTRIBUTIONS OF CHROMIUM - COPPER
ALLOY SPECIMEN. THE POSITION OF THE EMITTER FERMI
LEVEL IS SHOWN IN EACH CASE. ELECTRON ENERGY IS
XC AXIS (GOING FROM HIGH ENERGY TO LOW ENERGY LEFT
TO RIGHT). ELECTRON CURRENT PER UNIT ENERGY IS Y AXIS.

→
DECREASING ENERGY.



0.2eV/DIV



(I) A FURTHER 18 HOURS
UNDER U.H.V. AFTER (H).

FIG 67c ENERGY DISTRIBUTION OF CHROMIUM - COPPER
ALLOY SPECIMEN. THE POSITION OF THE EMITTER
FERMI LEVEL IS SHOWN. ELECTRON ENERGY IS X AXIS,
(GOING FROM HIGH ENERGY TO LOW ENERGY LEFT TO
RIGHT). ELECTRON CURRENT PER UNIT ENERGY IS Y AXIS.

Table 9

Chromium-copper alloy specimen at ambient temperature of 300K
(a) Energy Spectra.

Treatment	V _a (kV)	Gap (mm)	F.W.H.M ($\Delta E_{1/2}$) (meV)	High energy slope width $\Delta J(E)$ (meV)	Distribution shift (meV)	Peak separation (meV)
None (A in fig 67(a))	8.2	0.4	-	150	100	650
6 hrs under U.H.V. (B in fig 67(a))	7.2	0.4	350	250	350	650
Further 18 hrs under U.H.V. (C in fig 67(a))	8.3	0.6	300	150	200	-
Further 18 hrs under U.H.V. (D in fig 67(a))	7.8	0.5	350	150	250	-
Further 18 hrs under U.H.V. (E in fig 67(b))	7.8	0.5	350	150	250	-
Outgas at 50W for 2½ min (F in fig 67(b))	8.0	0.7	-	200	100	650
After further outgassing for 2½ min (G in fig 67(b))	8.5	0.6	-	200	150	650

Table 9(a) contd

Treatment	V_a (kV)	Gap (mm)	F.W.H.M (ΔE) (meV)	High energy slope width $\Delta J(E)$ (meV)	Distribution shift (meV)	Peak separation (meV)
30 mins after G (H in fig 67(b))	7.8	0.6	300	200	200	-
After a further 18 hrs under U.H.V. (I in fig 67(c))	7.2	0.6	300	200	200	-

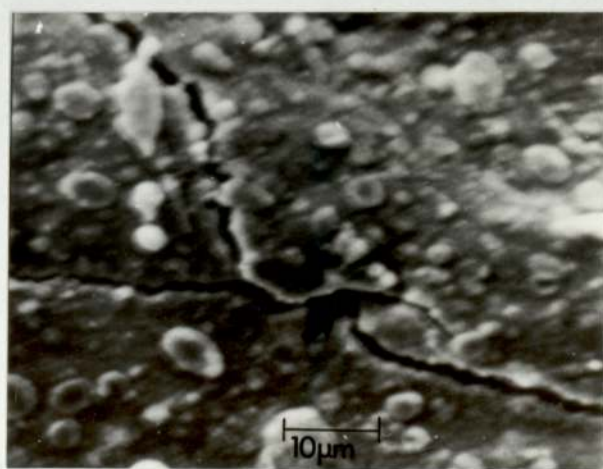
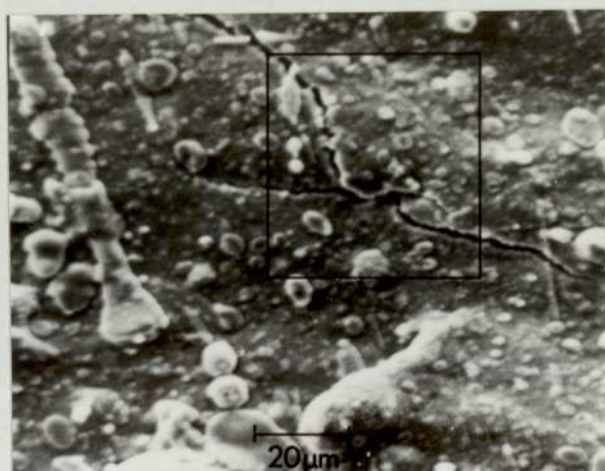
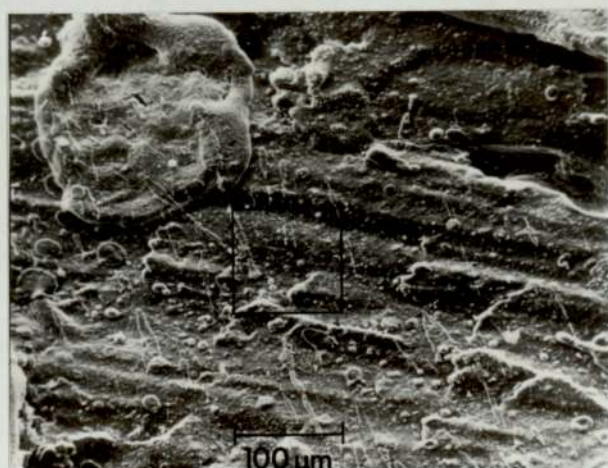
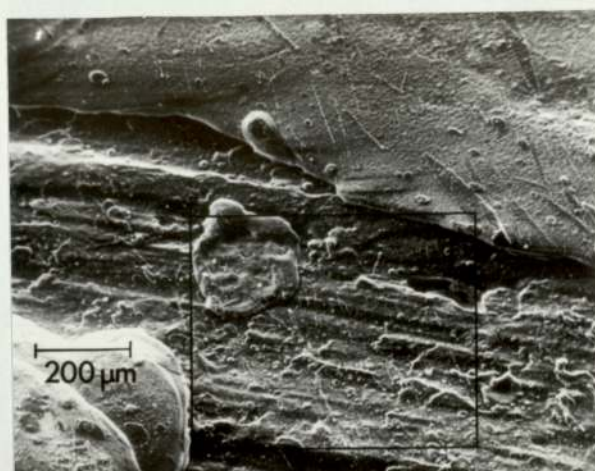
Table 9 (b) Emission site protrusion geometry for the Chromium Copper specimen as predicted from the Fowler-Nordheim graphs

Stage in the experimental sequence when Fowler-Nordheim graph data was measured.	β Factor (*)	Emitting Area $S(\text{am}^2)$	Cone Model		Cylinder Model	
			Height (nm)	Base Dia. (nm)	Height (nm)	Base Dia. (nm)
Electron Optical study	200	530	77 000	13 000	29 000	260
Spectrum A (Fig 67(a))	200	510	7 700	1 400	2 900	30
Spectrum C (Fig 67(a))	280	68	2 900	510	1 500	10
Spectrum F (Fig 67(b))	620	0.04	0.18	39	13	0.27
Spectrum I (Fig 67(c))	380	10	2 100	370	800	4.2

(*) Assuming $\phi = 4.5\text{eV}$.

Fig 68

A series of micrographs taken in the Cambridge SEM 2 scanning electron microscope after the energy spectra of the emission site had been measured in the electron spectrometer. The anomalous X-Ray spectrum of fig 69(b) was obtained from the crack arrowed in the final micrograph.



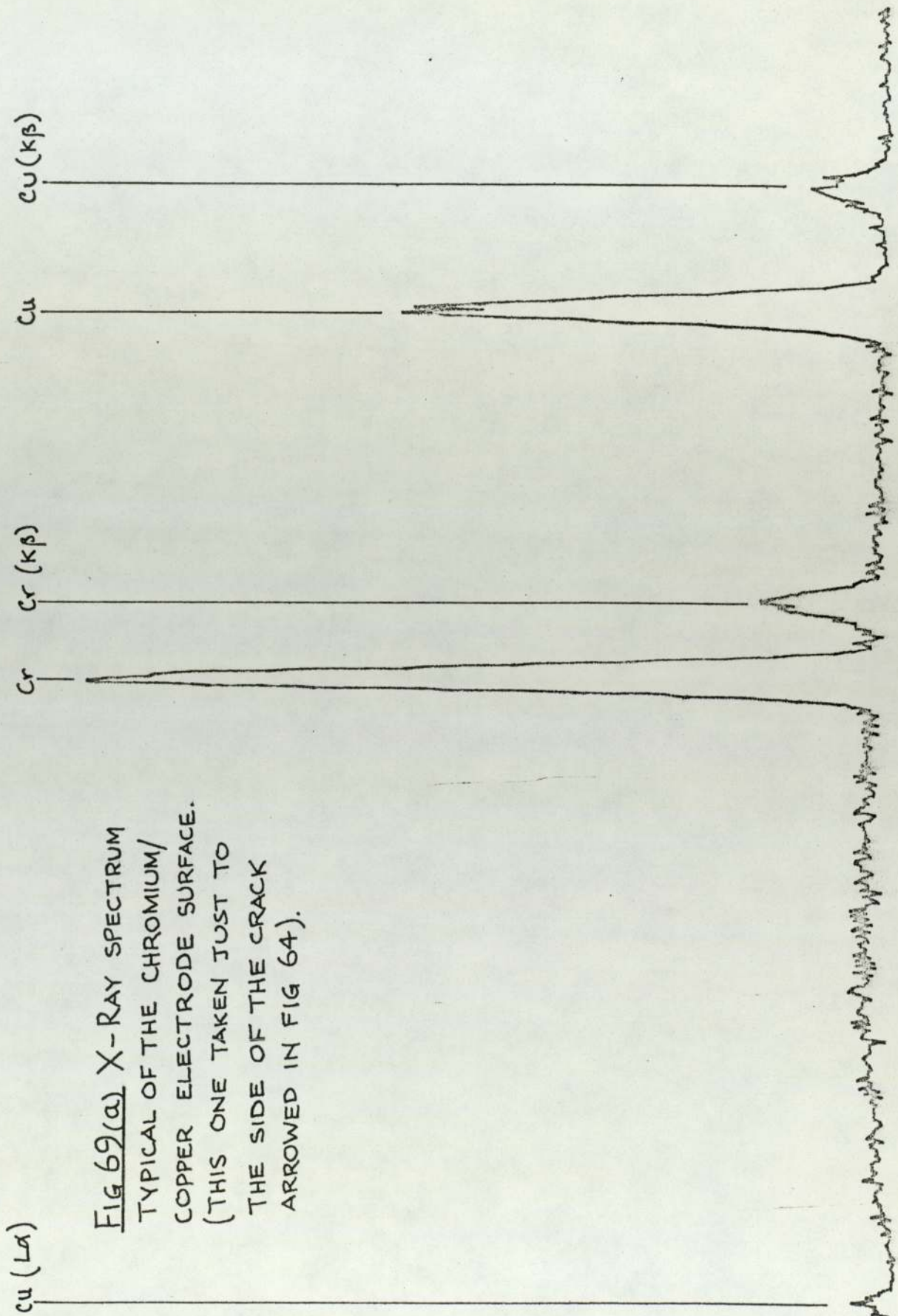
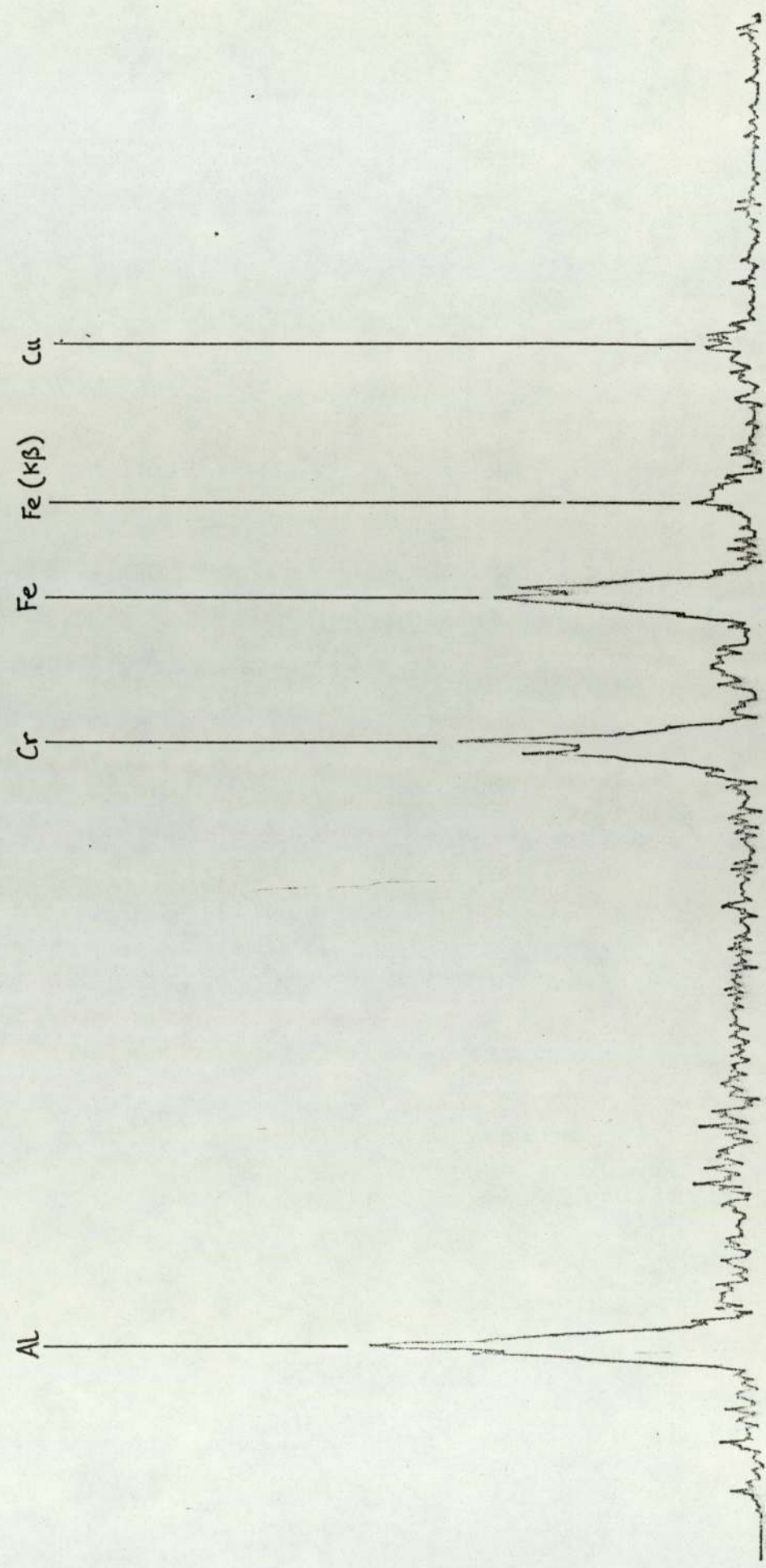


Fig 69(a) X-RAY SPECTRUM
 TYPICAL OF THE CHROMIUM/
 COPPER ELECTRODE SURFACE.
 (THIS ONE TAKEN JUST TO
 THE SIDE OF THE CRACK
 ARROWED IN FIG 64).

FIG 69(b): X-RAY SPECTRUM OF CRACK ON CHROMIUM / COPPER
ELECTRODE (ARROWED IN FIG 64).



electrode, there was one sub-microscopic region situated within the crack/grain boundary (arrowed in fig 64(d)) which displayed the anomalous spectrum of fig 69(b) with the strong Al and Fe impurity peaks. It is thought that the aluminium impurity at least was probably present as the oxide, owing to the alumino-thermic reduction process used in the manufacture of chromium. However, this could not be confirmed because the Kevex system is incapable of detecting oxygen.

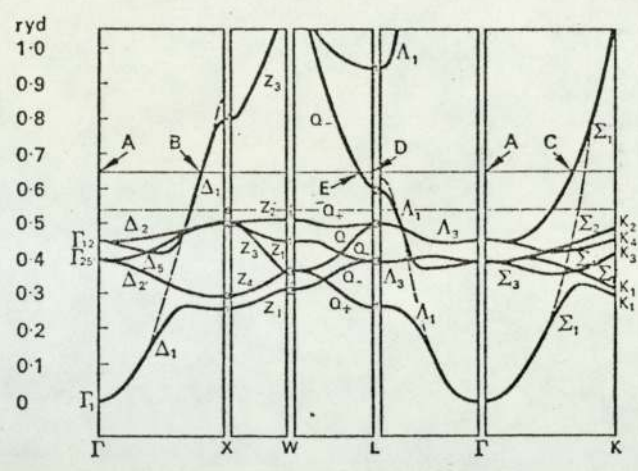
5.5.6 Whilst this finding was clearly of potential significance, alone it did not provide a direct identification of the emitting site. However, during the course of a subsequent detailed study of this site, which necessarily involved its extended bombardment by the electron probe at a power density of the order of 400GW/m^2 , the impurity inclusion disappeared, presumably as a result of some form of thermal activation. On returning the specimen to the electron spectrometer, it was found that the emission site had also disappeared. Although these observations are not absolutely conclusive, taken together, they indicate strongly a correlation between electron emission sites and sub-microscopic impurity inclusions apparently situated along surface defects such as cracks or grain boundaries.

6.0.0 Discussion of results

6.1.0 The energy spectra

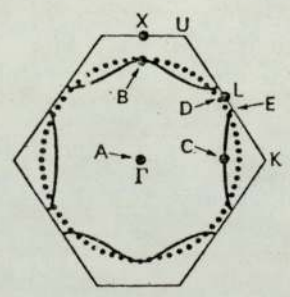
6.1.1 In order to attempt an explanation of the various spectra obtained from the different materials in chapters 4 and 5, it is useful to make comparisons with the theoretical and experimental results of FEED data that have been obtained elsewhere. Of the four electrode materials reported on here, none have been previously investigated in broad area form, and only one as a single tip emitter. This previous study was by Whitcutt and Blott [67] who investigated the field emission spectrum from copper using a retarding potential analyser. The emitter was not in bulk form but produced by vacuum deposition of copper onto the (110) plane of tungsten. Emission was obtained from the resultant (111) region of the copper and found to have the expected peak at the Fermi energy. However, when a crystal was grown having a particularly large (111) region ($\sim 1000\text{\AA}$), it was found that the spectrum at the edge of the region occupied the expected energy range but that the spectrum from the centre was displaced to lower energies by about 400meV. The authors explained this in terms of the hybridization of the 3d and 4s electron wave functions in the [111] direction.

6.1.2 The band structure of copper has been evaluated by Burdick [88] and is shown in fig (70) together with the Brillouin zone for the f.c.c. lattice. Some idea of the allocation of electrons in the bands can be obtained by looking in the FX direction. The first, Δ_1 , band will take 2 electrons; Δ_2 will also take 2. It turns out from some detailed theory that Δ_5 is doubly degenerate and takes 4 electrons. The last electron goes into the second Δ_1 which is thus half full, (the $4s^1$ can take 2 electrons) and the band is divided by the Fermi energy so that

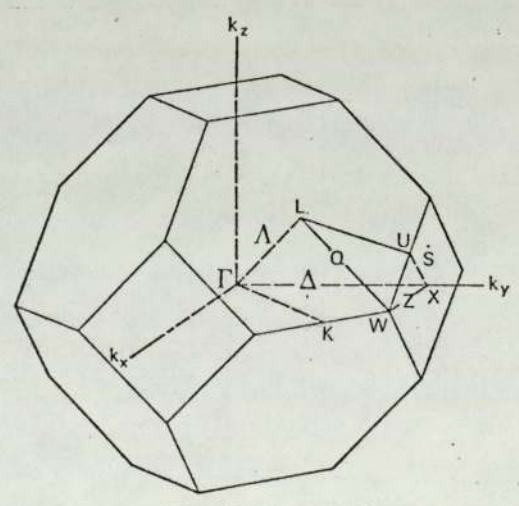


(a)

0.1 Å⁻¹



(b)



(c)

FIG 70. (a) THE BAND STRUCTURE OF COPPER ACCORDING TO BURDICK (88). THE FULL HORIZONTAL LINE IS THE FERMI ENERGY. (b) (110) SECTION OF THE FERMI SURFACE. (c) THE BRILLOUIN ZONE FOR THE f.c.c. LATTICE.

this band is empty near X. Since the d bands are well below the Fermi level the whole problem is not very different from the case where there is one electron in a single free electron band. Consequently, emission of electrons from this direction would reflect an almost free-electron like band structure with the maximum energy occurring at the Fermi level. Considering now emission along the direction ΓL which corresponds to $[111]$; here, the Fermi surface intersects the Brillouin zone in the well-known neck shape and the second Λ_1 band is always below the Fermi level. Thus emission from this direction would show a maximum in electron energy below the Fermi level. Kar and Soven [66] have pointed out that this effect would be difficult to observe experimentally, due to the finite resolution of any measuring instrument and intrinsic broadening caused by any departure from the semi-infinite geometry. The authors calculated that a plane size having a diameter of 50 - 60 lattice spacings would be necessary to detect the anomalous emission. This coincides with the evidence of Whitcutt and Blott that the effect was dependent on the size of the emission plane.

6.1.3 Although this effect is a superficially attractive explanation for the shift in the present broad area results, there are several compelling physical reasons for rejecting it. Firstly, whilst the typical shift obtained in the two cases is similar ($\sim 400\text{meV}$) this value was found to be insensitive to specimen position in the case of the broad area electrodes. Moreover, it seems highly unlikely that in the majority of cases the emission sites were oriented in the $[111]$ direction. Another important factor is that the broad area electrodes examined in the present study would inevitably have a surface oxide layer present as the in-situ outgassing treatment would not be severe enough to remove the strongly bound oxygen atoms. However, studies

have been carried out on the electronic structure of oxygen covered copper using photoemission and have shown that the presence of such a layer radically changes the spectrum, producing a peak $\sim 1.3\text{eV}$ below the Fermi level [89] with a very shallow high energy slope.

6.1.4 To check, therefore, that the shift obtained with the broad area electrodes was not simply due to a contaminated metal surface, an uncleaned tungsten tip was fitted into the spectrometer, the interfacing lens having first been removed and replaced with a phosphor coated screen. Fig (71) shows the spectrum obtained from this sample, which, although heavily contaminated (as shown by the unsymmetrical emission pattern on the phosphor screen and the broad distribution F.W.H.M.) and taking due account of the accuracy limits of the spectrometer, still had the Fermi level appearing in the correct position on the high energy edge of the distribution.

6.1.5 Thus the shifts and shape of the field emission spectra obtained from broad area copper electrodes - even assuming an oxide coating - do not seem to agree with field emission spectroscopy results from specially fabricated atomically clean copper tips or with photoemission studies of extended area single crystal copper surfaces.

6.1.6 In most cases the spectra from the emission sites on broad area electrodes have a greater F.W.H.N. and show a more symmetrical shape than those obtained from a clean tungsten emitter, this being partly due to the shallower slope of the high energy edge. It is therefore appropriate to deal with the half-width and high energy slope together. It has been shown in work already referred to [74] that the gradient of the distribution high energy slope is very sensitive to the state of cleanliness of the surface; this is probably a temperature effect and

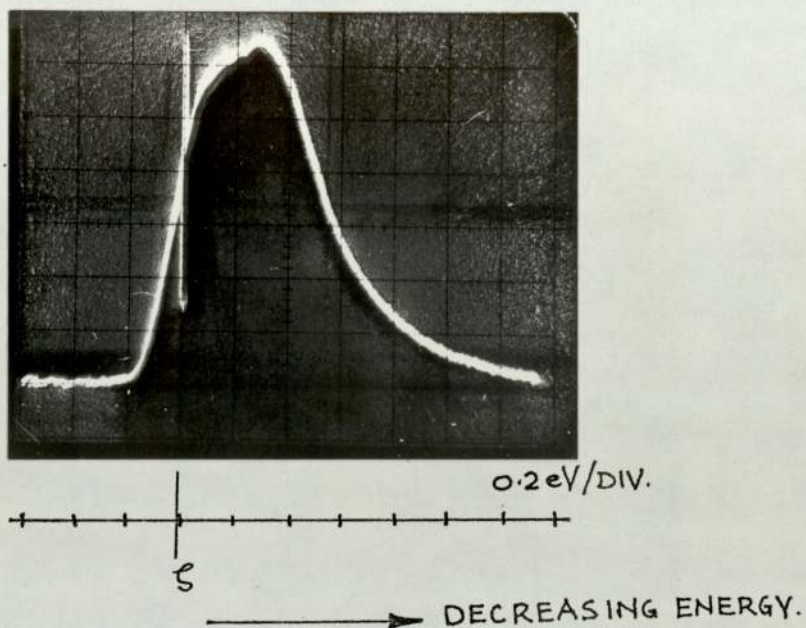


FIG 71. ENERGY DISTRIBUTION OF A CONTAMINATED TUNGSTEN TIP EMITTER. THE POSITION OF THE FERMI LEVEL IS SHOWN. ELECTRON ENERGY IN eV, 0.2 eV/DIV IS X AXIS (GOING FROM HIGH ENERGY TO LOW ENERGY LEFT TO RIGHT). ELECTRON CURRENT PER UNIT ENERGY IS Y AXIS.

may be quantified using existing equations. An expression for the current density per unit total energy $J'(\epsilon)$ relative to the Fermi level has been derived by Stratton [90] for a degenerate metal of arbitrary band structure and electron distribution $f(\epsilon)$ in momentum space:

$$J'(\epsilon) = J_0 f(\epsilon) \exp \epsilon/d \left[\frac{1 - \frac{1}{2\pi} \int_0^{2\pi} \exp - (E_m/d) d\phi_p}{d} \right] \quad (63)$$

Where J_0 denotes the total current density already derived by Young (eqn. 20(b)) and the term in brackets gives the band structure effects (E_m is the maximum value of the transverse energy component, and $\tan \phi_p = K_y/K_z$), this can be neglected when $E_m/d \gg 1$. Under usual field emission conditions $d \sim 0.15 - 0.25\text{eV}$ and for most degenerate metals exhibiting large Fermi energies E_m is sufficiently large that the band structure term is negligible (For transition metals with partially filled narrow d bands, the value of E_m may be sufficiently small to perturb $J'(\epsilon)$ through the band structure term. For example, this may account for the anomalous behaviour of the emission from tungsten along the (100) direction [48]). If the band structure term is neglected and the Fermi-Dirac distribution of $f(\epsilon)$ is assumed then

$$J'(\epsilon) = \frac{J_0 \exp \epsilon/d}{d(1 + \exp \frac{\epsilon}{pd})} \quad (64)$$

where $p = \frac{kT}{d}$ and is a dimensionless parameter.

The mathematical derivation of eqn (64) breaks down for $p \geq 1$ and becomes unreliable when p exceeds about 0.7. A graphical representation of $J'(\epsilon)$ versus ϵ/d yields a set of curves whose shape depends only on the dimensionless parameter, p , as shown in fig (72). These curves have also been verified experimentally by Swanson and Crouser [48]. As can be seen, the broadening in the F.W.H.M. of the distribution occurs because of a change in the slope of the high energy edge about the Fermi

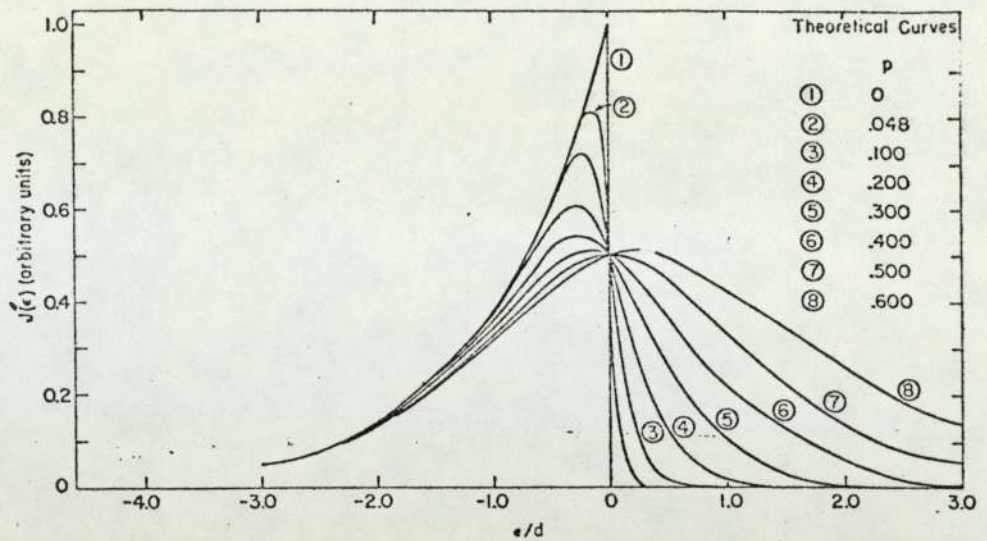


FIG 72. THEORETICAL TOTAL ENERGY DISTRIBUTION PLOTS BASED ON THE FREE ELECTRON MODEL AT VARIOUS VALUES OF p AS GIVEN BY SWANSON AND CROUSER (61). ϵ IS THE ELECTRON ENERGY RELATIVE TO THE FERMI LEVEL. $d = \hbar e F / 2(2m\phi)^{1/2} t(y)$, $p = kT/d$.

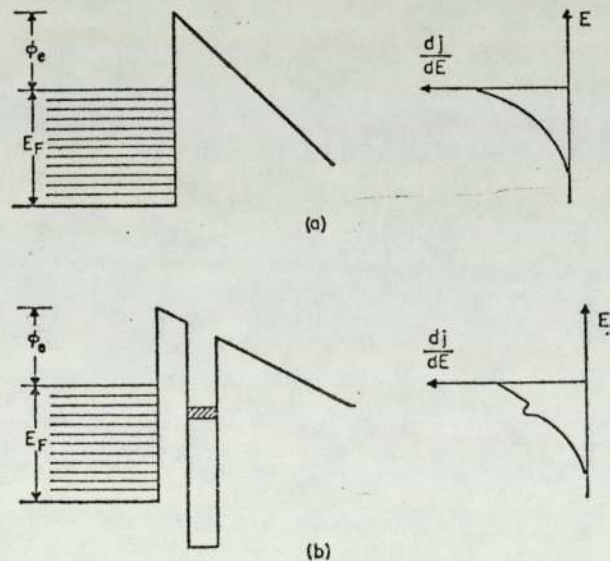


FIG 73(a) IDEAL MODEL OF POTENTIAL AND TOTAL ENERGY DISTRIBUTION FOR FIELD EMISSION FROM A FREE ELECTRON METAL.

(b) AS (a) BUT WITH RESONANCE TUNNELING FIELD EMISSION FROM A NARROW BAND ABSORBATE. (AFTER GADZUK (85)).

energy, ζ , due to the increased temperature of the electrons. Similarly, the decrease in the slope of the high energy edge in the spectra from the broad area electrode sites - although not occurring about the Fermi level because of the shift in the spectrum - could be attributed to the existence of "hot" electrons at the surface, a possibility that is further discussed in 6.5.0.

6.1.7 The outgassing procedure has already been described in previous chapters. There are several possible surface changes that can take place as a result of this treatment; principally these are

- (i) the desorption of occluded gas molecules
- (ii) the evaporation of more tightly bound species
- (iii) migration of chemi or physi-sorbed atoms over the surface
- (iv) annealing of the surface structure, particularly if it has been previously exposed to the very large physical stresses imposed by a high external electric field
- (v) local softening and subsequent change in the surface profile and,
- (vi) possible chemical reaction between the surface and neighbouring atoms as a result of the elevated temperature.

6.1.8 Experimentally, the results of outgassing the various specimens seem on first inspection to be rather inconclusive. The first copper specimen (fig 48) was affected by the initial outgassing, there being some decrease in the high energy slope width, and hence in F.W.H.M., with a shift in the spectrum towards the Fermi level. This possibly indicates some reduction in the level of surface contamination but further outgassing seems to have had little effect. Similarly, there seems to be some reduction in slope width and F.W.H.M. following outgassing on copper specimen number 2 (fig 49), but it had the opposite effect on the

position of the distribution relative to the Fermi level, i.e. it was shifted to lower energies.

6.1.9 The effect of outgassing on the third copper specimen (fig 51(b)) and on the copper chromium sample (fig 67) was quite different. In both cases the distribution split up into two peaks with a separation of 300meV for the copper and 650meV for the copper-chromium. Also both spectra moved higher in energy towards the Fermi level. The titanium alloy sample also gave a double peaked spectrum, in this case being formed after prolonged exposure to U.H.V. rather than outgassing. The peak separation was 500meV with some shift of the spectrum towards the Fermi level. It seems evident, therefore, that some special atomic surface re-arrangement has taken place in these cases. Possible explanations for this behaviour are discussed in 6.5.7 - 6.5.12.

6.1.10 The general features of the distributions may be summarised as follows:

- (i) There is a broad similarity between the spectra obtained from all of the emission sites studied on the various materials. Most notably, they all show a shift towards lower energies which is difficult to explain in terms of metallic emission but is characteristic of the behaviour of semiconductor emission.
- (ii) Most of the spectra show a rather broad F.W.H.M. due partly to the relatively shallow slope of the high energy edge. This is characteristic of emission from contaminated surfaces or those where there are "hot" electrons.
- (iii) Under certain conditions, a change in emission becomes possible as evidenced by the appearance of a second lower energy peak occurring at between 300meV and 650meV below the main one, the

actual peak separation apparently depending on the electrode material.

6.2.0 The Fowler-Nordheim Graphs

6.2.1 In every case where an i - V characteristic of an emission site was measured, it was found to follow the Fowler-Nordheim equation. Fig (56) shows the error bars for this measurement which is typical of all the F-N plots. It corresponds to a possible overall error in slope of $\sim 4\%$ and hence in this particular value of β of ~ 20 . Because all the F-N plots have such steep gradients, this error in the slope has a rather greater effect on the prediction of emitter size. On the stainless steel specimen, for example, if it is assumed that a hemispherically capped conical feature is responsible for the emission, the error of 4% on the slope gives an error of $\pm 30\%$ in the tip radius, cone height and base diameter when calculated as given in 2.3.2 - 2.3.3. However, for the case of the chromium-copper specimen where the surface was microscopically examined, the base of the cone at least should have been resolved even allowing for this margin of error.

6.2.2 One possible reason why the method of 2.3.2 - 2.3.3. leads to an apparently incorrect result can be considered by comparison with the emission from the (100) plane of tungsten. The spectrum from that particular crystallographic direction cannot be satisfactorily explained by the free electron model but the emission will still give a linear plot of the F-N characteristic [61][62]. This rather surprising result can be explained by the fact that it is the pre-exponential term of the Fowler-Nordheim equation which is modified in the non-free electron model (by the influence of the band structure term (eqn 63)). In a similar way, the emission from the sites on broad area electrodes may appear to

correspond to a Fowler-Nordheim graph because the exponential term is essentially correct, but the pre-exponential term is not free electron-like so that predictions of emitting area from this graph are quite misleading.

6.2.3 The values of β predicted from the F-N plots vary from 200 to 900 and thus all fall within what is generally called the "high β " type of emission site. It might be expected, particularly in the experimental sequence on the chromium-copper specimen where F-N plots were taken at a number of stages in the experiment, that there would be some correlation between the slopes of these graphs and the type of energy spectrum obtained. For example, plots are shown both during and after the two appearances of the double peak in the spectrum (fig 65), but there seems to be no systematic change in slope on appearance or disappearance of this feature. Shown in fig (74) are graphs of current versus field for the cases of single and double peak spectra to find out if there is any change in emission current for a given field with the two states. As can be seen there appears to be no systematic variation here either. On going from the initial double peak to the single peak (A \rightarrow C) there is a large increase in current for a given macroscopic field. However, the current again increases substantially on re-appearance of the double peak (i.e. after outgassing, C \rightarrow F) although it should be noted that this was measured \sim 10 mins after outgassing and so there may be a temperature effect involved. Finally, it will be noted that when the spectrum returned to a single peak again, there is a reduction in current (F \rightarrow I), the opposite of what had happened earlier in the observations when a similar sequence of events occurred. The possible significance of this series of results is discussed in 6.5.11.

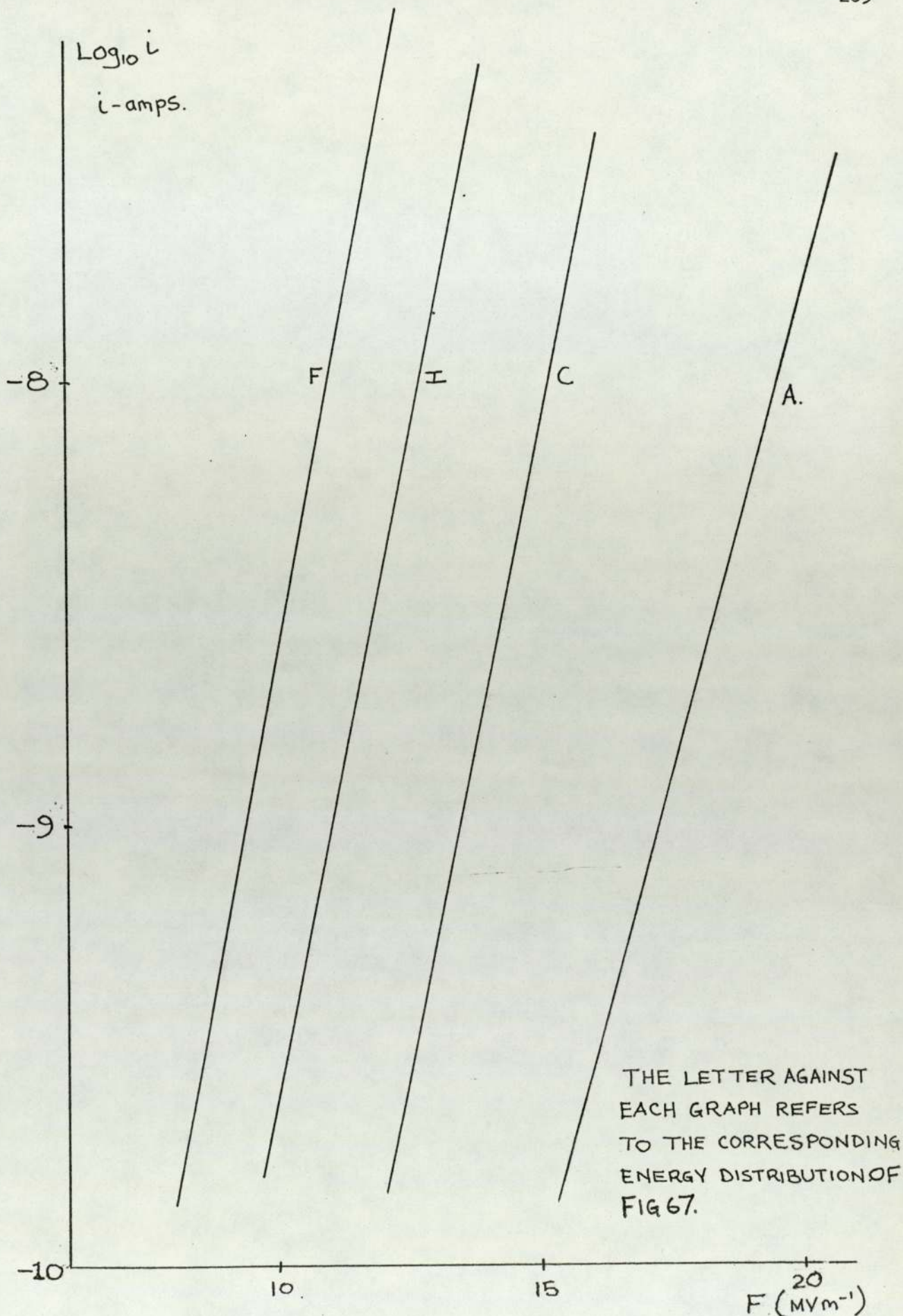


FIG 74. GRAPHS OF EMISSION CURRENT VERSUS APPLIED MACROSCOPIC FIELD FOR THE CHROMIUM-COPPER ALLOY SPECIMEN/ AT VARIOUS STAGES OF THE INVESTIGATION.

6.3.0 Proposed model of the surface structure at an emission site on a broad area electrode

6.3.1 In seeking a plausible physical model for explaining the apparently "non-metallic" nature of the emission spectra obtained from all the metallic specimens investigated, a number of basic requirements have to be borne in mind. Firstly, the model must account for the shift of the spectra to lower energies and show how this can vary under different circumstances. Secondly, it must explain the occurrence of emission at fields between two and three orders of magnitude lower than that normally required for field emission from either metals or semiconductors, since this and other studies have shown that there is no electron optical evidence of surface protrusions having the geometry to give the required level of field enhancement. Thirdly, the model should also suggest possible interpretations of the low energy peak that is sometimes present on the spectra; finally, the model should indicate why the emission sites are so localised. It must, however, be recognised that unlike specially fabricated emitters, where atomically clean surfaces of known crystallographic orientation can be prepared, the surfaces studied here are likely to be far more complex. The base material may be either a metallic element or a multispecies alloy and the surface itself will be covered in an oxide layer and may also contain impurity inclusions; consequently, it would be unrealistic to attempt more than a generalised qualitative explanation of the data in this present study.

6.3.2 Accordingly, a reasonable starting point for the model would be to assume that any microscopic region of an electrode surface may be characterised as consisting of a metal substrate with an overlying contaminant film - most probably the metal oxide - whose thickness and

electrical properties are likely to show variations over the surface; in addition this description would include the situation where other isolated impurities are present on the electrode surface. This model must be further complicated by recognising that there are also likely to be various species of adsorbed gas atoms on the surface contaminant film. Since it is well known that surface oxide coatings are usually electrically semiconducting, it is necessary to consider in some detail the electron energy band structure of semi-conductors in general in order to account for the effect of applying a strong electric field to the model of the surface just suggested.

6.4.0 Electronic structure of semi-conductors

6.4.1 From the point of view of electronic structure, semi-conductors differ primarily from metals in that there is a band gap between the valence and conduction bands, and, for an intrinsic semi-conductor at absolute zero, the valence band is full and the conduction band empty. At room temperature, for intrinsic semi-conductors such as germanium and silicon, thermal energy allows excitation of a small proportion of the electrons from the valence band into the conduction band. At these temperatures, therefore, the materials exhibit electrical conductivity, this arising both from the conduction band electrons and the holes in the valence band. In a semiconducting material like diamond, however, the band gap is sufficiently wide to prevent any appreciable thermal excitation at room temperature, and it therefore remains an insulator.

6.4.2 In metals, the Fermi energy, ζ , is defined as the energy of the highest occupied state at OK. More generally, however, ζ , is defined as the energy of a state for which the probability of occupation is $1/2$ and since for a pure (intrinsic) semi-conductor at OK the valence band is full

and the conduction band empty, ζ occurs in the middle of the band gap (fig 75(a)). The addition of certain impurities to a semi-conductor (which is then said to be extrinsic) can lead to permitted energy levels within the band gap which can give rise to either electron (n-type) or hole (p-type) conduction. This in turn alters the position of the Fermi level as shown in fig 75(b). When a semi-conductor is brought into contact with a metal, there will be a flow of electrons between the two materials to achieve an equilibrium state and the Fermi levels will become equal. In the case, for example, of contact being made between an n-type semi-conductor and a metal having a Fermi level lying within the semi-conductor band gap there will be a flow of electrons from the conduction band of the semi-conductor to the lower energy states in the metal. Equilibrium will be achieved when the resulting charge distribution sets up a field which prevents further electron flow across the boundary. A consequence of this internal field is to perturb the energy levels of the semi-conductor near the junction, this being represented by a bending of the bands as shown in fig 76(a).

6.4.3 A further difference in the electron energy band structure of metals and semi-conductors becomes apparent on applying a strong electric field to the surface. This difference results from the more limited conductivity of the semi-conducting material. When an electric field is applied to the surface of a metal or a semi-conductor, a surface charge is induced. The induced charge has little effect in the case of a metal because the number of additional charges involved is small compared to the number of available conduction electrons. For a semi-conductor, however, the position is different because the number of electrons in the conduction band is relatively small under most conditions. Consequently, the electric field may penetrate some distance into the

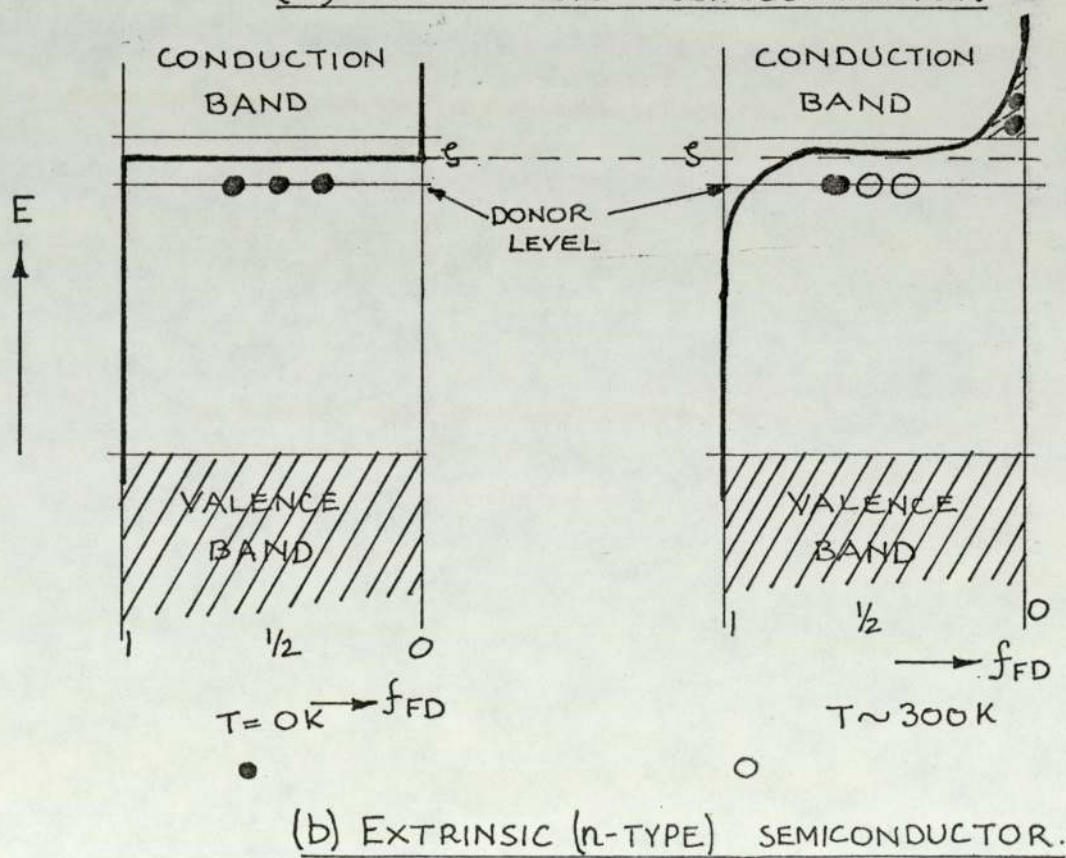
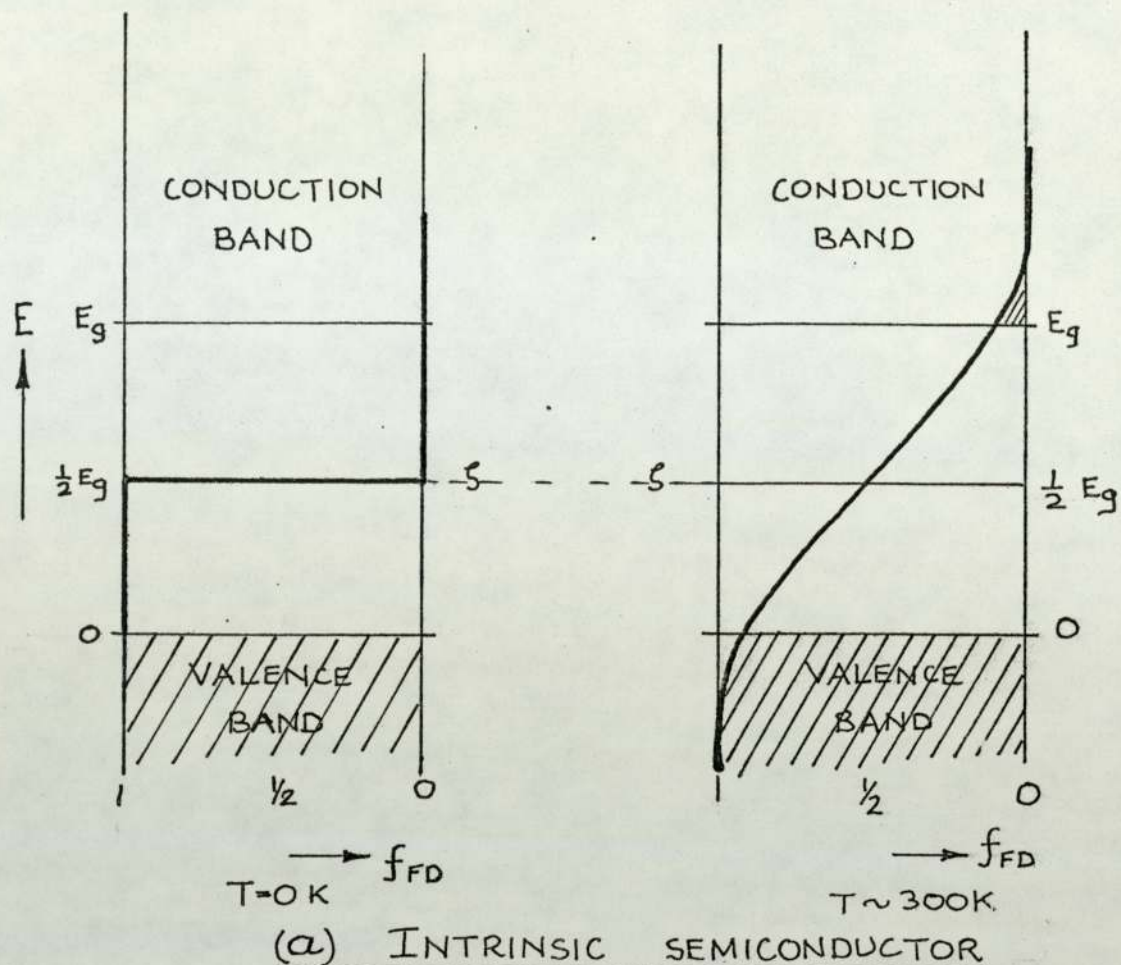
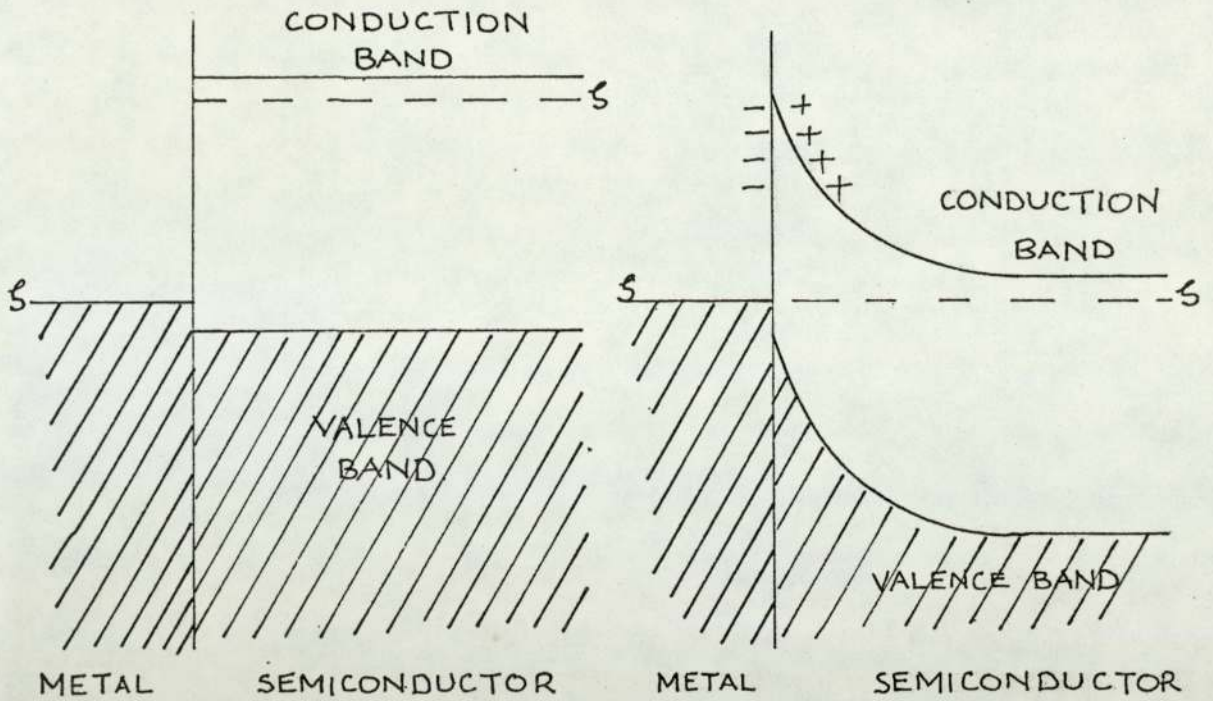


FIG 75. THE POSITION OF THE FERMI LEVEL (ξ) FOR A PURE (INTRINSIC) AND DOPED (EXTRINSIC n-TYPE) SEMICONDUCTOR AT TWO TEMPERATURES. f_{FD} IS THE FERMI-DIRAC FUNCTION $\left\{ = \left[\exp((E-\xi)/KT) + 1 \right]^{-1} \right\}$.



(i) BEFORE CONTACT (ii) AFTER EQUILIBRIUM.

FIG. 76(a) ENERGY BANDS AND FERMI LEVELS AT A METAL/ n -TYPE SEMICONDUCTOR JUNCTION, BEFORE AND AFTER EQUILIBRIUM IS ESTABLISHED.

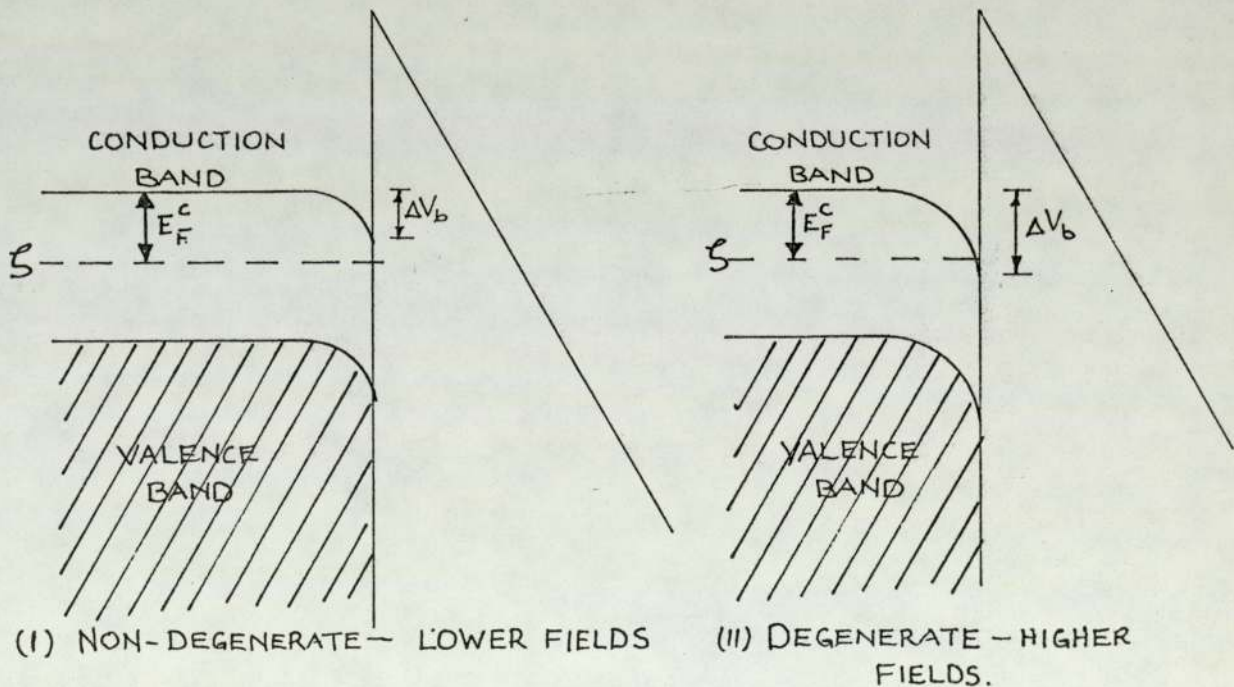


FIG 76 (b). BAND BENDING AT THE SURFACE OF A SEMICONDUCTOR ON APPLICATION OF A STRONG ELECTRIC FIELD.

semi-conductor surface and there will be a gradual change in electrical potential throughout that distance. The effect on the band structure is shown in fig 76(b); where the field penetrates the surface, the electron potential is reduced and this is represented by the downward bending of the energy bands. If the band bending is sufficiently severe for the conduction band to fall below the Fermi level, the semi-conductor is said to be degenerate. The amount of band bending, ΔV_b , depends on the strength of the applied field and the number of available free charges near the surface.

6.4.4 There is another effect which may arise at the surface of a material and may be of greater significance in a semi-conductor because of its more limited conductivity compared with a metal. At the surface of a semi-conductor the atomic arrangement is different because there are no atoms on the one side with which to form bonds. Thus the surface electrons have different discrete energy levels from those of the bulk. Those surface levels which lie below the Fermi level of the semi-conductor will be filled by electrons from the conduction band, giving a negative charge on the surface. This creates a depletion region just inside the surface layer and results in upward bending of the energy bands as shown in fig 76(c).

6.4.5 Finally, there is one further effect which may be present in semi-conductors which have a large resistivity; when a field emission current is flowing a voltage drop, ΔV_R , will develop down the shank of the emitter with a resulting variation in the Fermi level (fig 76(d)).

6.4.6 A theory of field emission from semi-conductors was put forward by Stratton [90] in 1962, and again with some modifications in 1964 [91], in which he derived equations for the field emission current density from

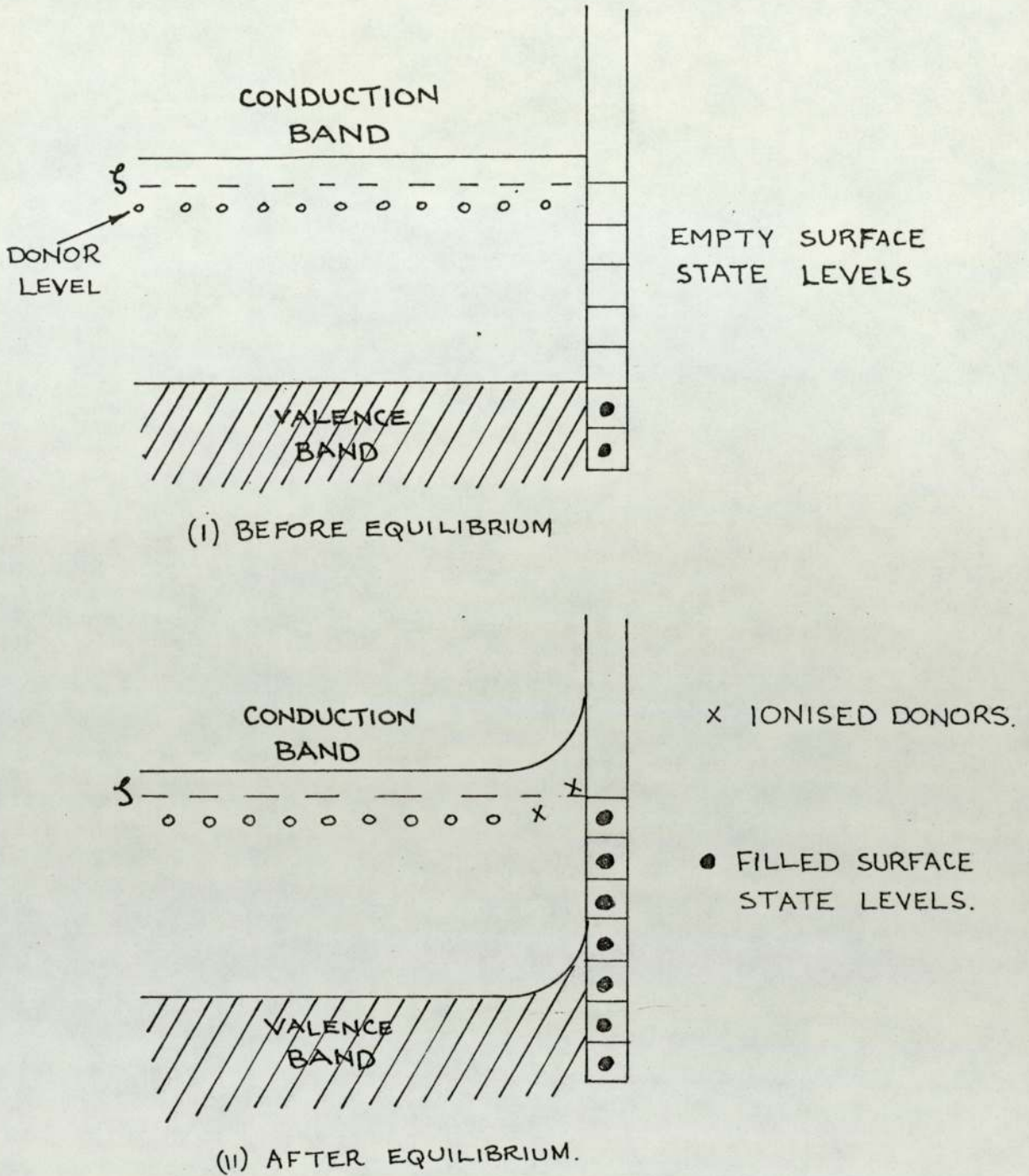
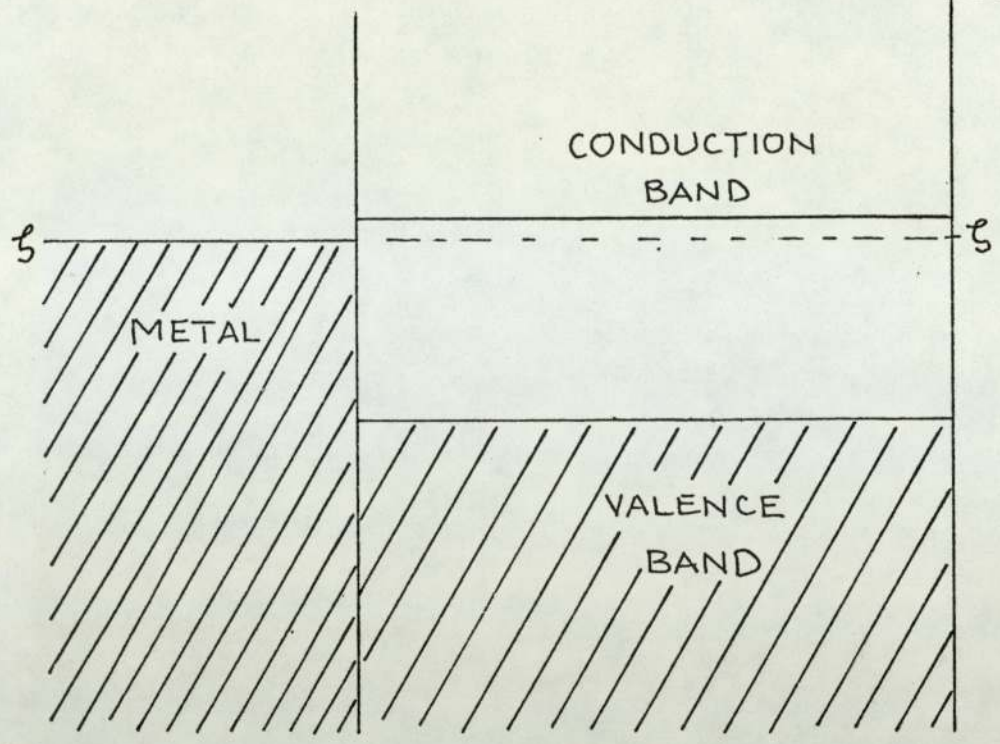
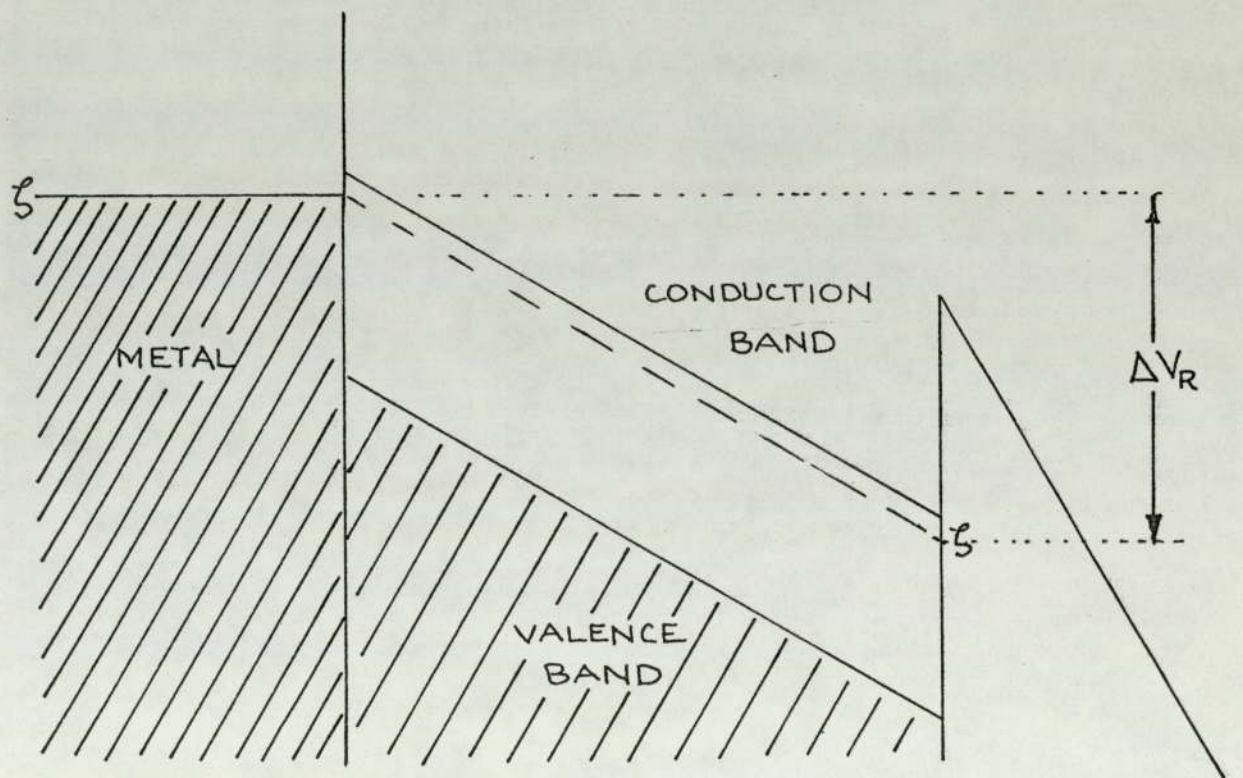


Fig 76 (c) THE EFFECT OF SURFACE STATES ON THE BAND STRUCTURE OF A SEMICONDUCTOR.



(a) NO CURRENT FLOWING.



(b) CURRENT FLOWING THROUGH SEMICONDUCTOR.

FIG 76 (d). THE INTERNAL POTENTIAL DROP, ΔV_R , IN A SEMICONDUCTOR DUE TO ITS BULK RESISTIVITY. (FOR CLARITY, THE BAND BENDING AT THE METAL/SEMICONDUCTOR AND SEMICONDUCTOR/VACUUM INTERFACES HAS BEEN OMITTED).

both the conduction and valence bands of a semi-conductor. The field emitted current density from a non-degenerate conduction band was given as:

$$I_c = \frac{4\pi M_c e (kT)^2}{h^3} \exp\left(\frac{E_F^c + eV_s}{kT}\right) \exp\left[-6.83\psi^{3/2} \left(\frac{10^7}{F}\right) v\left(\frac{\psi_i}{\psi}\right)\right] \quad (65)$$

and the corresponding total energy distribution is given by:

$$J_c(E^c) = \frac{4\pi m e}{h^3 C_o} f(E^c) \exp\left(C_o E^c - b_o\right) \left[1 - \exp(-C_o r_c E^c)\right] \quad (66)$$

The notation is:

$$b_o = 6.83\psi^{3/2} \left(\frac{10^7}{F}\right) v\left(\frac{\psi_i}{\psi}\right)$$

$$C_o = 10.25\psi^{1/2} \left(\frac{10^7}{F}\right) t\left(\frac{\psi_i}{\psi}\right) \quad (\text{in eV})$$

$$f(E^c) = \exp\left(\frac{E_F^c + eV_s - E^c}{kT}\right)$$

$$\psi_i = 1.2 \left(\frac{F}{10^7}\right) \left(\frac{\epsilon - 1}{\epsilon + 1}\right)^{1/2}$$

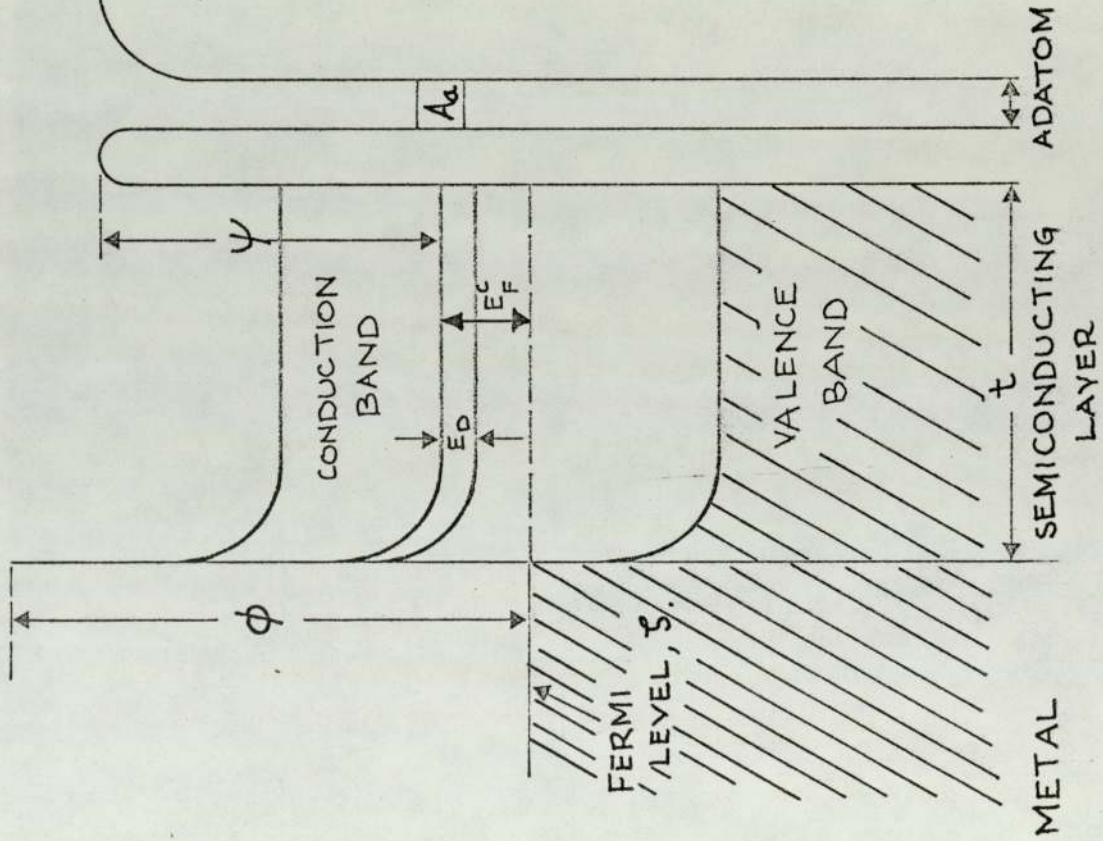
v and t are tabulated functions of their argument and for most practical cases $t \cong 1$ and $v \cong 0.7$. ψ is the electron affinity in eV in the bulk of the semi-conductor and ψ_i is the depression of the barrier height due to the image force. F is the applied field (volts/cm) and all energies are measured in eV. E_F^c is the Fermi level measured from the bottom of the conduction band in the bulk of the semi-conductor (fig 76(b)). E^c is the energy of the emitted electrons measured from the bottom of the conduction band at the surface. $r_c = M_c/m$ where M_c denotes an average effective mass for the conduction electrons and m is the electronic mass. V_s is the shift in the electrostatic potential at the surface due to the induced charge. ϵ is the dielectric constant of the semi-conductor. Similar equations apply for emission from the valence band. These

equations may be directly compared with equations 20(a) and 20(b) of Chapter 2 and serve to illustrate the greatly increased complexity of the semiconducting case.

6.4.7 More recently the specific case of germanium has been considered by Modinos [92] which used as a basis the model for a semi-conductor surface put forward by Handler [93] in which it is assumed that a band of surface states exists which range in energy from the top of the valence band to the lower part of the conduction band. Equations are then derived for the field electron emission current from the surface states, this being the sum of the current from the conduction band to the surface states and from the valence band to the surface states. According to this theory, at low emission current densities the emitted electrons come mostly from the surface states and from the valence band. At higher currents, emission from the conduction band is significant, but still a small proportion of the total emission current. The distributions obtained from these equations show reasonable agreement with the experimental results from germanium obtained by Shepherd and Peria [94].

6.5.0 Model of field emission from broad area electrodes

6.5.1 The concepts discussed in 6.4.1 to 6.4.7 may now be applied to the proposed model of a broad area electrode surface put forward in 6.3.2. The electronic band structure of such a surface is shown in fig (77). It consists of a metallic substrate and a semiconducting contaminant layer of thickness, t ; for the proposed emission mechanism this layer must be an n-type semi-conductor. The diagram also shows a further electronic energy band just outside the semi-conductor caused by the presence of a surface adatom, for example, a particular type of adsorbed gas. For simplicity, the possibility of surface states is not considered at this



- A_a - ENERGY BAND IN ADATOM LAYER
- ψ - ELECTRON AFFINITY OF LAYER
- ϕ - WORK FUNCTION OF METAL
- E_D - ENERGY DIFFERENCE BETWEEN BOTTOM OF CONDUCTION BAND AND DONOR IMPURITY LEVEL
- E_F^C - ENERGY DIFFERENCE BETWEEN BOTTOM OF CONDUCTION BAND AND FERMI LEVEL IN THE SEMICONDUCTING LAYER.

Fig 77. ONE DIMENSIONAL ENERGY DIAGRAM OF A METAL SURFACE COVERED WITH A SEMICONDUCTING LAYER.

stage. When an external electric field appropriate to field emission is applied to the semi-conductor surface described, the band structure will be altered to that shown in fig (78). This model of the band bending follows that given by Baskin et al [95] and assumes degeneracy of the electrons at the surface of the semi-conductor.

6.5.2 With the surface configuration just described, it is possible to envisage at least four mechanisms whereby electrons could undergo an intermediate tunnelling process from the metallic substrate to states in the semiconducting layer and subsequently be emitted below the reference Fermi level of the metal substrate (the level identified on the energy spectra results). Referring to fig (78) these are:

- (i) from the Fermi level of the substrate metal into states at the bottom of the conduction band in the semiconducting layer
- (ii) between the valence and conduction bands of the semi-conductor
- (iii) from the Fermi level of the metal to the conduction band of the semi-conductor via an impurity level in its band gap
- (iv) from the valence band of the semi-conductor via an impurity level into its conduction band.

It follows from fig (78) that, with the voltage drop ΔV_R , there is a possibility of an enhancement of the tunnelling probability, whereby those electrons that have tunnelled into the bottom of the conduction band of the film by one of the above mechanisms can be subsequently accelerated by the penetrating surface field to higher states and give a flux of "hot" electrons incident on a narrower part of the surface barrier. In strong support for the occurrence of such a mechanism are the broad high energy edges obtained on the emission spectra.

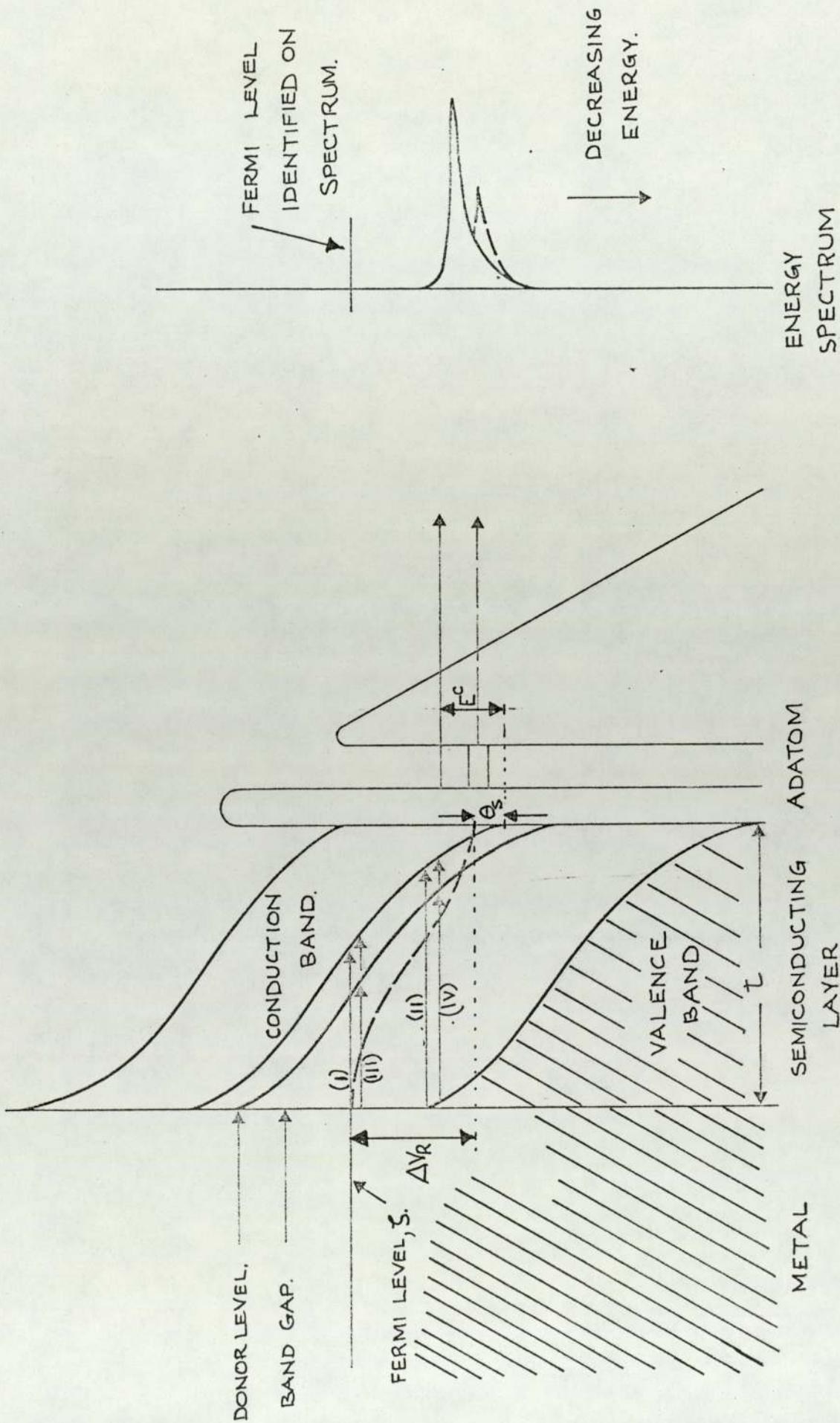


FIG 78. THE ENERGY DIAGRAM OF FIG 77 AFTER THE APPLICATION OF A STRONG ELECTRIC FIELD TO THE SURFACE.

6.5.3 An indication of the magnitudes of the various parameters involved in this model can be calculated as follows. In order for electron tunnelling to occur, the path length of the electron must be $\lesssim 50\text{\AA}$. The reduced potential barrier necessary at the surface in order to give the observed levels of field enhancement (say $\beta = 400$) can be estimated from eqn (1b); this gives $\phi \lesssim 0.1\text{eV}$; i.e. the electrons would have to be emitted close to or above the top of the potential barrier. A more accurate result could be obtained by using equation (65) and plotting $\log I_c \propto v^1/F$ and finding the reduced value for the electron affinity, assuming no field enhancement. However, the gain in kinetic energy of the electrons assuming unimpeded acceleration in the conduction band is likely to be in the range 2 - 5eV. The range of energy of these electrons and the level of the most energetic electrons can be found from the relevant spectra.

6.5.4 The potential drop in the layer due to its resistivity is ΔV_R . It is clear from the energy diagram of fig (76) that electrons from the bottom of the conduction band will be transmitted by the spectrometer when:

$$V_4 + \Delta V_R + \theta_s - E^c = \frac{e a}{e}$$

where θ_s represents the voltage difference between the bottom of the conduction band and the Fermi level, at the surface.

It can be seen from this model that as the emission current increases so too will ΔV_R , assuming that the semi-conductor resistivity remains constant. Thus as the field increases there should be a shift in the spectrum, and this kind of behaviour is illustrated in fig(45(a)); however, this result was not typical of all the spectra - in some cases no change in shift was

observed up to the maximum emission currents used - $\sim 10^{-7}$ A.

6.5.5 A similar mechanism was considered by Shcherbakov and Sokol'skaya for cadmium sulphide emitters in 1963 [96]; they measured both the variation in electrical conductivity and F.W.H.M. of the energy distribution as a function of the position of the energy spectrum. They found that the electrical conductivity remained constant up to a certain value of spectrum shift (several volts) whereupon it began to increase in a logarithmic way. The authors interpreted this as the onset of carrier multiplication by impact ionisation. Typically, this occurred at field emission currents of 10^{-8} - 10^{-7} amps. Comparing these results with the present data, there appears to be no departure from the linearity of the F-N characteristic up to the highest measured value of $\sim 10^{-7}$ A. Also, the spectral shifts obtained were far lower than obtained by Shcherbakov Sokol'skaya on cadmium sulphide; whilst some differences would be expected due to the likely variation in band gap and conductivity between different types of semiconducting material, the fact that in many cases the broad area electrode spectra showed no change in shift with field is difficult to explain. One possibility is that as the field increases the shift in the spectrum is exactly compensated by the increase in the energy of the "hot" electrons. In such a case, an increasing field should correspond to an increase in the width of the high energy edge of the spectrum but no rigorous tests have so far been carried out to investigate this effect.

6.5.6 In support of the model of "hot" electrons causing the apparent enhancement of emission current is the evidence of the "cathode spot" electroluminescent effects observed by Hurley and Dooley [39] which have been invariably found to accompany field emission from a broad area electrode surface. Such an effect requires the presence of electrons with sufficient energy to cause ionisation of atoms in the surface layer.

6.5.7 A number of possible explanations may be considered for the appearance of the second low-energy spectral peak that appears in some of the spectra at between 300 and 650meV below the main peak. These are:

- (1) Valence band emission
- (2) Impurity band emission
- (3) Adatom resonance tunnelling
- (4) Resonance tunnelling through a continuous double layer of foreign atoms.

Each of these mechanisms will now be discussed.

6.5.8 If the main peak obtained in the spectra comes from the conduction band then it seems unlikely that the low energy peak is valence band emission, since the separation between the two peaks is much smaller than the probable band gap of any oxide layer. In Cu_2O , for example, which is essentially a p-type ionic semi-conductor, the room temperature band gap is $\sim 2\text{eV}$. If, however, the band structure of the emission site is more complicated than so far considered and the main peak arises from a band of surface states, then the lower energy peak could be from the valence band in a similar way to the results obtained on germanium by Shepherd and Peria [94].

6.5.9 Although impurity band emission appears to be a likely possibility because of the relatively narrow separation of the spectrum peaks, it might be expected that if this were the case the peak would be obtained consistently with all spectra or at least with one emission site. From the results obtained, however, it appears that the lower energy peak is sensitive to the prevailing surface conditions indicating a surface rather than a bulk effect.

6.5.10 The phenomenon of resonance tunnelling has usually been studied for the case of individual atoms or fractions of a surface monolayer adsorbed onto a metallic emitter (84)(85). According to this model, if a particular adsorbed atom species has an energy level within the energy range of the emitted electrons from the substrate metal, then this can give rise to a subsidiary peak on the associated energy spectrum (fig 73(b)). The presence of the peak is critically dependent on the separation of the adatom from the substrate surface, the width of the potential well and the position of the energy level within it. This seems to concur with the observed transient nature of the low energy peak in the present studies. However, one feature that might have been expected with this model is a systematic change in emission current on appearance or removal of the resonance tunnelling effect. It has been shown by Duke and Alferieff [84] for example, that the adsorption of a foreign species of metallic adatom onto a metallic emitter should give rise to an increased emission current, whereas a neutral adatom should decrease the emission current. No such behaviour is evident in the present results, as shown in fig (74). It should be noted, however, that the case of a metallic or non-metallic adatom onto a semi-conductor emitter has not so far been studied.

6.5.11 Nicolaou and Modinos [97] have also studied the phenomenon of resonance tunnelling for the case of single and double continuous layers of germanium on tungsten; this was an attempt to explain the experimental results of this situation obtained earlier by Miles'hkina and Sokol'skaya [98]. In fact, Nicolaou and Modinos found that the experimental results could be well represented by the resonance tunnelling theory; by choosing suitable values for the position, width and depth of the potential well and also for the dielectric constant of the material, it was possible to reproduce the experimentally observed energy distributions. A further

interesting result was a comparison of the energy spectra and total emission current for the case of clean tungsten, incomplete monolayer (of germanium) coverage and full monolayer coverage. At incomplete monolayer coverage the spectrum had a single peak similar in position half-width to that of clean tungsten (fig 79). However, the full monolayer coverage gave a two-peaked spectrum, the main peak appearing at the clean tungsten position and the secondary peak appearing at lower energy and displaced by $\sim 1.0\text{eV}$ (fig 79). The total current, which was a maximum for clean tungsten, decreased steadily until approximately one monolayer coverage and then steadily increased again with increasing thickness (fig 80). Finally, the authors calculated the energy distribution assuming a double layer coverage of germanium on tungsten; although the main peak becomes shifted the peak separation is not greatly affected (fig 81).

6.5.12 Although the above results apply to resonance tunnelling from a metal substrate, rather than a semi-conductor, the mechanism is likely to be similar in both cases. The total current results of fig (80), in particular, suggest an interesting possibility for the explanation of the experimental results from the chromium-copper specimen given in fig (74). The arrows superimposed on fig (80) show how the experimental sequence could give rise to the observed results.

6.6.0 Measurement of work function

6.6.1 One of the original objectives of the present work was to measure the work function of the electrode material actually at the point of emission and, as discussed in the theory of Chapter 2, electron spectrometry is uniquely qualified to do this. Such a measurement would eliminate any ambiguity in the calculations to find β from the F-N plots, and hence also in the predictions of the dimensions of the emitter itself. However,

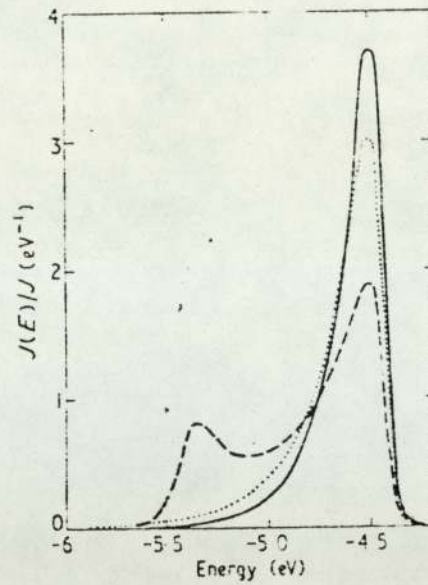


FIG. 79. ENERGY SPECTRA FOR GERMANIUM ON TUNGSTEN AS CALCULATED BY NICOLAOU & MODINOS [97]. FULL LINE: CLEAN TUNGSTEN. DOTTED LINE: INCOMPLETE MONOLAYER COVERAGE. BROKEN LINE: FULL MONOLAYER COVERAGE.

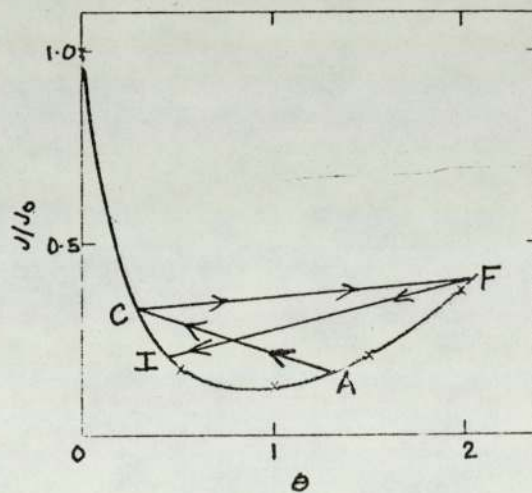


FIG. 80. RATIO OF THE TOTAL CURRENT ON A SORPTION OF GERMANIUM (J) TO THAT OF CLEAN TUNGSTEN (J_0) AS A FUNCTION OF ADSORBATE THICKNESS. $\theta = 1$ CORRESPONDS TO ONE COMPLETE MONOLAYER [97]. THE ARROWS SUPERIMPOSED ON THIS DIAGRAM ($A \rightarrow C$; $C \rightarrow F$; $F \rightarrow I$) INDICATE A POSSIBLE SEQUENCE OF EVENTS WHICH COULD EXPLAIN THE RESULTS OF FIG. 74.

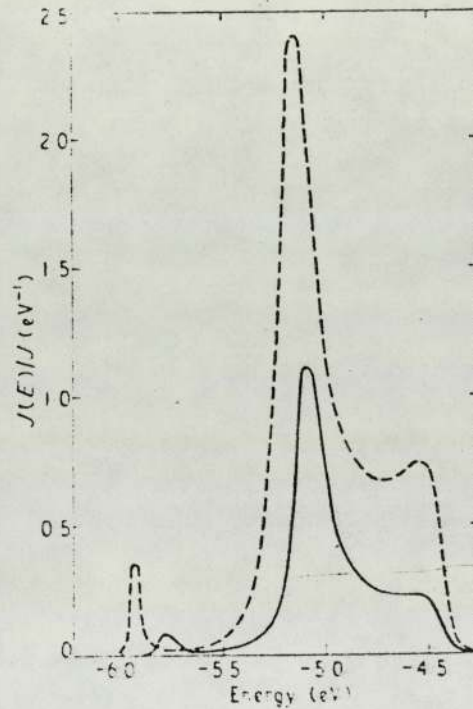


FIG 81. ENERGY SPECTRA FROM TUNGSTEN COVERED WITH A DOUBLE LAYER OF GERMANIUM ACCORDING TO NICOLAOU & MODINOS [97]. THE BROKEN LINE IS ASSOCIATED WITH AN INCOMPLETE SECOND LAYER, THE FULL LINE WITH A COMPLETE OR DENSELY POPULATED SECOND LAYER.

this objective was based upon the assumption that the field emission from these sites could be adequately described on a metallic free-electron model. As has already been shown in Chapter 2, the electron spectrometry technique is capable of being extended to measure the work functions even in the case of non-free electron behaviour in a metal. However, the energy spectra obtained from the broad area electrodes indicates that the emission is more typical of a semiconducting material.

6.6.2 The equations for the total energy distribution and the field emission current density have been given in 6.4.6 and serve to illustrate the greatly increased complexity of the semi-conductor case. Stratton [91] has also derived an equation for the F.W.H.M. of the total energy distribution from the conduction band and the valence band of a semi-conductor. At temperatures near 0K the equation for the conduction band is:

$$C_1 \Delta \rightarrow \ln [2/(C_1 + \exp - C_1 \zeta)] \quad (67)$$

$$\text{where } C_1 = 10.25 (\psi - \zeta)^{\frac{1}{2}} \left(\frac{10^7}{F} \right) t \left(\frac{\psi_i}{\psi - \zeta} \right) \quad (68)$$

Δ is the F.W.H.M. of the total energy distribution.

6.6.3 Stratton has carried out numerical solutions giving the variation in Δ with temperature for various values of Fermi energy and for various ratios of electron mass/effective mass. These results are difficult to interpret for the present case of the broad area electrodes since F , ψ and ζ are unknown. It can be seen from eqn (65) that a plot of $\log I_c v^{1/F}$ should give a straight line whose slope is proportional to the electron affinity, ψ . In principle, a value for the electron affinity and the field could be obtained independently by the combination of equations (65) and (67) in a similar way to the method outlined for metals in 2.3.8. However, in the present case this is not possible since ζ is also unknown.

Stratton obtained half-widths of between $2kT$ and $7kT$ for emission from the conduction band; similar equations apply for emission from the valence band and give half-widths in the range $3kT$ to $12kT$. Assuming emission takes place at room temperature, this gives considerably narrower half-widths than those obtained from the broad area electrodes, but these values are also considerably narrower than those obtained from atomically clean fabricated tip emitters. A possible explanation again is that "hot" electron emission means that it is incorrect to assume that $T \sim 300K$.

6.7.0 Results of the X-Ray analysis

6.7.1 Finally, further support for the existence of a semiconducting mechanism operating at emission sites on broad area electrodes comes from the evidence of the copper-chromium specimen detailed in Chapter 5. Firstly, within the limits of experimental error, there was no evidence of microprotrusions on the surface of the emitter which could give rise to the measured level of field enhancement when the specimen was first examined in the miniscan S.E.M. (fig 64) or subsequently when examined in the Cambridge microscope (fig 68). Secondly, the shift in the field emission spectra from this site (fig 67) can only be interpreted in terms of a semiconducting model. Thirdly, this very strong evidence must be combined with the results of the X-Ray analysis study (fig 69) which revealed the presence of certain foreign atoms within a very localised region in the estimated area of emission. Further, this impurity was located in a crack or grain boundary, a surface feature which has previously appeared in the microregion of field emission sites on broad area electrodes (34). It may also be significant that one particular impurity (Fe) found in the inclusion on the chromium-copper sample has been proposed as a possible cause of the electroluminescence found at emission sites

on copper by Hurley and Dooley [39]. Although it is impossible to be certain that the impurities detected by the X-Ray analysis were responsible for the observed electron emission (since the dimensions of the crack were far smaller than the accuracy of site location), the possibility is given further status by the additional evidence that removal of the impurities coincided with the disappearance of the emission site.

7.0 Conclusion

7.1 This thesis describes how a high resolution hemispherical type electron spectrometer, originally designed for measuring the energy spectra of electrons field emitted from fabricated micro-tip specimens, has been modified both electron optically and mechanically to obtain the spectra of the pre-breakdown electron currents emitted from localised sites on broad-area high voltage electrodes in U.H.V.

7.2 Four electrode materials have been examined, three of which (copper, stainless steel and titanium) are of interest in "passive" applications of high voltage vacuum insulation and one (chromium-copper alloy) which is used in the "active" application of high voltage vacuum switch contacts, where high current arcing continually alters the surface microtopography and may also result in phase changes in the alloy at the locally heated regions. Almost invariably, the energy spectra of the pre-breakdown electron currents show that the most energetic electrons are emitted from a level that is below the Fermi energy of the bulk metal electrode. Typically the spectra are shifted to low energies by $\sim 100 - 500\text{meV}$ compared to that normally obtained from a metallic field emission source. Generally, this shift is independent of the total site emission current for values $\lesssim 10^{-7}\text{A}$. Occasionally, however, sites on the copper specimens have a current dependent shift which is present even at the lowest measurable levels ($< 10^{-8}\text{A}$). Since the presence of a spectral shift is a property that is characteristic of micropoint semiconducting emitters, this behaviour suggests that a non-metallic emission mechanism is operating at the broad area electrode sites. In further support for this contention is the contradiction between the prediction of field enhancing "metallic" microprotrusions from the Fowler-Nordheim graphs and the electron optical studies of the microgeometry of

the cathode surface which shows no evidence of features capable of giving this predicted level of field enhancement.

7.3 A qualitative model has therefore been proposed that attempts to account for the observed results in terms of a semiconducting/insulating oxide or impurity microstructure overlaying the metallic electrode surface. The possibility that such an impurity microstructure is associated with an emission site is given additional support by the evidence obtained from a detailed X-Ray microprobe analysis on one of the sites studied. Another important feature of the spectra from some sites is the appearance of a second low-energy peak whose intensity is apparently dependent on the presence of adsorbed gas. Accordingly, this has been tentatively interpreted as being due to resonance tunnelling effects caused by adatoms on the semiconducting/insulating impurity microstructure.

7.4 In order to improve the understanding of this type of emission mechanism and to test the viability of the proposed model, further detailed investigations are necessary. Experimentally, these would include:

- (I) extending the range of measurements to a wider variety of materials in order to confirm whether or not the spectral shifts are characteristic of a particular material and hence of a particular impurity in that material.
- (II) the development of a more refined surface treatment technique which would allow a greater degree of control in the investigation of the effect of surface conditions on the emission spectra.
- (III) the development of an improved electron optical facility to gain more accurate location of emission sites and consequent high resolution imaging and elemental identification of the relevant

surface microstructure.

- (IV) further studies on the variation of the spectral shift with emission current to determine whether this is characteristic of a particular type of site.
- (V) correlation of the present work with the optical studies on electroluminescence at the emission sites to confirm whether or not they are consistent with the proposed model.

7.5 Theoretically, the most immediate requirement is to quantify the proposed model in order to substantiate its physical viability. This would involve calculations of the tunnelling probabilities between the metal/semiconductor and semiconductor/vacuum barriers to determine whether this agrees with the observed level of emission current. In conjunction with this it would be necessary to calculate the extent of electron heating in the conduction band and consequently the energy level at which the electrons tunnel through the semiconductor/vacuum potential barrier. If these calculations gave favourable support to the model it should then be possible to use these predictions for artificially constructing an experimental regime to simulate the known characteristics of the naturally occurring emission sites. If this was achieved, the final stage of the investigation would be to apply the knowledge to improve the insulation performance of high voltage electrodes in vacuum. This might involve, for example, the elimination of certain species of micro-impurities present in the electrode surfaces. The treatment necessary to do this would depend on whether the impurity was present as a micro-constituent of the electrode material or had become embedded in the surface during machining or polishing of the electrode surface. In the latter case an in-situ treatment under vacuum conditions might eliminate the impurity. Alternatively it might be found that some special metallurgical treatment

of the electrode material is necessary to rid the surface of a certain microstructure.

Brief mention should also be made of a further possible application of the findings of such simulation studies: this is the fabrication of a high current density "cold" electron source which would be of considerable interest in a number of industrial applications.

REFERENCES

- (1) R W Wood (1897) Phys. Rev. V, 1, 1-10.
- (2) R F Earhart (1901) Phil. Mag. 1, 147-159.
- (3) G M Hobbs (1905) Phil. Mag. 10, 617.
- (4) R A Millikan & R A Sawyer (1918) Phys. Rev. 12, 167-170.
- (5) R A Millikan & B E Shackelford (1920) Phys. Rev. 15, 239-240.
- (6) R A Millikan & C F Eyring (1926) Phys. Rev. 27, 51-67.
- (7) R A Millikan & C C Lauritsen (1928) Proc. Natl. Acad. Sci. (U.S.) 14, 45-49.
- (8) H W Anderson (1935) Elec. Eng. 54, 1315-1320.
- (9) E W Müller (1937) Z. Physik, 106, 541-550.
- (10) D Alpert (1953) J. App. Phys. 24, 860-876.
- (11) W P Dyke & J K Trolan (1953) Phys. Rev. 89, 799-808.
- (12) W P Dyke, J K Trolan, E E Martin & J P Barbour (1953) Phys. Rev. 91, 1043-1054.
- (13) W W Dolan, W P Dyke & J K Trolan (1953) Phys. Rev. 91, 1054-1057.
- (14) D Alpert, D A Lee, E M Lyman & H E Tomaschke (1964) J. Vac. Sci. Tech. 1, 35-50.
- (15) R H Fowler & L Nordheim (1928) Proc. Roy. Soc. (2nd Ser) A, 119, 173-181.
- (16) W S Boyle, P Kislink & L H Germer (1955) J. App. Phys. 26, 720-725.
- (17) H E Tomaschke & D Alpert (1967) J. Vac. Sci. Tech. 4, 192-198.
- (18) F Rohrbach (1966) Proc. 2nd Int. Symp. on Dischgs. & Elec. Ins. in Vac. Boston p.83.
- (19) F Rohrbach (1970) Proc. 4th Int. Symp. on Dischgs. & Elec. Ins. in Vac., Waterloo p.68.
- (20) L Cranberg (1952) J. App. Phys. 23, 518.
- (21) R P Little & S T Smith (1965) J. App. Phys. 36, 1502-1504.
- (22) R V Latham & E Braun (1968) Brit. J. App. Phys. 1, 1731-1735.
- (23) R V Latham & E Braun (1970) J. Phys. D, App. Phys. 3, 1663-1669.
- (24) A S Brah & R V Latham (1975) J. Phys. D, App. Phys. 8, L109-L111.

- (25) N F Olendzkaya (1968) Radio. Eng. Electron Phys. 9, 3.
- (26) E P Martynov (1972) Sov. Phys. Tech. Phys. 16, 1364-1369.
- (27) J Smalley (1976) J. Phys. D, App. Phys. 9, 2397-2401.
- (28) C Texier (1977) J. Phys. D, App. Phys. 10, 1693-1702.
- (29) R P Little & W T Whitney (1963) J. App. Phys. 34, 8, 2430-2432.
- (30) B M Cox & D E J Wort (1972) Vacuum 22, 453-455.
- (31) C S Walters, M W Fox & R V Latham (1974) J. Phys. D, App. Phys. 7, 911-919.
- (32) L Malter (1936) Phys. Rev. 49, 876-885.
- (33) R W Young (1973) Vacuum 4, 167-172.
- (34) B M Cox (1975) J. Phys. D, App. Phys. 8, 2065-2073.
- (35) B M Cox & W T Williams (1976) Proc. 7th Int. Symp. Dischgs. & Electrical Ins. in Vacuum Novosibirsk, 176-180.
- (36) B M Cox & W T Williams (1977) J. Phys. D, App. Phys. 10, L5-L9.
- (37) B Jüttner, V F Puchkarvov & W Rohrbeck (1975) Akademie der Wissenschaften der DDR Zentralinstitut für Elektronenphysik. Preprint 75-3.
- (38) B Jüttner, H Wolff & B Altricher (1975) Phys. Stat. Sol. (a) 27, 403-412.
- (39) R E Hurley & P J Dooley (1977) J. Phys. D, App. Phys. 10, L195-L201.
- (40) B N Klyarfel'd & A S Pokrovskaya-Sobolera (1970) Sov. Phys.-Tech. Phys. 15, 149-152.
- (41) B I Bleaney & B Bleaney (1976) Electricity & Magnetism, Oxford Press, p.48.
- (42) E Kemble (1937) The Fundamental Principles of Quantum Mechanics, M^cGraw-Hill, New York, p.90.
- (43) R H Good & E W Müller, "Field Emission" in Handbuch der Physik, Vol. XXI, Springer-Verlag, Berlin, 1956.
- (44) W P Dyke & W W Dolan (1956) Adv. in Elect. & Elect. Phys. 8, 89-185.
- (45) O A Richardson (1903) Phil. Trans. Roy. Soc. (2nd ser.) A 201, 497-549.
- (46) W B Nottingham (1941) Phys. Rev. 59, 906-907.
- (47) F M Charbonnier, R W Strayer, L W Swanson & E E Martin (1964) Phys. Rev. Letts. 13, 397-401.

- (48) L W Swanson, L C Crouser & F M Charbonnier (1966) Phys. Rev. 151, 327-340.
- (49) I Engle & P H Cutler (1967) Surf. Sci. 8, 288-306.
- (50) R D Young (1959) Phys. Rev. 113, 1, 110-114.
- (51) R D Young & E W Müller (1959) Phys. Rev. 113, 1, 115-120.
- (52) S G Christov (1978) Surf. Sci. 70, 32-51.
- (53) E L Murphy & R H Good (1956) Phys. Rev. 102, 1464-1473.
- (54) G E Vibrans (1964) J. App. Phys. 35, 2855-2857.
- (55) P A Chatterton (1966) Proc. Phys. Soc. 88, 231-245.
- (56) G P Beukema (1972) Physica 61, 259-274.
- (57) J M Bermond (1975) Surf. Sci. 50, 311-328.
- (58) F M Charbonnier & E E Martin (1962) J. App. Phys. 33, 1897-1898.
- (59) R D Young & E W Müller (1962) J. App. Phys. 33, 1, 91-95.
- (60) A G J Van Oostrum (1966) Philips Research Reports Supplements 1, 1-102.
- (61) L W Swanson & L C Crouser (1967) Phys. Rev. 163, 1, 622-641.
- (62) E W Plummer & A E Bell (1972) J. Vac. Sci. Tech. 9, 583-590.
- (63) N Nicolaou & A Modinos (1975) Phys. Rev. B 11, 3687-3696.
- (64) A Modinos & N Nicolaou (1976) Phys. Rev. B 13, 1536-1547.
- (65) A Modinos (1978) Surf. Sci. 70, 52-91.
- (66) N Kar & P Soven (1976) Solid State Comm. 19, 1041-1043.
- (67) R D B Whitcutt & B H Blott (1969) Phys. Rev. Letts. 23, 12, 639-640.
- (68) S L Weng (1977) Phys. Rev. Letts. 38, 434-437.
- (69) J J Czyzewski (1973) Surf. Sci. 39, 1-20.
- (70) R D Young & H E Clark (1966) Phys. Rev. Letts. 17, 7, 351-353.
- (71) R D Young & H E Clark (1966) App. Phys. Letts. 9, 7, 265-268.
- (72) T V Vorburger, D Penn & E W Plummer (1975) Surf. Sci. 48, 417-431.
- (73) C E Kuyatt & E W Plummer (1972) Rev. Sci. Inst. 43, 108-111.

- (74) E Braun, R G Forbes, J Pearson, J M Pelmore & R V Latham (1978)
J. Phys. E. Sci. Inst. 11, 1 - 7.
- (75) E W Plummer & J W Gadzuk (1970) Phys. Rev. Lett. 25, 21, 1493-1495.
- (76) E M Purcel (1938) Phys. Rev. 54, 818 - 826.
- (77) C E Kuyatt & J A Simpson (1967) Rev. Sci. Inst. 38, 1, 103-111.
- (78) A B El-Kareh & J C J El-Kareh, Electron beams, lenses and optics,
Vol. I, 57-59, Academic Press, 1970.
- (79) D W O Heddle, R G W Keesing & J M Kurepa (1973) Proc. Roy. Soc. A.
334, 135-147.
- (80) J Pearson. Private Communication.
- (81) E Munro (1972) Ph.D. Dissertation, University of Cambridge.
- (82) O Klemperer (1953) Electron Optics, Cambridge University Press, p.34.
- (83) R D Young & C E Kuyatt (1968) Rev. Sci. Inst. 39, 10, 1477-1480.
- (84) C B Duke & H E Alferieff (1967) J. Chem. Phys. 46, 3, 923-937.
- (85) J W Gadzuk (1970) Phys. Rev. B. 1, 5, 2110-2129.
- (86) E W Plummer & R D Young (1970) Phys. Rev. B. 1, 5, 2088-2109.
- (87) G E Gardner, O Lloyd & R J Urwin (1974) C.E.G.B. Research. 1. 20-28.
- (88) G A Burdick (1963) Phys. Rev. 129, 138-150.
- (89) P O Gartland & B J Slagsvold (1975) Phys. Rev. B 12, 10, 4047-4058.
- (90) R Stratton (1962) Phys. Rev. 125, 1, 67-82.
- (91) R Stratton (1964) Phys. Rev. 135, A 794 - A 805.
- (92) A Modinos (1973) Surf. Sci. 42, 205-227.
- (93) P Handler (1960) J. Phys. Chem. Solids. 44, 1-8.
- (94) W B Shepherd & W T Peria (1973) Surf. Sci. 38, 461-498.
- (95) L M Baskin, O I Lvov & G N Fursey (1971) Phys. Stat. Sol. (b) 47,
49-62.
- (96) G P Shcherbakov & I L Sokol'skaya (1963) Sov. Phys. - solid state 4,
12, 2581-2588.
- (97) N Nicolaou & A Modinos (1971) J. Phys. c. 4, 2859-2874.
- (98) N V Mileshkina & I L Sokol'skaya:
(1964) Sov. Phys. - solid state 5, 9, 1826-1832.
(1965) Sov. Phys. - solid state 7, 4, 838-843.
- (99) H H Race (1940) GEN ELECT REV. 43, 365 - 369.

ACKNOWLEDGEMENTS

The work described in this thesis was carried out during the tenure of an S.R.C. grant.

I would like to thank my Supervisor, Dr R V Latham, for many useful discussions and for his encouragement throughout the course of the work. I should also like to express my thanks to the Central Electricity Generating Board for permission to use the electron microscope facility at the Marchwood Engineering Laboratories and for financial support during my visits there. I am indebted to Mr O Lloyd and particularly Mr B M Cox for guidance and advice while working at Marchwood. I am also grateful to Mr F Lane and his workshop staff at Aston University for making a number of intricate components. Finally, I should like to thank Miss A Donaghy for typing the manuscript.



VIII International Symposium on
Discharges and Electrical Insulation
in Vacuum

5th - 7th September 1978



Sandia Laboratories
Albuquerque, New Mexico 87185
U.S.A.

A COMPARISON OF THE ELECTRON ENERGY SPECTRA OBTAINED FROM HIGH- β
EMISSION SITES ON BROAD-AREA HIGH-VOLTAGE ELECTRODES OF
COPPER, TITANIUM AND STAINLESS STEEL

N.K. Allen and R.V. Latham

Dept. of Physics, University of Aston, Birmingham B47ET, U.K.

ABSTRACT

A high resolution electron spectrometry facility has been used to measure the energy spectra of stable emission sites found on extended-area electrodes of copper, titanium and stainless steel. In all cases, the spectra indicate a non-metallic type of emission process similar to that observed with laboratory fabricated semiconductor emitters. Accordingly, qualitative interpretation has been given in terms of composite tunnelling processes from a metallic substrate through the semiconducting ambient oxide films found on commercially prepared electrode surfaces.

INTRODUCTION

The most widely favoured physical interpretation of the prebreakdown currents that flow across a high voltage vacuum gap assumes the presence of field-emitting metallic microprotrusions on the cathode surface, where the microscopic gap field is geometrically enhanced by a factor β to a microscopic value $> 10^9 \text{ V m}^{-1}$ which is the threshold for 'metallic' field emission to occur. It follows from this model that the value of β can be found indirectly from the slope of the Fowler-Nordheim (F-N) plot of the prebreakdown current/voltage characteristic, where typically $10 < \beta < 1000$; in addition, the area of the emitting site can be found from the intercept of the F-N plot.

This model would appear to provide a satisfactory explanation of the low- β (≤ 100) emission sites found on electrodes that have suffered surface damage in the form of microcoating following microdischarges or arcing, where independent electron optical evidence of surface profiles show microprotrusions of appropriate geometry. However, for stable undamaged electrode pairs, there is no complementary electron-optical evidence of surface microfeatures having geometries that would give β -values much greater than ~ 100 . Accordingly, it has been previously suggested by Latham and Braun [1] and Walters et al [2] that there is probably an alternative emission-mechanism that gives rise to 'high- β ' prebreakdown currents. More recently, Cox [3] has developed an in situ electron-optical technique for examining electron emission sites on broad-area electrodes and has in fact confirmed that those having high- β characteristics are not necessarily associated with protruding microstructure.

In order to obtain more information about the electron emission mechanism that gives rise to these high- β sites, a high-precision, electron spectrometry technique has been developed for obtaining the energy spectra of electrons field emitted from these high- β sites. Such spectra are extremely valuable since their shape, half-width and the position of the high-energy edge of the distribution relative to the Fermi level of the emitter give quantitative information about the emission mechanism. The first measurements to be made with this new facility compared the energy spectra of a reference tungsten field emitting tip with that obtained from the sites found on broad-area copper electrodes. The most important conclusion from this initial study, as reported in a recent publication, [4] was that these broad-area sites had a non-metallic character, suggesting

at they originated from semiconducting inclusions in the electrode surface. The present paper reports on the extension of this new type of measurement to other electrode materials with the aim of determining whether high- β features are always associated with non-metallic processes, irrespective of the electrode material.

EXPERIMENTAL

The experimental facility consists of a high-voltage test gap interfaced with a 180° electrostatic deflection electron energy analyser and is shown schematically in Figure 1; the whole system being mounted in a UHV chamber with an operating pressure of $\sim 10^{-10}$ torr. For these experiments, the test cathodes (C) are in the form of 14mm diameter discs of thickness 1mm with rounded edges and form part of a plane-parallel electrode geometry. The anode (A) is of highly polished stainless steel with an axial 1mm diameter probe hole (P). A bellows-linked external mechanical scanning facility allows the specimen to be moved parallel to the two electrodes. There is also a 50W electron bombardment facility to provide in situ outgassing of either cathode or anode by the appropriate positioning of the low voltage filament F. The specimens used in this investigation had freshly polished "test" surfaces and were spirit cleaned in an ultrasonic bath prior to mounting in a specimen holder that is insulated for applying voltages to ~ 15 kV.

The spectrometer, with a resolution of ~ 25 meV, is based upon a 180° hemispherical deflecting element, H, with associated input and output lenses and O respectively. The function of the input lens assembly is to de-energise the electrons to the analysing energy of 2 eV and focus them on to the entrance aperture (D) of the deflecting element. Those electrons which have the correct energy to be transmitted by the deflecting element are

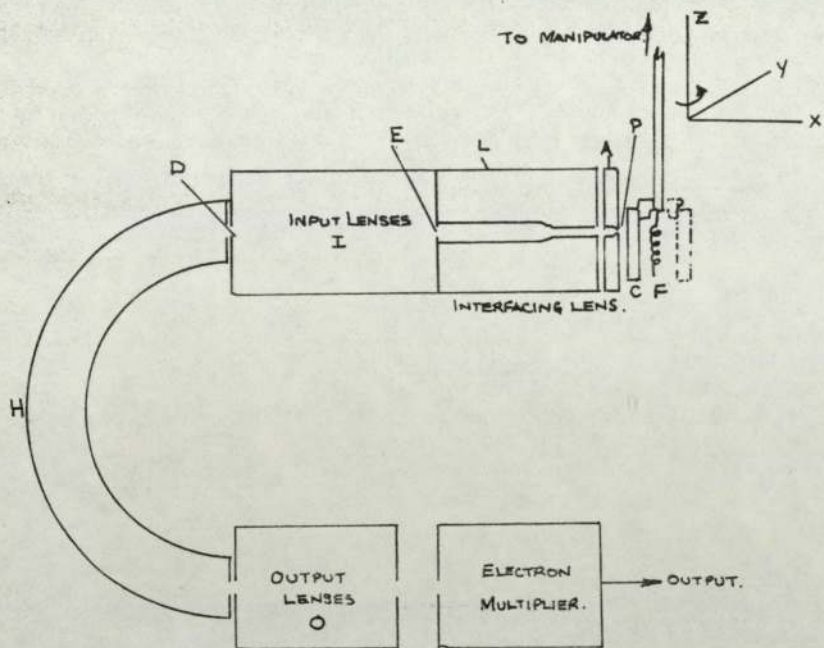


Figure 1.

en reaccelerated by the output lenses and focused on to an electron multiplier. Full details of the construction, operation and performance of this instrument can be found elsewhere [5].

An electrostatic lens has been designed to interface the electrons emerging from the high-voltage "test" gap with the input requirements of the analyser. This is a two-element lens formed from the anode (A) and a second component (L) and has two main functions: (i) to focus the diverging beam of electrons leaving the probe hole (P) into a parallel beam at E and (ii) to decelerate the electrons from a typical energy of ~ 5 keV at (P) to ~ 2 keV at E. Further information about the lens design and other experimental details of the technique are to be published in a forthcoming paper now in preparation.

A standard experimental procedure is followed for all new specimens. The first step is to apply an increasing voltage between C and A to determine whether there is a site present on the cathode that will emit within the available field range; this is limited by a maximum gap voltage of ≥ 10 kV that, typically, can only be sustained across gaps > 0.5 mm if flash-over is to be avoided. To position a site opposite the probe hole (P) the specimen is scanned in a raster pattern in front of P until the emission current is registered at L. Micro-adjustments are then made to maximise this current and centralise the site with respect to the probe hole: under these circumstances, the total emission current from the site passes through P and is recorded at L. The current-voltage characteristics of the site is now measured, which may then be interpreted in the form of an I-N plot to provide complimentary information about such sites. By applying a suitable positive voltage to the electron beam can be focused to pass into the analyser input lens (I). Adjustments to the focusing of the analyser can then be made to obtain the energy distribution of the electron beam.

RESULTS

The principle of this new type of measurement is illustrated in figure 2(a). This compares (i) a typical energy distribution previously obtained from a reference tungsten emitter [4][5] with (ii) that from a site on a broad-area copper electrode at an identical temperature and pressure.

Similar measurements have now been made on the sites found on titanium and stainless steel electrodes. These materials are of particular interest since they are commonly used in high voltage vacuum technology as providing stable electrode pairs. The energy spectra obtained from typical stable

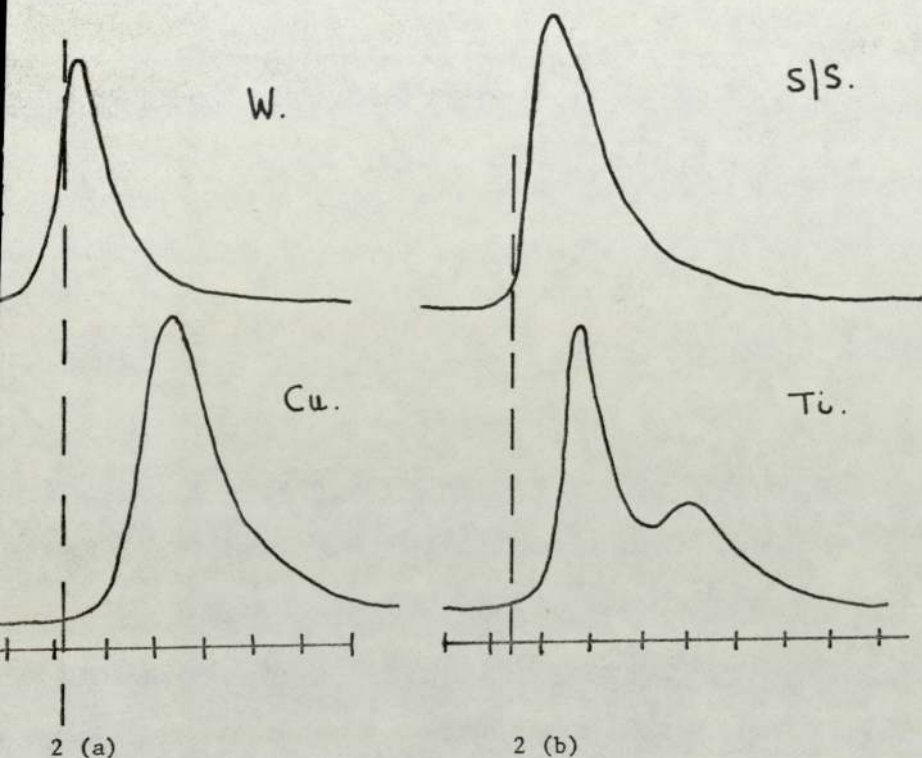


Figure 2. The electron energy spectra obtained from Copper, Stainless Steel and Titanium broad area electrodes compared with that obtained from a reference Tungsten emitter. The position of the Fermi level in each case is shown by the vertical broken line. Electron energy in eV, 0.2 eV/div - x axis (going from high energy to low energy left to right). Electron current per unit energy - y axis. [4] [5].

Figure 2.

sites found on these materials are reproduced in Figure 2(b), where the Fermi level of the emitter has again been marked. It will be noted that the spectrum from the titanium electrode has a double-peak structure extending further into the low-energy range where the separation of the peaks is ~ 500 meV. The complimentary F-N plots for these sites are shown in Figure 3, which also includes the characteristic for the earlier copper result.[4].

For the purposes of the subsequent discussion, it is convenient to correlate this experimental data in terms of four parameters: (i) the displacement δE of the 73% point up the high-energy slope from the Fermi level (see Discussion section), (ii) the half-width of the distribution in $(\Delta E)_{\frac{1}{2}}$, (iii) the high-energy slope width and (iv) the β -values of the sites, measured from the F-N plots. The values of these parameters found for the emitters on the three electrode materials are presented in Table 1.

Table 1

Material	$\frac{1}{2}$ Width (ΔE) $_{\frac{1}{2}}$ (mV)	Energy Slope Width (eV)	Shift δE (mV)	β value
Copper	350	0.16	300	700
Stainless Steel	250	0.14	100	400
Ti	250	0.14	250	500

DISCUSSION

Four main conclusions can be drawn from Figures 2(a) and 2(b)

(i) compared with the spectrum from the reference tungsten emitter, the spectra from the sites on broad area electrodes are shifted in the low energy direction so that no electrons are emitted from above the Fermi level (FL). The extent of this shift (δE) is shown in Table 1, where δE is the difference in the energy between a point 73% up the high-energy slope of the spectrum obtained from the tungsten emitter - which theoretically defines the position of the Fermi level [6] - and the same point on the spectra obtained from emitters on the broad area electrodes.

(ii) all spectra have comparably steep high energy slopes, and, with the exception of copper, have comparable half-widths for the main peak.

(iii) the double-peaks of the Ti spectrum, with their separation of ~ 500 meV, suggests that there is an additional emission mechanism operating with this material.

(iv) the β -factors of all sites, as determined indirectly from the F-N plot of the current voltage characteristics (Figure 3), are generally high (400-700) and would therefore require somewhat unrealistic geometries for the metallic emitter model.

The most notable of these features is the low-energy shift in the broad area spectra since this indicates a non-metallic type of emission mechanism. In fact, reference to the literature [7] strongly suggests that their character is more closely related to the spectra obtained from semiconducting emitters. On this basis, the shift could, in principle, be interpreted in terms of (a) a resistive drop along the emitter due to

the current flowing in it, (b) electron emission only occurring from states below the Fermi level and (c) a combination of (a) and (b). Alternative (a) is normally only observed with long thin artificially fabricated emitters drawing currents in excess of 10^{-4} amp. In the present experiments, emitters could only be sub-microscopic in dimension, where the total emission current drawn from a site whilst recording its spectrum is only 10^{-10} amps; moreover, the shift is insensitive to an order of magnitude change of the emission current. For these reasons, mechanism (a) is not thought to provide a viable physical explanation for the shift.

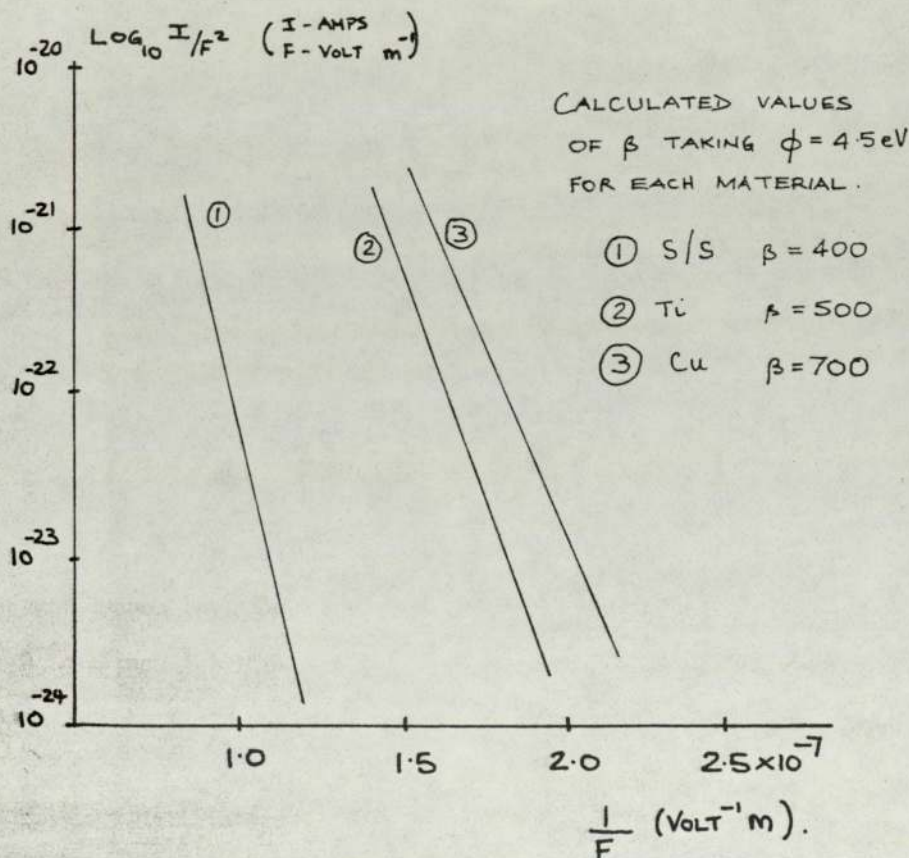
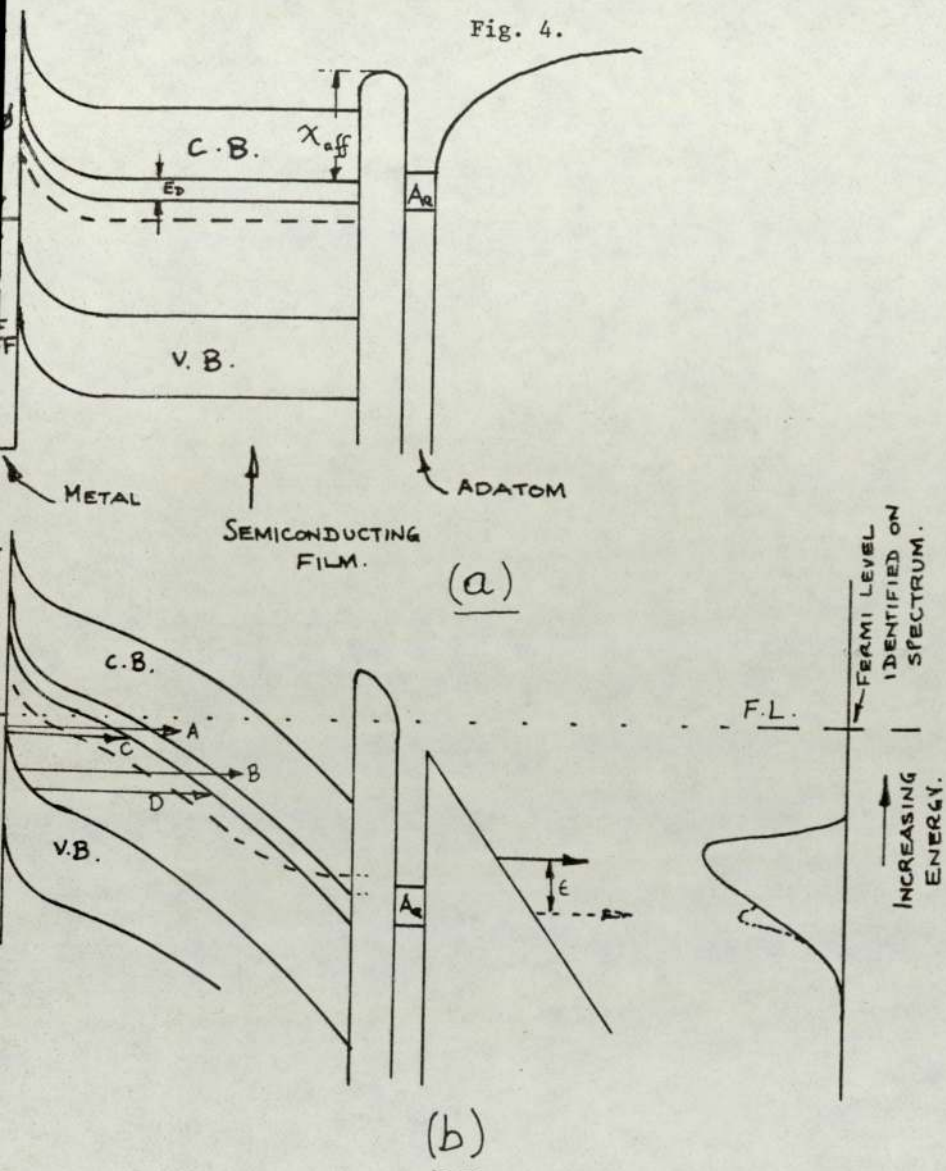


Fig. 3.

In considering mechanism (b), it has to be appreciated that despite U.H.V. conditions and outgassing of electrodes, it is still not possible to precisely define the state of the surface in atomic terms as is the case with field emitting tips. Thus, the present broad-area electrode surfaces will have a complicated and variable atomic composition due to the likely presence of a multi-species oxide covering of variable thickness: in addition, the situation may be further complicated by the presence of adsorbed gas atoms and contaminant inclusions. Consequently, it would be unrealistic to attempt more than a generalised qualitative model at this stage, since even the theory for atomically clean semi-conducting tips is still not complete. It would seem reasonable to suppose however, that any region on the cathode is likely to be characterised by a metal substrate overlaid with a semi-conducting oxide film. Consequently, a simple energy band representation of such a surface, together with the associated potential barrier might appear as shown in Fig. 4(a). When a high positive electric field is applied to the surface the energy band structure would be modified to the form shown in Fig. 4(b). On the basis of this model, it is possible to envisage at least four distinct two-stage electron tunnelling mechanisms: A - from the Fermi level (FL) of the metal into the conduction band of the semiconducting layer, followed by a further tunnelling through the surface potential barrier into the vacuum; B - between the valence and conduction bands of the semiconducting layers, followed again by vacuum tunnelling; C - from the FL of the metal to an impurity level in the band gap of the semiconducting layer and hence through the surface potential barrier and D - from the valence band of the semiconducting layer into an impurity level, followed again by vacuum tunnelling. It is of particular

Fig. 4.



- (a) One dimensional energy diagram of composite metal/semiconducting overlayer. C.B. is the conduction band of the film and V.B. the valence band. A represents an energy band in the adatom layer. ϕ is the work function of the metal and E_F the Fermi level. χ_{aff} is the electron affinity level in the film and E_D the energy gap between the conduction band and a possible impurity level. The broken line indicates the position of the Fermi level, F.L. which is identical in the metal and the bulk of the semiconducting film.

b) The effect on the energy diagram of (a) on application of a high positive electric field to the surface resulting in field penetration (see, for example, Baskin et al. (8)). F.L. is the Fermi level in the bulk of the metal which is the reference identified on the energy distributions. The proposed emission mechanisms are (A), (B), (C) and (D). In addition there is the possibility of enhanced emission at an energy ϵ below the main peak if there is an appropriate adatom energy level present.

Significance that in the case of mechanisms A and B it is possible for the electrons to be accelerated within the conduction band as a result of field penetration and thereby give rise to a flux of hot electrons arriving at the potential barrier. In terms of the energy band diagram, this means that they would be occupying higher energy states and therefore "see" a thinner barrier through which to tunnel. Accordingly, they would have a greater probability of tunnelling into the vacuum levels which would result in an enhanced electron current as is inferred by the high β -factors calculated from the F-N plots of Figure 4. A further point in favour of this process is that it could give rise to excitation of surface atoms that could lead to the "cathode-spot" electroluminescent effects recently reported by Harley & Dooley [9].

In considering the double-peak Ti spectrum, it can be reasonably concluded that the high energy peak originates from one of the tunnelling processes discussed above. However, an additional explanation is required for the second peak which occurs at an energy of ~ 500 meV below the first. One possible explanation is by a resonance tunnelling process caused by the presence of a particular adatom species on the surface which has an energy level opposite the conduction band of the semiconducting layer (see Figure 4(b)).

It should be finally noted that with the widely varying atomic surface composition already discussed, it is likely that there will only be isolated sites on an electrode surface at which the band structure etc. has a configuration that is potentially favourable for one of the emission mechanisms to occur. This conclusion would seem to be in agreement with the experimental fact that this type of emission process is highly localised with only one or two such sites generally being found on a given specimen.

REFERENCES

- R.V. Latham and E.Braun, J.Phys.D., Appl.Phys. 1, 1731, (1968).
C.S.Walters, M.W.Fox and R.V.Latham, J.Phys.D., Appl.Phys.7,911,(1974).
B.M.Cox, J.Phys.D.,Appl.Phys. 8, 2065, (1975).
N.K.Allen and R.V.Latham, J.Phys.D.,Appl.Phys. 11, L55, (1978).
E.Braun, R.G.Forbes, J.Pearson, J.M.Pelmore and R.V.Latham,
J.Phys.E., Sci.Instrum. 11, 222, (1978).
R.D. Young, Phys.Rev., 113, 110, (1959).
W.B. Shepherd and W.T. Peria, Surface Sci. 38, 461, (1973).
L.M. Baskin, O.I. Lvov and G.N.Fursey, Phys.Stat.Sol.(b), 47, 49,(1971).
R.E. Hurley and P.J. Dooley, J.Phys.D., Appl.Phys. 10, L195, (1977).

LETTER TO THE EDITOR

The energy spectra of high- β electron emission sites on broad-area copper electrodes

NK Allen and RV Latham

Department of Physics, University of Aston, Gosta Green, Birmingham B4 7ET

Received 5 January 1978

Abstract. An original high-resolution electron spectrometry technique has been developed to obtain the energy spectra of electrons field emitted from localised sites on high-voltage electrodes. From a comparison of these spectra with those obtained from a reference tungsten emitter, it appears that the sites are non-metallic.

It is now generally accepted that the prebreakdown currents flowing between clean broad-area high-voltage electrodes in ultra-high vacuum originate from highly localised field electron emission sites. There remains however, considerable doubt as to the precise mechanism operating at these sites. The most widely favoured model assumes the presence of field-emitting metallic microprotrusions on the cathode surface, where the macroscopic gap field is geometrically enhanced by a factor β to a microscopic value $\geq 10^9 \text{ V m}^{-1}$ which is the threshold for 'metallic' field electron emission to occur. In this case, the value of β can be found indirectly from the slope of the Fowler-Nordheim (F-N) plot of the prebreakdown current/voltage characteristic, where typically $10 < \beta < 1000$.

However, there is no complementary electron-optical evidence of surface micro-features having geometries that would give β -values much greater than ~ 100 . Accordingly, it has been previously suggested (Latham and Braun 1968, Walters *et al* 1974) that there is probably an alternative emission mechanism that gives rise to 'high- β ' prebreakdown currents. More recently, Cox (1975) has developed an *in situ* electron-optical technique for examining electron emission sites on broad-area electrodes and has in fact confirmed that those having high- β characteristics are not necessarily associated with protruding microstructure.

This letter describes a new, high-precision, electron-spectrometry technique for obtaining original measurements of the energy spectra of electrons field emitted from these high- β sites. Such spectra are extremely valuable since their shape, half-width and the position of the high-energy edge of the distribution relative to the Fermi level of the emitter give quantitative information about the electron emission mechanism.

The experimental facility, which is mounted in a UHV chamber with an operating pressure of $\sim 10^{-10}$ Torr, is shown schematically in figure 1. It consists of a high-voltage test gap interfaced with an electrostatic deflection electron energy analyser. The 'test' high-voltage gap has a plane parallel geometry consisting of the specimen cathode (C) and a highly polished stainless steel anode (A) with an axial 1.0 mm diameter probe hole (P). A mechanical scan facility allows the specimen to be moved parallel to the

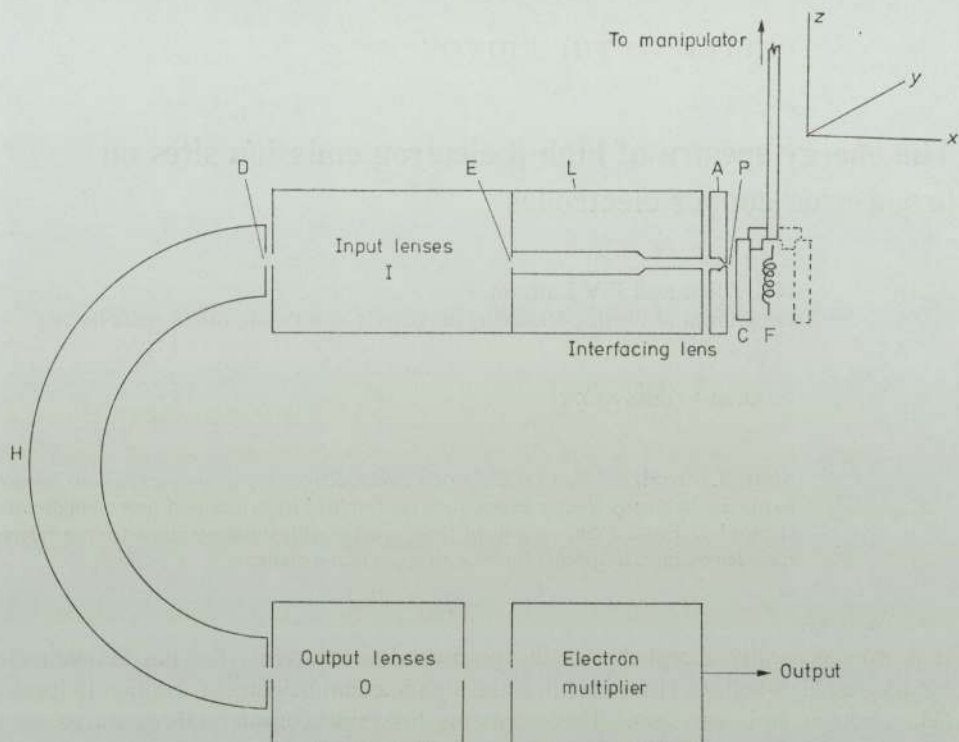


Figure 1. A schematic diagram showing the lay-out of the spectrometer, ancillary electron lens systems and the 'test' high-voltage gap.

anode in the y - z plane, whilst maintaining a known constant gap between the two electrodes. The specimens used in this work are copper discs 14 mm in diameter and 4 mm thick having a suitably rounded edge profile. They have a freshly machined 'test' surface and are spirit cleaned in an ultrasonic bath prior to mounting in a specimen holder that is insulated for applying voltages of up to ~ 15 kV. A 50 W electron bombardment facility provided by a low-voltage heated filament (F) is used for either out-gassing the specimen or the front anode.

The spectrometer, with a resolution of ~ 25 meV, is based upon a 180° hemispherical deflecting element, H, with associated input and output lenses I and O respectively. The function of the input lens assembly is to decelerate the electrons to the analysing energy of 2 eV and focus them on to the entrance aperture (D) of the deflecting element. Those electrons which have the correct energy to be transmitted by the deflecting element are then reaccelerated by the output lenses and focused on to an electron multiplier. Full details of the construction, operation and performance of this instrument can be found elsewhere (Braun *et al* 1978).

The probe hole (P) and electrode (L) form an electrostatic lens which has been specially designed as an interfacing element between the test gap and the analyser. It has the twofold action of (i) focusing the diverging beam of electrons leaving the probe hole (P) into a parallel beam, and (ii) decelerating the electrons from a typical energy of ~ 5 keV at P to the ~ 2 keV requirements at the entrance aperture (E) of the analyser.

The first stage in the experiment is to increase the voltage between C and A until a specimen current is recorded at A indicating the presence of emitting sites. To position a

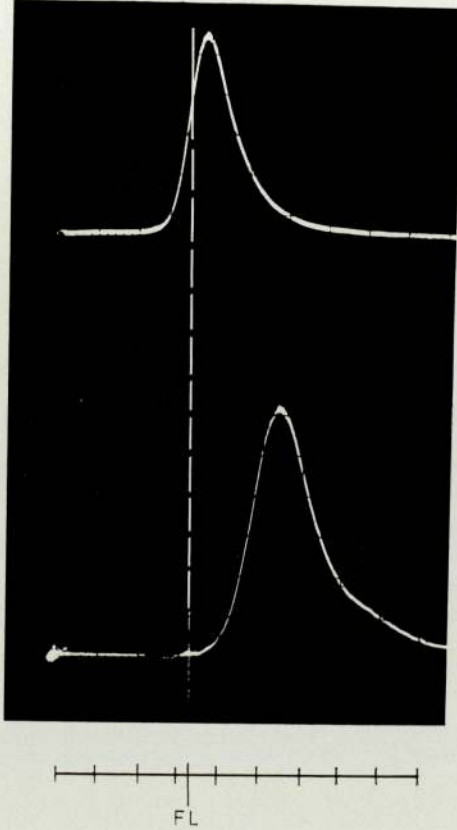


Figure 2. Electron energy spectrum obtained from (i) a reference tungsten emitter and (ii) a site on a broad-area copper cathode. The position of the Fermi level (FL) of each emitter is also shown. Electron energy in eV, 0.2 eV/div, is x axis (going from high energy to low energy left to right). Electron current per unit energy is y axis.

site opposite the probe hole (P), the specimen is scanned in a raster pattern in front of P until a current is registered at L. Micro-adjustments are then made to maximise this current and centralise the site with respect to the probe hole. At this stage, a voltage-current characteristic, and hence Fowler-Nordheim plot of the site, can be measured. By applying a suitable positive voltage to L, the electron beam can be focused to pass into the analyser input lens (I). Adjustments to the focusing of the analyser can then be made to obtain the energy distribution of the electron beam.

Figure 2 (plate) compares (i) a typical energy distribution previously obtained from a reference tungsten emitter at room temperature and a pressure of $\sim 10^{-10}$ Torr using this instrument (Braun *et al* 1978) with (ii) that obtained under identical temperature and pressure conditions from a site situated near the centre of one of the copper samples used in the present investigation. In both cases, the spectra are stable with time and are reproducible from specimen to specimen. It should be noted that the electron energy is decreasing from left to right. From a previous calibration of the instrument (Braun *et al* 1978) it is also possible to identify the Fermi level (FL) of the emitter. The corresponding Fowler-Nordheim plot for the copper site predicts a β -value of ~ 750 if a work-function of 4.5 eV is assumed for the emitter.

From a comparison of the two spectra of figure 2, three important differences in the emission characteristics can be immediately identified: (i) unlike the reference tungsten emitter all electrons from the site on the copper electrode are emitted from states well below the Fermi level, (ii) the half-width of the copper distribution (~ 360 mV) is broader than that of the tungsten emitter (~ 240 mV), (iii) the shape of the copper spectrum is more symmetrical, i.e. lacking the characteristic sharp high energy slope found for tungsten. In addition to these observations, the β -value of ~ 750 obtained from the F-N plot is unrealistically high for the metallic whisker model.

It can be concluded that the general character of the electron energy spectra obtained from broad-area emission sites differs markedly from that to be expected from metallic emitters. Whilst the wide half-widths and symmetrical shape of the distributions could possibly be explained in terms of tip contamination (Braun *et al* 1978), the shift of ~ 0.35 eV in the position of spectrum relative to the Fermi level cannot be explained in terms of the Fowler-Nordheim free-electron model. In fact, the type of spectral shift obtained in the present investigation more closely resembles the behaviour of semiconducting emitters (Shepherd and Peria 1973). These findings would therefore appear to support the contention that broad-area electrodes can support a more complicated field electron emission mechanism (Walters *et al* 1974, Cox 1975), possibly involving semiconducting inclusions. No specific model is proposed at this stage of the investigation, since more comprehensive experimental data is required from a wider range of electrode materials and surface conditions.

Acknowledgment

The authors wish to thank the SRC for their support of this work.

References

- Braun E, Forbes R G, Pearson J, Pelmore J M and Latham R V 1978 *J. Phys. E: Sci. Instrum.* **11** at press
- Cox B M 1975 *J. Phys. D: Appl. Phys.* **8** 2065-73
- Latham R V and Braun E 1968 *J. Phys. D: Appl. Phys.* **1** 1731-5
- Shepherd W B and Peria W T 1973 *Surface Sci.* **38** 461-98
- Walters C S, Fox M W and Latham R V 1974 *J. Phys. D: Appl. Phys.* **7** 911-19